Development of Higher-Order-Mode (HOM) Absorbers for KEKB Superconducting Cavities

Tsuyoshi Tajima

Doctor of Philosophy

Department of Accelerator Science
School of Mathematical and Physical Science
The Graduate University for Advanced Studies

1999

Table of Contents

List of Abbreviations

AR	Accumulation Ring
CEBAF	Continuous Electron Beam Accelerator Facility, (an accelerator at TJNAF)
CESR	Cornell Electron Storage Ring
DESY	Deutsches Elektronen-Synchrotron in Hamburg
EDX	Energy Dispersive X-ray (analysis)
FWHM	Full-Width-at-Half-Maximum
HER	High Energy Ring
HIP	Hot Isostatic Press
HOM	Higher Order Mode
IP	Interaction Point
IR	Infrared
JAERI	Japan Atomic Energy Research Institute
KEKB	KEK, B Factory project accelerator
LBP	Large Beam Pipe
LER	Low Energy Ring
LHC	Large Hadron Collider
MR	Main Ring
RF	Radio Frequency
RGA	Residual Gas Analyzer
SBP	Small Beam Pipe
SCC	Superconducting Cavity
SEM	Scanning Electron Microscopy
SLAC	Stanford Linear Accelerator Center
SOR	Synchrotron Orbit Radiation
SRF	Superconducting Radio Frequency
TE	Transverse Electric
TESLA	TeV Energy Superconducting Linear Collider
TJNAF	Thomas Jefferson National Accelerator Facility
TM	Transverse Magnetic
TRISTAN	Transposable Ring Intersecting Storage Accelerator in Nippon

List of Symbols

α	Momentum compaction factor
c	Speed of light
D	Dipole moment
e	Charge of electron (1.6×10^{-19} C)
E_{acc}	Accelerating field
E_0	Nominal energy of particle
ε	Permittivity
f	Frequency
f_r	Revolution frequency
f_a	Applied frequency
ϕ	Synchronous angle
I	Beam current
λ	Line density of particles
M	Number of bunches
μ	Permeability or an integer (in case of mode number of instability)
N	Number of particles per bunch
p	An interger
q	Charge
Q	Quality factor
Q_0	Unloaded quality factor
Q_L	Loaded Q
R_s	Shunt impedance
R/Q	Effective shunt impedance
σ_x	Horizontal beam size
σ_y	Vertical beam size
σ_z	Longitudinal beam size
T_0	Revolution time
τ	Instability growth time
V_c	Cavity voltage
W_Z	Longitudinal wake function
W_T	Transverse wake function
ω_s	Angular synchrotron frequency
ω_r	Angular resonant frequency
Z	Impedance
$Z_{//}$	Longitudinal impedance
Z_T	Transverse impedance

Abstract

KEKB, B-Factory at KEK, is a double ring collider of 3.5 GeV positrons and 8 GeV electrons. The two rings were named LER (Low Energy Ring) and HER (High Energy Ring) after their energies. They were constructed in the tunnel that was used for TRISTAN. One of the main physics objectives of this facility is the detection of so-called CP-violation, which may give an answer to the question why the amount of matter and anti-matter is not the same.

With regard to the accelerator, KEKB is a very challenging accelerator in the sense that it has to deal with ampere-class current (2.6 A for LER and 1.1 A for HER), which is about two orders of magnitude higher than that of TRISTAN and has never been used with any machine before. To achieve a high current without suffering from single bunch instabilities, the beam will consist of some 5000 bunches, i.e., every RF bucket filled with a bunch of several 10^{10} positrons/electrons. In this case, the HOM (Higher Order Mode) fields that are excited by a bunch at accelerator components, such as RF cavities, are likely to affect the following bunches because the decay times of the fields are sometimes longer than the bunch interval, e.g., 2 ns for KEKB.

This situation makes the beams susceptible to coupled bunch instabilities, i.e. intolerable growth of the oscillatory coupled-bunch motions. For the success of KEKB, it is essential to lower the HOM impedances so that the threshold currents are higher than the designed currents or they are manageable with a bunch-by-bunch feedback system. The most effective way to achieve this is to lower Q's (quality factors) and R/Q's (effective shunt impedances) of most HOM's in RF cavities since RF cavities are normally the main source of HOM's.* This can be embodied by so-called HOM-damped structures. At KEK, we use two types of such structures, one is called ARES (Accelerator REsonantly coupled Structure) and the other is SCC (Superconducting Cavity).

ARES is the invention of creative people at KEK. Using a three-cell structure with a large energy-storing cell, it can lower the R/Q of fundamental mode to 15. Whereas, SCC is inherently suited for high intensity machines, such as KEKB, since the aperture of the beam pipe can be larger with enough accelerating gradients, i.e., reduced interaction with a beam, and by virtue of the high gradients, the number of total cavities can be reduced and thus the total impedance can be lowered as well as saving capital costs. Furthermore, at KEK, we can utilize the refrigerator that was used for TRISTAN, a substantial cost saving.

The damped structure for SCC has large beam pipes with absorbing material. Most of the HOM's go through these pipes and are absorbed. This scheme, however, that puts microwave absorbing material, such as ferrite, in the same SCC structure and vacuum was a

*In large-diameter rings such as KEKB, accelerating mode can also be a source of instability so we need to reduce R/Q to avoid it.

new approach and its feasibility had to be proved. Therefore, one of the key components for the success of this scheme was the HOM absorber, which is the subject of this thesis.

The HOM absorber for SCC requires sufficient HOM damping, power handling capability (5 W/cm^2 <), UHV (Ultra High Vacuum) compatibility (~$1x10^{-9}$ Torr[†] >), free of particulates that enter and degrade the cavity, and some surface electric conductivity to prevent charge-up and sparks.

Due to the favorable results of preliminary tests on HOM damping, outgassing rate, high availability and short delivery time, we chose to use a microwave-absorbing ferrite IB-004 from TDK, Inc. However, the most difficult part of the development was to bond this material with high integrity to meet the above-mentioned requirements. Neither brazing nor soldering of commercial tiles (60 x 60 x 4 mm^3) were successful due to cracking during the cooling down from brazing/soldering temperatures. Also, we thought of making a cylindrical-shaped ferrite, but experts at TDK commented that making a thin (~4 mm) cylinder of large diameter (220/300 mm) ferrite would be very difficult and probably crack. Forming a thin layer with, for example, plasma spraying, would probably result in a very porous surface and be incompatible with UHV and free-of-particulate conditions.

The idea, that we demonstrated its usefulness and high potential for more applications, is sinter-bonding of pre-sintered ferrite powder directly onto the inner surface of a copper beam pipe with HIP (Hot Isostatic Press). Having developed the proper tooling and optimizing the conditions, we succeeded in establishing a technique to make full-size absorbers that met all the requirements. SEM (Secondary Electron Microscopy) and EDX (Energy Dispersive X-ray) analyses showed high integrity of the bonding, namely, a 90 μm-wide transition region was formed, which consists of a mixture of ferrite and copper with a narrower band of silicon. This firm bonding appears to have been accomplished by a combination of interlocking and diffusing the copper and ferrite. In addition, acoustic tomography showed high uniformity of the bonding through the entire area.

A 1/3-size (109 mm in ferrite outer diameter) model was first manufactured for various evaluation tests using a TM01 mode of 2.45 GHz 5 kW power source. A maximum absorbed power of 3.95 kW (average power density of 8.3 W/cm^2 with the maximum density of 29 W/cm^2) was reached without any problem. In addition, at this experiment, the effectiveness of having tapers at the edges to avoid excess heating was confirmed, thereafter 25-mm-long tapers have been machined on both ends.

Then, two full-size absorbers, 220/300 mm in outer diameter of ferrite, 120/150 mm in length and 4 mm in thickness, were manufactured. A milestone experiment, the first beam test, was performed at TRISTAN MR (Main Ring) in 1995. We installed a full-size (300-mm in diameter) absorber at the Nikko section of the ring with tapers on both sides and tested its

---

[†] We use Torr throughout this thesis. 133 Torr = 1 Pa.

performance. There was no spark, discharge, damage or degradation up to an available maximum single bunch current of 4.4 mA or 2.8 x 10^{11} electrons per bunch, which is 20 times that of KEKB-HER.

The second important test was carried out at TRISTAN AR (Accumulation Ring) in 1996. A fully equipped superconducting cavity of KEKB shape was assembled with HOM absorbers attached on the upstream and downstream sides, installed in the east tunnel and tested for three periods of time. SCC could store 0.57 A, about half of the design current at KEKB-HER, without any instability due to cavity HOM's. No degradation of cavity performance was observed and up to a total power of 4.2 kW was recorded at the absorbers without any problem, which is about 80 % of the power expected at KEKB-HER. After these tests, micro-cracks (10 μm >, invisible with the naked eye) were found in the ferrite, but the following intense investigation showed that these cracks were present before these tests and were caused by baking. In other words, these tests demonstrated that cracks do not affect the necessary performance of superconducting cavities.

Finally, a total of 8 absorbers were assembled with four KEKB-HER superconducting cavity modules and installed in the Nikko D11 tunnel in the summer of 1998. These modules have shown gap voltages of 2.5-3 MV without beams, which is much higher than the design value of 1.5 MV, assuring a significant margin for stable operation. Since the commissioning started in December of 1998, the system has been operating very smoothly. As of January 31, 2000, the maximum current achieved so far is 0.51 A, about half of the designed value. All HOM absorbers have been showing similar behavior and the maximum power absorbed so far is about 2.5 kW per module, which is consistent with calculations.

Chapter 1

Introduction

1.1 Background

1.1.1 Accelerators and SRF

In the past decades, accelerators have been improving very rapidly. They have been aimed at two frontiers, higher energy (~TeV) and higher intensity or beam current (~Amperes). The former has been pushed for the search of higher energy elementary particles, such as top quark, and the latter for other physics areas such as CP violation and various researches using brighter X-rays. In both frontiers SRF (Superconducting Radio Frequency) cavities have been considered, constructed and operated. In the past 15 years large scale applications of SRF cavities prevailed in the world, starting from TRISTAN at KEK, followed by HERA at DESY, LEP at CERN, and CEBAF at TJNAF. All the machines have been successfully operated and the SRF technology has become more matured.

The accelerators presently under commissioning, being constructed or planned in both frontiers with SRF are CESR-III [82], KEKB [80], LHC (Large Hadron Collider) [79], TESLA (TeV Energy Superconducting Linear Accelerator) [81], JHF (Japan Hadron Facility)[1] [77], ESS (European Spallation Source) [94], and SNS (Spallation Neutron Source) [78]. SRF is certainly one of the key technologies for accelerators in the 21st century.

Although there have been tremendous improvements in the understanding of field emission with studies using high-speed thermometry and computer simulations [76], there are, however, subjects that remain to be more understood, improved and controlled for the stable operation of the machines at higher fields and intensities. They include field emission related issues, such as the sources and their preventive measures or trips during operation and their causes and preventive measures.

1.1.2 KEKB

KEKB, B-factory at KEK, is one of the higher-intensity-frontier machines.[2] It is an asymmetric energy collider with 8 GeV electron and 3.5 GeV positron beams that was constructed in the previous TRISTAN tunnel. One of the physics goals was to make a detailed study of the B-meson, in particular to observe possible CP violation effects in its

[1] Joint project of KEK and JAERI.

[2] PEP II is a similar machine at SLAC (Stanford Linear Accelerator Center), U.S.A.

decay. The energy difference between the electron and positron beams gives a boost to the produced B-meson pairs. This enables the measurement of time dependent features of B-meson decay where a large CP asymmetry is predicted to show up [70]. However, to observe CP asymmetry, more than 10 million B-meson pairs are required, which translates into a luminosity of 1 x 10^{34} $cm^{-2}s^{-1}$, a luminosity that no machine has ever reached.

To achieve this luminosity it is necessary to build a machine that carries a beam current of the order of amperes for the following reason.

Luminosity, L, is given by [3, 83]

$$L = 2.2 \times 10^{34} \xi (1 + r) \left(\frac{E \cdot I}{\beta_y^*} \right), \qquad (1.1.2\text{-}1)$$

where ξ is the beam-beam tune shift, r the ratio of the vertical beam size (σ_y) to the horizontal beam size (σ_x) at the IP (Interaction Point), which is usually very small compared to 1, I the current in ampere, E the beam energy in GeV and β_y^* the β-value at the IP in cm. The parameter ξ is a measure of the beam-beam force between colliding bunches and usually takes a value between 0.03 and 0.05. The β_y^* is a measure of beam focusing at the IP. The minimum attainable value of β_y^* is determined by a chromaticity produced by the final focus quadrupole magnets. From a practical point of view, the minimum obtainable value is about 1 cm, because, as β_y^* gets too small, the chromaticity cannot be corrected with sextupoles. Substituting L = 1x10^{34}, ξ = 0.05, E = 3.5 and 8, and β_y^* = 1 results in the required currents of 2.6 A and 1.1 A for positrons and electrons, respectively.

The main parameters for KEKB and the parameters related to accelerating cavities are shown in Tables 1.1.2-1 and 1.1.2-2, respectively. In order to avoid single bunch instability, the beam will consist of about 5000 bunches, i.e., almost all the RF buckets filled with a bunch along the perimeter of KEKB, except for the ion-clearing buckets. This results in bunch intervals of 2 ns. Since cavity fields decay with a decay time of $Q/2\omega$ (ω: angular resonant frequency), Q should be very low to prevent resonant build-up in the field. For example, HOM at 1 GHz should have a Q lower than 25 for the field to decay in 2 ns. Practically, however, there are HOM's that cannot be lowered this much. Then, the remaining fields affect the successive bunches and eventually the oscillations of all bunches couple and, in some cases, grow exponentially to an intolerable level. This is called coupled bunch instability and this instability is one of the major concerns in designing accelerator components of high intensity machines such as KEKB. As will be discussed in more detail in Section 2.2, in theory, if the growth time of each dangerous mode is longer than the radiation damping time, instability will not occur. This requires R/Q (effective shunt impedance) to be sufficiently low.

Table 1.1.2-1: Main parameters of KEKB. [3]

Ring	LER	HER	Unit
Energy	3.5	8.0	GeV
Circumference	3016.26		m
Luminosity	1×10^{34}		$cm^{-2}s^{-1}$
Crossing angle	±11		mrad
Tune shifts	0.039/0.052		
Beta function at IP	0.33/0.01		m
Beam current	2.6	1.1	A
Natural bunch length	4		mm
Energy spread	7.4×10^{-4}	6.7×10^{-4}	
Bunch spacing	0.59		m
Particles/bunch	3.3×10^{10}	1.4×10^{10}	
Emittance	$1.8 \times 10^{-8}/3.6 \times 10^{-10}$		m
Synchrotron tune	0.01 – 0.02		
Betatron tune	45.52/45.08	46.52/46.08	
Momentum compaction factor	$1 \times 10^{-4} - 2 \times 10^{-4}$		
Energy loss/turn	0.81*/1.5**	3.5	MeV
RF voltage	5 - 10	10 – 20	MV
RF frequency	508.887		MHz
Harmonic number	5120		
Longitudinal damping time	43*/23**	23	ms
Total beam power	2.6*/4.5**	4.0	MW
Radiation power	2.1*/4.0**	3.8	MW
HOM power	0.57	0.15	MW
Bending radius	16.3	104.5	m
Length of bending magnet	0.915	5.86	m

*Without wiggler , **With wiggler

Table 1.1.2-2: Parameters related to accelerating cavities for KEKB [55].

Ring	LER	HER	
Cavity type	ARES	SCC	ARES
Number of cavities	20	8	12
Relative phase	-	10 degrees	
Total RF voltage (MV)	10	17.9	
R/Q (>/cav)	14.8	93	14.8
Q_L (x 10^4)	3.0	7.0	3.0
Input β	2.7	-	2.7
Voltage (MV/cav.)	0.5	1.5	0.5
Input power (kW/cav.)	375	250	340
Wall loss (kW/cav.)	154	-	154
Beam power (kW/cav.)	221	240	173
Number of Klystrons	10	8	6
Klystron power*(kW)	810<	270<	730<

* 7% loss at waveguide system is included.

1.2 Superconducting cavities

Because resistivity is orders of magnitude lower, superconducting cavities have a number of advantages. They include:

- Low operating cost

A virtue of the superconductivity is that the negligible amount of wall plug power leads to substantial savings in operating costs, even when taking into account the cost of refrigerating cavities.

- Low capital cost

The capability of producing higher gradients with lower power makes it possible to reduce the number of cavities, power sources and RF components.

- High gradient

Again, the negligible amount of wall plug power allows more current on the cavity surface, thereby producing higher accelerating fields. It has been 3 to 5 times higher than normal conducting cavities in the past.

- Low impedance

As a natural consequence of the above advantages, the beam pipe radius can be large without losing the energy gain, which leads to low impedance together with a reduced number of cavities owing to the higher gradients.

The reputation of the SRF systems has been increasing and nowadays people are beginning to believe that the system is in fact reliable! However, we should remember that this reliability has been established because of the tight contamination control during surface treatments and assembly of the cavities, precaution and care that people in the SRF community and industry have taken, as well as the increase in understanding and improvement in technique.

1.3 Motivation and history of the development

1.3.1 Motivation

As discussed in Section 1.1.2, one of the key issues for accelerating cavities at KEKB was to develop cavities that have resonant modes with lower Q and R/Q so that coupling bunch instability will not limit the beam current. In regards to this, the inherent nature of high gradients and high stored energy makes the SCC's attractive. To lower the Q's of HOM, we adopted a scheme that allows most HOM's to travel out through the beam pipe and be absorbed. The reasons why we adopted this scheme are: 1) by properly designing the cavity, one can lower the dangerous HOM's to a sufficiently low level and 2) by putting an absorbing/coupling device at room temperature, the problems with condensed gases and multipacting will be avoided.

Cornell University also has a similar project to upgrade CESR for B physics. Figure 1.3-1 shows the superconducting cavity module at Cornell Univ. [84]. This single-cell cavity has beam pipes of 24 cm in diameter. One of which is a fluted pipe so the two lowest dipole modes (TE111 and TM110), whose frequency is lower than the cut-off of the 24-cm beam pipe, can expel from the cell. This allows the length of the beam pipe at both ends to be equal, giving a shorter overall length [85].

The cavity module designed at KEK is shown in Fig. 1.3-2. Instead of having a fluted beam pipe, it has an enlarged pipe on one side to let the dipole modes leak out from the cavity. This shape allows us to electropolish our cavity easily since the distance from the electrode does not vary in the beam pipe.[1] The diameters of each beam pipe are 220 mm and 300 mm.

As for the HOM absorbers, both Cornell and KEK use ferrite for better absorption. Cornell uses C48, a Nickel Zinc ferrite [74] and KEK uses IB-004, a Manganese Zinc ferrite from TDK, Inc. Figure 1.3-3 shows a Cornell-type absorber. Ferrite tiles are electroplated for

[1] At KEK, electropolishing is normally used to finish the surface, whereas at Cornell they use a chemical polish.

better wetting and soldered with *Elkonite* (a composite of tungsten and copper), then bolted to the inner surface of the beam pipe [74]. Figure 1.3-4 shows a KEK-type absorber. A 4-mm thick ferrite layer is formed on the copper beam pipe by sinter-bonding pre-sintered ferrite powder with HIP. These bonding techniques will be discussed in more detail in Section 3.4 and Chapter 7.

The development of the technique to make practical HOM absorbers for superconducting cavities is crucial to the success of present and future projects that require absorbers. The technique, we developed and describe in this thesis, has been proven to be one of the best methods to make full-size absorbers with ferrite (and can be applied to other materials).

1.3.2 A brief history of the development

In 1992, when we started working on the development, similar work was going on at Cornell University using ferrite tiles as an absorbing material. We chose a commercially available ferrite tile, IB-004, a product of TDK, Inc., which was sold as a microwave absorbing material. The measurements on electromagnetic properties, such as ε and μ showed good damping capability, but the question was how to bond the tiles (nominal size is 6 cm x 6 cm x 4 mm) to the inner wall of a beam pipe. According to TDK, it is not possible to make a thin, large diameter (~30 cm) cylinder made of this ferrite without cracking. As will be described in Chapter 5, bonding tiles by either brazing or soldering was unsuccessful due to the low bending strength of the ferrite tile. The idea of using powder came up while dealing with the problem of bonding. The concept was to use pre-sintered ferrite powder as a starting material, then employ a relatively new technique of HIP (Hot Isostatic Press), and finally to apply the sintering and bonding to the outer layer at the same time. If this way of manufacturing is possible, we could not only be make an absorber, but also open up another possibility for making new materials or improving a material by adding powder.

Measurements of various properties using samples showed that the ferrite made with this technique has better properties such as less porosity and higher DC conductivity, as compared to commercial tiles.

In 1994, after developing the tools and fixtures for HIPping, we started HIPping full-size absorbers. Although there were leaks during HIP and voids, delamination, and cracks after HIP, most of these problems were solved by improving the tools and conditions.

In 1995, by installing an absorber in TRISTAN MR (Main Ring), the first beam test was carried out. This test did not show any problems and encouraged us to make more absorbers with this technique.

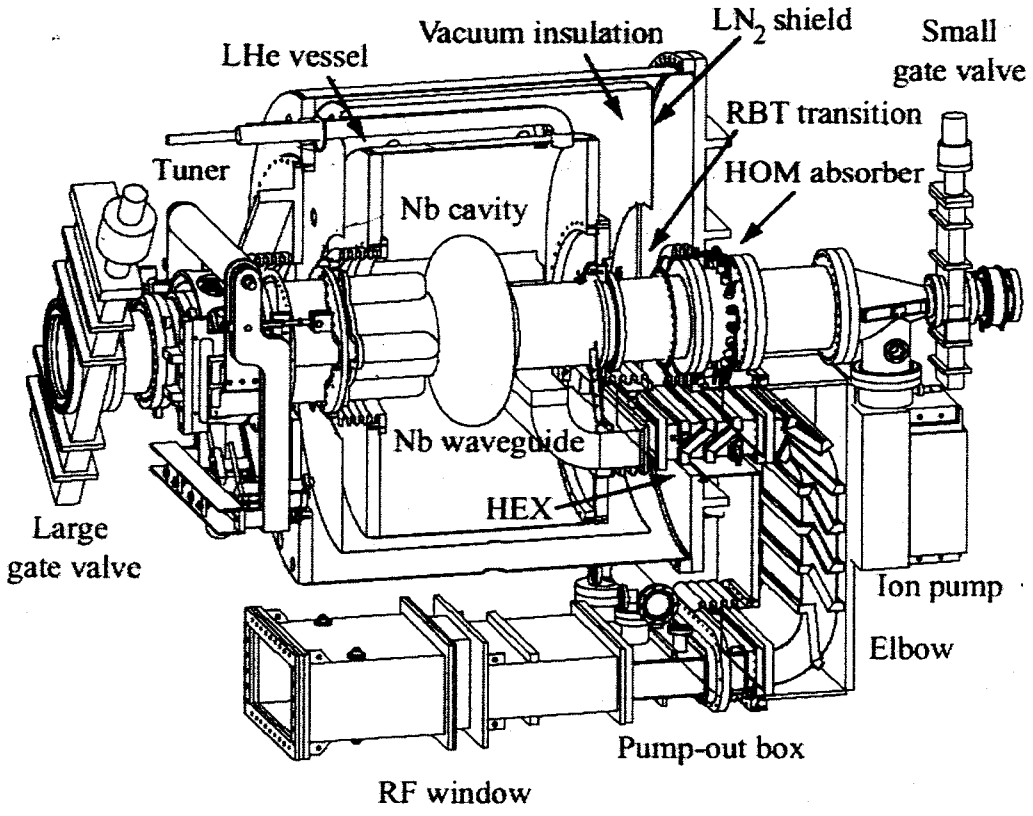

Fig. 1.3-1: Cornell B-Factory superconducting cavity module [84].

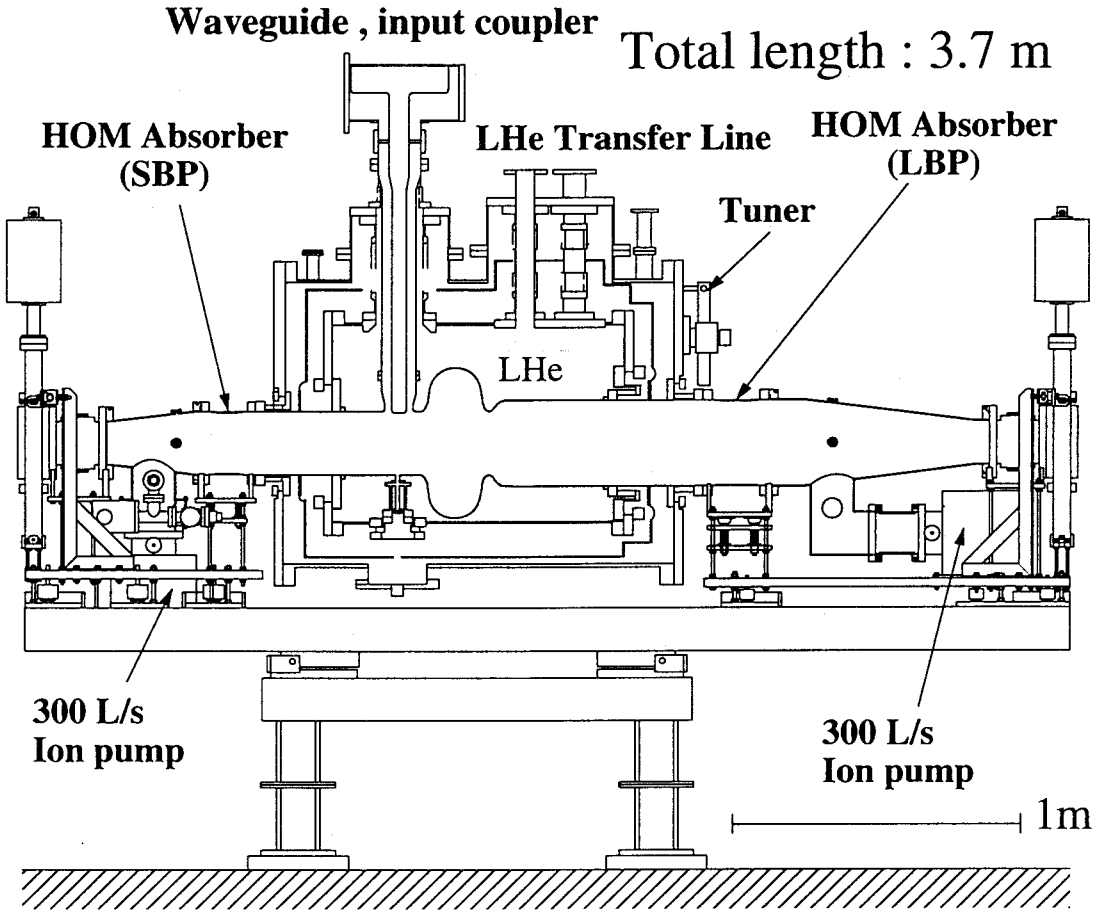

Fig. 1.3-2: KEKB superconducting cavity module.

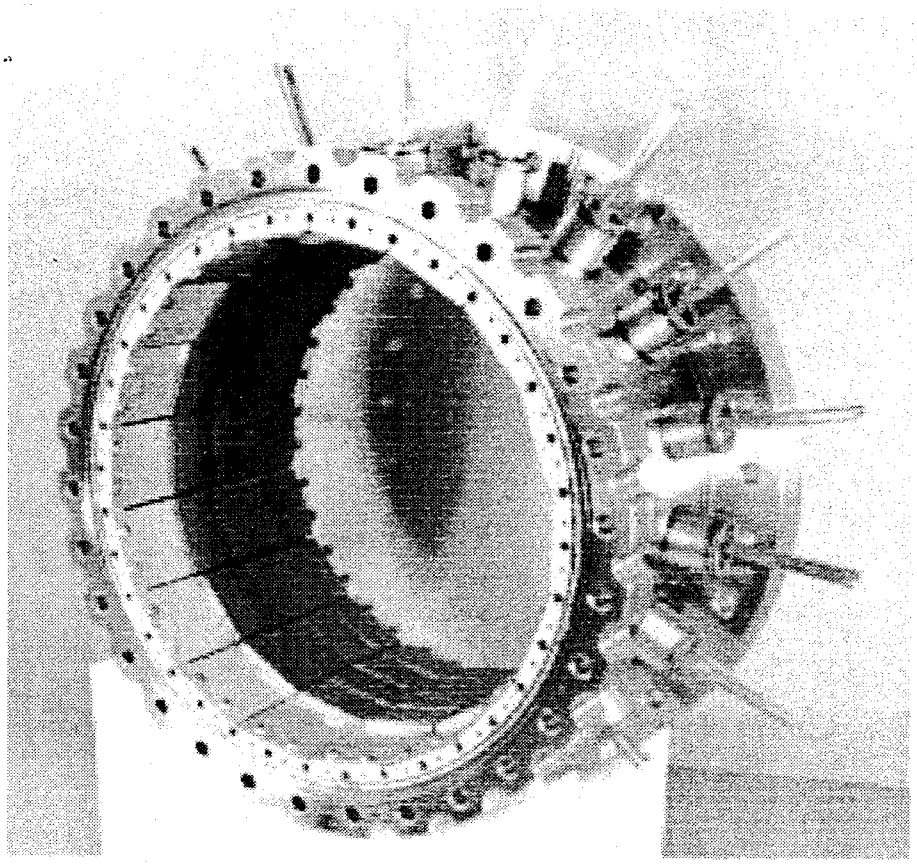

Fig. 1.3-3: Cornell type HOM absorber [86]. Inner diameter is 240 mm. Ferrite tiles,3.2-mm thick, are soldered on to a tungsten/copper composite metal and bolted.

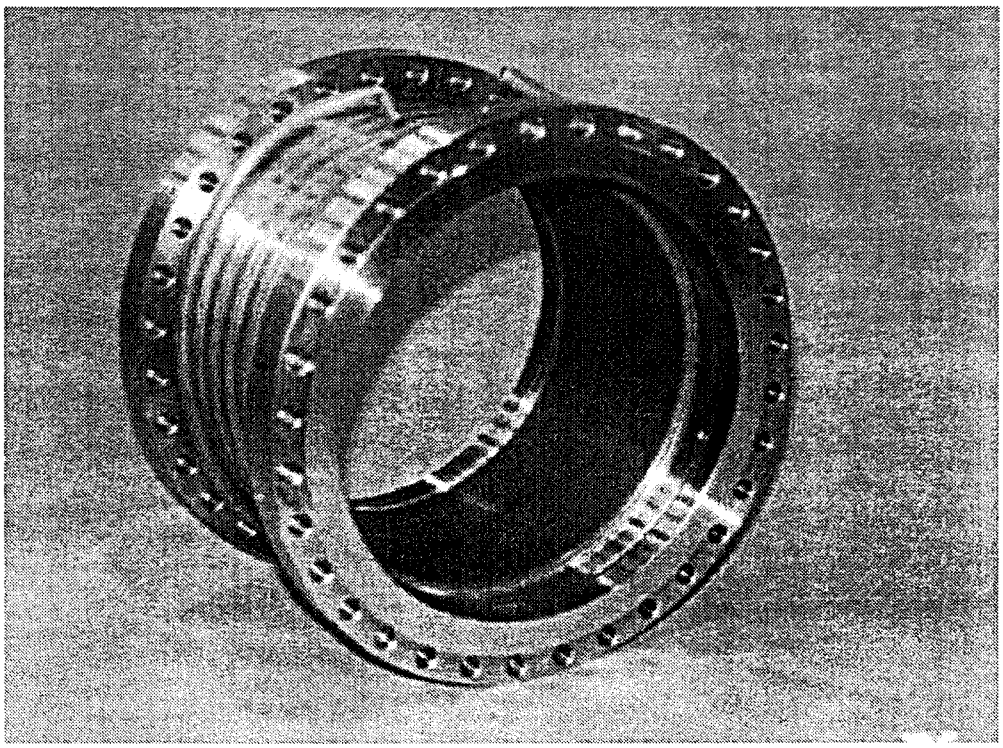

Fig. 1.3-4: KEK type absorber. Inner diameter is 220/300 mm. A 4-mm thick ferrite layer is made with HIP.

In 1996, a SCC module with HOM absorbers was tested with beams in the TRISTAN AR (Accumulation Ring) for the first time. There were three test periods. These tests showed that, if excess amounts of gas flows into the cavity, RF trips would occur. That suggested we should lower the dynamic pressure of the neighboring beam ducts. Although there was no symptom of degradation with the gases from the HOM absorbers, it was thought to be important to check the outgassing rate of absorbers again and decrease it to a sufficiently low level.

Based on these successful beam tests, we manufactured the absorbers for KEKB HER. Four SCC modules were constructed and installed at Nikko D11 (Fig. 1.3-5) by August, 1998. Since the commissioning started in Dec, 1998, these modules have been showing excellent performance and the absorbers have been operating as we expected. This thesis describes the development work of the absorber.

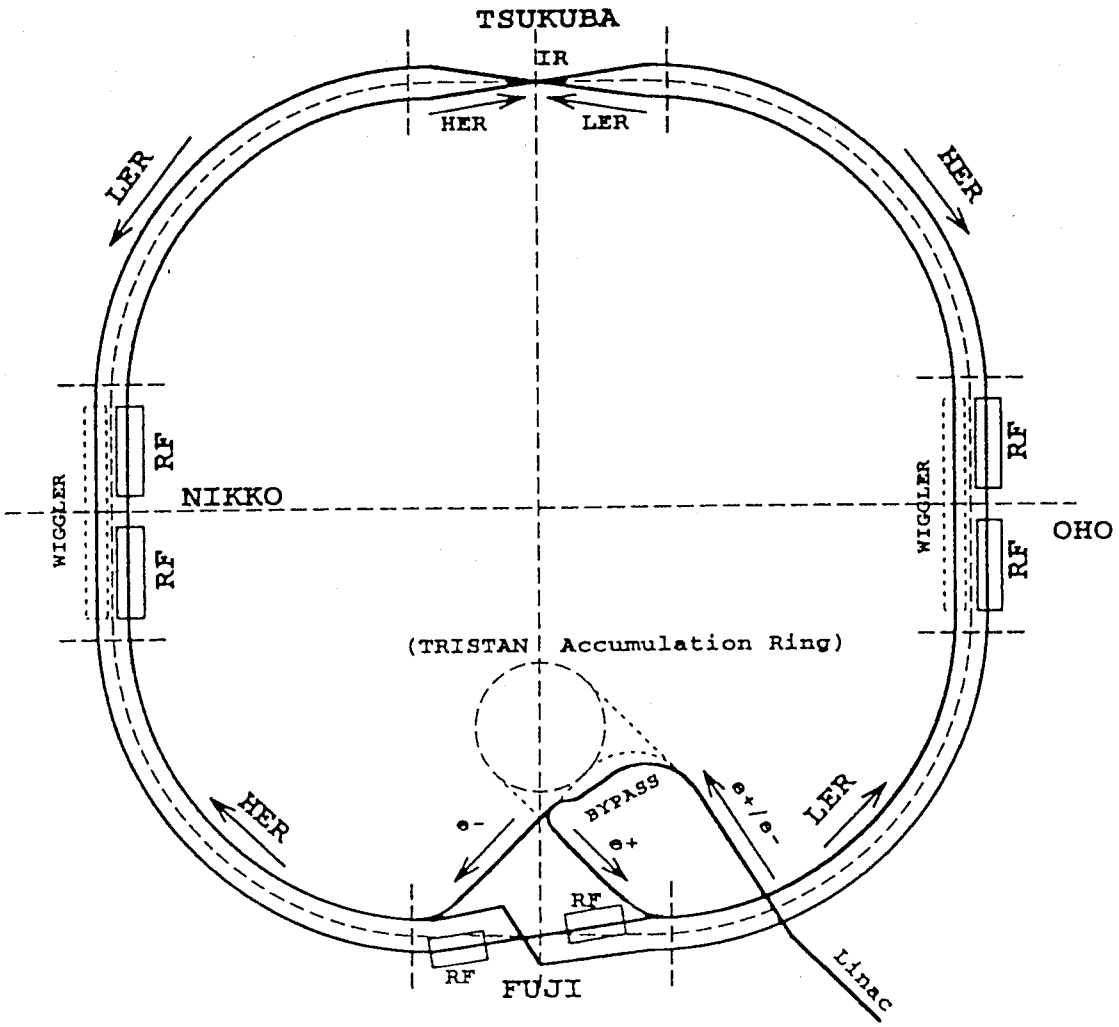

Fig. 1.3-5: Configuration of the KEKB accelerator system [53].

1.4 Organization of the thesis

The following chapter (Chapter 2) gives a brief outline of HOM and the coupled bunch instabilities, together with some examples of the techniques to suppress them as well as the requirements for absorbers.

Chapter 3 provides the general concept of absorbers. It describes the mechanisms of absorbing microwaves, the materials that absorb microwaves, and the several ways of bonding such materials.

In Chapter 4, we show the measurements of the fundamental properties of ferrite. They are permittivity, permeability, DC conductivity, density (porosity), thermal conductivity, thermal expansion coefficient, power handling capability, outgassing rate and mechanical strength. We chose IB-004 as a candidate for our absorber. Since it had never been used in an accelerator before, we had to measure the fundamental properties that we needed for designing our absorber. In addition, because we used a pre-sintered ferrite powder that was extracted in the middle of the manufacturing process, many properties are different from the values written in the catalogue.

Chapter 5 is devoted to the experimental evaluation of bonding. It includes brazing, soldering and HIP. Analyses of bonding are made by microscopes, X-ray radiography, SEM-DEX and acoustic tomography.

In Chapter 6, we describe how we designed the size and positioned our absorber using computer codes. Also, high power tests on a 1/3-size model of the full-size absorber using a 2.45 GHz 5 kW microwave source are depicted. Since the size is smaller, even with a 5 kW power source, the power density can be "magnified" and simulate tripled total power. Furthermore, with the smaller size, the RF components are easier to handle during tests compared to the tests with full-size absorbers.

Chapter 7 focuses on the development of the technique to make full-size absorbers using HIP technology. Although HIP is not a new technology, sinter-bonding pre-sintered IB-004 powder was a new trial. So, we had to start from almost "scratch". Designing tooling for various tests for packing powder, and determining HIP conditions such as pressure and temperature. These developments are related to the problems we encountered during the tests, thus we describe those problems as well.

From Chapter 8, tests on the full-size absorbers made with the technique described in Chapter 7 are described. Chapter 8 illustrates various bench tests, including outgassing rate measurements and high power tests with a 508 MHz coaxial line.

Chapter 9 provides the results of beam tests carried out at TRISTAN MR (Main Ring) and AR (Accumulation Ring). The former was carried out with an absorber alone and the latter with a SCC module.

Chapter 10 depicts the details of the final installation for KEKB and some operating experiences, including the performance of the HOM absorbers and SCC modules together with the vacuum in terms of the outgassing rates and condensed gases.

Chapter 11 summarizes and concludes the thesis.

Chapter 2

Higher-Order-Modes (HOM's) and Requirements for the Absorber

2.1 Introduction

When a bunch of electrons pass through a structure, depending on the shape of the structure and the bunch, the beam leaves energy with electromagnetic fields of various frequencies. An exception would be if the structure is an infinitely conducting and uniform-diameter tube. On the other hand, if the structure has its own intrinsic resonant frequencies, some fields can grow resonantly if the fields formed by successive bunches are in phase. Instability occurs when the built-up fields affect the motion of bunches and make the beam orbit unstable. This chapter explains these instabilities with some examples.

2.2 Instabilities

The word "instability" in the field of accelerators is used for the situation in which the oscillatory motions of particles grow exponentially by some forces generated with fields caused by the environment surrounding the beam or particles, e.g. beam ducts, accelerating cavities, bellows, gate valves, etc. The motion of bunches are generally categorized into two, longitudinal (or the direction of a beam axis) and transverse (or the plane normal to a beam axis).

There are two ways to approach the problem of treating instabilities. One is time domain and the other is frequency domain. In the real world, we see things in time domain, but sometimes it is easier to evaluate phenomena by frequency domain, which is the Fourier transformation of time domain.

2.2.1 Wake function

For the particle (charge e) at (r, θ), which is following a particle (charge q) at (r_0, θ_0) with a distance s, wake functions for longitudinal and transverse directions are defined as follows [17].

$$W_z(r_0,\theta_0,r,\theta,s) \equiv -\frac{1}{eq}\int dz F_z\left(r,\theta,z,t=\frac{z+s}{v}\right) \qquad (2.2.1\text{-}1)$$

$$\vec{W}_T(r_0,\theta_0,r,\theta,s) \equiv \frac{1}{eD}\int dz \vec{F}_T\left(r,\theta,z,t=\frac{z+s}{v}\right) \tag{2.2.1-2}$$

where, F_z and F_T are longitudinal and transverse forces and

$$F_z = eE_z \tag{2.2.1-3}$$

$$\vec{F}_T = e(\vec{E}_T + c\vec{u}_z \times \vec{B}_T) \tag{2.2.1-4}$$

where $\vec{u}_z$ is a unit vector of z direction or longitudinal direction, and D is the dipole moment of the leading particle,

$$D = qr_0 \tag{2.2.1-5}$$

From Eqs. (2.2.1-1) and (2.2.1-2), one can say that the wake function is the voltage that is acquired by the test particle that follows a unit charged particle. Also, when the leading particle is not a single particle, but a bunch that has some density distribution of the particles in the longitudinal direction, the integration of the wake functions is called longitudinal wake potential and is defined as follows,

$$\overline{W}_z(r_0,\theta_0,r,\theta,s) \equiv \frac{1}{q}\int ds' W_z(r_0,\theta_0,r,\theta,s-s')\lambda(s') \tag{2.2.1-6}$$

where, $\lambda(s')$ is line density of particles and is related to charge q and current I as follows.

$$q = \int \lambda(s')ds = \int I(t)dt \tag{2.2.1-7}$$

2.2.2 Impedance

Impedance is a Fourier transformation of the wake function and is written as follows.

- **Longitudinal mode**

$$Z_{//}(\omega) = \frac{R_s/2}{1+iQ\left(\frac{\omega_r}{\omega}-\frac{\omega}{\omega_r}\right)} \tag{2.2.2-1}$$

where R_s: shunt impedance, ω_r: resonant frequency and Q: quality factor.

- **Transverse mode**

$$Z_T(\omega) = \frac{\omega_r}{\omega} \frac{R_T/2}{1 + i\,Q\left(\frac{\omega_r}{\omega} - \frac{\omega}{\omega_r}\right)} \qquad (2.2.2\text{-}2)$$

where

$$R_T \equiv \frac{c}{\omega_r} \frac{1}{P} \left(\frac{V_z(r = r_1, \theta = 0)}{r_1} \right)^2 \qquad (2.2.2\text{-}3)$$

is the transverse shunt impedance, in which V_z is voltage in a longitudinal direction at $r=r_1$ and at an angle of the dipole moment.

- **Growth rate of longitudinal mode instability**

The growth rate of longitudinal instability, i.e. time scale of the exponential growth of oscillation, is written as

$$\tau^{-1} = \frac{e^2 N M \alpha}{2 T_0 E_0 \omega_s} \sum_{p=1}^{\infty} \left\{ \omega_p(\mu)^+ \mathrm{Re}Z(\omega_p(\mu)^+) - \omega_p(\mu)^- \mathrm{Re}Z(\omega_p(\mu)^-) \right\} \qquad (2.2.2\text{-}4)$$

where

$$\omega_p(\mu)^+ = \{(p-1)M + \mu\}\omega_0$$

$$\omega_p(\mu)^- = (pM - \mu)\omega_0 - \omega_s$$

where,

e: charge of electron (C) , 1.6×10^{-19} C ,

N: number of particles per bunch, for HER 3.3×10^{10} ,

M: number of bunches, in HER without bunch gaps, 5120,

α: momentum compaction factor, 1×10^{-4} - 2×10^{-4},

T_0: revolution time (s), 1.00542×10^{-5} s, assuming the circumference is 3016.26 m,

E_0: nominal energy of particle, 8 GeV for HER,

ω_s: angular synchrotron frequency (radian/s), 6.249×10^3 - 1.250×10^4 , assuming the tune shift is 0.01 - 0.02,

Z: impedance

p: an integer,

μ : an integer 0, 1, 2..... M-1, which describes oscillation modes of bunches.

Figure 2.2.2-1 represents the meaning of Eq. (2.2.2-4). If the frequency dependence of the impedance is known, you can find whether the growth rate is positive (excite) or negative

(damp). For example, as one can see in Fig. 2.2.2-1, for μ=0 mode, if the peak of the real part of the impedance is on the right of the frequency pMf_0, the growth rate is positive and vice versa. Even when the growth rate is positive, if the growth time, τ, is longer than the natural damping time, called radiation damping time, the oscillation will not grow.

The first term in the parentheses of Eq. (2.2.2-4) shows the growth and is proportional to the real part of the impedance. For example, since the radiation damping time of KEKB HER is 23 ms, the growth rate or the right hand side of Eq. (2.2.2-4) should be less than 43.5. Otherwise, the instability would grow faster than the radiation damping.

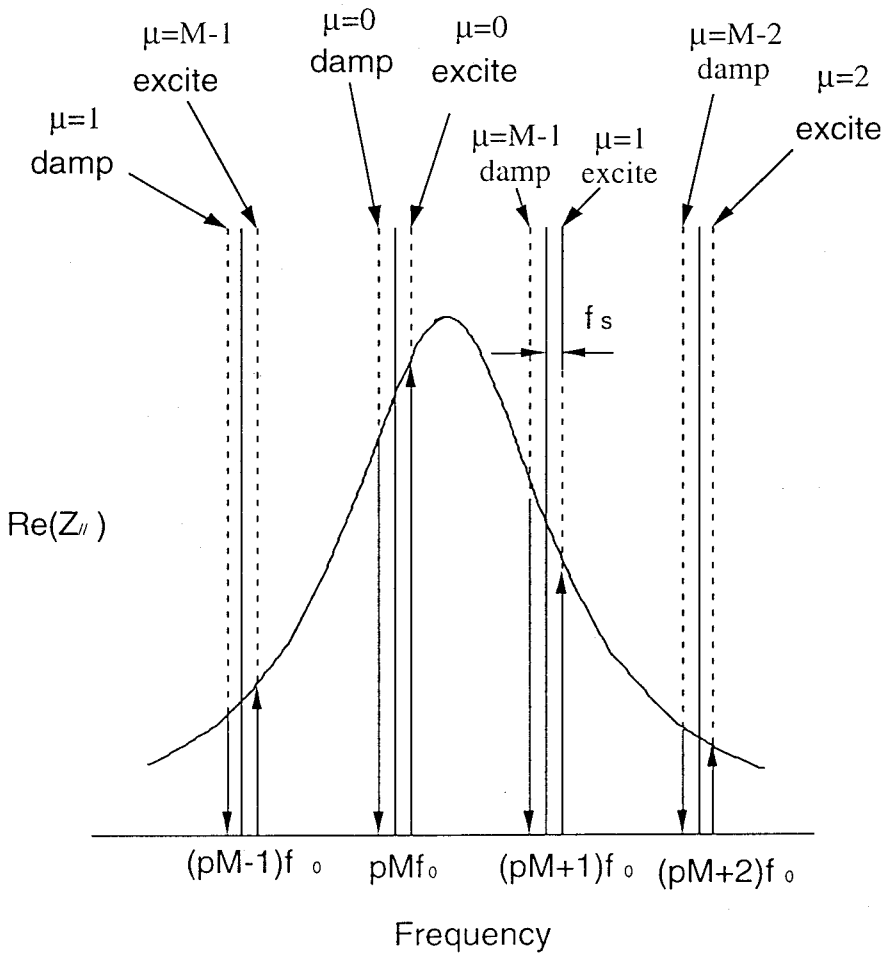

Fig. 2.2.2-1: The real part of a longitudinal impedance. A schematic to explain Eq. (2.2.2-4).

- **Growth rate of transverse mode instability**

If all the bunches have the same number of particles and are spaced equally, with a betatron frequency ω_β, the growth rate of the transverse mode instability is written as follows [17],

$$\tau^{-1} = -\frac{e^2 cNM}{2T_0{}^2 E_0 \omega_\beta} \sum_{p=1}^{\infty} \left\{ \mathrm{Re}\, Z_T(\omega_p(\mu')^+) - \mathrm{Re}\, Z_T(\omega_p(\mu')^-) \right\} \quad (2.2.2\text{-}6)$$

where,

$$\omega_\beta \equiv N_\beta \omega_0 + \delta\omega_\beta \quad , N_\beta : \text{an integer}$$

$$\omega_p(\mu')^+ \equiv \{(p-1)M + \mu'\}\omega_0 + \delta\omega_\beta$$

$$\omega_p(\mu')^- \equiv (pM - \mu')\omega_0 - \delta\omega_\beta$$

$$\mu' \equiv \mu + N_\beta$$

Like the longitudinal mode instability, one can calculate the growth time if the frequency dependence of the transverse mode impedance is known.

- **Instability due to fundamental mode**

To get so-called optimum tuning while feeding power to the cavities, it is necessary to shift the fundamental frequency of a cavity by the following amount.

$$\Delta f = -\frac{I \sin\phi}{2V_c}\left(\frac{R_a}{Q_0}\right) \times f_a \quad (2.2.2\text{-}5)$$

where f_a is the applied frequency and ϕ is the synchronous angle ($\cos\phi = P_b/IV_c$ in case of optimum coupling) [17]. As one can see in Eq. (2.2.2-5), the frequency has to be moved so that it becomes lower, and the amount increases with current and decreases with cavity voltage. For example, let us take the case of KEKB-HER, R_a/Q_0=93, V_c=1.5 MV, I=1.1A, P_b=4.0 MW, f_a=508.877 MHz, then Δf=-17 kHz. Since this detuning frequency does not exceed the revolution (99.39 kHz), no instability is induced.

- **Instability due to HOM**
  - Longitudinal mode

Figure 2.2.2-3 shows the real part of a longitudinal impedance of a TM_{011} mode without absorbers at KEKB SCC that was calculated from Eq. (2.2.2-1) with the Q and shunt impedance obtained using the computer code CLANS [19].

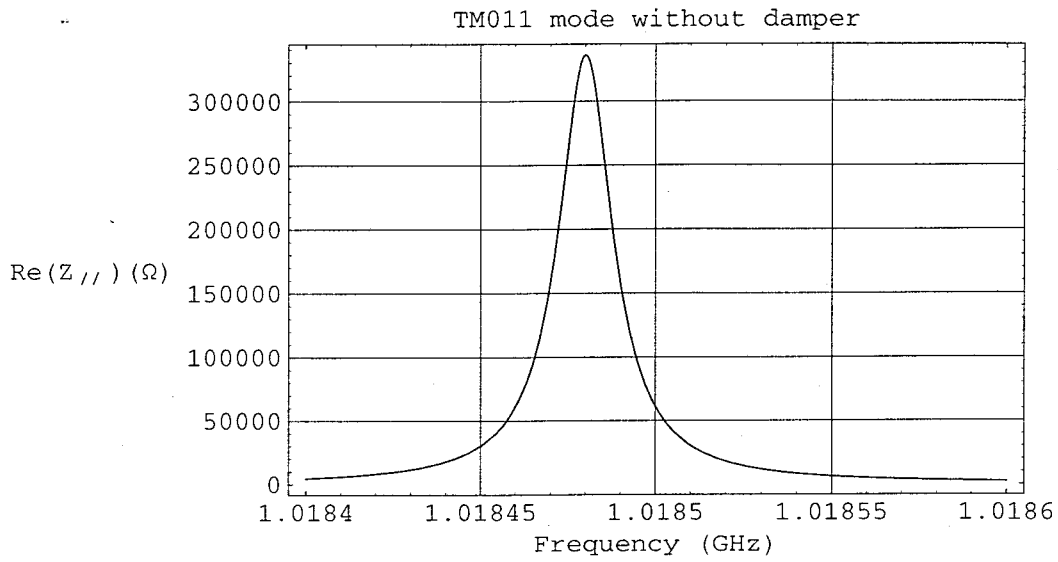

Fig. 2.2.2-3: The real part of a longitudinal mode impedance of a TM_{011} without absorbers.

Although computer codes give the resonant frequencies, they are often slightly different from the actual ones. Therefore, to be safe, we calculated the growth rate as a function of resonant frequency and found the worst case. Figure 2.2.2-4 shows the result around the frequency of a TM_{011} mode. As one can see in the figure, the worst growth time can be as fast as 1.5 ms, which is much faster than the radiation damping time of 23 ms. As a result, longitudinal coupled bunch instability can occur if there is no absorber.

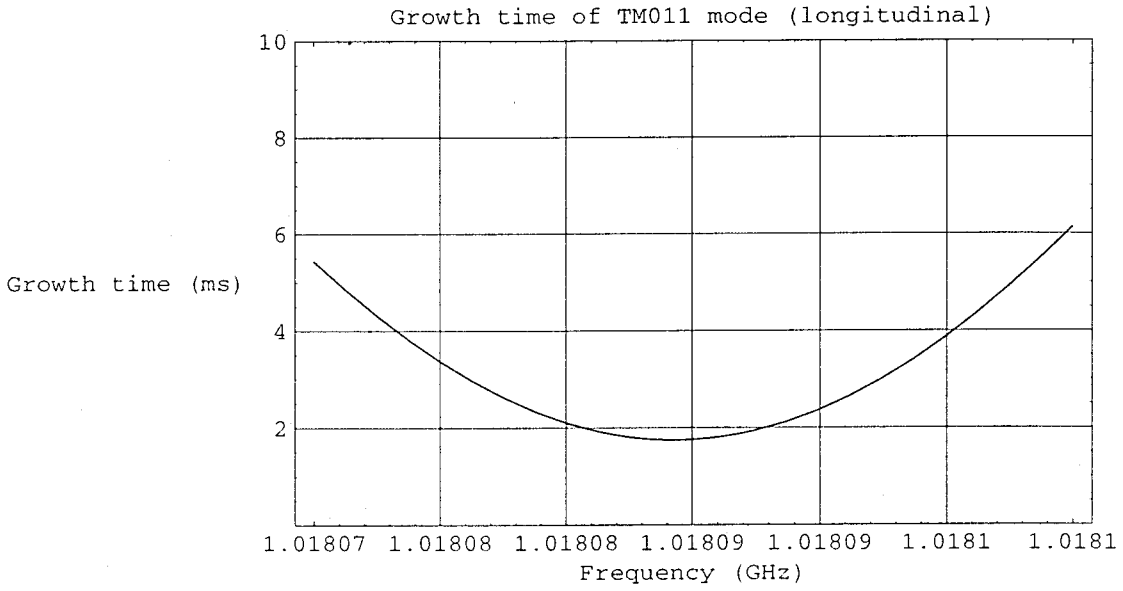

Fig. 2.2.2-4: The growth time of a TM_{011} mode without absorbers.

As a comparison, Figs. 2.2.2-5 and 2.2.2-6 show the corresponding results with absorbers. As seen in the figure, the fastest growth time is about 80 ms. Thus, no instability due to this HOM will occur even in the worst case.

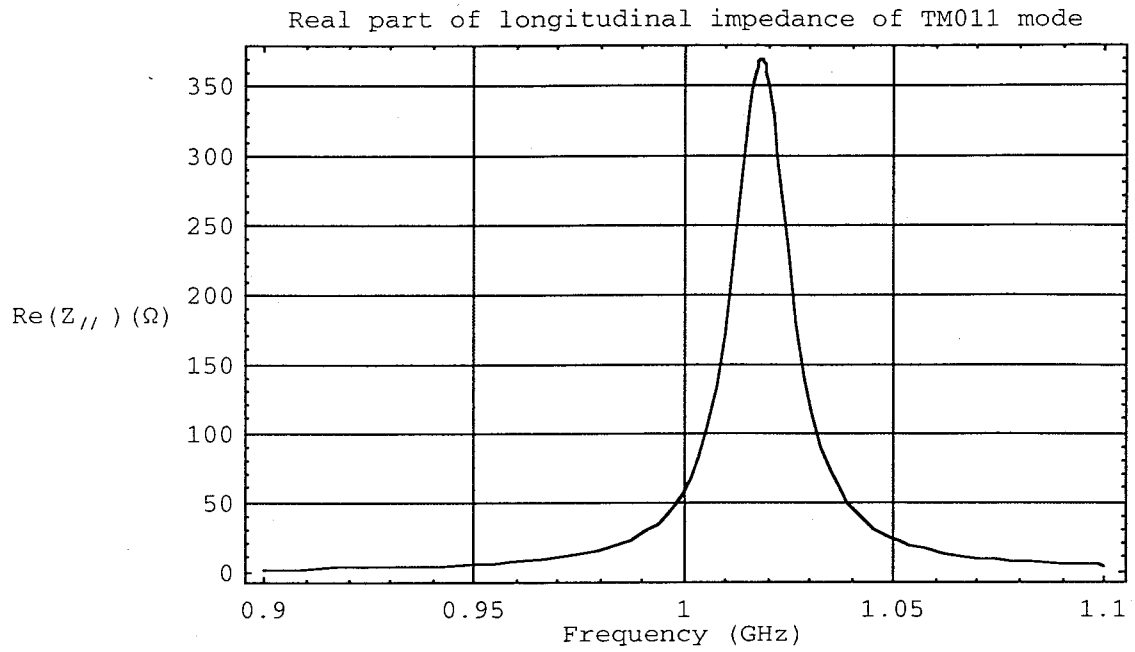

Fig. 2.2.2-5: The real part of a longitudinal mode impedance of a TM_{011} mode with absorbers.

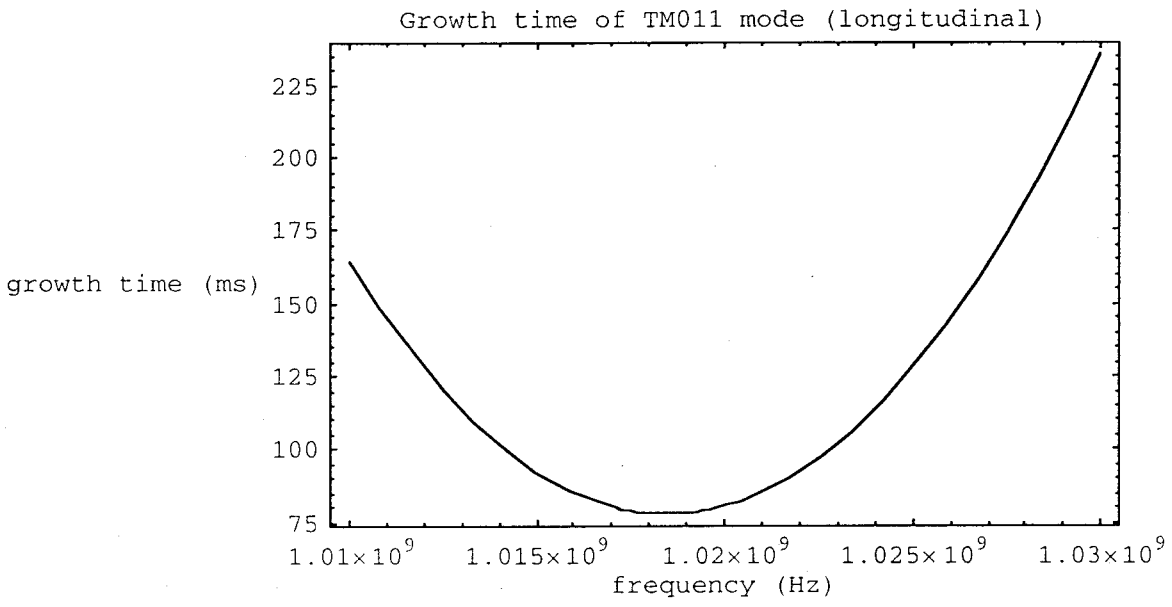

Fig. 2.2.2-6: The growth time of a longitudinal instability with a TM_{011} mode. α=1.5 x 10^{-4}, f_s=1.492 kHz assumed with the other parameters written above.

2.3 Suppression of HOM

As has been discussed, avoiding the instabilities is important to keep the beam in a stable orbit and to obtain sufficient lifetime for physics experiments. Since one of the main causes of the instabilites is HOM's, suppression of HOM's is one of the keys to the success of the stable operation of accelerators [95].

There are two ways to suppress HOM's, one is to extract them through couplers, i.e. antennas, loops or waveguides to couple with the HOM fields, and the other is to design the shape of the cavity structure in such a way that most of the HOM's can travel out of the cell and couple with absorbing material that is attached to the cavity along the beam pipes (called a HOM damped structure). In the following subsections, some examples of these two methods are described.

2.3.1 Extraction with couplers

This method utilizes so-called couplers, usually made from metal antennas, loops or waveguides, which electromagnetically couple out the RF power via cables or waveguides to be then dissipated in resistive loads located outside the cavity. Figures 2.3.1-1 through 2.3.1-3 show these types of couplers that have been used for superconducting cavities. These couplers often have chokes to reject fundamental mode.

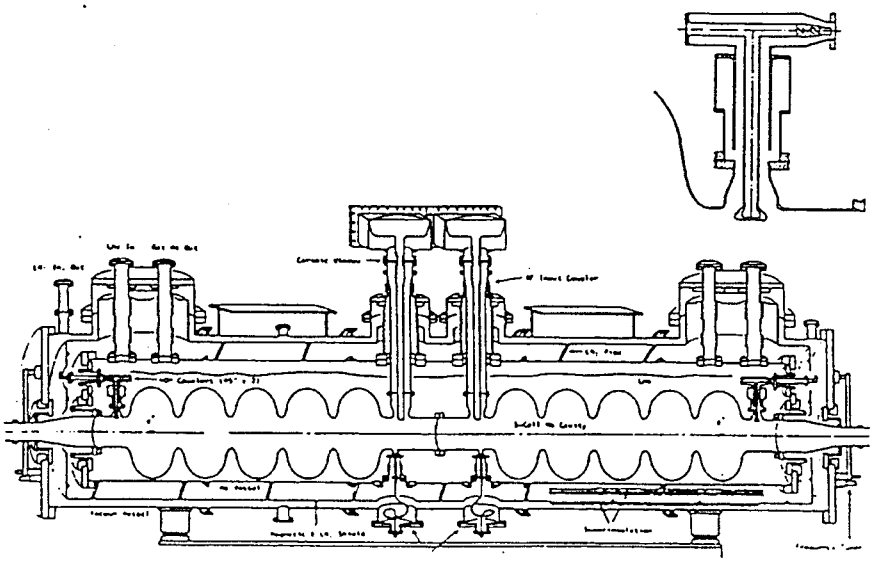

Fig. 2.3.1-1: The HOM coupler used with the TRISTAN cavity. [28]

In the past, however, there have been problems related to these types of couplers when used with superconducting cavities. The problems related to HOM couplers in TRISTAN at KEK (Fig. 2.3.1-1) were (1) multipacting at the capacitive gaps caused by the condensed gases in the coupler [97] and (2) heating of N-type ceramic connectors and cables in the insulation

vacuum [98]. Figures 2.3.1-2 show the loop and antenna type HOM couplers used for 3-cell SC cavity that was tested in TRISTAN AR in 1984 [27, 99, 100]. HOM couplers were attached on the equator of the end cells, whereas they were attached on the end beam pipes in the case of the TRISTAN 5-cell cavities as seen in Fig. 2.3.1-1.

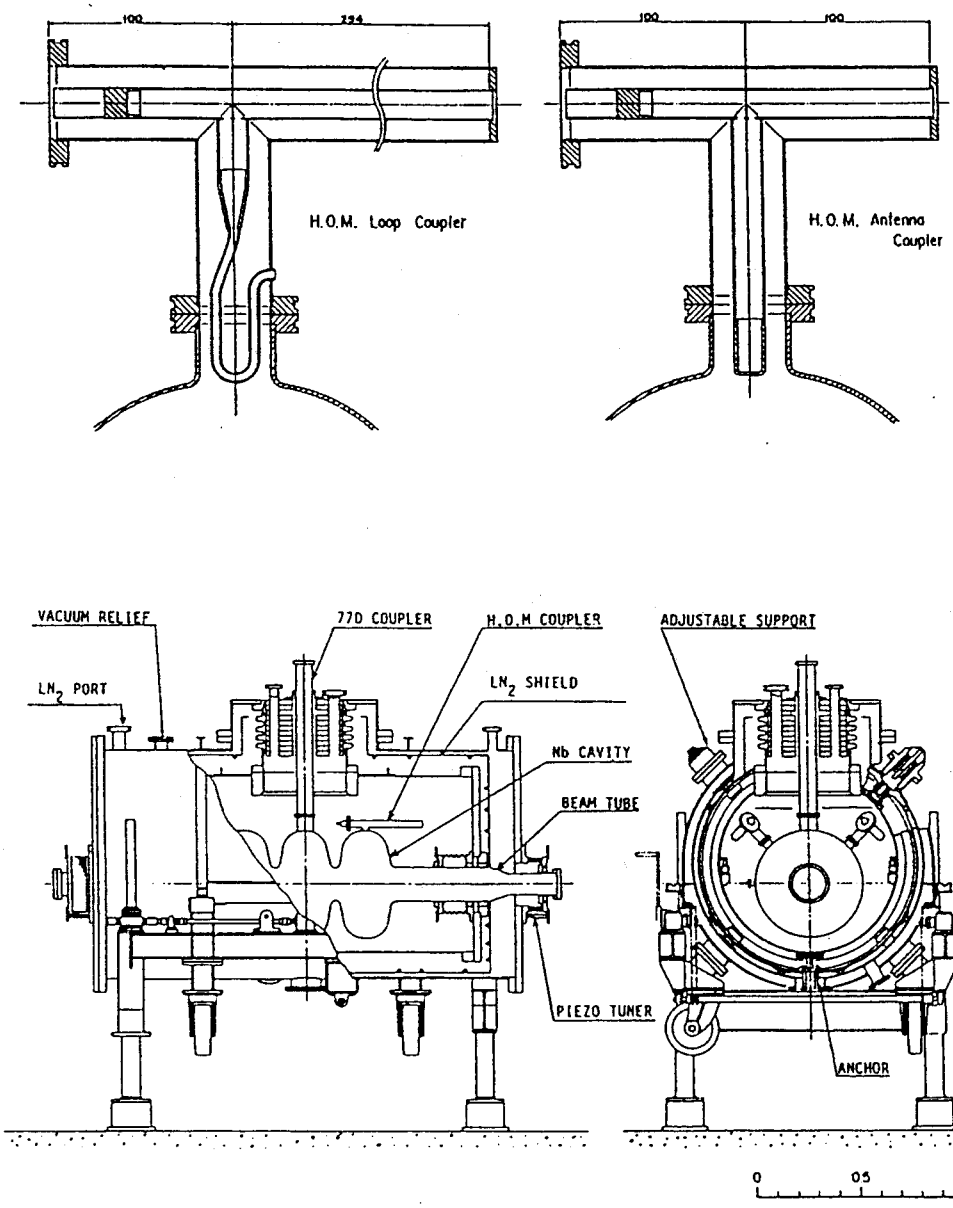

Fig. 2.3.1-2: Loop and antenna type HOM couplers tested with a 3-cell cavity in KEK TRISTAN AR (Accumulation Ring) [27].

The waveguide coupler adopted for CEBAF/Cornell type cavities, and various antenna type couplers employed at Saclay, CERN and DESY are also shown in Fig. 2.3.1-3.

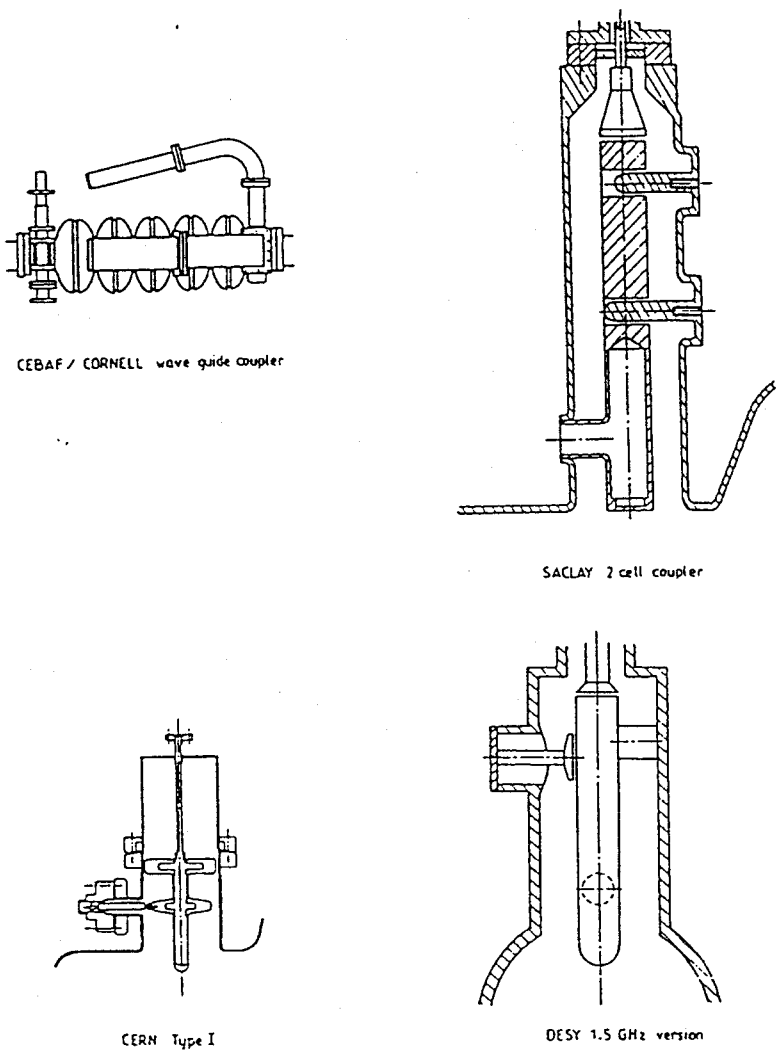

Fig. 2.3.1-3: Various types of HOM couplers successfully applied at CEBAF/Cornell, Saclay, CERN and DESY . [29]

2.3.2 HOM damped structures

The next method to suppress HOM's is to design a so-called deQed structure, which describes what it is more directly, i.e. Q values of the resonant modes are lowered so that the decay times of the HOM's become short enough so as not to cause coupled bunch instabilities. Normally, the required Q's are about 100 or less for B-Factories, whose currents are of the order of amperes, although Q's of some modes can be higher if the R/Q is sufficiently low.

To meet such requirements various types of structures have been proposed, manufactured and operated. Yamazaki summarized these structures in his lecture [95]. Figure 2.3.2-1 shows such structures. Among them, the "single-mode cavity" designed by Weiland [96] was adopted with superconducting cavities because of its simplicity and manufacturability. However, this cavity is not exactly a single-mode cavity because some dipole modes such as

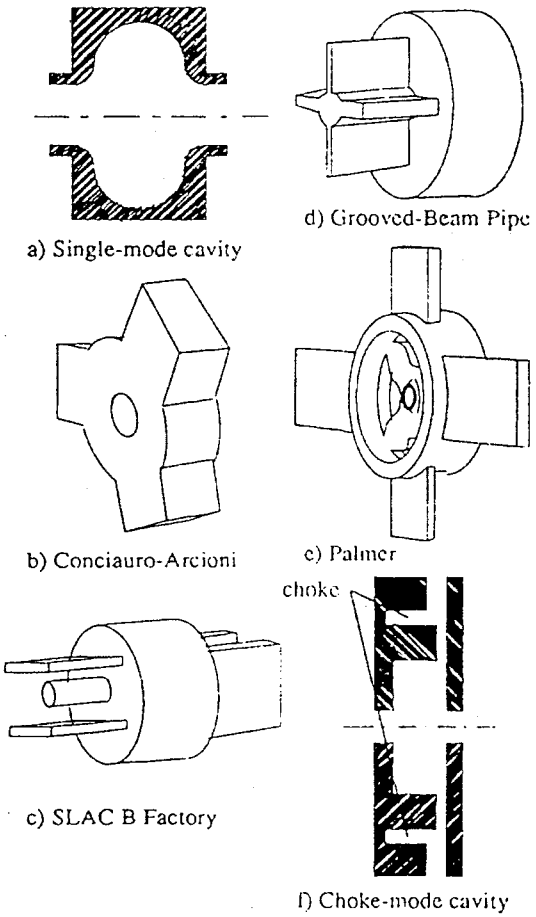

Fig. 2.3.2-1: Various types of HOM damped structures. [95]

TE111 and TM110 modes are trapped in the cell. To let this mode couple out to the beam pipe either flutes or enlarged beam pipe were attached at Cornell and at KEK, respectively. The advantage of each type is shorter length (Cornell type [85]) and easier manufacturing and surface treatment (KEK type). According to reports from these laboratories, both types have been working fine [84, 69].

2.4 Other requirements

The absorber to be used for SCC requires

- **UHV(Ultra High Vacuum) compatibility**

For sufficient beam lifetime, 1 x 10^{-9} Torr or lower is required. Also, to avoid trips, the outgassing rate should be as low as possible.

- **High power handling capability**

Since a dissipation of 5 kW/cavity is expected at KEKB, a power handling capability up to ~10 kW is required for the safety margin.

- **Free of particulates**

If some particle enters the cavity, it can be the source of field emission that causes discharge or quenches, which results in trips [76]. Therefore, there should be no particulates entering the cavity.

- **Some DC surface conductivity**

If an increase in charge occurs on the surface, it can lead to an electric breakdown or spark, so there should be some electric conductivity on the surface.

Chapter 3

Absorbing materials and bonding

3.1 Introduction

In this chapter we discuss the mechanisms of absorption and give examples of absorbing materials to absorb microwaves in Sections 3.2 and 3.3. In Section 3.4, we discuss bonding techniques for absorbing materials, especially for ceramic and the like on to metals.

3.2 Mechanisms of Absorption

There are three chief mechanisms of absorbing microwaves, in other words, loss mechanisms. They are resistive, dielectric and magnetic losses. In the following subsections, each mechanism will be explained.

3.2.1 Resistive loss

This must be the most popular loss mechanism because it occurs basically from a DC field. This loss is also called Ohmic loss and is based on the fact that, when there is a current along a cable or a metal, one can see the voltage between the two ends, which is proportional to the current. This coefficient of the proportion is called resistance. Microscopically speaking, it is the scattering of electrons with atoms.

3.2.2 Dielectric loss

When subjected to an electric field, materials polarize and cause losses with an oscillating field [23]. This loss can be expressed as delay of phase. Let us assume that the field is oscillating at an angular frequency ω and the delay of phase is δ, then the electric flux density, $\hat{D}$, can be written as

$$\hat{D} = D_0 e^{j(\omega t - \delta)} \qquad (3.2.2\text{-}1)$$

The electric flux density comes from the applied electric field (E) and the electric polarization ($\hat{P}$), i.e.,

$$\hat{D} = \varepsilon_0 \cdot E + \hat{P} \equiv \hat{\varepsilon} E \qquad (3.2.2\text{-}2)$$

$$\hat{\varepsilon} \equiv \varepsilon_0 (\varepsilon' - j\varepsilon'')$$

where ε_0 (=8.85 x 10^{-12} F/m) is the permittivity of free space. The dielectric constant, K, is

the relative permittivity of the material, i.e.

$$K = \hat{\varepsilon} / \varepsilon_0 = \varepsilon' - j\varepsilon'' = \frac{D_0}{\varepsilon_0 E}\cos\delta - j\frac{D_0}{\varepsilon_0 E}\sin\delta \qquad (3.2.2\text{-}3)$$

The power absorbed per unit volume, W, is [24]

$$W = \frac{1}{2}E^2\omega\varepsilon_0\varepsilon'' \qquad (3.2.2\text{-}4)$$

3.2.3 Magnetic loss

The following are the losses associated with magnetic materials such as ferrite [23, 25]

- Hysteresis loss: This occurs from irreversible domain wall displacements.
- Eddy current loss: This comes from field-induced electric currents.
- Magnetic after effects: This is associated with electron diffusion, usually from Fe^{2+} to Fe^{3+}.
- Dimensional resonances: This comes from electromagnetic standing waves.
- Magnetic resonance: This occurs from precessional motion of unpaired dipole magnetic moments.
- Domain wall oscillations: This appears when the boundaries of the magnetic domains oscillate.

These losses can be characterized in a similar fashion as dielectric losses using complex permeability μ. Let us assume the magnetic field, H, varies at an angular frequency ω as $H = H_0 e^{j\omega t}$ and the loss term is expressed as delay of phase, δ, then, the magnetic flux density, $\hat{\mathbf{B}}$, is

$$\hat{B} = B_0 e^{j(\omega t - \delta)} \qquad (3.2.3\text{-}1)$$

$$\hat{B} = \hat{\mu} H \qquad (3.2.3\text{-}2)$$

$$\hat{\mu} \equiv \mu_0(\mu' - j\mu'') \qquad (3.2.3\text{-}3)$$

where μ_0 ($4\pi \times 10^{-7}$ H/m) is the permeability of free space.

As will be shown later, the real part (μ′) and imaginary part (μ″) of the relative permeability can be measured with a network analyzer.

The power absorbed per unit volume, W, is

$$W = \frac{1}{2}H_0^{\,2}\omega\mu_0\mu'' \qquad (3.2.3\text{-}4)$$

3.3 Materials for absorbing microwaves

Depending on which mechanism is applied, there are several types of materials to absorb microwaves. Here, we describe resistive materials, ferrites, SiC (silicon carbides) and some composite materials.

3.3.1 Resistive material

Alumina is often used as thin coatings. There are several techniques to make thin layers of absorbing materials, e.g. ion sputtering, CVD (Chemical Vapor Deposition), ion implantation and plasma spraying. However, these techniques cannot be applied to a layer with a thickness of a few mm or more, which is sometimes necessary for absorbers to lower the Q values to the order of 100 or less, because of the non-uniformity of the film or brittleness.

At CERN, resistive layers deposited by the thin film technique (NiCr-film) have been used for HOM damping in the ISR (Intersecting Storage Rings) cavities [46].

3.3.2 Ferrite

Ferrites are ferrimagnetic oxides and insulators. Their insulating properties permit penetration of electromagnetic waves into the materials with little reflection [36]. They are also dielectric materials and have loss components. In some industries, more efforts have been made to reduce losses in electronic devices, but there are ways to use the loss mechanisms of ferrite, such as in electromagnetic shields and reducing ghost signals in receiving TV signals which are caused by reflecting microwaves from walls of nearby buildings.

As for applying to accelerators, apart from the absorbing capability, the important requirements are Ultra High Vacuum (UHV) compatibility and electric conductivity. The UHV compatibility guarantees a long beam lifetime without producing ions that scatter the beams. Electric conductivity assures that the surface won't be charged with electrons and lead to a discharge or spark.

At CERN [46], a ferrite TT2-111R (Transtech, Inc.) has been used to damp microwaves in AAC (Antiproton Accumulator Complex). Also, the same ferrites with anti-static coating have been developed and been used both at CERN and FNAL's antiproton source. Moreover, for LEP (Large Electron Positron Storage Ring), an attempt to mix ferrite powder with enamel to achieve a glassy smooth surface is underway [46].

At Cornell Univ, ferrites have been adopted as HOM absorbers for CESR-B and extensive studies have been done on the properties and methods to manufacture full-size absorbers [47, 48]. Also, Hartung and coworkers tested the interaction between ferrite and the beam by

installing a "magnified" ferrite load (TT2-111R of 2.5 times smaller in diameter and 6 times longer than a full-size load)[75]. Presently, they use a ferrite named C-48 that has an absorption frequency range that covers the CESR III SRF cavity HOM spectrum [74].

3.3.3 SiC (Silicon Carbide)

SiC is a versatile material. It has been used as abrasives, cutting tools, electrical resistors, etc. Recently, more applications in the areas of coatings and thin films deposited from the vapor phase have been added [37].

Some SiC have a few valuable properties to apply to accelerators, for example, very low outgassing rate, e.g. $3x10^{-12}$ Torr L/s cm^2 at room temperature after baking at 150 °C for 24 hours, and high thermal conductivity, e.g. 120 W/mK [38]. SiC has been successfully adopted as HOM absorbers at ISSR [39,44], KEK-PF [40], KEK-ARES [41,42] and the ATF damping ring [43]. There are two types depending of the usage. One is a bullet shape and the other is a cylindrical type that looks similar to the ferrite absorber described in this thesis.

Some drawbacks of using SiC as an absorber are less loss for the same volume, because the loss comes only from its dielectric property, or no magnetic loss. The reproducibility of electromagnetic properties can also be a problem since SiC had not been used for electronic devices like ferrite, whose reproducibility is very important. Also, because thermal contact of the cylindrical absorber is given by shrink fit, it could get weaker as the temperature gets high due to the lower thermal expansion coefficient of SiC compared to the surrounding metal, e.g. copper, because contact is made only by mechanical touching.

3.3.4 Others

One of the other materials is an artificial dielectric. When conducting particles are placed inside an insulating dielectric matrix, the dielectric properties of the original matrix are modified. The basic loss mechanism is the scattering of electrons within each elementary grain from the current induced in each grain by electromagnetic waves. At CEBAF, AlN-glassy carbon, one of such materials, has been used as a HOM absorbing material [49]. Features of this artificial dielectric are that one can control the dielectric constants and losses as well as the frequency bands.

Other materials can be 'plastic', such as polyimides, although there are few such materials that are UHV compatible due to their water absorption. The benefit of this kind of material is its elasticity.

3.4 Bonding

Bonding includes brazing, gluing, soldering, and welding. Among these, only brazing and

soldering are discussed in Sections 3.4.1 and 3.4.2 as candidates for bonding the ferrite (and ceramic) of interest. In Section 3.4.3, we discuss HIP (Hot Isostatic Press), which is a technique to consolidate and diffusion-bond powder materials to metals. This technique has proved to be the best for bonding our absorbing ferrite as will be discussed.

3.4.1 Brazing

For optimal brazing conditions good wettability of the filler metals is important. Wettability is usually described as the contact angle of the filler metal to the material as shown in Fig. 3.4.1-1. If this contact angle, θ, is less than 90 degrees, the filler metal is said to wet well.

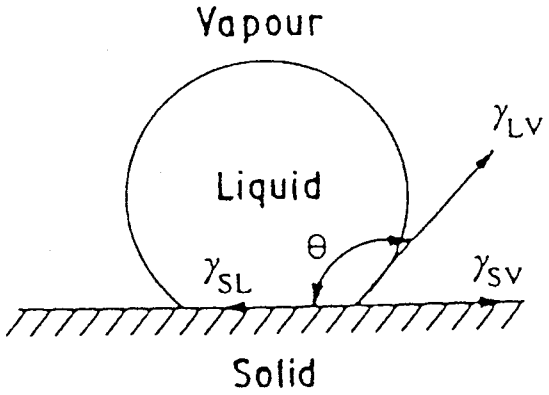

Fig. 3.4.1-1: Schematic to show of filler metal wetting [33].

The wetting of non-reactive metals with ionocovalent oxides were discussed by Li based on the work of adhesion, free energy from the formation of the corresponding oxides, bandgap energies of the oxide. This theory of wetting can be translated to the electron density at the interface [34]. The work of adhesion, *W*, which is defined as the work per unit area to separate a solid/liquid interface, is described as

$$W = \gamma_{LV} (1 + \cos \theta), \qquad (3.4.1\text{-}1)$$

where γ_{LV} is the surface tension of the liquid and θ the contact angle. As one can see in Eq. (3.4.1-1), adhesion increases with the decrease of the contact angle and becomes 0 when θ = 180°. This indicates that the bond strength increases with a decreasing contact angle, which has been verified experimentally [33].

There are two types of brazing, direct brazing and indirect brazing. In direct brazing, active component such as titanium is often added to the filler metal to improve the wettability since oxides/ceramics have few filler metals that have suitable wettability. In indirect brazing, oxides/ceramics are metallized prior to brazing for better bonding integrity.

3.4.1.1 Direct brazing

Brazing without pre-coating is called direct brazing. It is simple and straightforward, but not

many braze metals wet well with oxides such as ceramics. Typical values of contact angles of pure metals on oxides (Al_2O_3, SiO_2, ZrO_2, MgO, etc.) lie between 80 and 145° [35]. Usually active metals such as Ti is added to a normal braze metal to improve wetting.

3.4.1.2 Indirect brazing

Indirect brazing uses pre-coating to help the wetting. Usually, since ceramics do not wet well, various types of pre-coating are used. As shown in the next Section, Cornell University also does pre-coating using solderable metal such as Nickel-vanadium prior to soldering.

Sometimes several layers of different materials are coated, as a barrier for another coating so the first coating is not scavenged off.

3.4.2 Soldering

At Cornell University, soldering has been used for bonding the ferrite tiles [74]. A composite material of 58 % W and 42 % Cu named *Elkonite* was chosen as a heat sink because its thermal expansion coefficient nearly matches ferrite's nominal 9 x 10^{-6}/C. It is electroplated with 0.001" of Cu to help wetting in the brazing copper cooling tube as well as soldering with the ferrite. Prior to the soldering with ferrite, a copper cooling pipe is brazed onto one side with *Elkonite* using Cusil as a filler with a 780 °C eutectic liquidus, typically heated to 820 °C with a 10 min. soak at this temperature. After brazing, the assembly is tamped onto a flat surface to restore flatness before soldering with the ferrite [74]. Ferrite tiles are pre-cleaned with an alkaline solution by the manufacturer, and upon delivery ultrasonically cleaned in methanol baths, 6 cycles of 15 minutes each while replacing of the methanol between cycles. Tests showed that after the 3rd ultrasound bath, no more particulates leave the ferrite. Then the ferrites are fired in air with 100 °C/hr ramp up to 900 °C, soaked for 2 hrs at 900 °C, and cooled down at 100 °C/hr to reduce the outgassing and help homogenize the ferrite. The final soldering is performed with a 90 % Sn/10 % Ag filler having a 221 °C solidus and 295 °C liquidus. The 0.004" Sn-Ag foils are sandwiched between the ferrite and *Elkonite* then heated to 370 °C in a vacuum furnace with several intermediate soaks and a 10 min. soak at temperature. Then it is slowly cooled (8 hrs<) without gas backfilling to prevent the Ni-V coating from being scavenged.

3.4.3 HIP (Hot Isostatic Press)

In HIP the pressurizing medium is typically a gas and the process is carried out at elevated temperatures for specific time periods [72]. HIP is utilized to densify parts fabricated by CIP or by more conventional methods, to heal casting defects and voids, to bond similar or dissimilar materials, and to form net or near-net shapes from metal, ceramic, cermet and graphite powders.

Tooling, when required, is typically a metal or glass container. HIP is not size or shape limited, and results in optimized material conservation.

This rapidly advancing technology offers many possibilities. New applications are constantly being discovered. In the last decade it has become a reliable process for commercial applications.

The basic function of a hot isostatic press is "to uniformly heat a given workload, while gas pressure is applied to all surfaces, with accurate control of temperature and pressure." The pressure medium is a gas, such as argon, nitrogen, helium or air. A variety of heating elements can be used for the different temperature ranges. Thermocouples provide precise control of the temperature of both the heating elements and the workload.

The furnaces are of various types, to suit particular requirements: Oxygen resistant kanthal heating elements for temperatures up to 1200 °C. These allow hot loading and unloading of the workpieces. Molybdenum heating elements for temperatures up to 1450 °C; used mainly for densification of materials sensitive to surface contamination. Graphite heating elements for temperatures of 2000 °C or above; permit treatment of materials in either an argon or nitrogen atmosphere.

The heat shield assembly provides thermal insulation of the pressure vessel, and controls the conduction, convection and radiation of the internal gas.

Hot isostatic presses are built: with inside diameters: 50 to 1500 mm and larger, for pressures: from vacuum to 3000 atm, for temperatures: from 500 °C to 2200 °C.

HIP has proved to be a generally recognized process for improving metallic and non-metallic materials.

It is currently used for:

- Forming metallic and ceramic powders into billets or near-net shapes.
- Densification of castings and weld joints to improve radiographic quality mechanical properties and pressure-tightness after machining.
- Diffusion bonding of metals and ceramics.
- Rejuvenation of service-affected components.

The process using powder includes powder atomization, screening, blending, loading, hot outgassing and consolidation by HIP [73]. Use of this process has been limited by the risk of delays and costs due to the current trial-and-error design practices for suitable containers. Although there are projects that develop computer-aided modeling tools for the design and simulation of HIPed Powder/Metal parts such as in Ref. [73], these modeling tools have not been used in relatively small companies in Japan, to my knowledge.

Figure 3.4.3-1 is a sketch of our first plan to HIP pre-sintered ferrite powder [21].

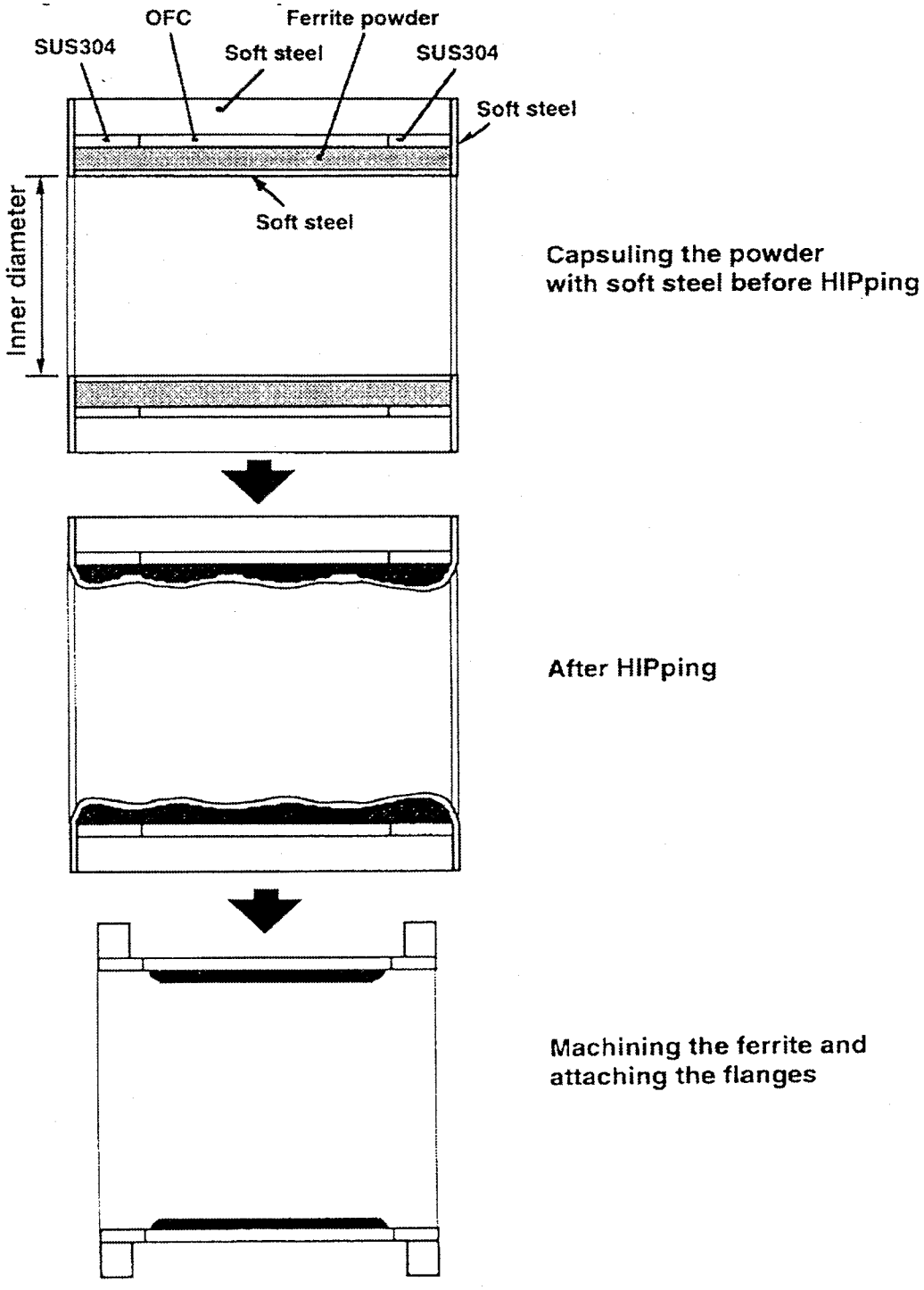

Fig. 3.4.3-1: Sketch of our first plan of HIPping pre-sintered ferrite powder.

Chapter 4

Measurements of fundamental properties of ferrite

When we chose IB-004[1] as a candidate for our absorber, since it had never been used in an accelerator before, we had to measure the fundamental properties that we need for designing our absorber. Moreover, since we later used a pre-sintered ferrite powder that was extracted in the middle of the manufacturing process, many properties changed from the values written in the catalogue.

The properties we measured are permittivity, permeability, DC conductivity, density (porosity), thermal conductivity, thermal expansion coefficient, power handling capability, outgassing rate and mechanical strength. In the following subsections, these properties are described with results. Most of the measurements were carried out using small samples (up to 6 cm). Tests on a 1/3-size model and full-size absorbers will be described in Chapter 6 and Chapter 8, respectively.

4.1 Permittivity (ε) and Permeability (μ)

As described in Section 3.2, lossy materials can be characterized with complex permittivity $\varepsilon = \varepsilon_0(\varepsilon' - j\varepsilon'')$ and complex permeability $\mu = \mu_0(\mu' - j\mu'')$. The real parts and imaginary parts of these values can be calculated with S parameters measured using a network analyzer.

To obtain these properties, we made a coil-shaped sample as shown in Fig. 4.1-1. Then, the S parameters of the coaxial line, filled with ferrite, was measured using a network analyzer. With the S parameters, one can calculate ε and μ [20].

[1] A commercially available microwave-absorbing ferrite manufactured by TDK, Inc.

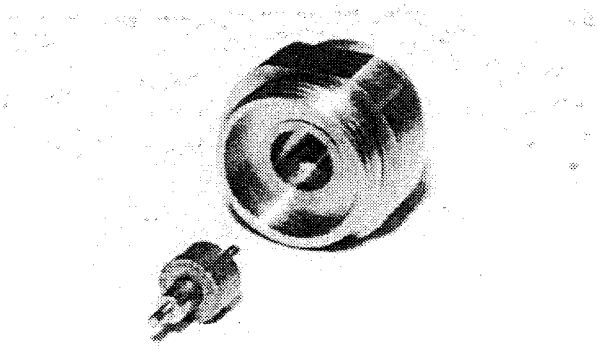

Fig. 4.1-1: A coil-shaped ferrite sample to measure ε and μ. The dimensions of the ferrite sample are 3 mm i.d., 7 mm o.d. and a few mm in length.

Figures 4.1-2 through 4.1-5 show the normalized permittivities and permeabilities of standard IB-004 and HIPped samples. Here, ε and μ are normalized by ε_0 and μ_0.

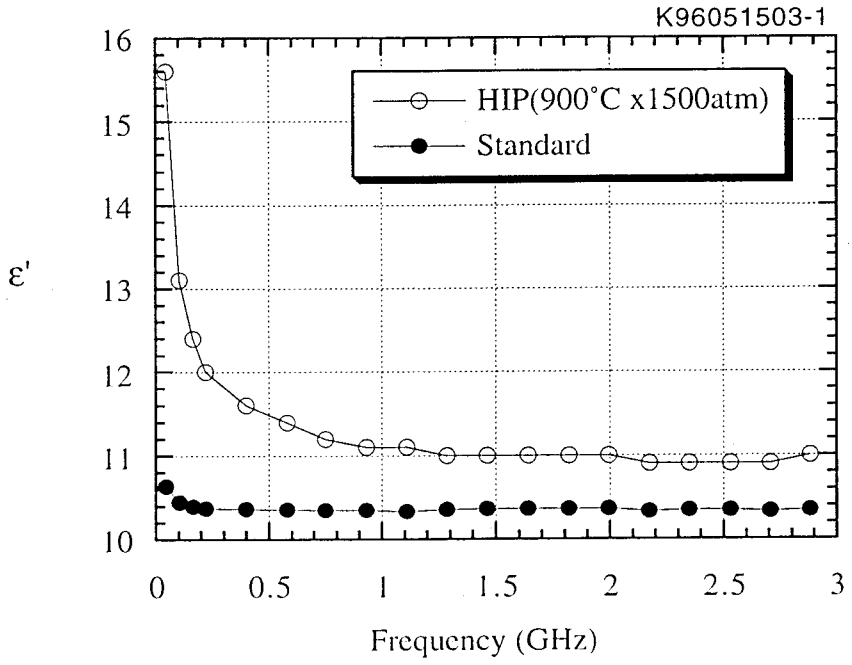

Fig. 4.1-2: The real part of permittivity of commercial IB-004 ferrite (Standard) and HIPped ferrite.

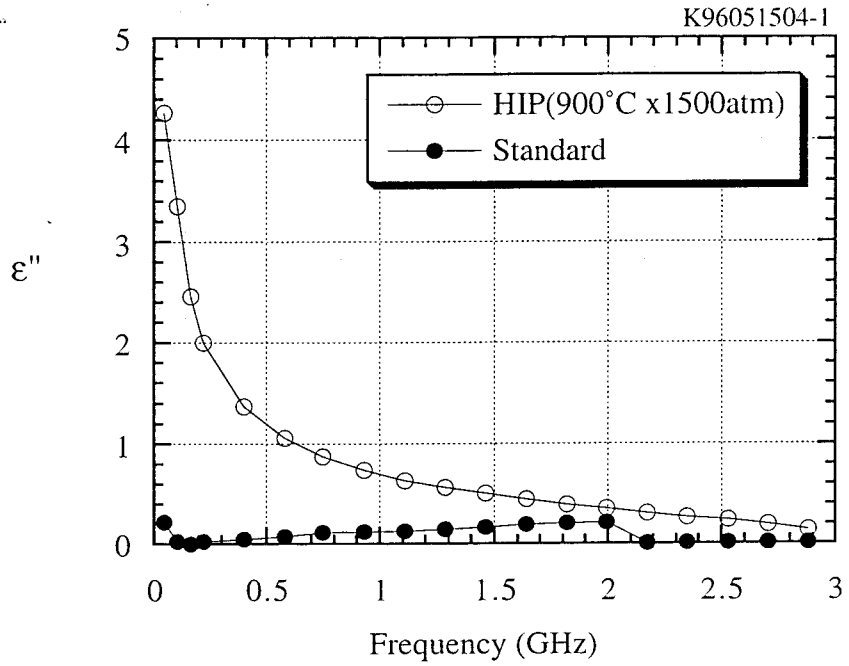

Fig. 4.1-3: The imaginary part of permittivity of commercial IB-004 ferrite (Standard) and HIPped ferrite.

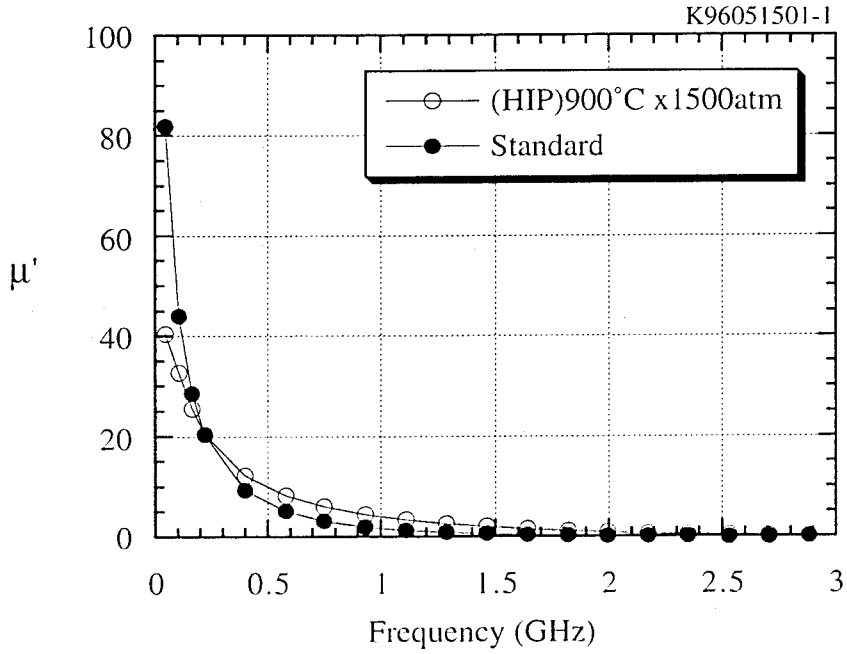

Fig. 4.1-4: The real part of permeability of commercial IB-004 ferrite (Standard) and HIPped ferrite.

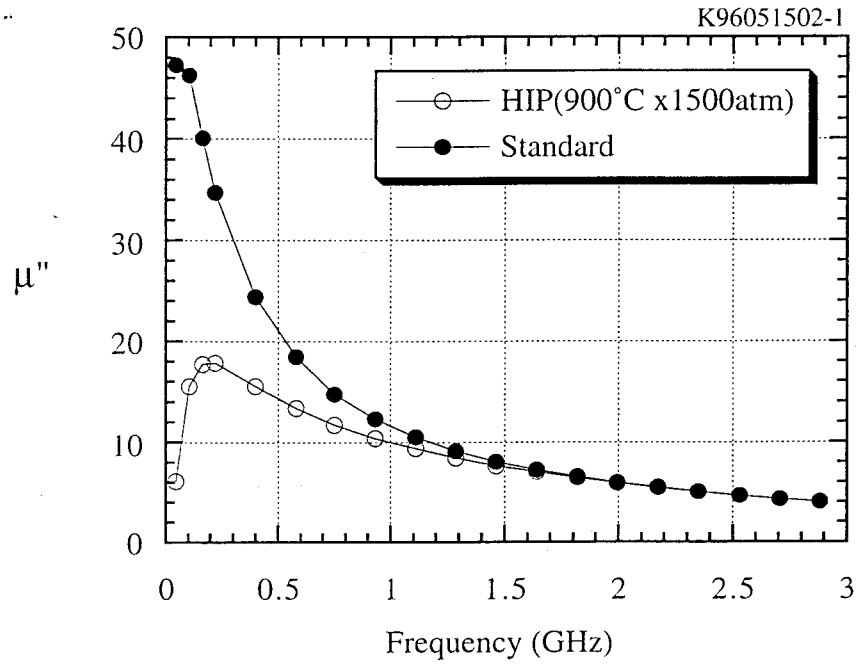

Fig. 4.1-5: The imaginary part of permeability of commercial IB-004 ferrite (Standard) and HIPped ferrite.

4.2 DC conductivity (resistivity)

Resistivity was measured using HP3458A Digital Multi Meter (DMM). The shape of the sample and the measurement set-up are shown in Fig. 4.2-1. The electrodes were soldered with the ultrasonic solder Cerasolzer W123.

DC resistivities of the samples (3 mm x 3 mm x 10 mm) made from a standard (tile), HIPped and baked at 1050 °C in air, were measured. Figure 4.2-2 shows the results. As one can see, HIPped samples (designated as "powder HIP") show resistivities of 3-6 x 10^4 Ωcm, which are more than one order of magnitude less than the standard IB-004 (~1 x 10^6 Ωcm). This improved conductivity is caused by the metallic impurities that diffuse from the inner capsule to the ferrite during the HIP process. This conductivity appears to be enough to prevent an increase in charge on the ferrite surface.

The sample baked at 1050°C in the vacuum showed higher resistivity, which suggests that some impurity plays an important role in giving a certain amount of conductivity.

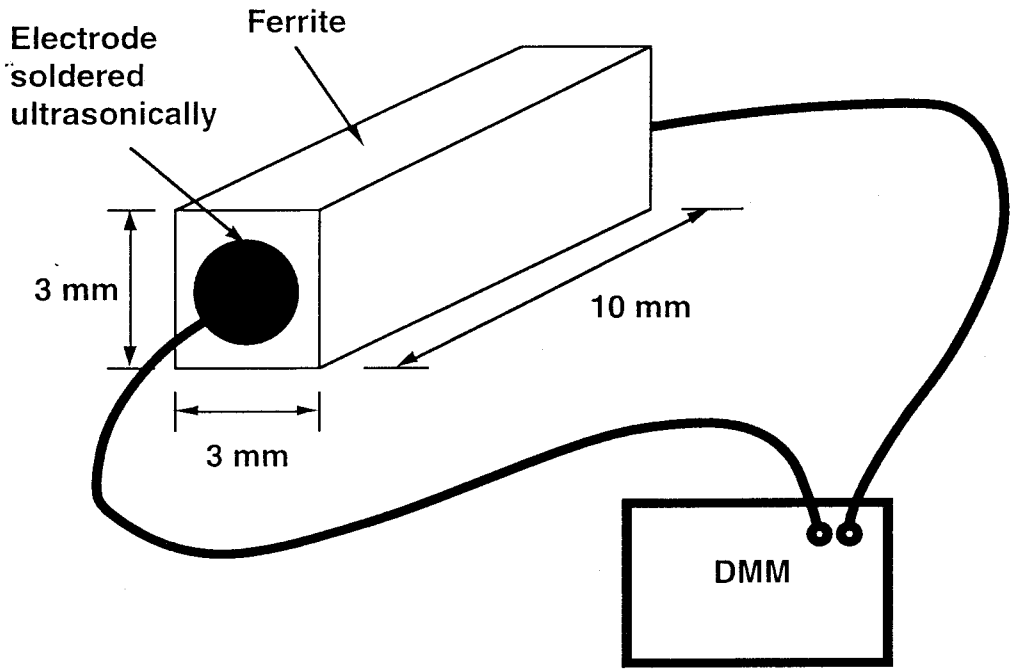

Fig. 4.2-1: Shape of the sample and measurement setup for DC conductivity.

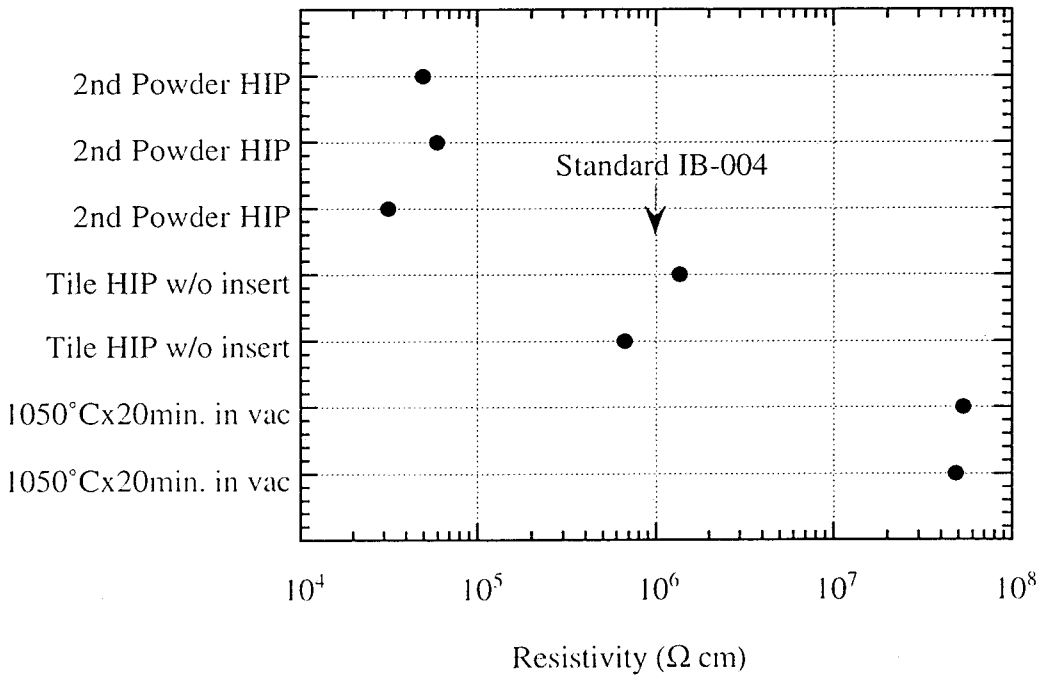

Fig. 4.2-2: Resistivity of ferrite made using various methods.

4.3 Density (porosity)

We calculated the density by measuring the weight of the sample. Since the sample was machined with precision, we obtained the density by dividing the weight by the volume. The porosity was defined as follows,

$$\text{Porosity}(\%) = \frac{(\text{Ideal density}) - (\text{measured density})}{(\text{Ideal density})} \times 100 \qquad (4.3\text{-}1)$$

where the ideal density is 5.45 g/cm , which was theoretically calculated using the composition of the ferrite.

Table 4.3-1 summarizes the results. As one can see, HIPping at 900 °C x 1000 atm for 5 hours gave the same density as 1000 °C x 300 atm for one hour, which suggested that 900 °C is enough to complete the sintering if the powder is under 1000 atm ≤ and for 5 hours or more. So, taking into account that the temperature should not be too high to prevent melting the copper, we decided the HIP temperature should be at 900 °C with 1000 atm ≤ for 5 hours.

Also, we checked the temperature dependence on the density. We measured the samples HIPped at every 25 °C intervals from 850 °C through 950 °C at 1000 atm. The result did not show strong dependence on temperature and the data scattered between 5.15 and 5.30 g/cm^2.

Table 4.3-1: Summary of density (porosity) of ferrite IB-004 in different conditions.

Type	Density (g/cm^3)	Porosity (%)
Standard IB-004	4.84	11
Tile HIP 850°C x 1h, 1000 atm	4.95	9
Powder Hot press 1000°C x 1h, 300 atm	5.23	4
Powder HIP 850°Cx 2h, 1000 atm	4.95	9
Powder HIP 900 °C x 3h, 1000 atm	5.15	5.5
Powder HIP 900 °C x 5h, 1000 atm	5.23	4

4.4 Thermal conductivity

Thermal conductivity was measured using the laser flash method [62, 63]. A pulsed laser was irradiated on one side of a 2 mm-thick , 10 mm-diam. ferrite disc while the time evolution of the temperature of the opposite side of the disc was recorded. Specific heat, the heat diffusion rate and thermal conductivity were calculated by the following formulas.

$$C_p = Q/(l \cdot \rho \cdot \Delta T_{max})$$

$$K = 1.37\ (l/\pi)2/t_{1/2}$$

$$\lambda = K \cdot Cp \cdot \rho$$

where

C_p: Specific heat

Q,: Absorbed energy

l : Thickness of the specimen

ρ : Density of the specimen

ΔT_{max}: Maximum temperature rise

K: Heat diffusion rate

$t_{1/2}$: Time for the rear side temperature to rise to half of ΔT_{max}

λ: Thermal conductivity

Figure 4.4-1 shows the temperature dependence of thermal conductivity. It was found that thermal conductivity increases with HIP temperature up to about 930 °C as shown in the figure. If possible, it is preferred to perform HIPping at 930 °C or above to densify and complete the sintering. To avoid softening the copper too much, we set the HIP temperature at 900 °C.

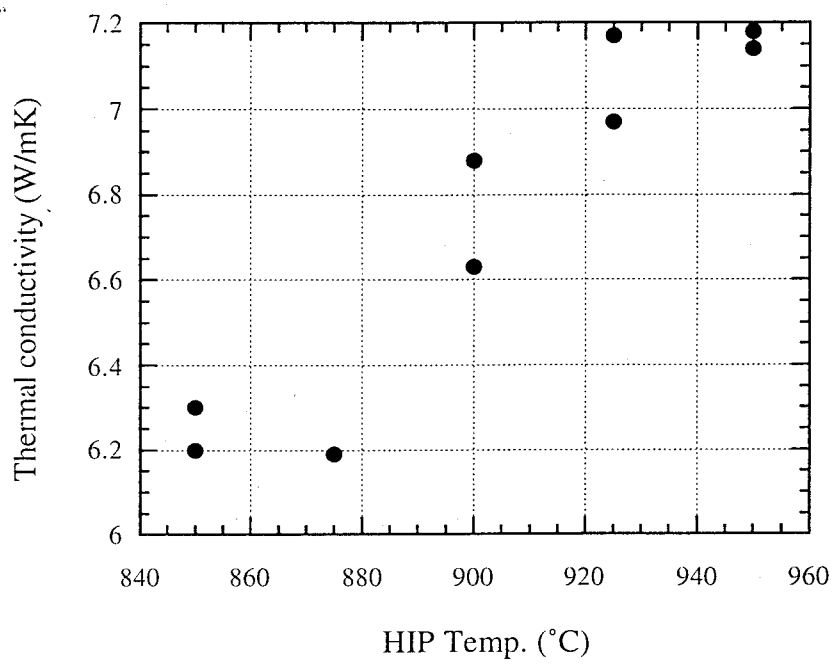

Fig. 4.4-1: Thermal conductivity of IB-004 HIPped ferrite as a function of HIP temperature. HIP pressure was 1000 atm. The holding time at this temperature was 5 hours.

4.5 Thermal expansion coefficient

In order to understand thermal stress during HIP and other situations such as baking, it is important to know the thermal expansion coefficient and its dependence on temperature.

The shape of the sample was the same as the one used for the measurement of conductivity(resistivity) shown in Fig. 4.2-1. The length was monitored as the temperature was raised at a rate of 5 °C/min. The two samples that were HIPped at 900 °C and 925 °C were measured [22]. Both samples gave the same results and the result for 900 °C is shown in Table 4.5-1. The data shown are averaged every 50 degrees. Both samples cracked around 500-530 °C during the measurements.

Table 4.5-1 : HIP ferrite sample thermal expansion coefficient (HIP condition was 900°C x 5h) [22]

Temperature (°C)	$\Delta L/L$ ($x10^{-3}$)	Average expansion coefficient ($x10^{-6}/K$)
50 - 100	0.39	7.9
100 - 150	0.48	9.5
150 - 200	0.48	9.5
200 - 250	0.53	10.6
250 - 300	0.58	11.5
300 - 350	0.62	12.4
350 - 400	0.58	11.6
400 - 450	0.54	10.9
450 - 500	0.61	12.2

4.6 Power handling capability [51]

In order to know some of the properties when high power is involved, this test was conducted using an IB-004 tile (6 cm x 6 cm x 4 mm) with a 2.45 GHz, 1.5 kW power source. A TE10 mode was used. Figure 4.6-1 shows a schematic of the test set-up. One tile was set in various ways on a surface of a rectangular waveguide as shown in Fig. 4.6-2. The surface temperature of the ferrite tile was measured with an IR (Infra Red) camera through a slit made in the wall of the waveguide as shown in Fig. 4.6-3. Figures 4.6-4 and 4.6-5 show the ferrite attached to the waveguide and the whole measurement set-up, respectively.

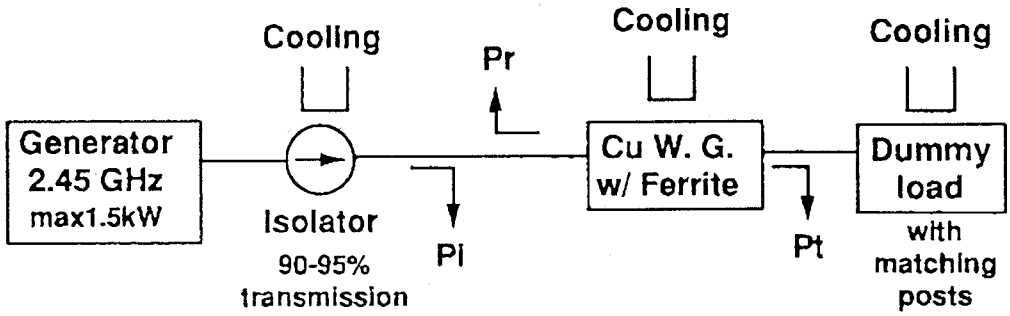

Fig. 4.6-1: Schematic of the experimental set up to test the ferrite tile.

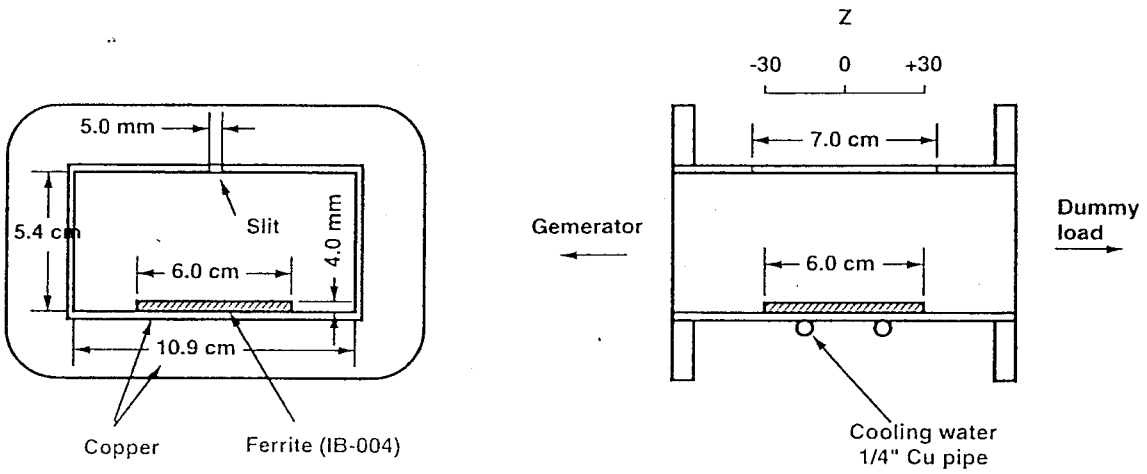

Fig. 4.6-2: Set-up of ferrite in the 2.45 GHz rectangular waveguide.

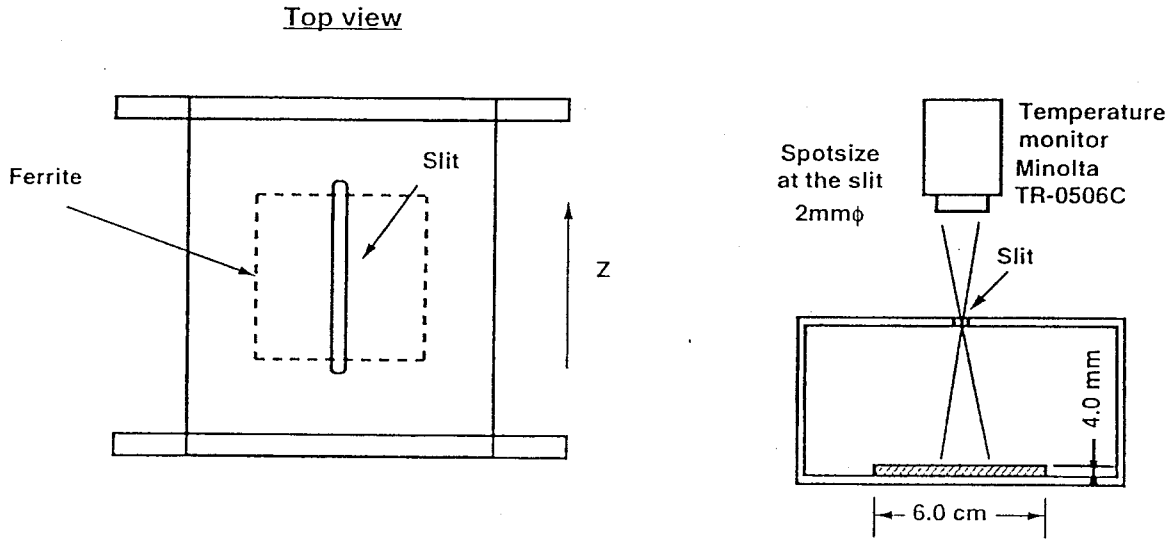

Fig. 4.6-3: Temperature monitoring the ferrite surface using an infrared radiation thermometer.

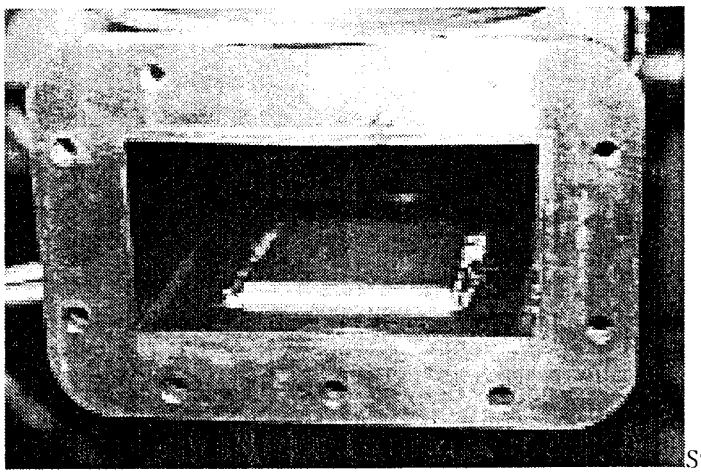

S99040802

Fig. 4.6-4: The ferrite tile (6 cm x 6 cm x 4 mm) soldered on to the copper waveguide.

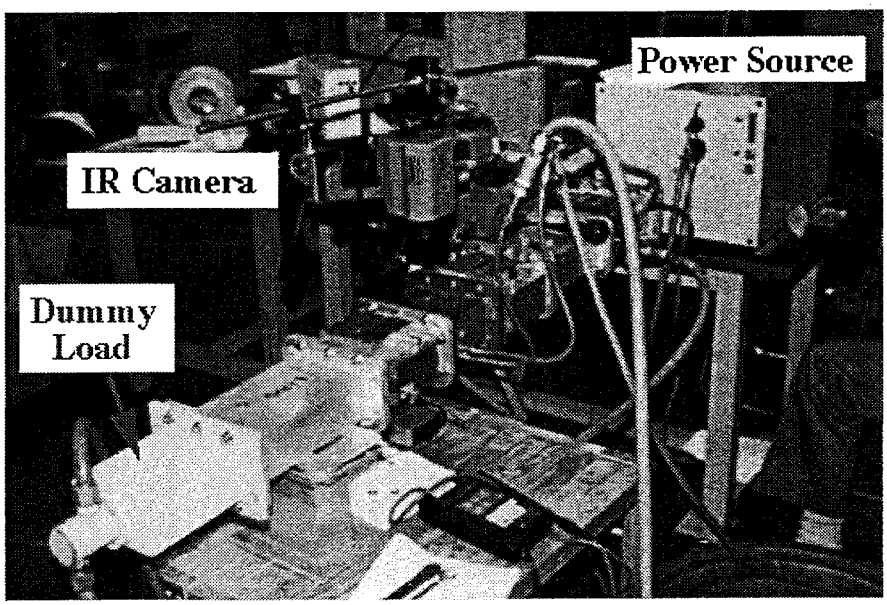

Fig. 4.6-5: The experimental set up.

It was found that the absorption decreases with the surface temperature and the temperature at which it ceased to absorb corresponds with Curie point (~280°C for IB-004) as shown in Fig. 4.6-6.

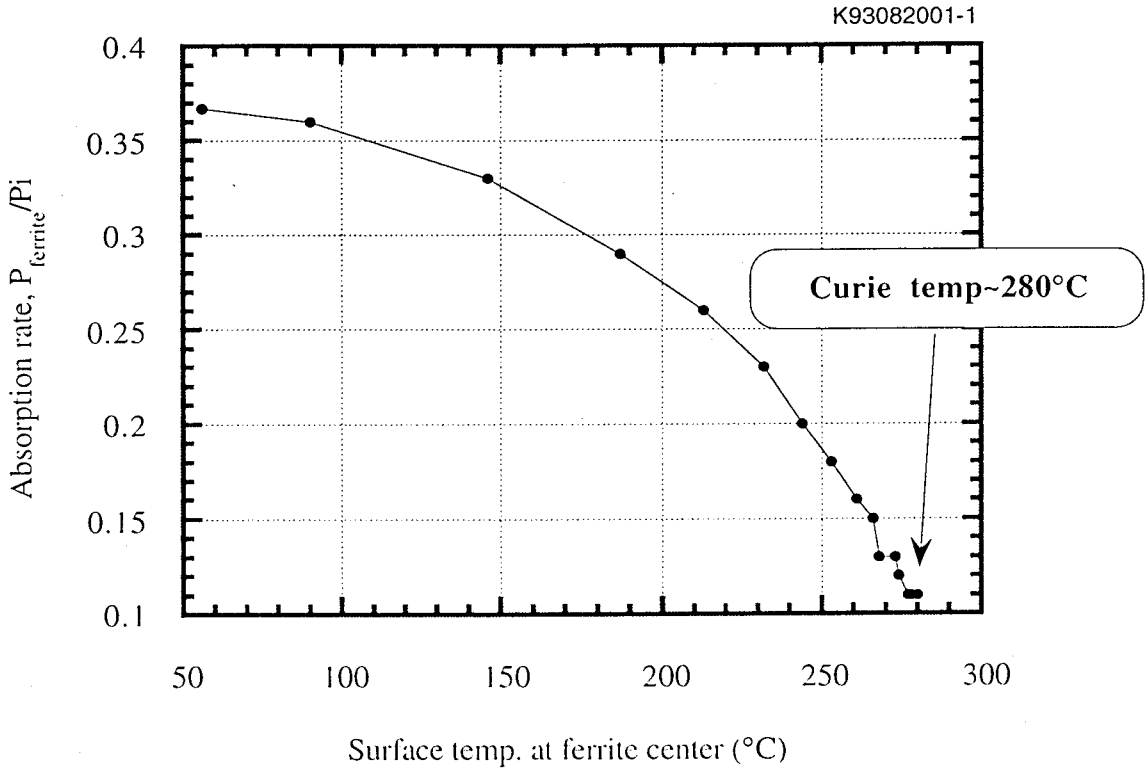

Fig. 4.6-6: Absorption rate as a function of surface temperature.

Figures 4.6-7 and 4.6-8 show the absorbed power density and surface temperature as a function of input power, respectively. To check the effect of bonding integrity on heat transfer, we tested three types, 1) no bonding, 2) glued with a tape and 3) ultrasonically soldered. As seen, the ferrite tiles that were not bonded or bonded with an aluminum tape could not absorb as much as the ones bonded firmly with ultrasonic soldering because the ferrite temperature rose due to the poor heat transfer. Even when this experiment was carried out in the air, it showed the importance of firm bonding.

The other important result is that the absorption is not proportional to the volume of the ferrite. A ferrite tile, 2 mm thick, could absorb about 90 % of the power that a 4 mm thick tile could absorb.

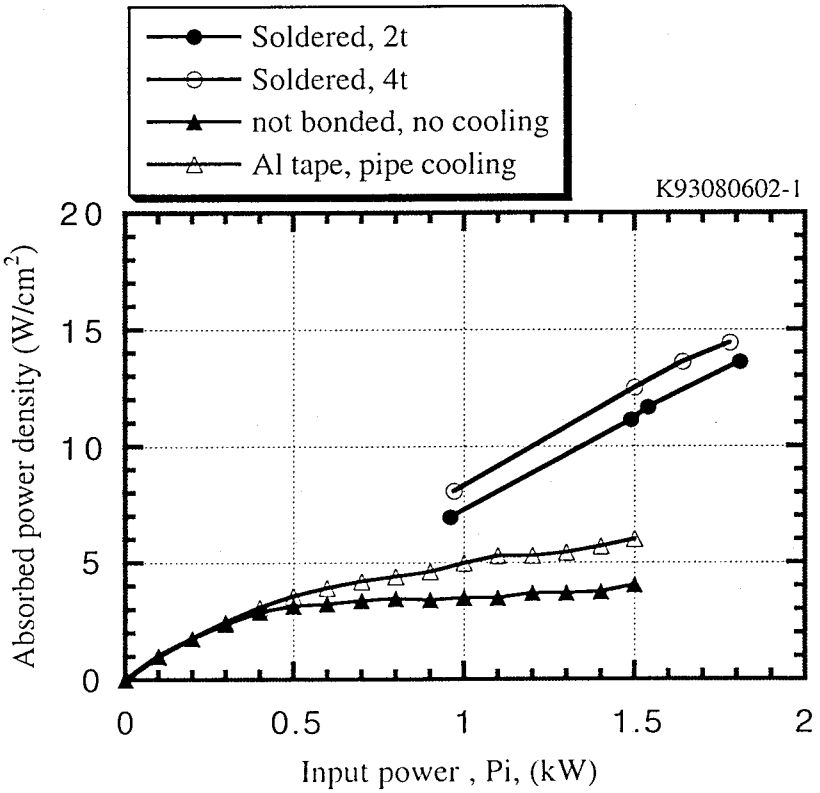

Fig. 4.6-7: Absorbed power density as a function of input power in various bonding conditions.

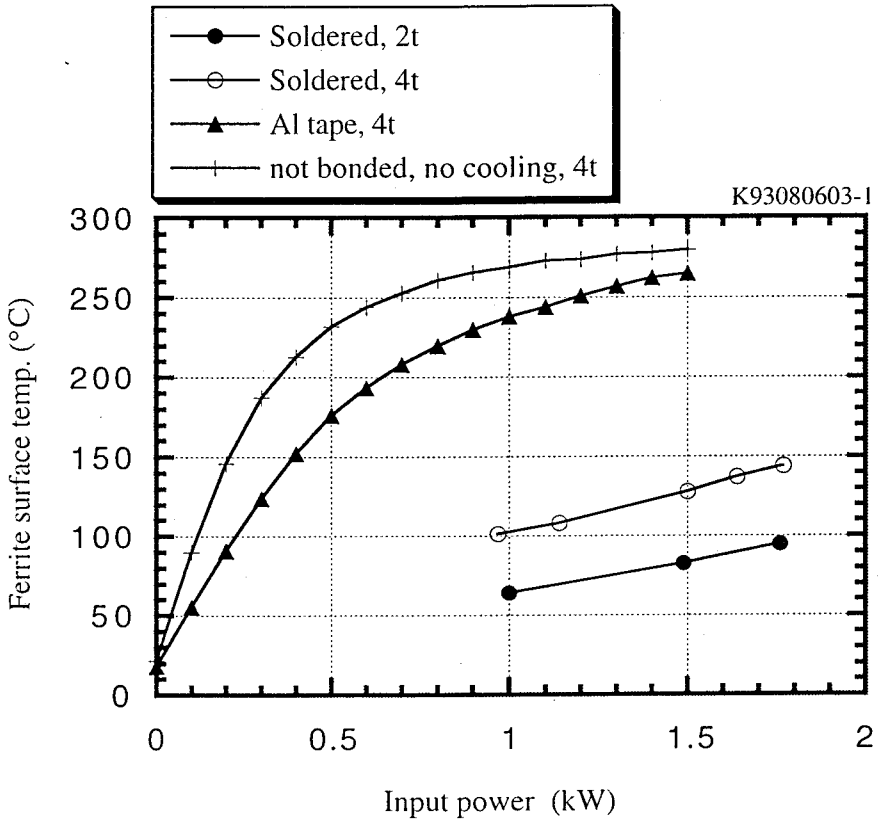

Fig. 4.6-8: Surface temperature as a function of input power in various bonding conditions.

Figure 4.6-9 shows the surface temperature as a function of absorbed density. As all the data showed linear behavior, it can be said that the condition of heat conduction at the interface did not change as the temperature rose. As seen in the figure, at 8 W/cm^2, 4-mm thick ferrite reaches 100 °C. As will be shown in the next Section, the outgassing rate rises significantly with the temperature, which can cause exceeding condensation of gases and lead to trips. Therefore, again, it is very important to bond the absorber firmly.

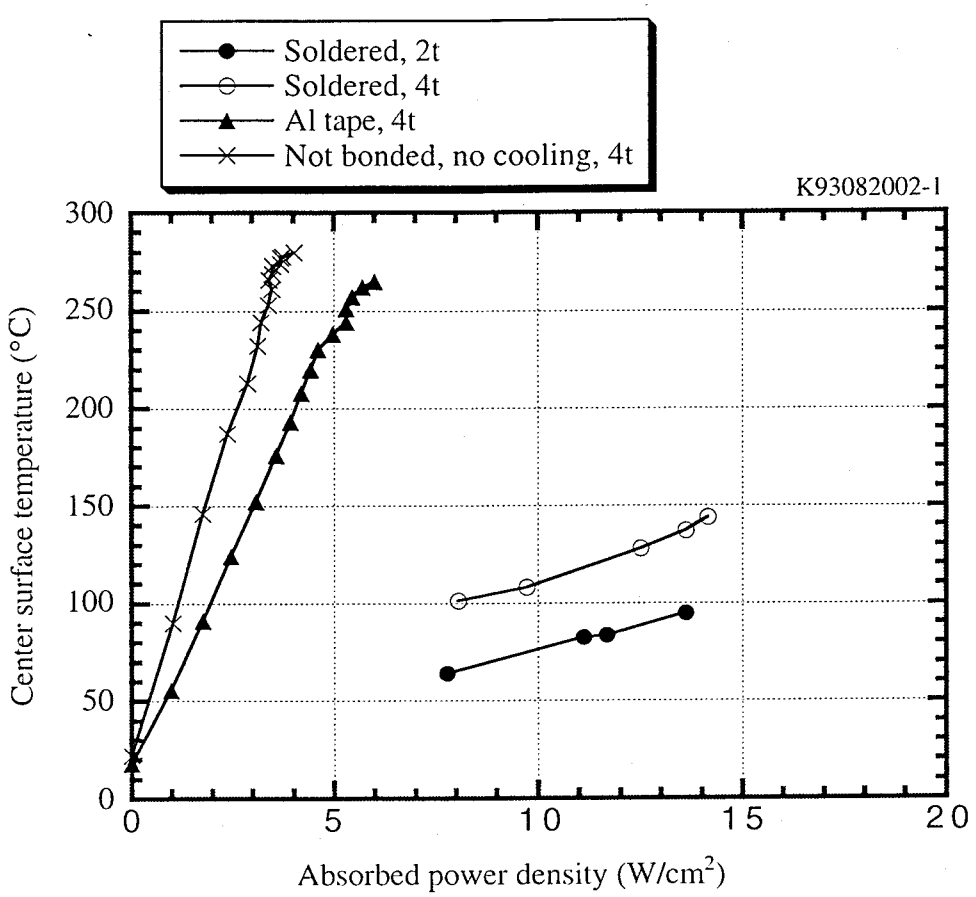

Figure 4.6-9: Surface temperature as a function of absorbed power density in various bonding conditions.

Figure 4.6-10 shows the longitudinal profile of the surface temperature. It was found that reducing the thickness has a significant effect on the surface temperature, which is probably due to the poor thermal conductivity of the ferrite (~6 W/mK).

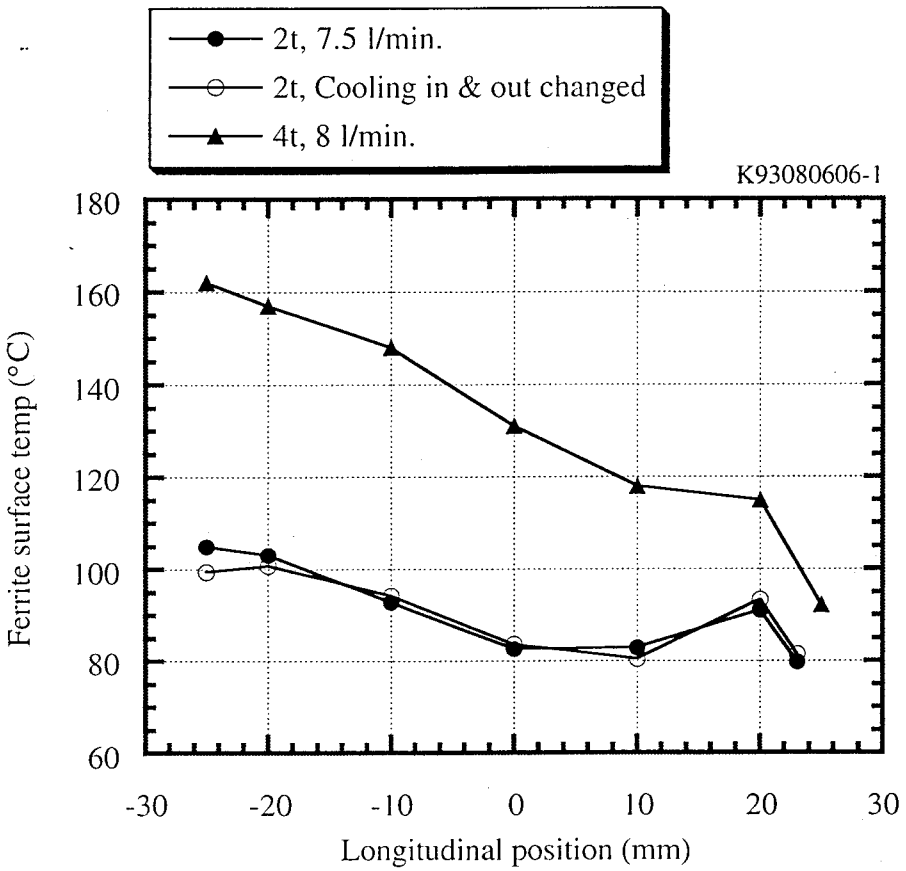

Fig. 4.6-10: Longitudinal surface temperature profile of ferrite tiles with different thickness.

The highest average power density was 14 W/cm^2. At the front edge, the estimated power density was about 19 W/cm^2.

After the test, it was found that part of the front edge of the 4-mm thick tile had cracked during the test. Assuming that it cracked at the maximum temperature, the temperature gradient was calculated to be 30 °C/mm from the rear side to the surface.

4.7 Outgassing rate

We checked the outgassing rate of the commercial IB-004 tile [50]. The rate at room temperature (R.T.) and when heated were measured by the so-called through-put method, i.e. the pressure difference through an orifice, whose conductance is known, is measured. The configuration of the measurement is shown in Fig. 4.7-1. If a ferrite sample is in the chamber with a pressure of P2 and the pressure of the other chamber is P1, the outgassing rate is calculated as C(P2-P1), where C is the orifice conductance, which was 3.3 L/s in our case. The outgassing rate from the heated ferrite was measured by irradiating its surface through a quartz glass with an infrared light as shown in Fig. 4.7-1. By using an elliptical mirror, the light was focused only on the ferrite, thereby avoiding an increase of the outgas from the chamber wall and quartz window.

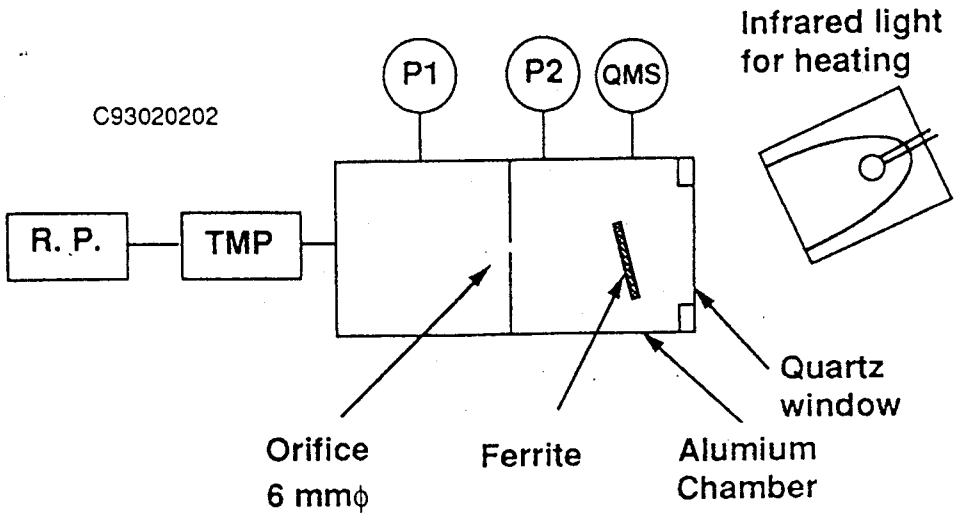

Fig. 4.7-1: Apparatus to measure the outgassing rate of ferrite.

In Fig. 4.7-2, the outgassing rate of as-received ferrite at R.T. is shown as a function of the time after starting to pump. The outgassing rate at R.T. after about 150 hours of pumping, including baking at 140 °C for about 25 hours, was about 5 x 10^{-11} Torr L/s cm^2 as shown in Fig. 4.7-2.

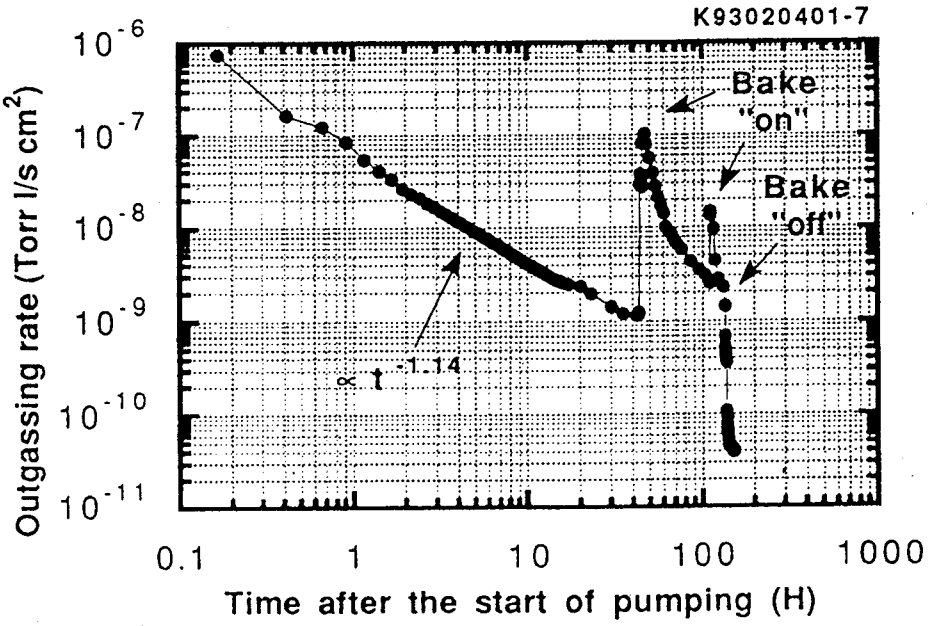

Fig. 4.7-2: The outgassing rate from the TDK ferrite IB-004 (commercially available) tile.

The outgassing rate when the ferrite is heated is shown in Fig. 4.7-3. It remained at around 2 x 10^{-9} Torr L/s cm^2 at 245 °C even after baking for a considerable time, i.e. about 70 hours at 130-400 °C.

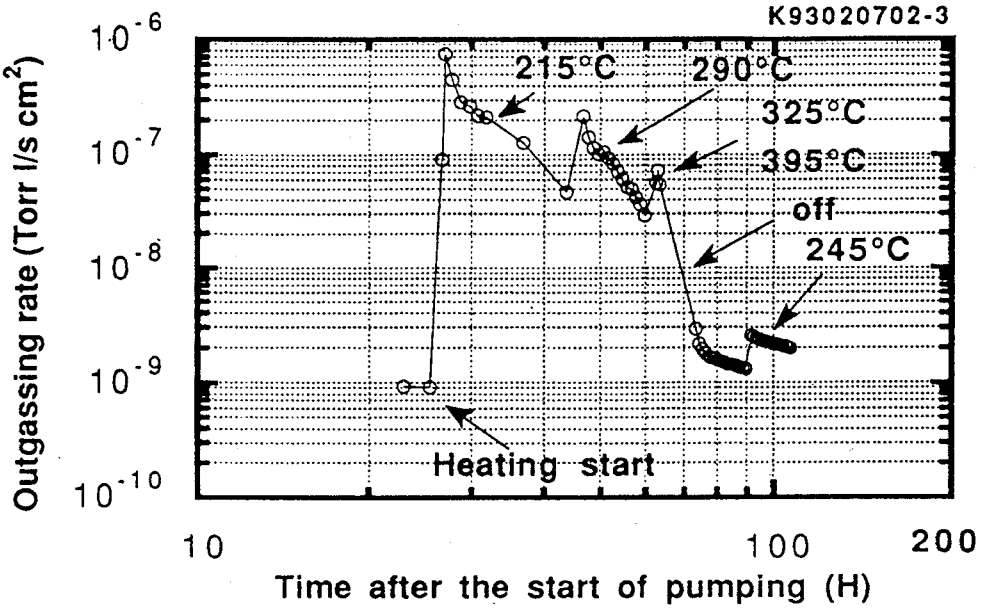

Fig. 4.7-3: The outgassing rate of IB-004 when heated by an infrared light.

The outgassing rate of the HIPped tile with copper was also measured [87]. Configuration of the measurement used for the HIPped tiles is shown in Fig. 4.7-4. Table 4.7-1 summarizes the results.

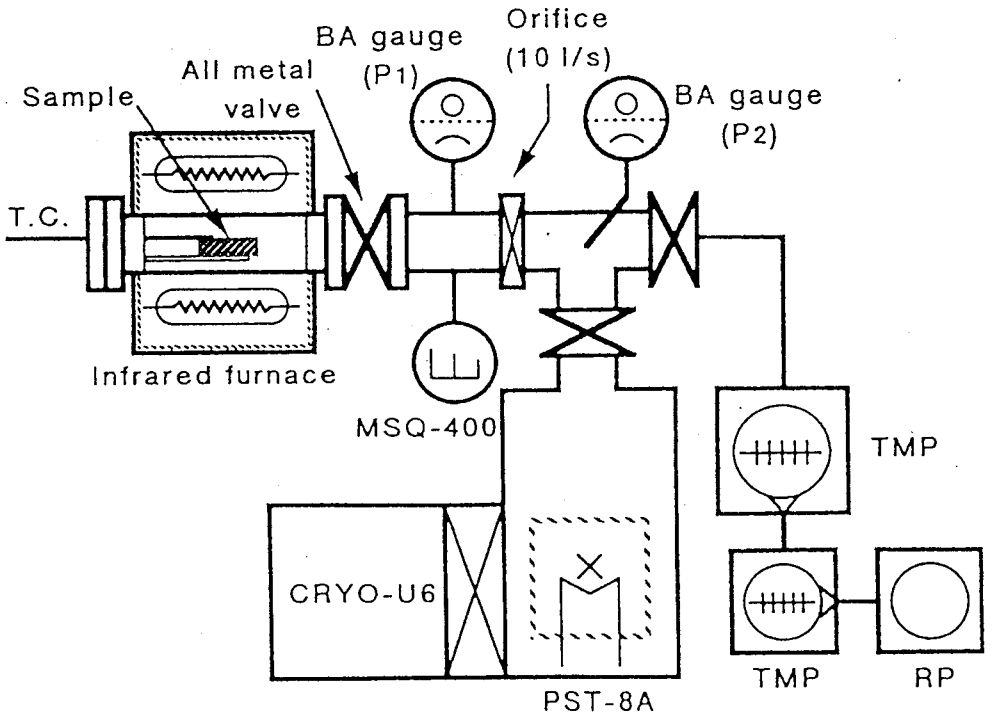

Fig. 4.7-4: Configuration of outgas measurement [87].

Table 4.7-1: Summary of outgassing rate of IB-004 sample.

Sample	Condition	Outgassing rate/area (Torr·L/s·cm^2)
Standard IB-004	at room temperature after 140 °C x 24h bake	5 x 10^{-11}
Standard IB-004	while heating at 245 °C	2 x 10^{-9}
HIPped tile on copper	at room temperature after 140 °C x 24h bake	1.4-2.5 x 10^{-11}
HIPped tile on copper	while heating at 280 °C for 230 hours	2.2 x 10^{-9}

4.8 Mechanical strength

As for the mechanical strength, we elected not to measure the samples of the HIP-bonded ferrite/copper composite taken from the full-size cylindrical pipe because the sample tends to break when being taken out due to the release of some stress that remains in the body.

4.9 Summary

To design and fabricate HOM absorbers, we measured the fundamental properties of the ferrite that we chose to use. Then the measured complex permittivity (ε) and permeability (μ) were used to calculate the electromagnetic field in the cavity in order to design the size and location of the absorber. The other measurements showed that: 1) DC resistivity of the ferrite made with HIP is 3-6 x 10^4 Ωcm, which is about a factor 25 lower than that made with standard method. This helps prevent an increase in charge of electrons on the ferrite surface. 2) Porosity reduced from 11 % to 4 % by HIP, which helps to produce less particles from the surface, makes it harder and gives a smoother surface as compared to standard ferrite. 3) Thermal conductivity increases with HIP temperature up to ~930 °C. 4) Ferrite breaks at 500-530 °C due to internal stress. 5) Thermal expansion coefficient increases with temperature at low temperature ranges (50 – 300 °C). 6) Power absorption of this ferrite decreases with temperature and ceases at 280 °C, which is the Curie temperature of this ferrite. 7) Thermal contact or high quality bonding with the substrate is important to keep the ferrite temperature low. 8) The outgassing rates of a standard tile and HIPped tile are 5 x 10^{-11} and 1.4-2.5 x 10^{-11} Torr·L/s·cm^2 at room temperature after a 140 °C x 24 hrs bake, respectively. The outgassing rate of the powder HIPped absorber will be discussed in Section 8.3.

Chapter 5

Experimental evaluation of bonding

5.1 Introduction

In this chapter we discuss the evaluation of ferrite bonding onto a metal.[1] It includes brazing, soldering and HIP (Hot Isostatic Press). Among them, HIP falls into two categories, 1) bonding a ferrite tile and 2) bonding pre-sintered ferrite powder on to the inner surface of a cylindrical metal pipe. In actual fact, at the early stages, HIP technique was not considered as a method of bonding. It was an idea that emerged when trying to overcome the difficulty of bonding using other methods.

We tried several ways to evaluate or diagnose the bonding integrity. They were (1) Micrograph, (2) SEM (Scanning Electron Microscopy) and EDX (Energy Dispersive X-ray analysis), (3) X-ray radiography and (4) Acoustic tomography. Among them, as will be shown later, we have beeb using acoustic tomography to check the entire surface and inside of the ferrite of full-size absorbers since it is a non-destructive method. Moreover, the X-ray radiography that we used did not have enough resolution for the HIPped samples.

5.2 Brazing

As discussed in Section 3.4, brazing is one of the most popular techniques to bond metals, ceramics and other materials. We evaluated both direct and indirect brazing of IB-004 with a metal. As shown in Fig. 5.2-1, due to the low bending strength of ferrite, cracks occur during the cool-down from a brazing temperature. To avoid the cracks, we found that the tiles should be 2 cm or smaller [50]. Thus, in all the tests 20 x 20 x 4 mm^3 ferrite tiles were used.

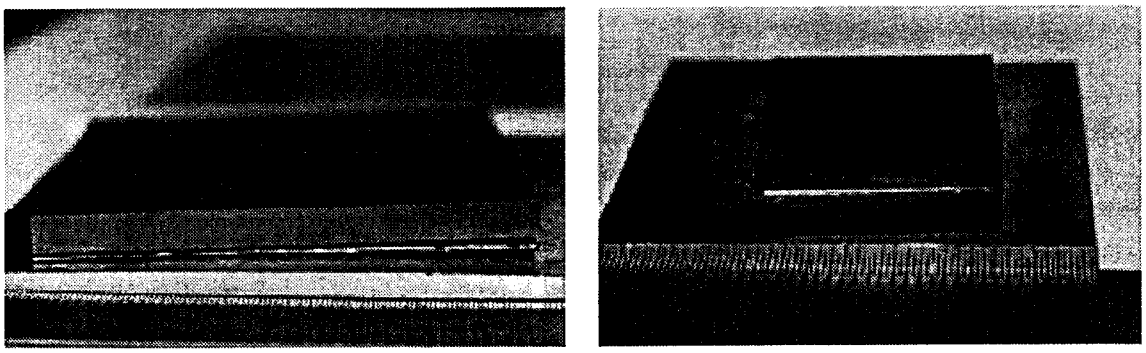

Fig. 5.2-1: Micrographs of bonding 4-mm thick ferrite tiles on 3-mm thick copper plates by brazing. The 6-cm ferrite broke (left), and in the case of 2 cm (right), ferrite could survive from cracking.

[1] We evaluated the bonding of IB-004 (microwave absorbing ferrite manufactured by TDK) only.

5.2.1 Direct brazing

The filler metals we have tested are listed in Table 1 of Ref. [21] with the test conditions and results. To avoid voids and oxidation of the copper, brazing was performed in a vacuum. The average vacuum during the tests was about 2 x 10^{-4} Torr. After confirming that the absorption characteristics does not change after heating at 870 °C for 40 min and at 1 x 10^{-5} Torr, we performed the braze tests.

We tested the brazed samples with an X-ray. Figure 5.2-2 shows the set-up of the tests [21, 62] and Figure 5.2-3 the image of the poorly brazed samples. The white areas are the voids caused by the insufficient wetting of the filler metal. Details of the tests are described in Ref. [21].

To summarize the results briefly, we could find a way to bond commercially available ferrite tiles on copper with a filler metal named BAg-8 (Silver:Copper=72:28) at 850 °C for 40 min with a pressure of 7.5 - 25 kg/cm^2. However, using this technique to braze a number of small pieces on to an inner surface of a large beam pipe was another problem. We did not go any further with this approach and chose to concentrate on the development of the HIP bonding.

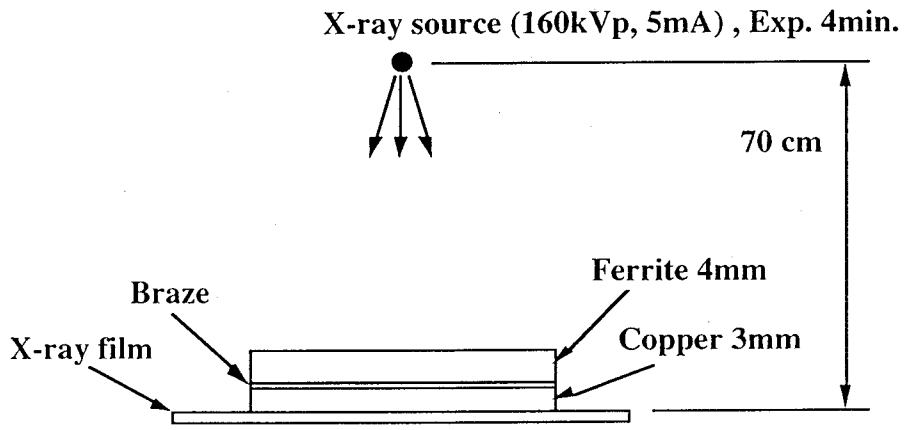

Fig. 5.2-2: Schematic of X-ray imaging set-up [21].

5.2.2 Indirect brazing

To help the ferrite wet well against the filler metal, we tried coating the ferrite with three layers of metals, i.e. Ti, Pt and Au of 0.2 μm thick each. This coating is normally used to bond SiC to metals at Hitachi Co., Ltd. The coating itself was firm and excellent, but the result of the brazing tests using both BAg-8 and BCuP (P:Ag:Cu=5:15:80) were unsuccessful. This was probably due to the inclusion of Ti in the coating because the interface looked similar to the direct braze with the Ti-contained filler metal. We stopped going further with this approach since this method is more complex and expensive compared to direct brazing.

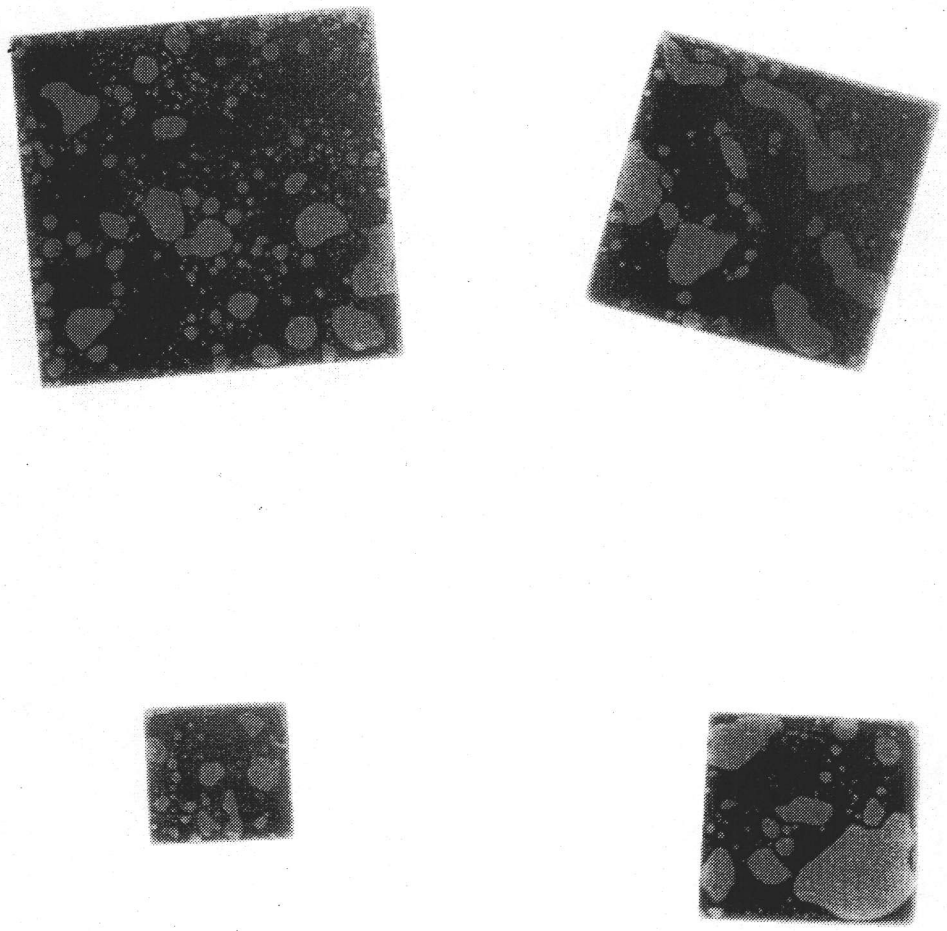

Fig. 5.2-3: X-ray radiograph of brazing that did not wet well. Voids clearly seen as white areas in the figures.

5.3 Soldering

Ultrasonic soldering was tested as a method to improve the wetting on the ferrite. We tried a solder called Cerasolzer, manufactured by Asahi Glass Company, which was developed for soldering glass and ceramics with metals. This solder is similar to the usual Pb-Sn solder except for the small addition of Zn, Sb, Al, Ti, Si and Cu. Table 5.3-1 shows the properties of Cerasolzer W123 and W297 that we used. Due to the easiness and relatively low temperature needed, this soldering was used for the high power tests of ferrite tile samples in non-vacuum conditions [51].

After putting the solder on both ferrite and copper with a vibrating bonder, we held them together at a slightly higher temperature than melting point. An X-ray test was performed to check the boundary [21]. The X-ray images of the soldered 6 cm x 6 cm x 4 mm ferrite tile with 3 mm-thick copper showed no typical voids, i.e. round bubbles, but some string-like lines were seen. When the sample was cut, it split in the interface. The micrograph of the cracked cross section revealed that cracks ran not in the interface but in the solder. This might have been caused by the oxidized surface of the solder during brazing because we

performed the soldering in atmospheric pressure. Later we tried to solder in an N_2 atmosphere. Though there was no crack in the solder, the ferrite tile cracked during the cool-down again due to its low bending strength.

In summary, we could not succeed to solder without cracking. There may be some solution if smaller tiles, say 1 cm x 1 cm, are used so there would be less bending stress exerted on the ferrite.

The outgassing rate from the 6 cm x 6 cm x 4 mm ferrite and 8 cm x 8 cm x 3 mm copper soldered together with Cerasolzer W297 was measured to be 2.5×10^{-7} Torr l/sec at 25°C after 163 hours of baking at 160°C. The outgassing rate at 160°C was 5.2×10^{-7} Torr l/s. Compared to the outgassing rate of the HIP bonding, 2.5×10^{-9} Torr l/s at 22 °C after 25 hours of baking at 140°C [51], this rate is 2 orders of magnitude higher and would be intolerable in the accelerator.

So, we did not go any further because we could achieve better success with the hot press technique. The technique we developed will be described in detail in a later section.

Table 5.3-1: Solders used for ultrasonic soldering, Cerasolzer.

Name	Composition	Melt. Point (°C)	Hardness 20°C, H_v	Th. Exp. Coeff. 15-110°C ($\times 10^{-6}$)	Elec. Resist. ($\times 10^{-6} \Omega$cm)
W123	50Cd/46In + Zn, Sb	123	4.63	-	10.4
W297	90Pb/5Sn + Al,Sb,Zn,Ti,Si,Cu	297	12.6	28.7	21.0

5.4 HIP

We tried 2 types of bonding using HIP. One was to bond a commercially available ferrite tile (60 x 60 x 4 mm^3) on to a metal plate. The other was to bond a pre-sintered ferrite powder onto the inner surface of a copper cylinder, which involves final sintering of ferrite as well. In this section, we discuss the latter since we adopted it as the fabrication method of full-size absorbers. As for the HIPping of the tiles, the result showed a good bond, but the final fabrication of the full-size absorber seemed to be more complicated than the powder HIPping [21]. The detailed analyses of tile HIPping are shown in Ref. [21].

As for powder HIPping, at first, we had to know in what conditions we could consolidate the powder. We tried hot pressing to check this and to measure any changes of the various properties after consolidation.

5.4.1 Hot press

Before testing the idea of pressing powder onto an inner surface of a beam pipe at a sintering temperature, we checked the properties of the hot pressed powder. Pre-sintered ferrite powder IB-004 was used. The average size of the powder was about 1 μm. Pressure was exerted with a hydraulic press and was limited by the mechanical break limit of the carbon pusher.

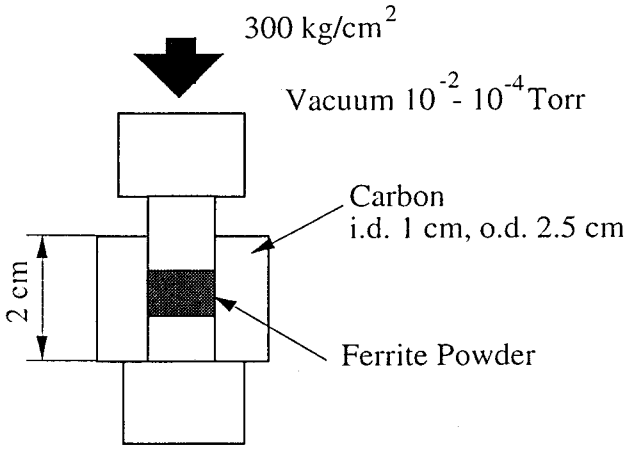

Fig. 5.4.1-1: Schematic representation of the apparatus for the hot pressing test.

Figures 5.4.1-1 and 5.4.1-2 show the dimensions of the fixtures and some images of the apparatus, respectively [21]. Figures 5.4.1-3 (a) and 5.4.1-3 (b) show micrographs of a commercially available tile IB-004 and a hot-pressed pre-sintered powder at 1000 °C and 300 atm for 2 h, respectively [21]. The consolidation of the ferrite was complete and, as one can see in Fig. 5.4.1-3 (b), the size of the pores reduced significantly in the hot pressed sample. The differences of the physical properties are summarized in Table 5.4.1.

Table 5.4.1: Properties of hot-pressed ferrite powder compared to a standard ferrite.

Kind	Density (g/cm^2)	Porosity (%)	Thermal Conductivity (W/mK)
Standard IB-004*	4.84	11	6.28
Hot Pressed	5.23	4	7.39

*Commercially available ferrite. Sintered in air without pressure.

We decided, however, to lower the temperature when HIPping with copper so as the copper would not get too soft and melt, although we could increase the pressure since the pressuring medium was gas.

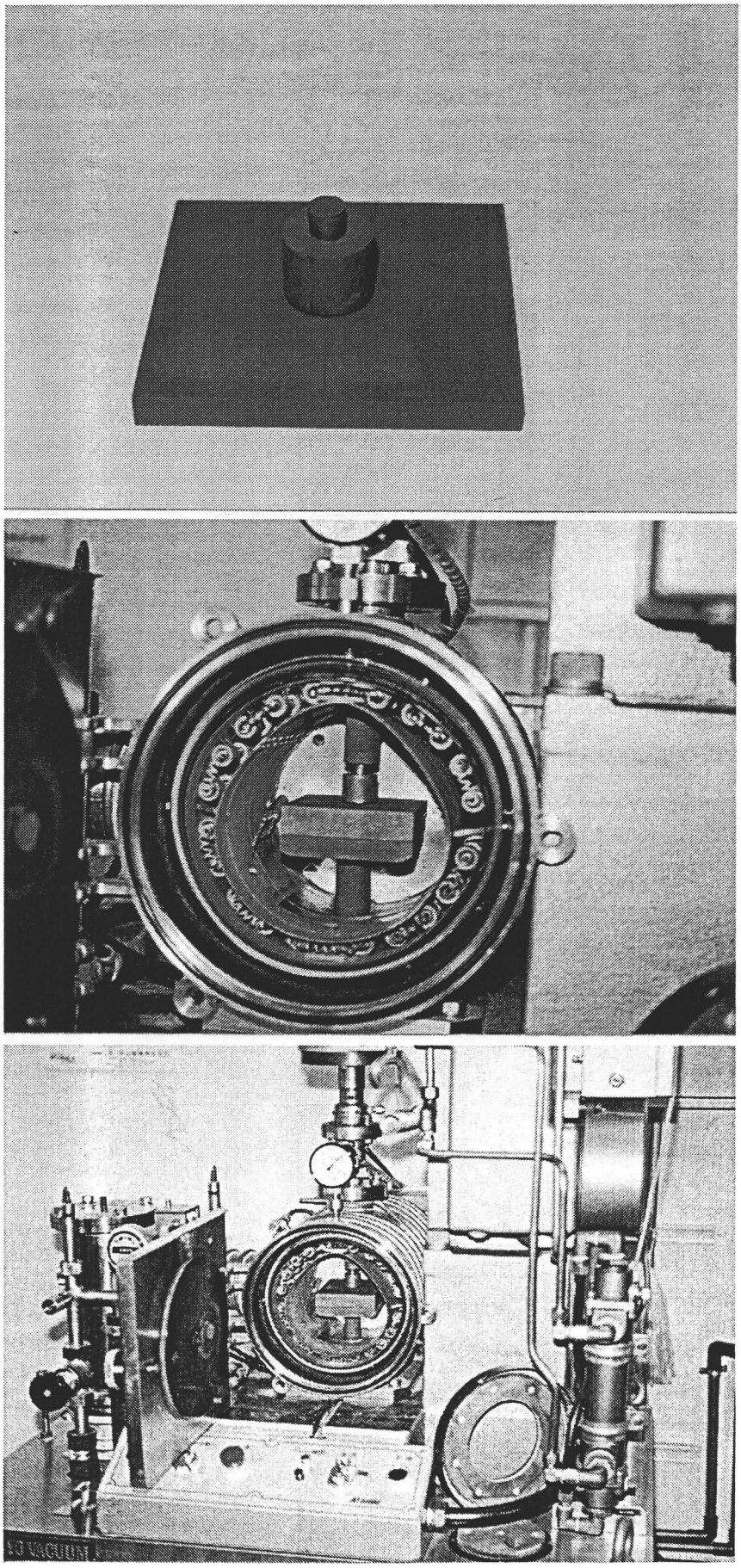

Fig. 5.4.1-2: Carbon pusher(top), inside of the furnace (middle) and the whole apparatus (bottom) [62].

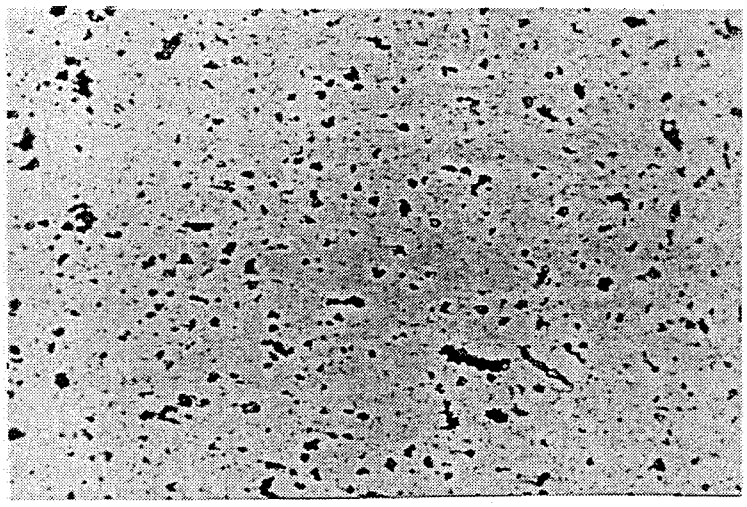

Fig. 5.4.1-3 (a): Standard IB-004 (Full width = 300 μm)

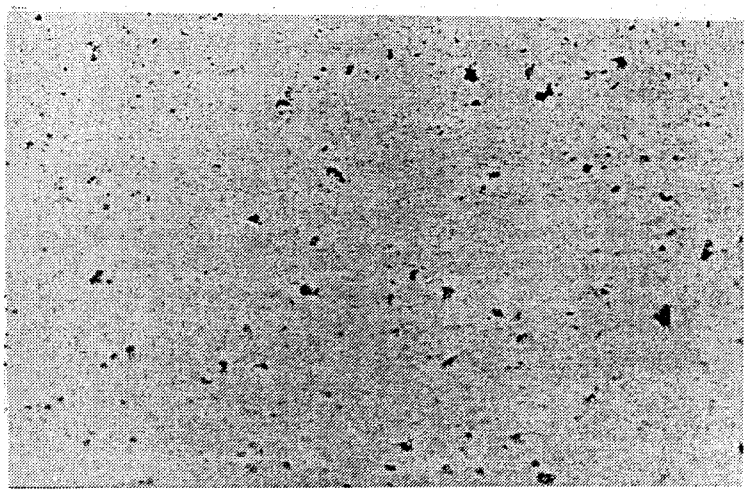

Fig. 5.4.1-3 (b): IB-004 hot-pressed powder. (Full width = 300 μm)

5.4.2 HIP

The details of the optimized HIP conditions to make full-size absorbers will be described in Chapter 7. The evaluation here shows the results obtained in the course of the development. When we HIP a full-size absorber, we always include a small sample to evaluate the properties of the ferrite and bonding. Although we usually evaluate only those samples, we cut the whole full-size absorber once, to check the integrity of the whole absorber as shown in Fig. 5.4.2-1. Figure 5.4.2-2 is a magnified view of part of the ring. In the figure, "STKM" is the soft steel outer capsule, and the inner capsule, "SPCE", is made of another soft steel that has a higher elongation rate to allow enough deformation.

Figures 5.4.2-3 and 5.4.2-4 show the Ferrite/Copper boundary and its magnified view. As one can see, a transition region of about 100 μm was found at the boundary. Figure 5.4.2-5 shows a magnified view of this region. There were no voids or defects at the boundary.

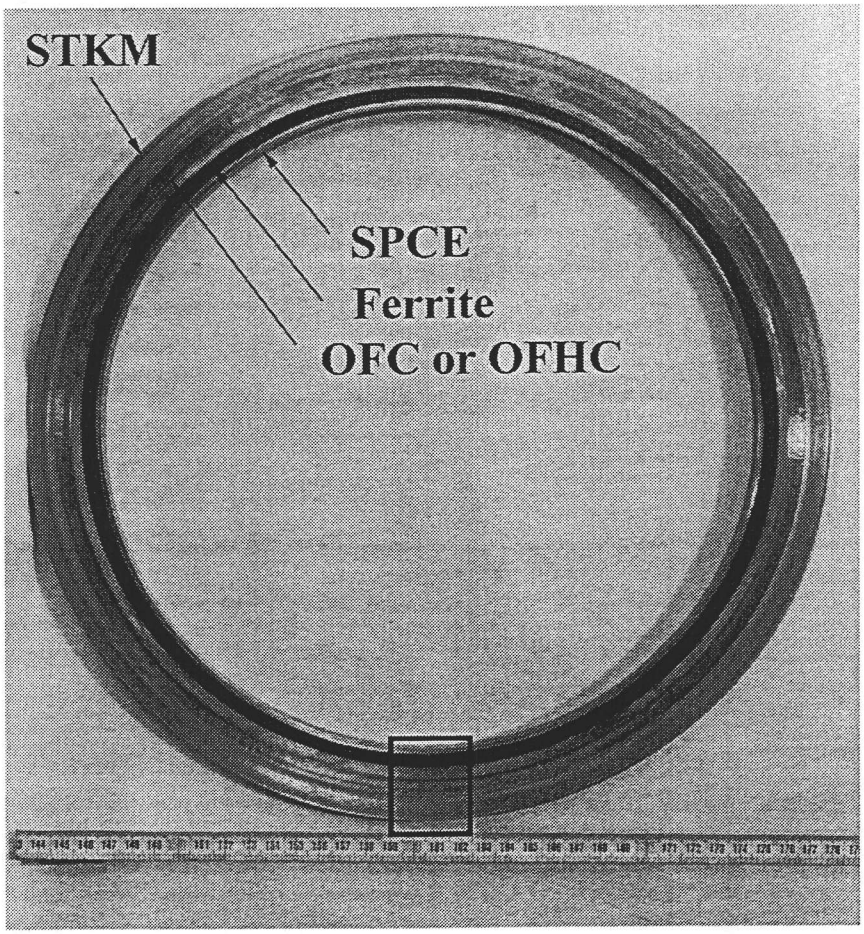

Fig. 5.4.2-1: After HIPping and before removing the soft steel inner capsule (SPCE). An absorber of about 300 mm in diameter was cut in a plane normal to beam axis to check the HIP bonding.

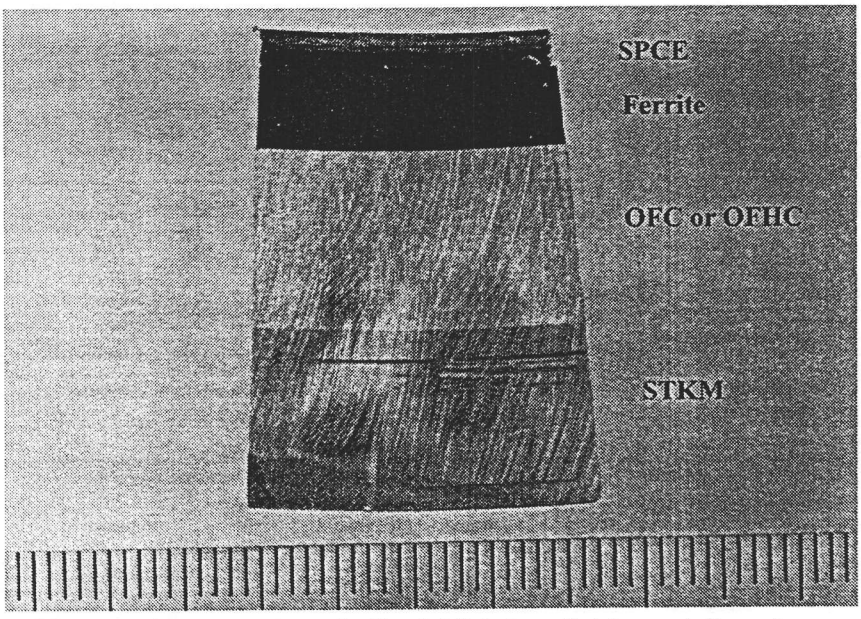

Fig. 5.4.2-2: Magnified view of the marked area in Fig. 5.4.2-1. (one division scale/1 mm).

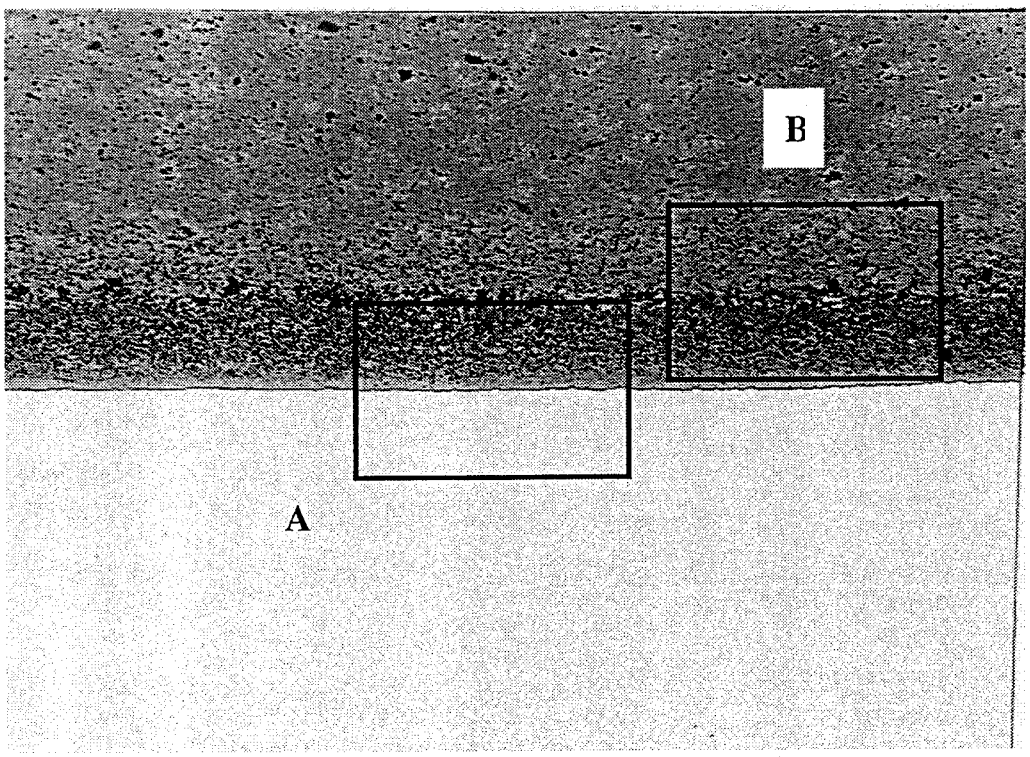

Fig. 5.4.2-3: Ferrite(top)/copper(bottom) boundary area (full image width = 940 μm).

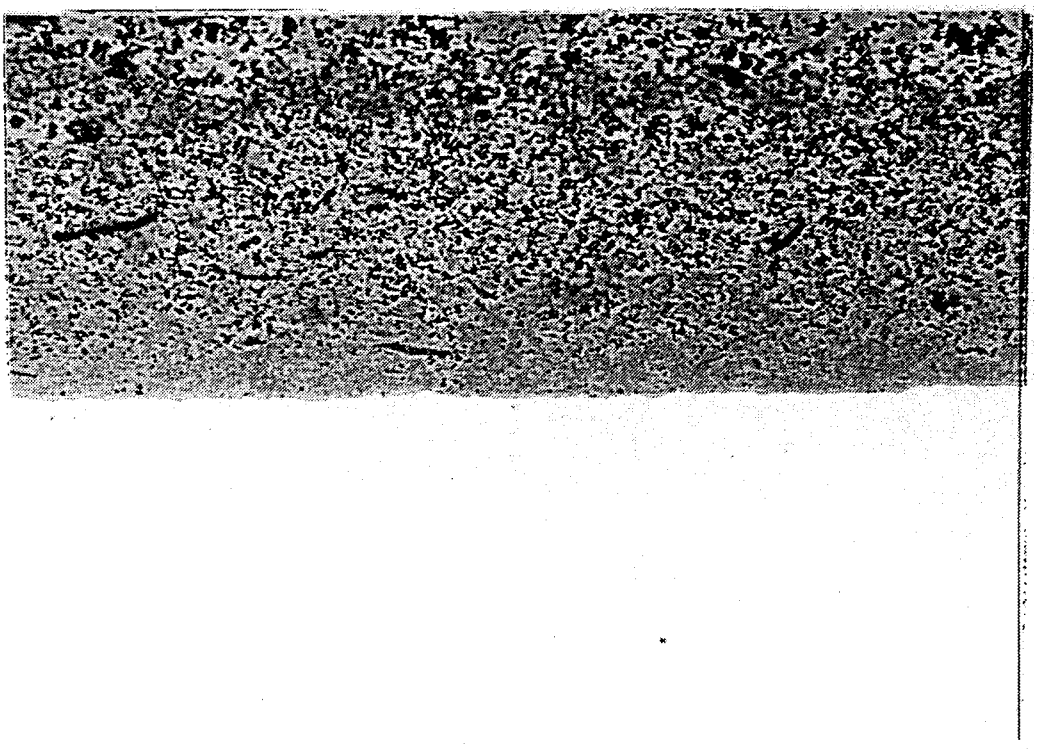

Fig. 5.4.2-4: Magnified view of marked area "A" in Fig. 5.4.2-3. (full width = 235 μm)

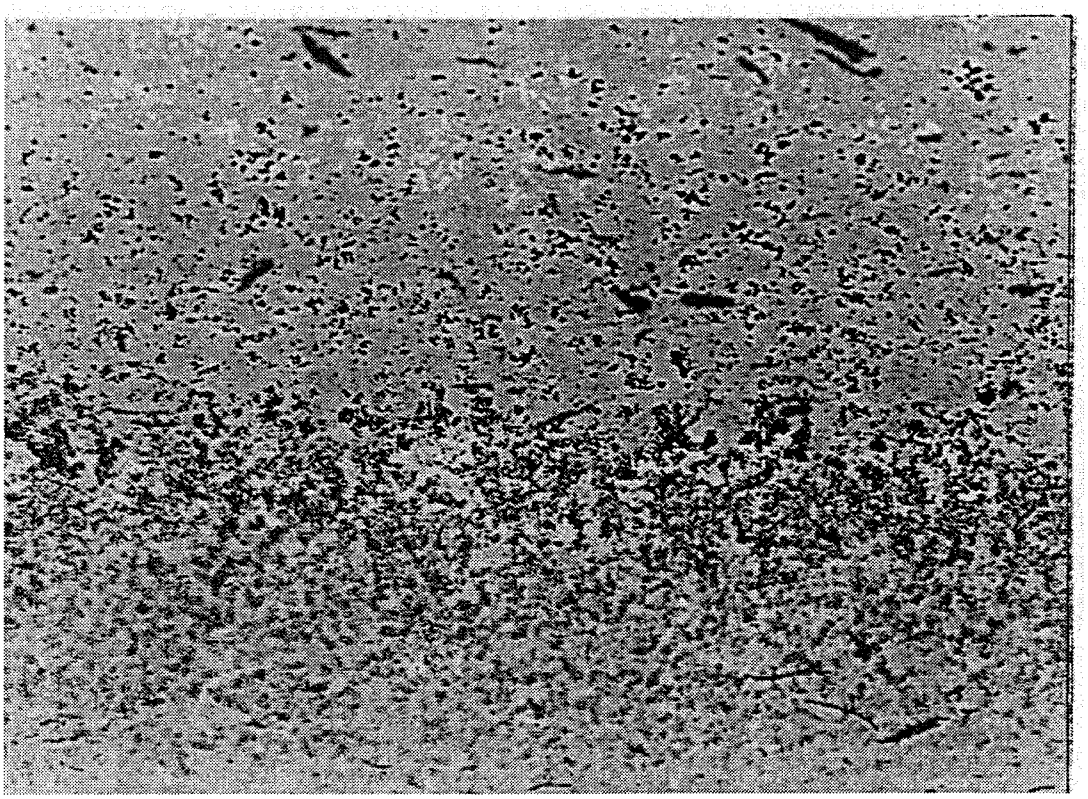

Fig. 5.4.2-5: Magnified view of area "B" in Fig. 5.4.2-3. (full width = 235 μm).

- **SEM-EDX analyses**

Figures 5.4.2-6 and 5.4.2-7 show this transition region and its magnified view with SEM (image is rotated 90° CCW). The HIP conditions were 1000 atm at 900 °C for 5 hours. Figures 5.4.2-8 and 5.4.2-9 show the EDX analyses of the region shown in Fig. 5.4.2-7 of copper and silicon, respectively.

In these analyses we found that this transition region consists of ferrite, copper and silicon. Basically the bonding is made by interlocking the ferrite and copper as well as diffusing the copper with this mixing band of about 90 μm.

In addition, the darker region in the transition area was found to be silicon, although we could not identify why it was there. It seems that small amounts of silicon were included in the pre-sintered powder and migrated near to the interface during HIP.

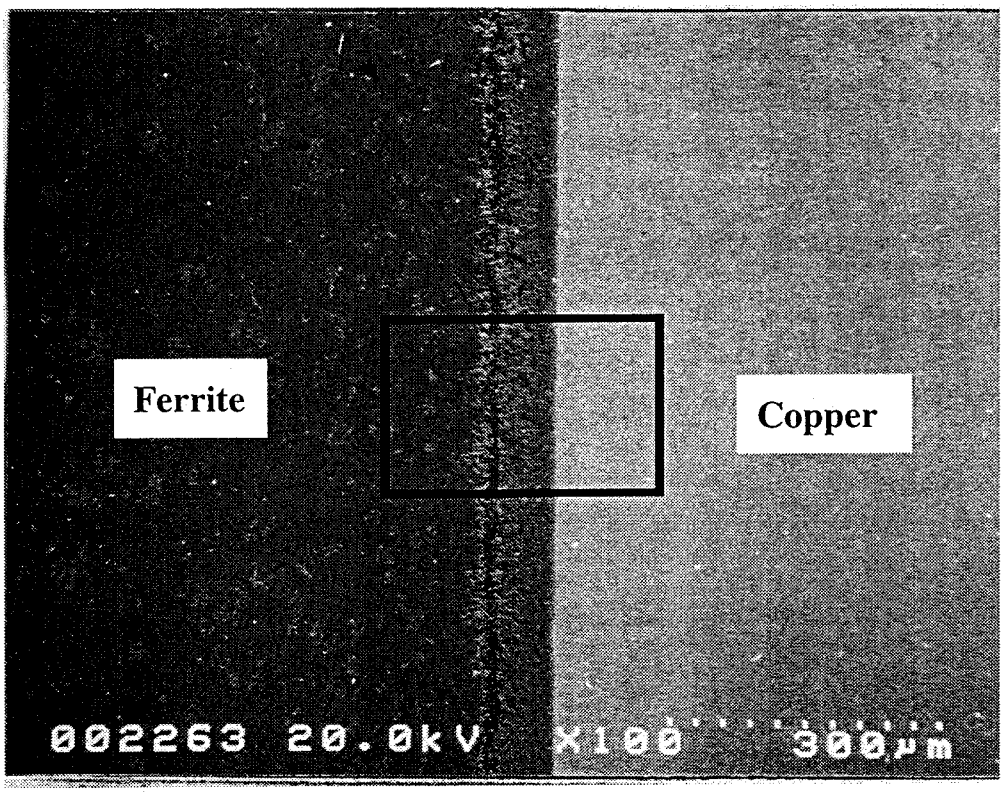

Fig. 5.4.2-6: SEM image of Ferrite/Copper boundary (full image width = 1.1 mm). HIP was carried out at 1000 atm x 900 °C x 5h.

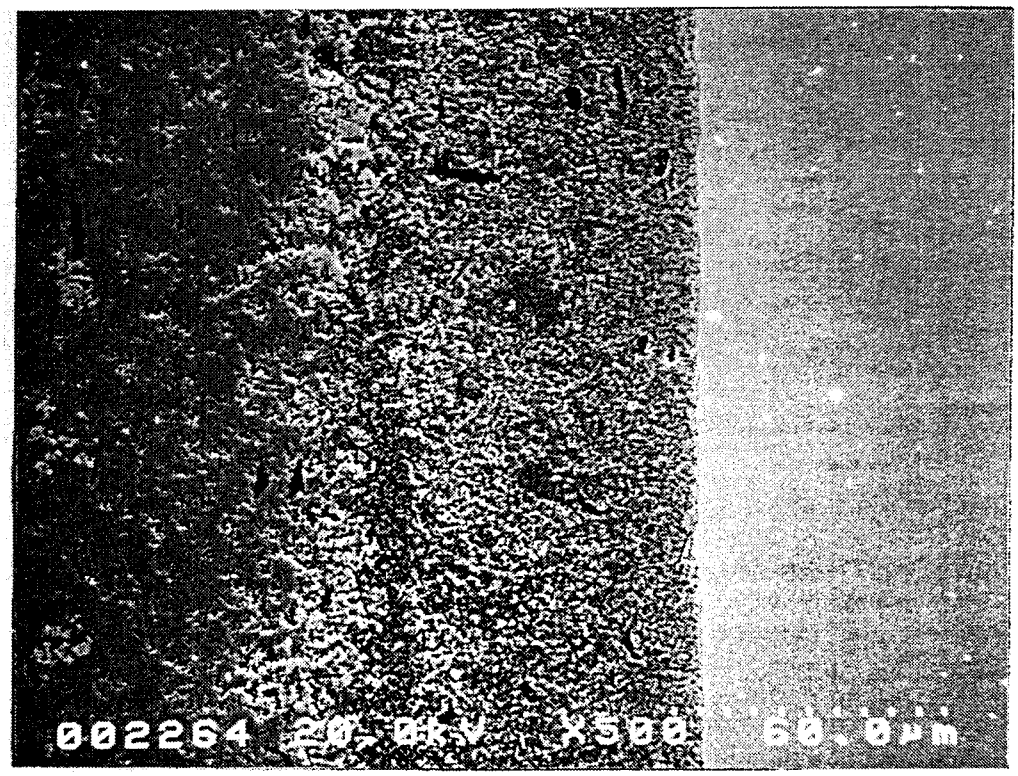

Fig. 5.4.2-7: Magnified view of marked area in Fig. 5.4.2-6 (full width = 220 µm). 1000 atm x 900°C x 5h.

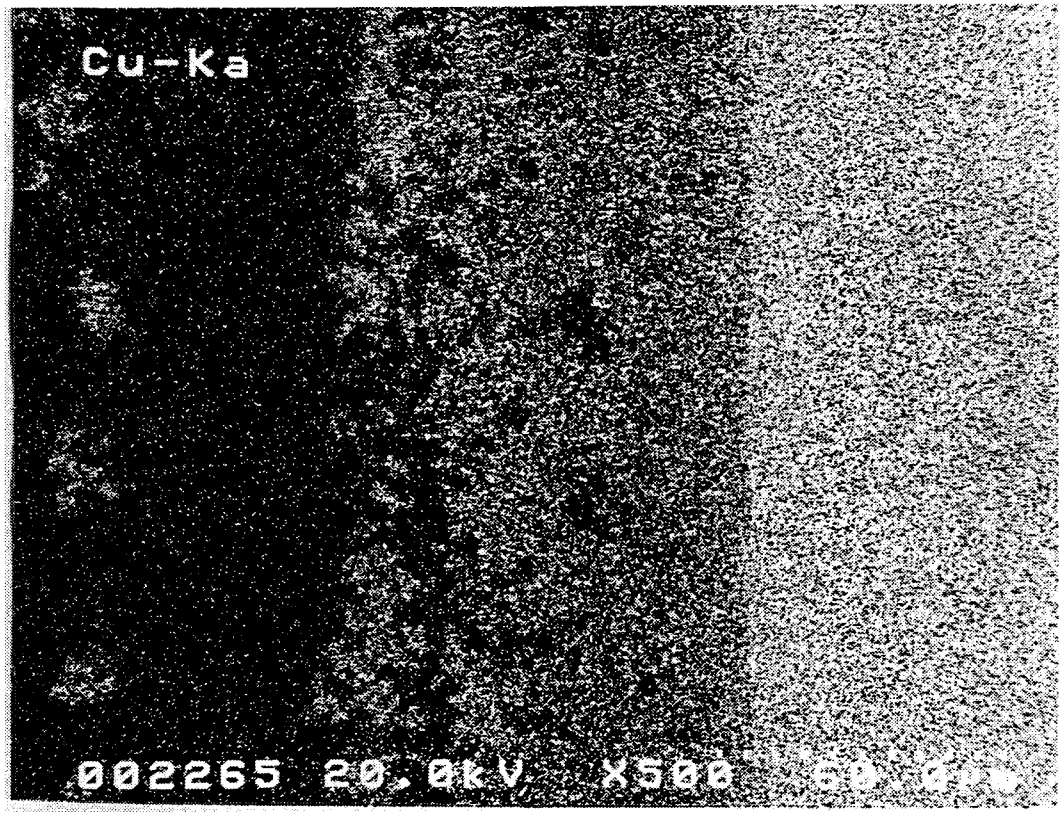

Fig. 5.4.2-8: Distribution of copper (bright area) in Fig. 5.4.2-7.

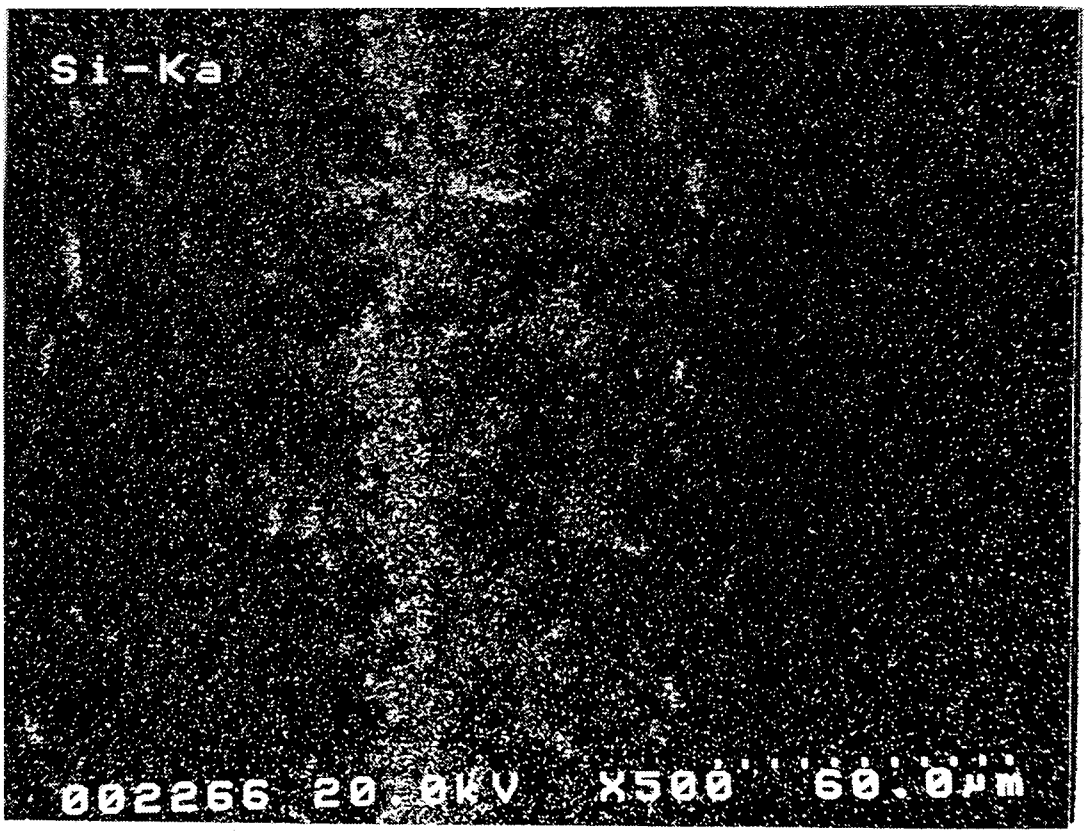

Fig. 5.4.2-9: Distribution of silicon (bright area) in Fig. 5.4.2-7.

Figures 5.4.2-10 through 5.4.2-13 show similar SEM-EDX analyses of the HIPped sample at 1500 atm and at 900 °C for 5 hours.

It was found that bonding ferrite and copper is done by diffusing the copper (~90 μm) as well as mixing or interlocking the ferrite and copper. Moreover, silicon was found to migrate near the boundary and the region of silicon becomes wider at 1500 atm compared to 1000 atm as seen in Figs. 5.4.2-9 and 5.4.2-13.

Figure 5.4.2-14 shows a magnified view of the area "①" in Fig. 5.4.2-11. The lower section of Fig. 5.4.2-14, Figs. 5.4.2-15 and 5.4.2-16 show the EDX analyses of three components found in the upper section of Fig. 5.4.2-14. As one can see in the figure, this region consists of ferrite ("A"), copper ("B") and silicon ("C").

Figures 5.4.2-17 and 5.4.2-18 show A magnified view of the area "②" in Fig. 5.4.2-11 and EDX analysis of the marked point "+". The marked component was copper as shown in Fig. 5.4.2-18. The softened copper mixed with the ferrite powder

5.5 Summary

Bonding ferrite with copper using brazing, soldering and HIP were evaluated experimentally. Due to the low bending strength of ferrite, neither brazing nor soldering of commercial tiles (6 x 6 x 0.4 cm^3) were possible without cracking. The only option seems to be to use small (2 cm >) tiles with a pressure of 7.5 – 25 kg/cm^2, where brazing/soldering many pieces of tiles would be complicated and there would be more instances of defects and particles produced.

As for bonding using HIP, we could succeed to bond commercial tiles, but we were more interested in using powder because one entire layer could be made with powder. It was confirmed that pre-sintered ferrite powder could be consolidated at a fairly low temperature where copper will not get too soft or melt. The SEM-EDX analyses of the bonding interface showed a mixing band (~90 μm) of ferrite and copper at the boundary. Bonding was performed by interlocking and diffusing the two components that assured a firm bonding quality. Migrated silicon was also found, but the source or the effects of the migration were unknown.

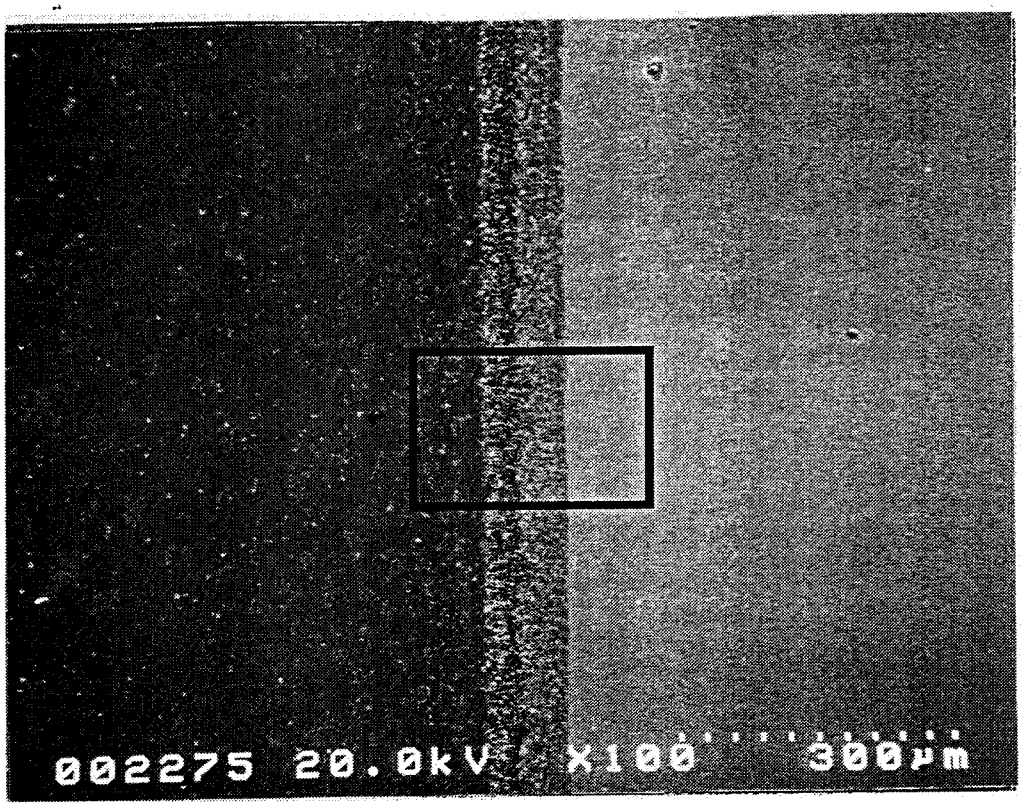

Fig. 5.4.2-10: SEM image of Ferrite/Copper boundary (full width = 1.1 mm). 1500 atm x 900 °C x 5h.

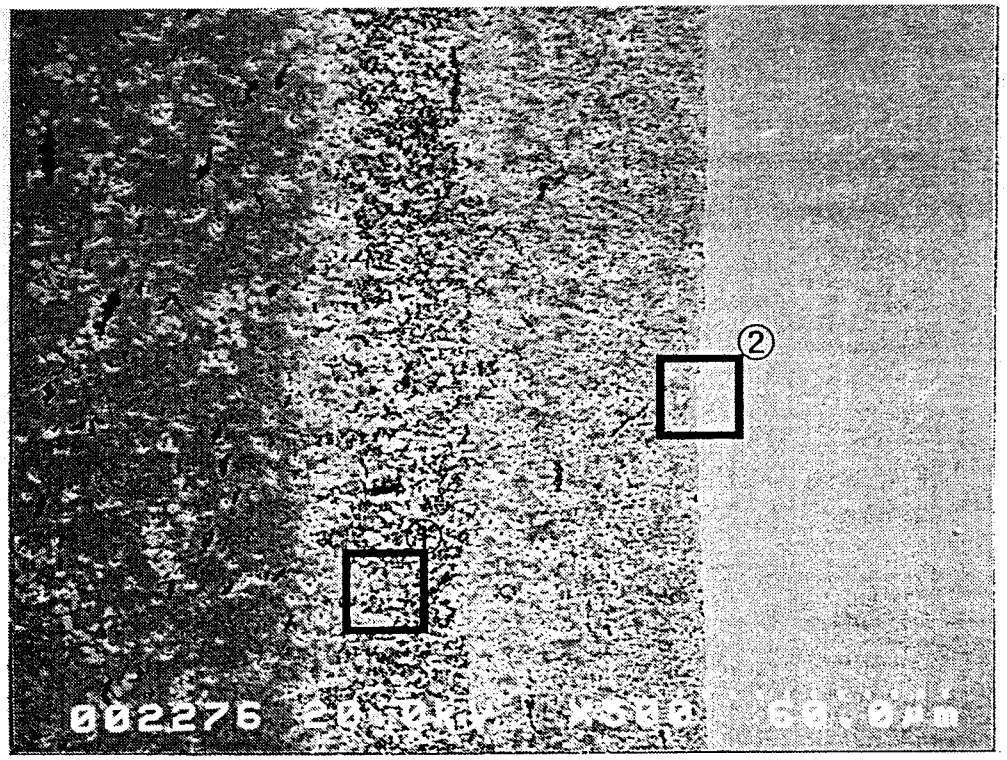

Fig. 5.4.2-11: SEM image of marked area in Fig. 5.4.2-10 (full width = 220 µm).

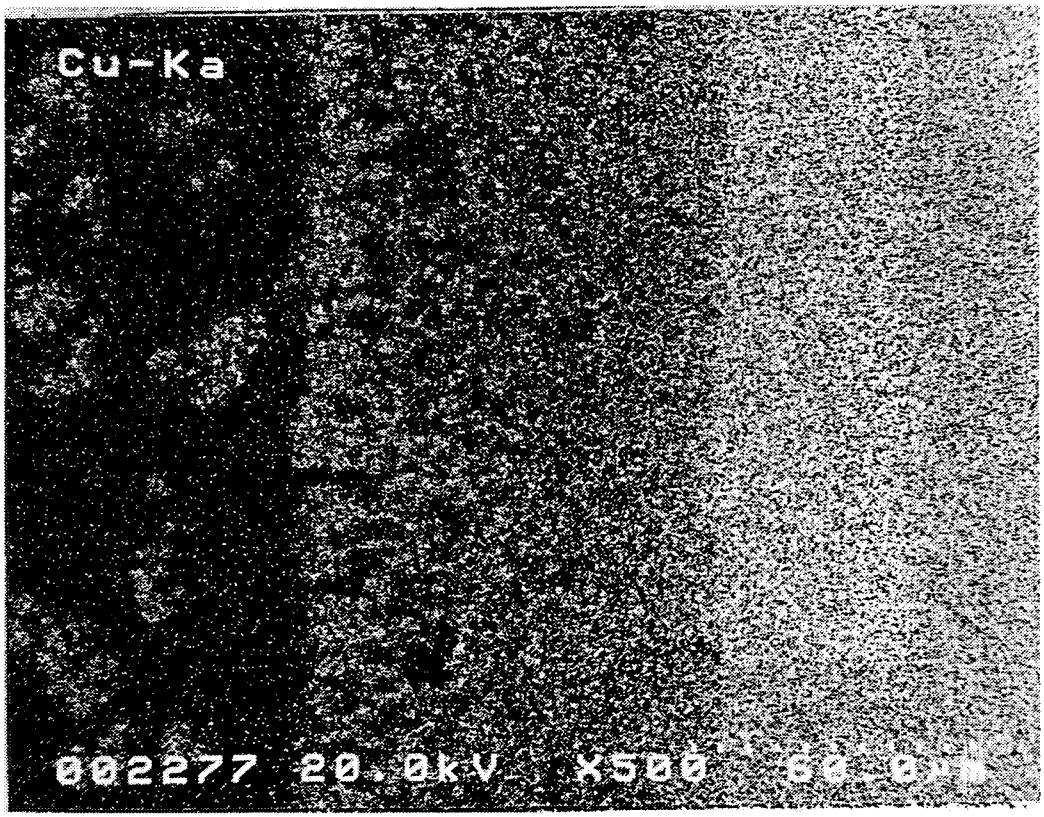

Fig. 5.4.2-12: Distribution of copper (bright area) in Fig. 5.4.2-11.

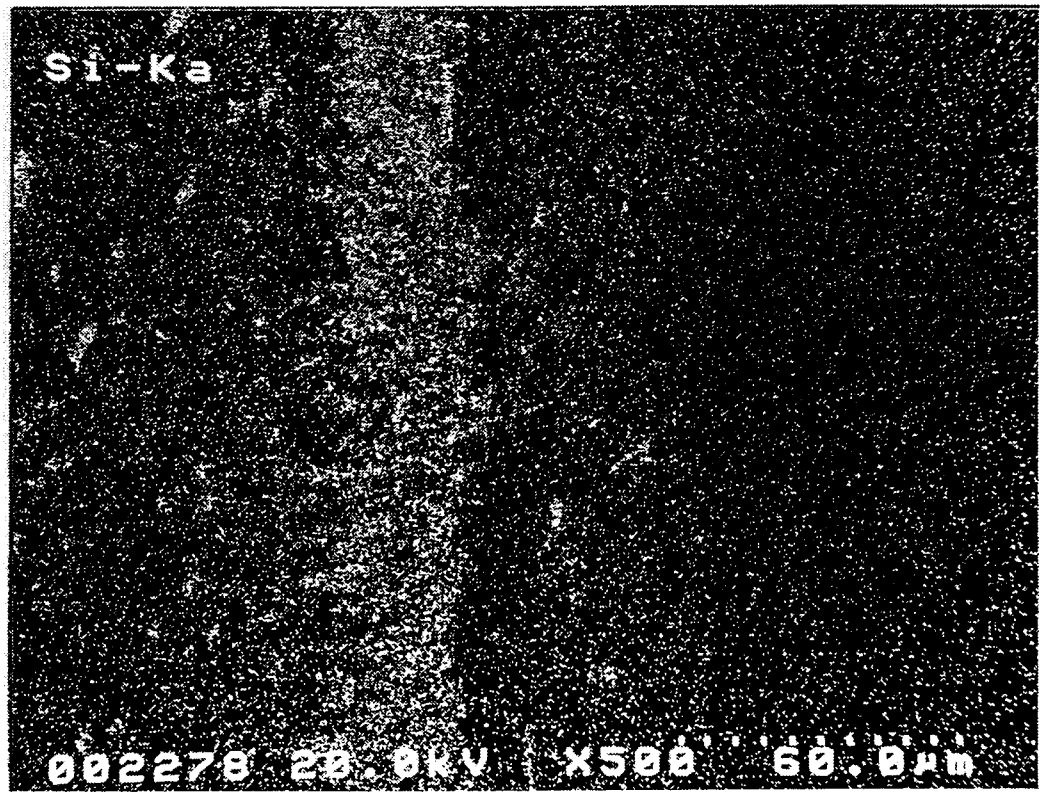

Fig. 5.4.2-13: Distribution of silicon (bright area) in Fig. 5.4.2-11.

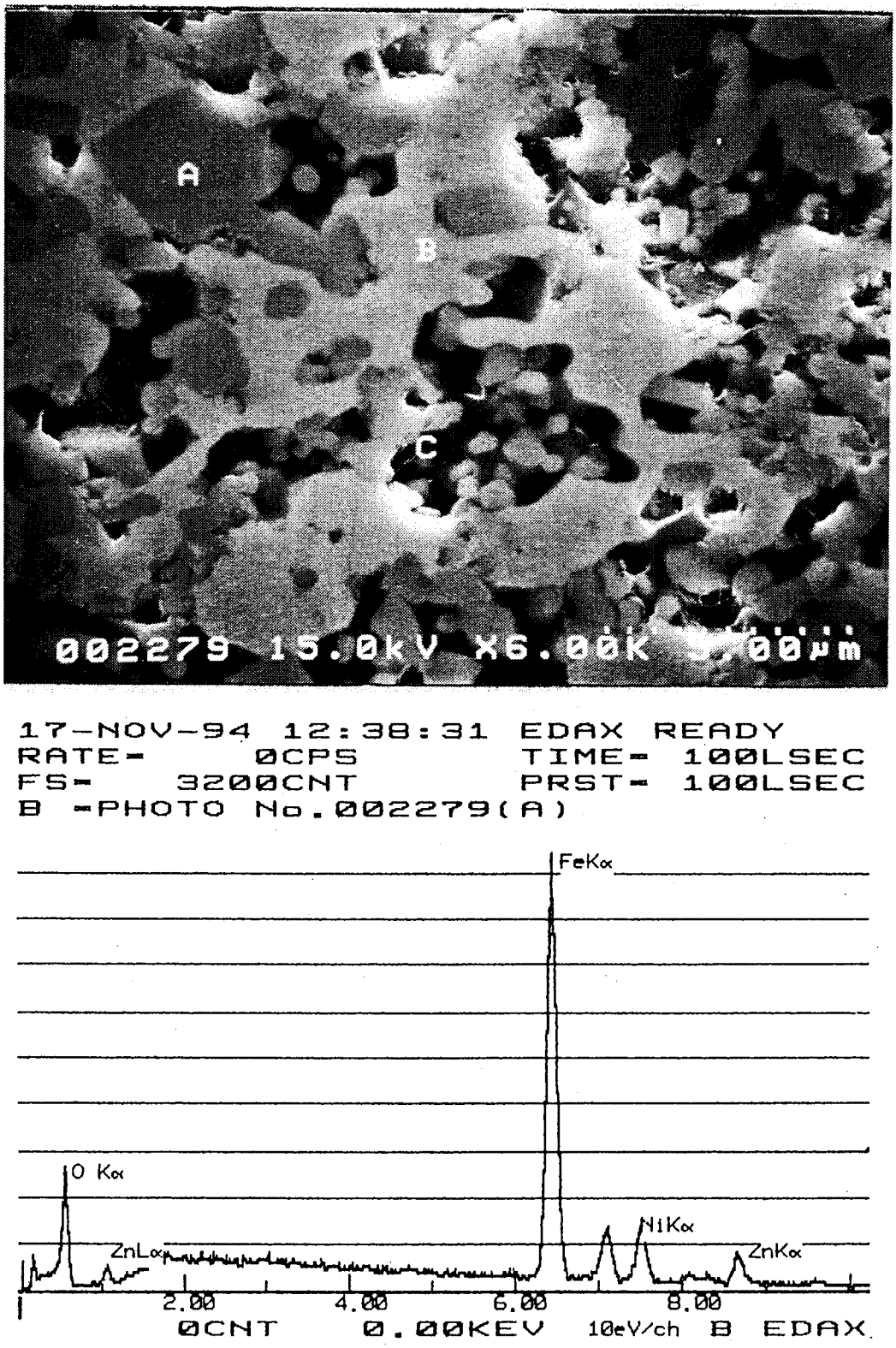

Fig. 5.4.2-14: Magnified view of marked area "①" in Fig. 5.4.2-11 (top) and EDX analysis of point "A" (bottom).

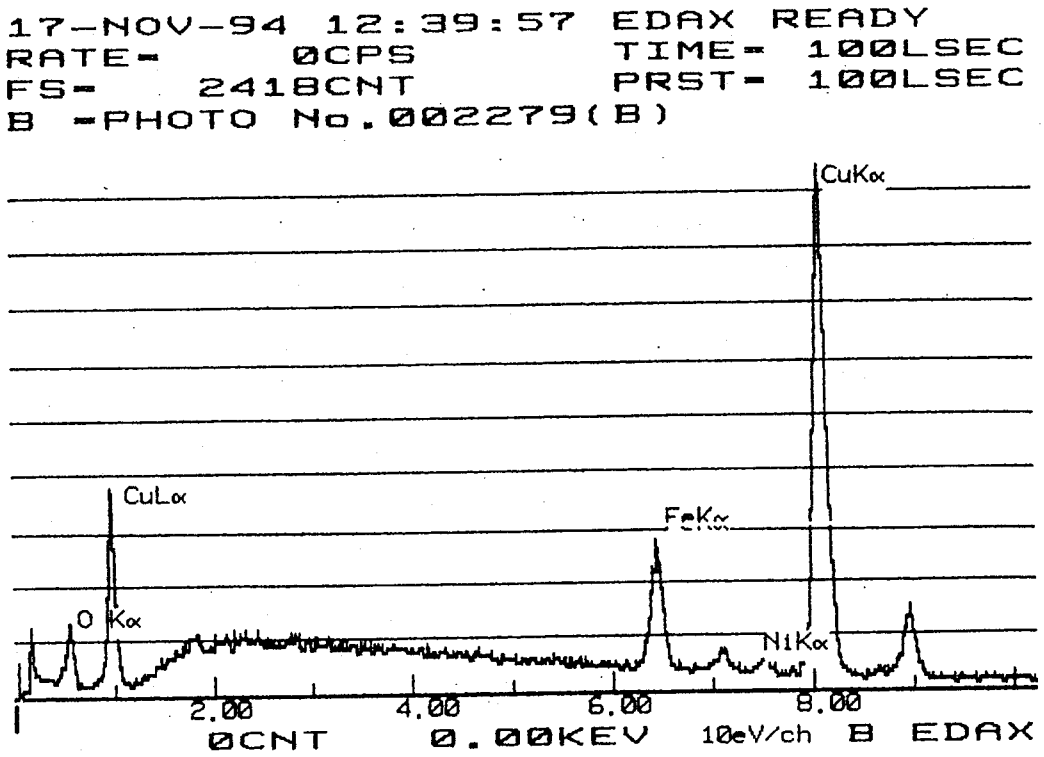

Fig. 5.4.2-15: EDX analysis of point "B".

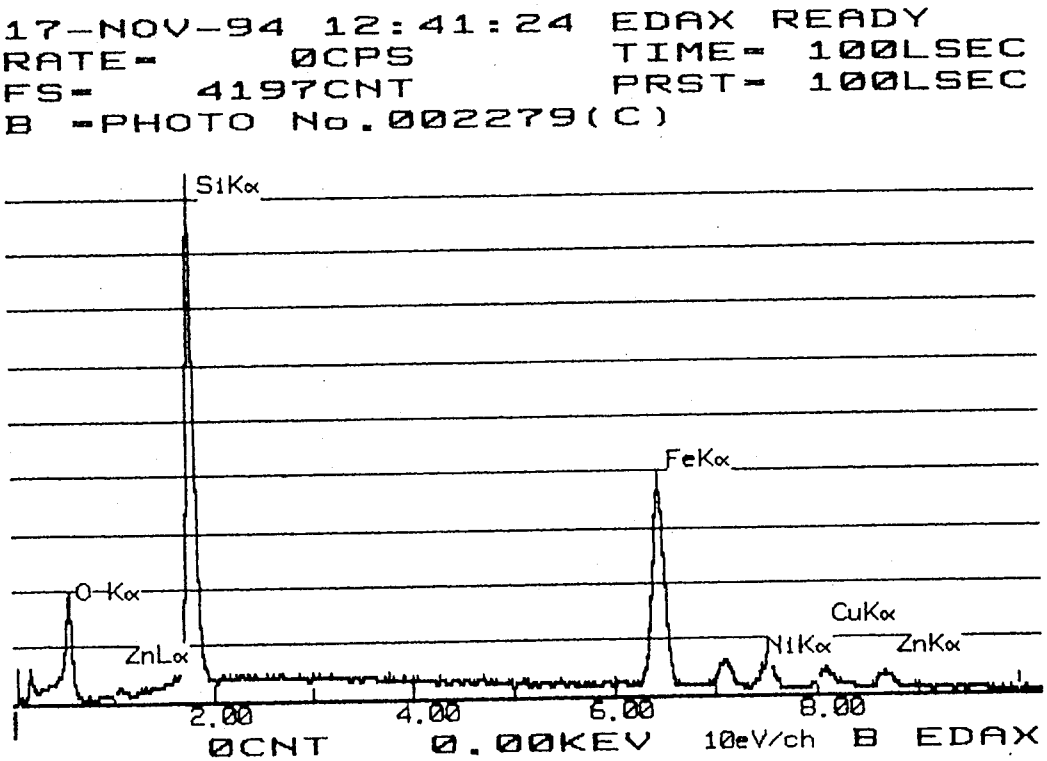

Fig. 5.4.2-16: EDX analysis of point "C".

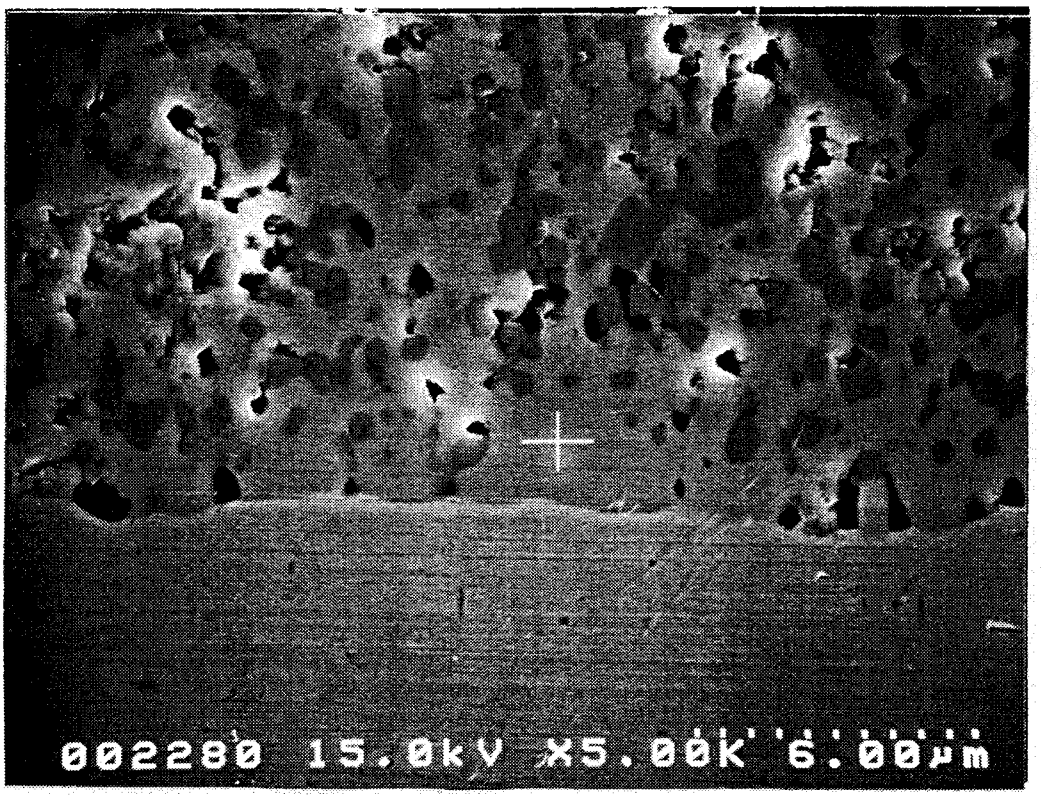

Fig. 5.4.2-17: Magnified view of marked area "②" in Fig. 5.4.2-11. Image is 90° rotated. Bulk copper is at the bottom.

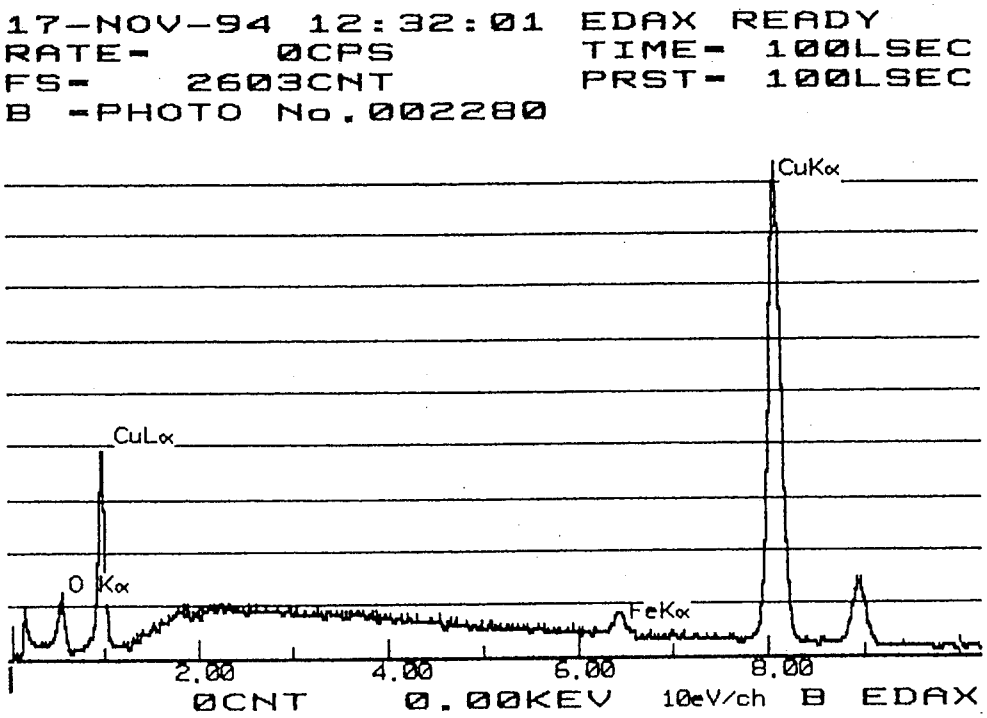

Fig. 5.4.2-18: EDX analysis of the marked point "+" in Fig. 5.4.2-17 found to be copper.

Chapter 6

Design and 1/3-size model tests

6.1 Introduction

After measuring ε and μ, we used a computer code that can calculate frequencies and Q values to design the sizes and locations of the absorbers. In this Chapter, we discuss the design using computer codes and the power requirements that can be obtained from calculations using the Q values. In addition, we discuss the high power tests with a model that has a diameter of 109 mm, which is about one-third of a full-size absorber. These tests were performed to check the power handling capability with a "magnified" power density.

6.2 Optimization of size and location

To determine the size and location of HOM absorbers, we used a program named SEAFISH, which is a complex version of SUPERFISH, in which lossy materials such as ferrite can be included. The outputs are resonant frequency, Q and field pattern. The dependencies of location, ferrite length and thickness on Q were studied for the TM011 mode since this mode was expected to be the most dangerous and to generate major power.

Figures 6.2-1 shows the Q as a function of the distance from the end of the taper as shown in the figure in the case of a 6 cm long ferrite layer, whereas Fig. 6.2-2 shows the same graph for a 15 cm long ferrite layer. In both figures, thickness is another parameter, e.g. 3^t means a 3-mm-thick ferrite layer.

Figure 6.2-3 shows the Q as a function of length for the ferrite located 17 cm away from the taper. As one can see, for a 2-mm-thick case, the Q is much more sensitive to the ferrite thickness than the cases of 4 mm and 6 mm. The ferrite length should be longer than 15 cm for a ferrite thicknss equal to or thicker than 2 mm.

Figure 6.2-4 shows the Q as a function of μ" in the case where the ferrite thickness is 4mm, length is 15cm, and distance from the taper is 19 cm. As one can see, the Q does not change much when the μ" is greater than about 5. Other parameters, such as ε', ε" and μ', are found to have little influence on the Q.

Figure 6.2-5 shows the Q's as functions of the ferrites` location and length. As seen, the minimum Q was found to be at the point where the ferrite's length is 15cm and distance from the taper is 19 cm.

Figures 6.2-6 and 6.2-7 show the designed sizes and locations of the absorber, and the field patterns when the absorbers are set at the optimized position.

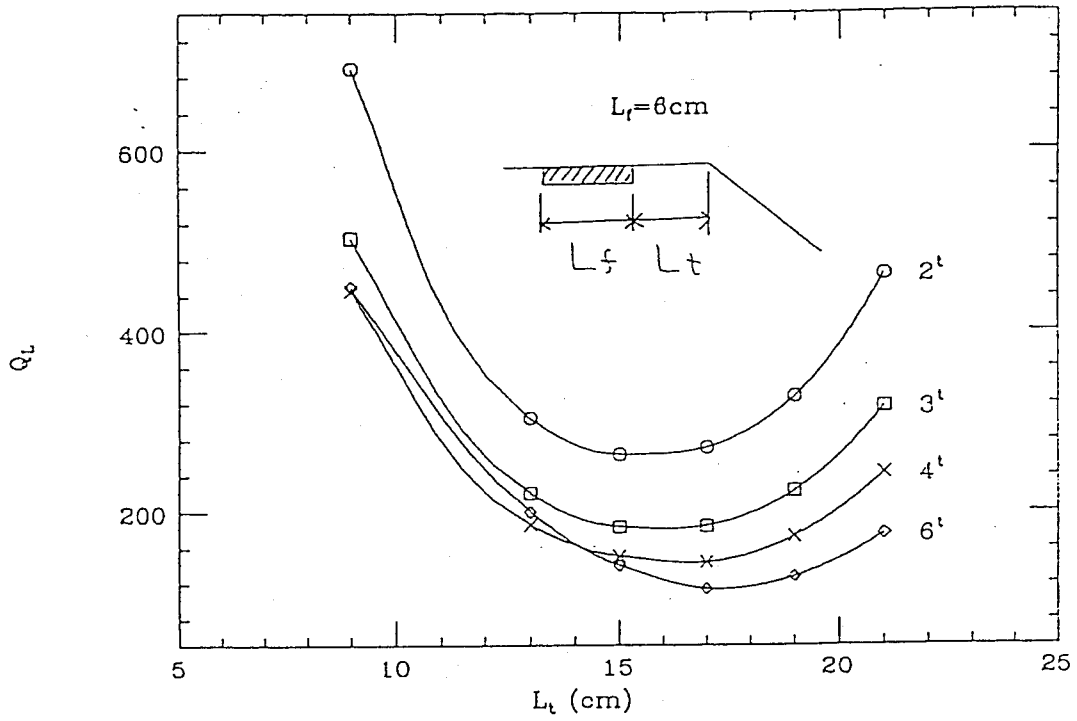

Fig. 6.2-1: Q as a function of the distance from the taper, L_t, in the case of a 6cm long ferrite layer. The ferrite thickness was taken as another parameter.

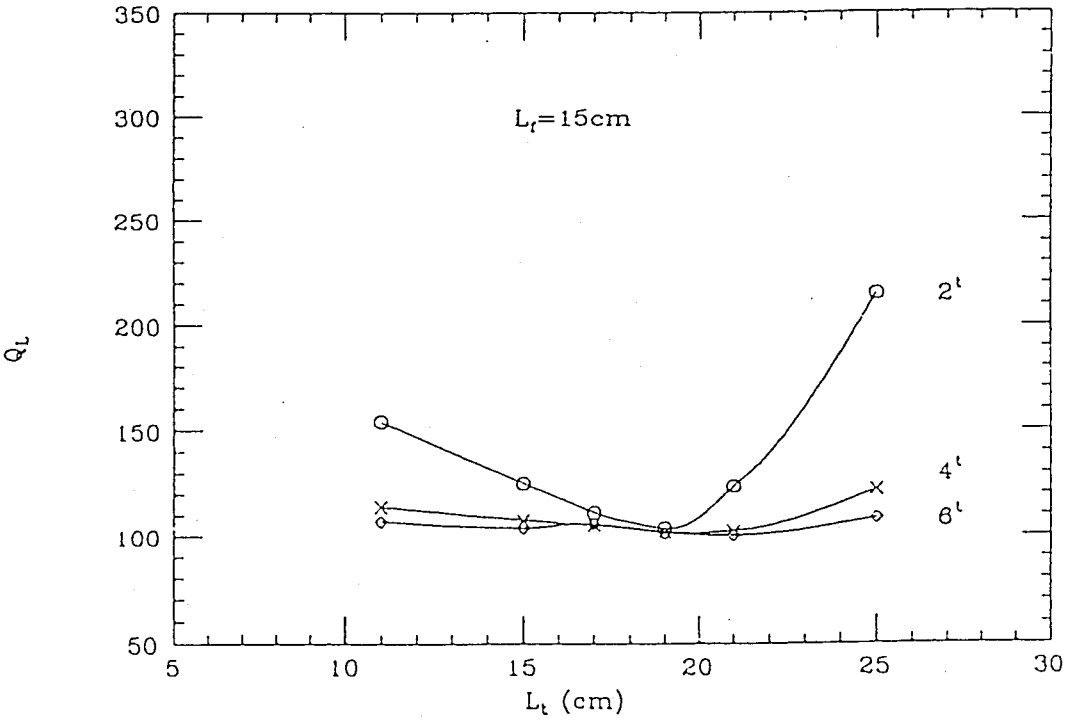

Fig. 6.2-2: Q as a function of the distance from the taper, L_t, in the case of a 15cm long ferrite layer. The ferrite thickness was taken as another parameter.

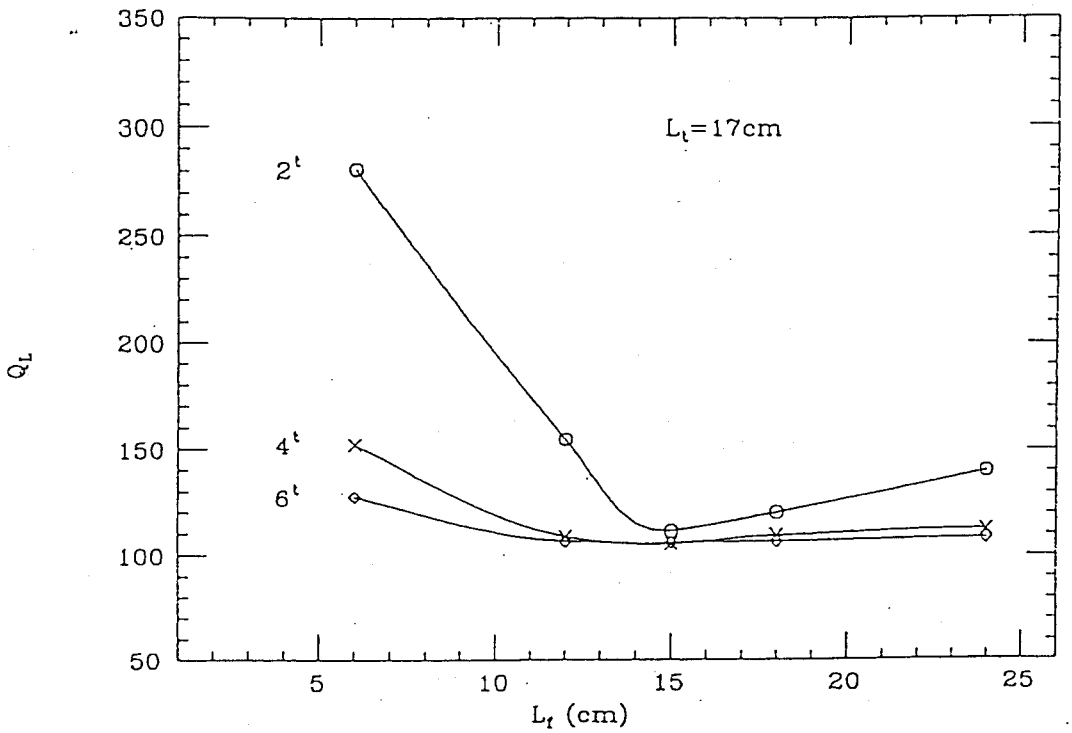

Fig. 6.2-3: Q as a function of ferrite length, L_f, when the distance from the taper is 17cm. Thickness was taken as another parameter.

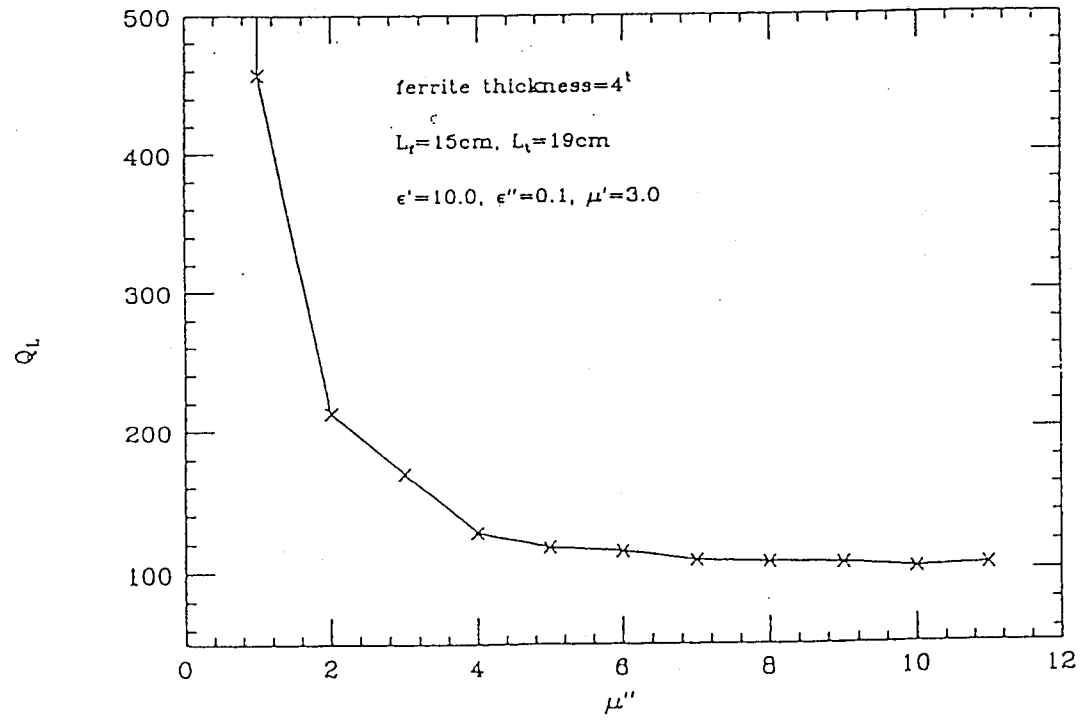

Fig. 6.2-4: Q as a function of the imaginary part of the relative permeability, μ'', in the case where the ferrite thickness is 4mm, length is 15 cm and position is 19 cm away from the taper.

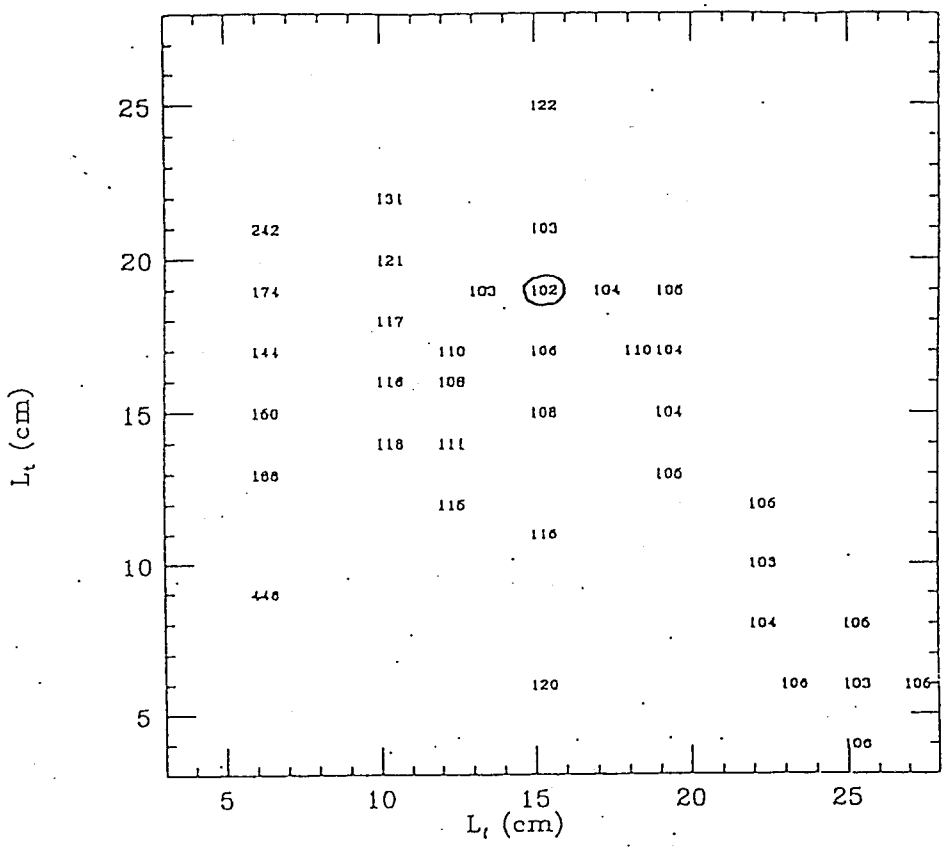

Fig. 6.2-5: Q as functions of ferrite length, L_f, and distance from the taper, L_t.

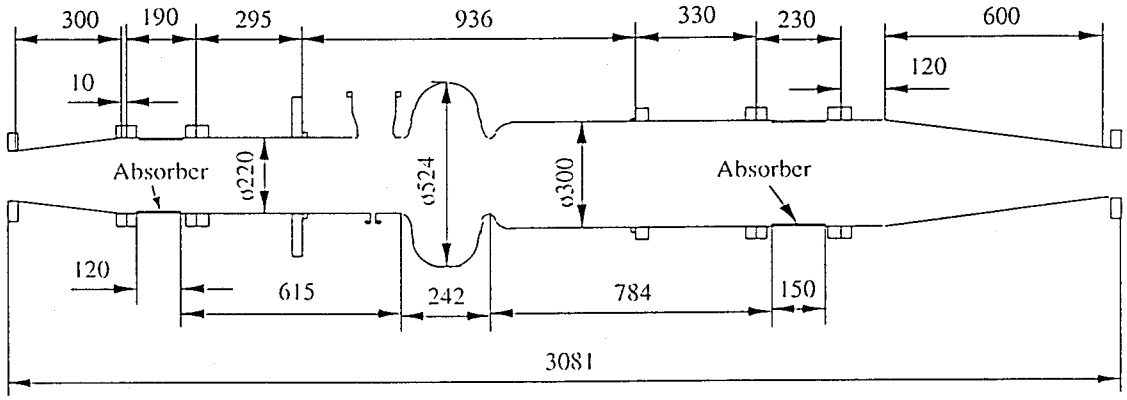

Fig. 6.2-6: Designed sizes and locations of HOM absorbers.

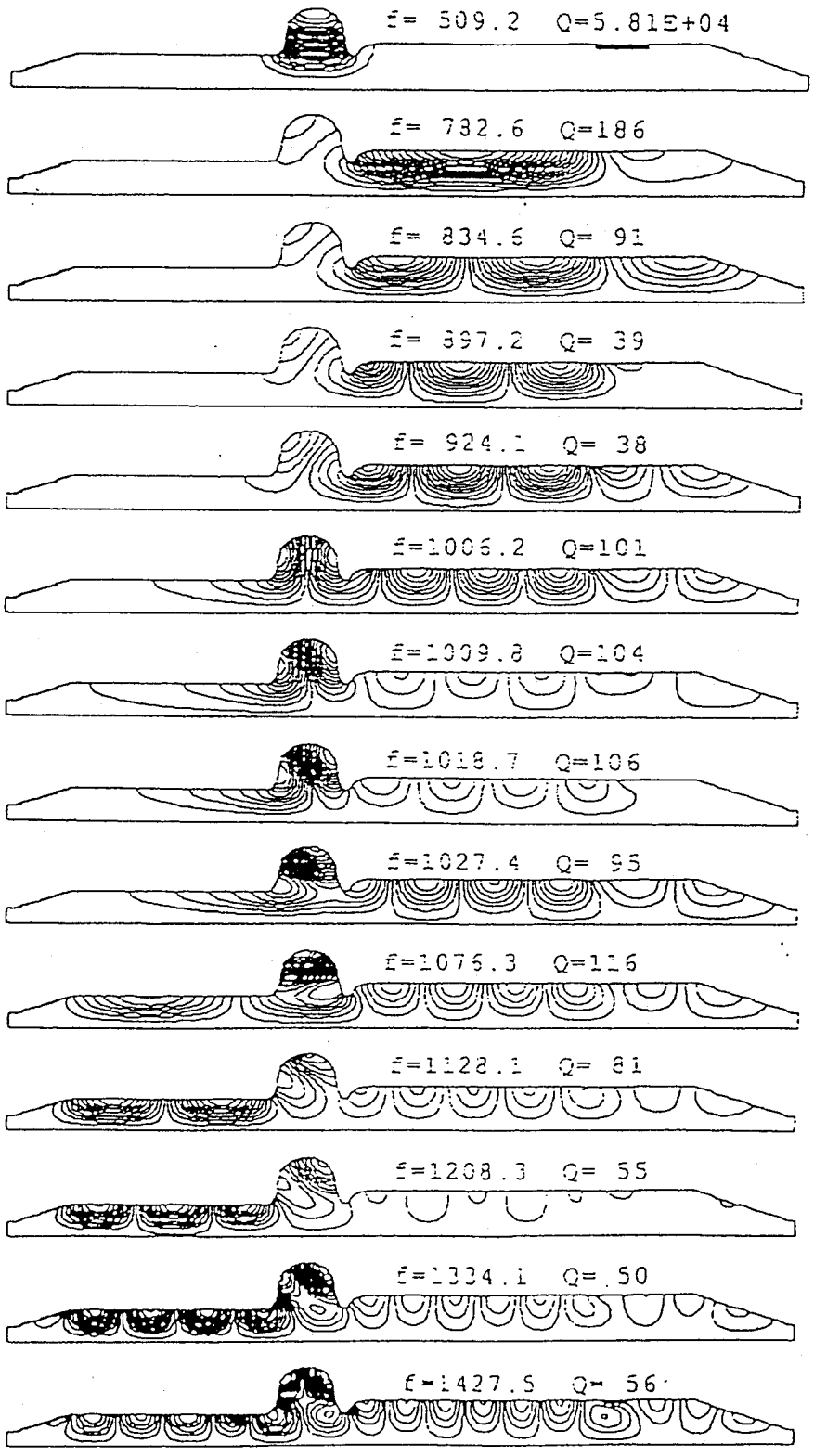

Fig. 6.2-7: Field patterns calculated with SEAFISH, L_t = 15 cm and L_t = 19 cm.

6.3 Power requirements

When decay time (τ_d) is longer than the bunch interval (τ_b) , i.e. $\tau_d > \tau_b$, fields can build up by superpositioning in the subsequent bunch passages.

The final voltage in the limit t -> ∞ is obtained by summing up the fields induced by all the previous bunch passages as [92],

$$V_b = \frac{\Delta V_b}{2} \cdot F(\tau) = \frac{\omega}{4}\frac{R}{Q} \cdot q \cdot F(\tau) \ , \tag{6.3-1}$$

where

$$F(\tau) = \frac{1 - 2e^{-2\tau}}{(1 - 2e^{-\tau}\cos\delta + e^{-2\tau})} \ , \tag{6.3-2}$$

$$\tau = \frac{\tau_b}{\tau_d} = \frac{\tau_b \omega}{2Q_L} \ , \tag{6.3-3}$$

$$\delta = (\omega - \omega_h)\tau_b \ , \tag{6.3-4}$$

$$\omega_h = h \cdot \omega_r \ ,$$

ΔV_b : an induced voltage when charge q passes the structure,

h : harmonic number, and

ω_r : angular revolution frequency.

When $\delta = 0$ or $\omega = \omega_h$, $F(\tau)$ becomes maximum, i.e. fields build up.

$$\text{If } \tau_d >> \tau_b \ , \quad F(\tau) = \frac{1 + e^{-\tau}}{1 - e^{-\tau}} \approx \frac{2}{\tau} = \frac{4Q_L}{\omega \tau_b} . \tag{6.3-5}$$

Combining Eqs. (6.3-1) and (6.3-5), one gets

$$V_b = \frac{q}{\tau_b} \cdot \frac{R}{Q} \cdot Q_L \quad . \tag{6.3-6}$$

Similarly, one can obtain the power deposited by bunch trains as

$$P_b = I_b^{\,2} \cdot \frac{R}{Q} \cdot Q_L \quad . \tag{6.3-7}$$

Using Eq. (6.3-7) and the Q and R/Q obtained by CLANS calculations, in the worst case, the highest power is ~ 900 W (TM011 mode) at 1.1 A. If all the modes up to 1.5 GHz build up, a total of ~ 4 kW is deposited in the worst case. As will be discussed in Section 9.3.3, the loss factor with a broadband impedance would be 1.84 V/pC, resulting in a deposit power of ~5 kW at 1.1 A. Therefore, in the worst case HOM power would be ~9 kW , which is translated into an average power density of 4.6 W/cm^2 (SBP) and 3.8 W/cm^2 (LBP).

6.4 1/3-size cylindrical model tests

The next step was to make a small scale (~1/3 of LBP) model using HIP and check the power handling capability using a 5 kW 2.45 GHz magnetron power source [8]. In this case, we used the TM01 mode by attaching a TM-TE converter to both sides of the absorber. Figures 6.4-1 and 6.4-2 show the configuration and a view of the experimental set-up.

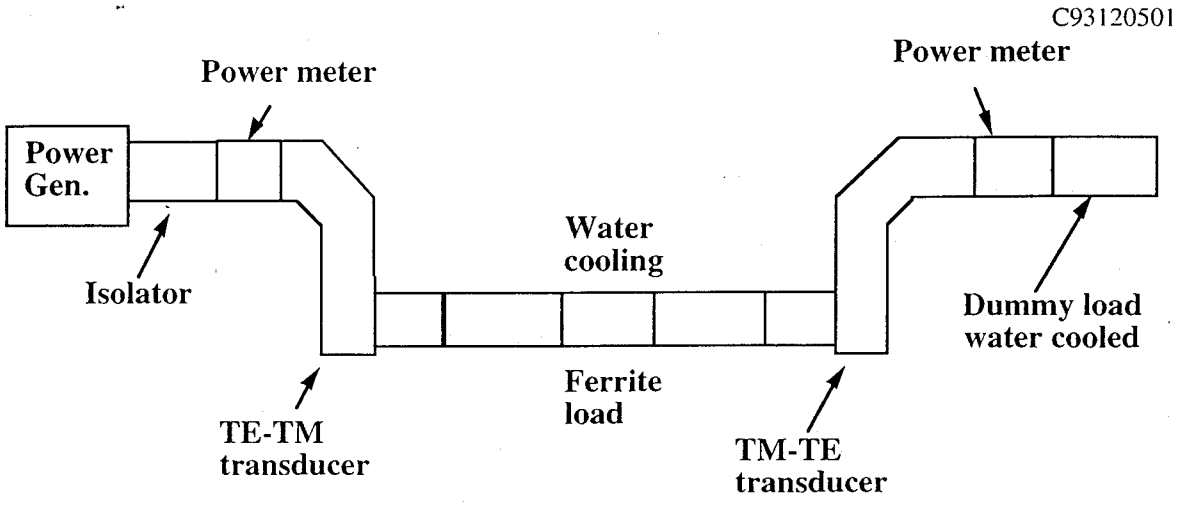

Fig. 6.4-1: Configuration of the high power test set-up for cylindrical absorber (109 mm o.d. x 114 mmL x 3 mmt).

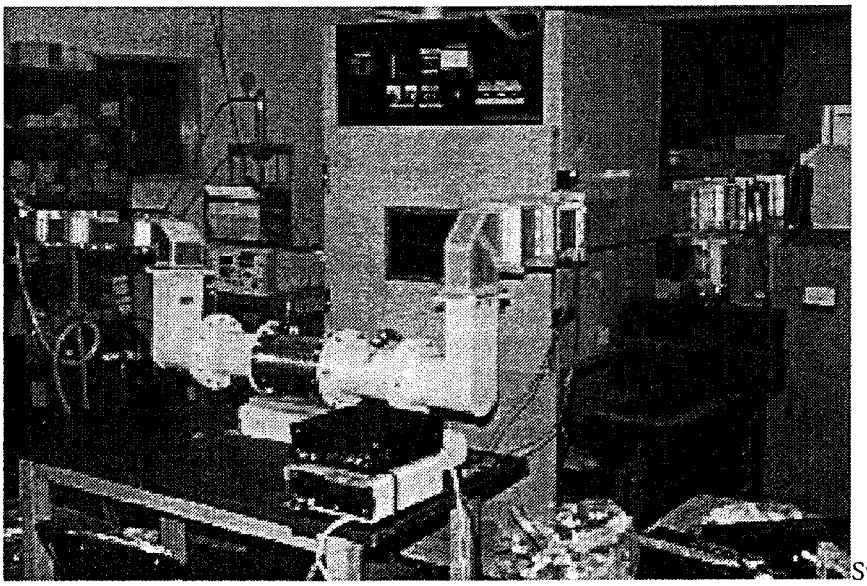

S99040807

Fig. 6.4-2: The test set-up. Power goes from right to left.

Figure 6.4-3 shows the absorption rate as a function of input power. It decreases with input power which is probably due to the increase of the temperature as discussed in Section 4.6.

Figure 6.4-4 shows the longitudinal profile of the surface temperature measured with thermo labels, which change their color at specified temperatures with a resolution of 5-10 °C. It was found that the temperature at the front edge increases up to 140 - 150 °C when the absorbed power is 2.55 kW.

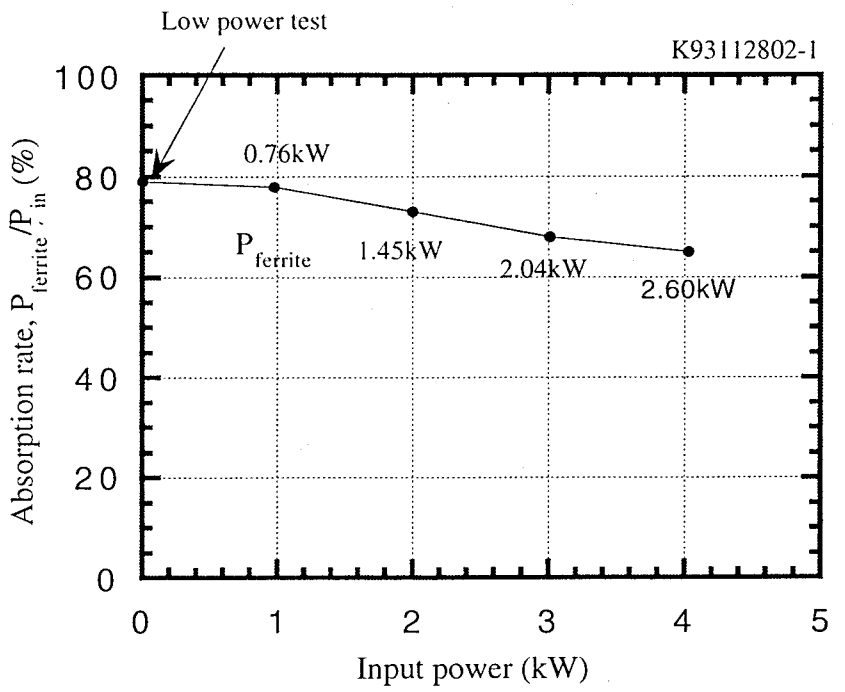

Fig. 6.4-3: Absorption rate as a function of input power.

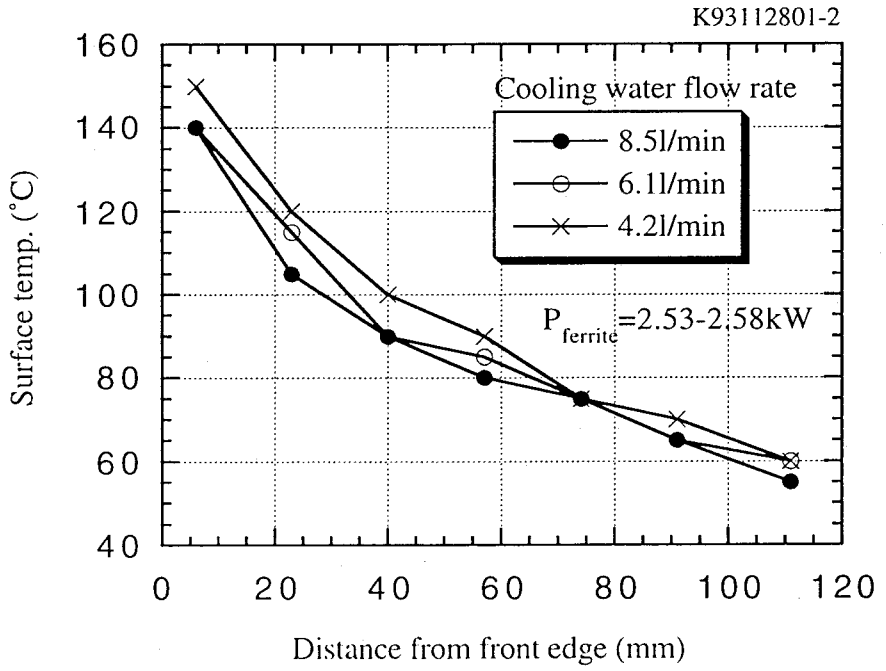

Fig. 6.4-4: Longitudinal surface temperature profile.

To avoid excess increase in heat at the front edge, tapers were tested. Figure 6.4-5 shows the result. At an absorbed power of 3.3-3.4 kW, the temperature at the point 5 mm from the front edge decreased from 200 °C to 80 °C with the taper. The taper length was 50 mm in this test but since the full-size absorbers did not have enough total length, we decided to make them into 25 mm tapers on both sides. Thereby the outgassing rate could be decreased. In this experiment, the cooling water flow rate was 3 L/min.

The maximum absorbed power was 3.95 kW and the average power density was 8.3 W/cm^2. Assuming the exponential decay of power, the estimated maximum power density at the front edge without a taper was 29 W/cm^2. Even with this power density, there were no cracks or any damage.

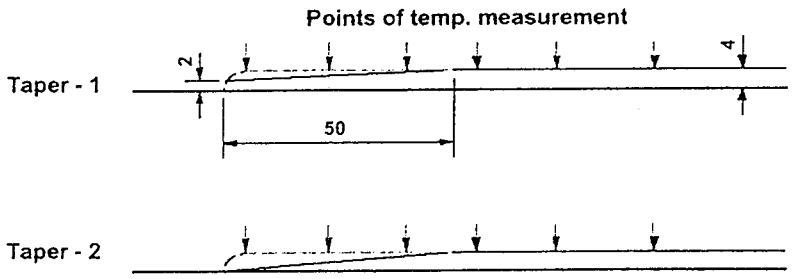

Fig. 6.4-5 (a): Tapers used in the tests.

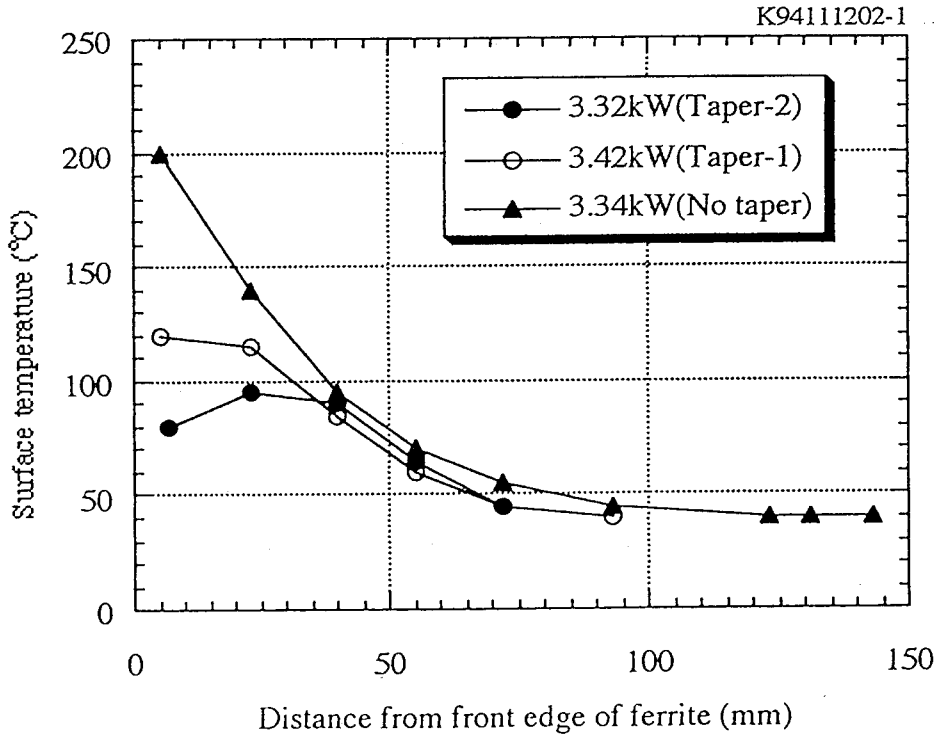

Fig. 6.4-5 (b): The effect on tapers at a length of 50 mm. The ferrite thickness at the front edge was 2 mm (Taper-1) and 0 mm (Taper-2).

6.5 Summary

We discussed the design of the absorbers using the computer codes SEAFISH, CLANS and CLANS2. The optimizated size and location of the absorber was analyzed, focusing on the Q value of the TM_{011} mode. It was found that the thinner the ferrite the more sensitive to the location it was, although there was a position which gives the same Q values. Finally, considering the low thermal conductivity of ferrite, we decided to make the thickness 4 mm and the length 15 cm.

The power deposited in the worst case of resonant build-up was calculated using the R/Q and Q values obtained with CLANS. At 1.1 A, the maximum power deposited on the TM_{011} mode is ~900 W. Also, if all the modes ($f < 1.5$ GHz) build up, they will amount to ~4 kW. As will be discussed in Section 9.3.3, the loss factor with broadband impedance is 1.84 V/pC , resulting in a deposit power of ~5 kW at 1.1 A. Therefore, in the worst case the HOM power is ~9 kW , which can be translated into an average power density of 4.6 W/cm^2 (SBP) and 3.8 W/cm^2 (LBP).

A "magnified" power test on a 1/3-size cylindrical absorber was made using the same technique as full-size absorbers. Up to an average power density of 8.3 W/cm^2 (an estimated local power density of 29 W/cm^2) was absorbed without any problem. This confirmed the high integrity of bonding and that there was enough power handling capability.

Chapter 7

Developing the technique to make HIPped full-size absorbers

7.1 Introduction

The superconducting cavity module for KEKB has two absorbers, one, SBP (Small Beam Pipe) on the up-stream of the circulating electron beams, and the other, LBP (Large Beam Pipe) on the down-stream. The outer diameters of the ferrite layers are 220 mm and 300 mm and the lengths are 120 mm and 150 mm, respectively. The thickness of both absorbers is 4 mm. To lower both reflections of the microwave and the surface temperature, there are 25-mm tapers at the front and rear ends, ranging from a thickness of 1 mm.

Having confirmed the consolidation of ferrite powder by hot pressing, as described in Section 7.4.5, we started designing the tools and fixtures to make the full-size absorbers. In the next section, we describe these and the detailed fabrication process. In Section 7.2, we discussed optimizing the conditions of HIPping, such as temperatures and pressure. Section 7.3 shows how we determined the HIP conditions. Section 7.4 is devoted to the problems we faced in the course of the development and their solutions.

7.2 Design of tooling and detailed process

7.2.1 Design of tools and fixtures

- Size of outer and inner capsules

To prevent the movement of copper, a thick (12 mm) soft steel pipe called STKM was chosen as an outer layer of the OFC (Oxygen Free Copper). Although we found that at the central area STKM deforms up to ~0.5 mm during HIPping, we did not change the thickness since it was within tolerable deformity.

As for the inner capsule, it should move towards the copper wall to press the powder, thus a thin (2.3 mm) and more expandable soft steel, named SPCE, was chosen.

- Tools to pack the powder

To avoid excessive deformation of the inner capsule, which might cause a leak, the packing density of the powder should be more than 50 % of the final solid density. Vibration packing is commonly used for a few of the100 μm powder, but it is not usable for fine particles due to the lack of gravity. Since the size of the powder we could get from a manufacturer was about 1 μm, we decided to use a mechanical press and later combined it with the vibration packing.

A schematic representation of the mechanical press is shown in Fig. 7.2.1-1. On the right of the schematic, the improved pusher end is depicted. With the end at the top, the pusher often stuck due to friction with the other walls. We found that the end at the bottom is the best.

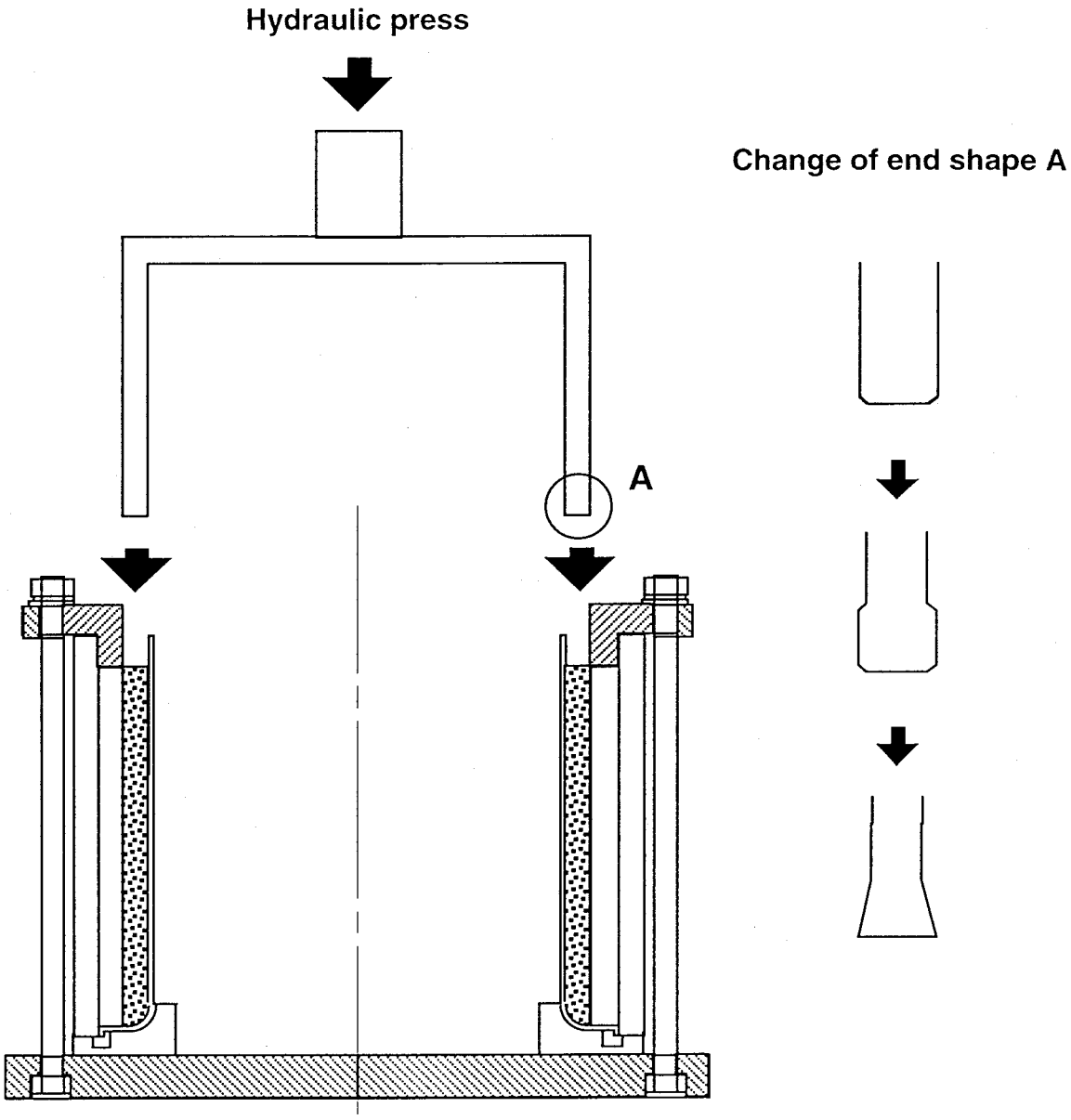

Fig. 7.2.1-1: Improvement to the tip of the pusher.

The changes of the shape of the capsule and the configurations for sealing are shown in Fig. 7.2.1-2. The bottom of the inner capsule was changed to a seamless end to avoid leaks during HIP, as will be discussed in Section 7.4.1. Also, we changed the sealing at the top so that the gas pressure could assure a better seal by pressing the walls together.

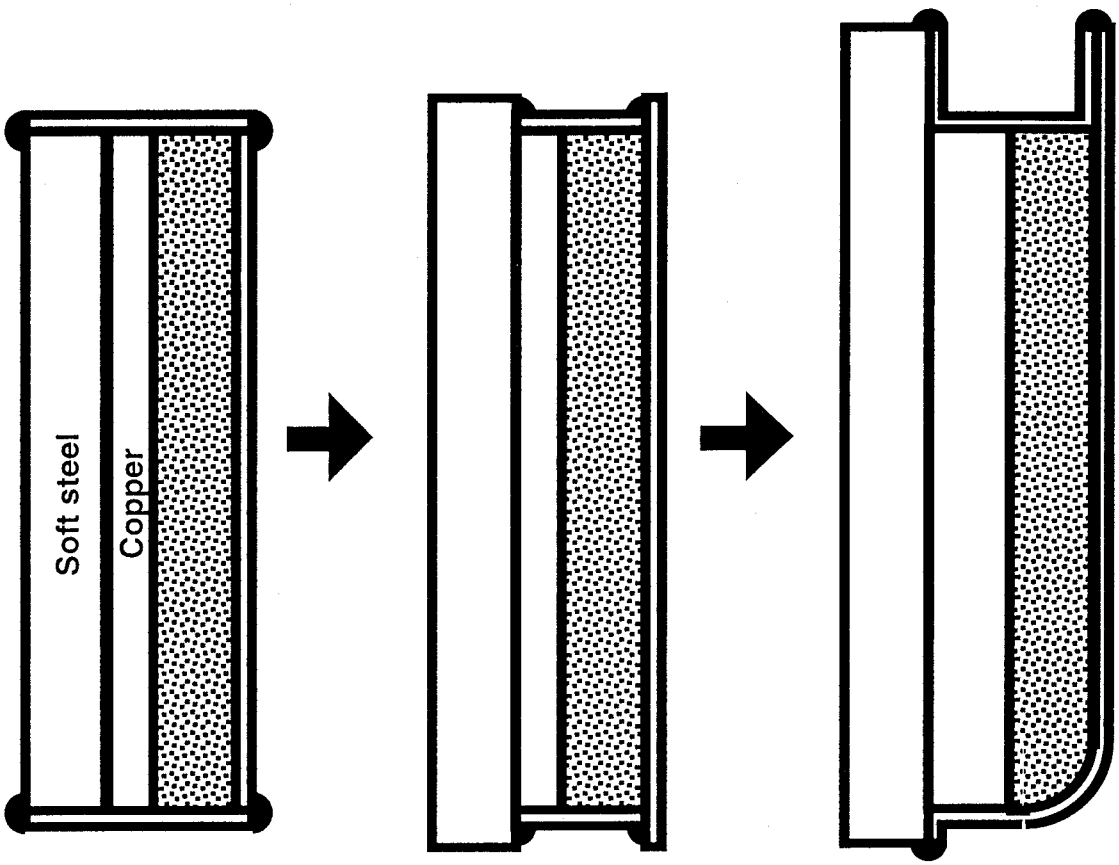

Fig. 7.2.1-2: Improvement to the canning structure.

- EBW (Electron Beam Welding) of flanges

Figure 7.2.1-3 illustrates the EBW configuration of the flanges. The flanges are made of SUS304. Thus, EBW of SUS304/OFC was performed. As one can see, the rotating axis is tilted by 10 degrees to allow EBW. The most important improvement here was the heat sink made of copper. At an early stage, the ferrite cracked due to excess temperature rises (200 °C <). Since copper has a good thermal conductivity, ferrite can be heated up easily. When we tried the heat sink depicted in Fig. 7.2.1-3, the temperature decreased to less than 60 °C, which enabled EBW without cracking. The bolt in the middle exerts radial force for thermal contact of the heat sink with the copper layer.

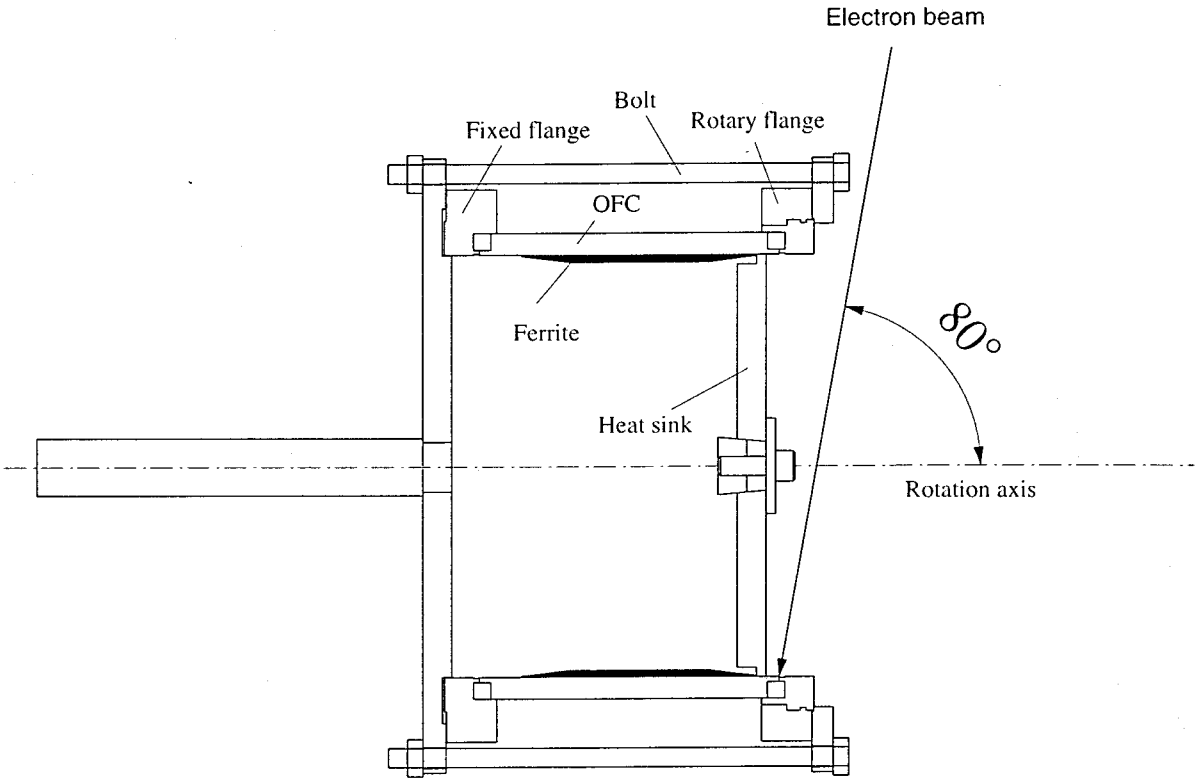

Fig. 7.2.1-3: The set-up for EBW (Electron Eeam Welding).

7.2.2 Detailed process

There are two processes that precede the process illustrated in Fig. 7.2.2.

They are:

- Degassing of pre-sintered ferrite powder.

Before packing a pre-sintered powder into the gap between the inner capsule made of soft steel and the copper pipe, the powder is baked in a nitrogen atmosphere in order to remove water from the surface of the powder. A test conducted to know the amount of water that the powder has on its surface revealed that the powder retained an enormous amount of water due to the size (~1 μm) of each particle of the powder, i.e. huge total surface area. Actually, from measurements on the outgassing rate, it was found that the powder degassed beforehand showed about an order of magnitude lower outgassing rate compared to the one without this pre-baking [8].

- Degassing of OFC (Oxygen Free Copper) at 900 °C for an hour.

Before inserting the 12-mm-thick OFC cylinder, which will be the outer layer that surrounds the ferrite, into a 12-mm-thick soft steel, this OFC is degasses so that the gas contained in the OFC will not degrade the HIPping.

The steps that follow these two steps are illustrated in Fig. 7.2.2. Also, some pictures are shown in Appendix B.

A more detailed explanation of the steps is:

1) Pack ferrite powder between inner capsule and outer copper pipe using hydraulic press (~ 200 kg/cm^2), which makes the average packing density reach about 60 % of the final solid density.
2) TIG-weld the lid and two evacuation ports, evacuate and degas ferrite at 400 °C till the pressure gets 1 - 2 x 10^{-3} Torr at 400 °C,
3) Chip off and carry out HIP with Ar gas at 1500 atm and 900 °C for 5 hrs, the detailed HIP pattern is shown in Fig. 7.3,
4) Remove inner capsule with a lathe,
5) Machine/shape ferrite with a diamond grinder,
6) Remove outer soft steel and EBW (Electron Beam Weld) end flanges,
7) Make a spiral round groove on the copper layer for a cooling pipe and
8) Press-insert a copper cooling pipe (3/8" in outer diameter and 0.8 mm in thickness).

Figure 1.3-4 is an example of absorbers made this way.

In addition, between steps 5) and 6) we put flanges on the ends and baked the ferrite at 150 °C for at least two weeks. This was to prevent cracks in the ferrite, which occurs at 60 °C < T without the outer layer, as shown in Section 7.4.5.

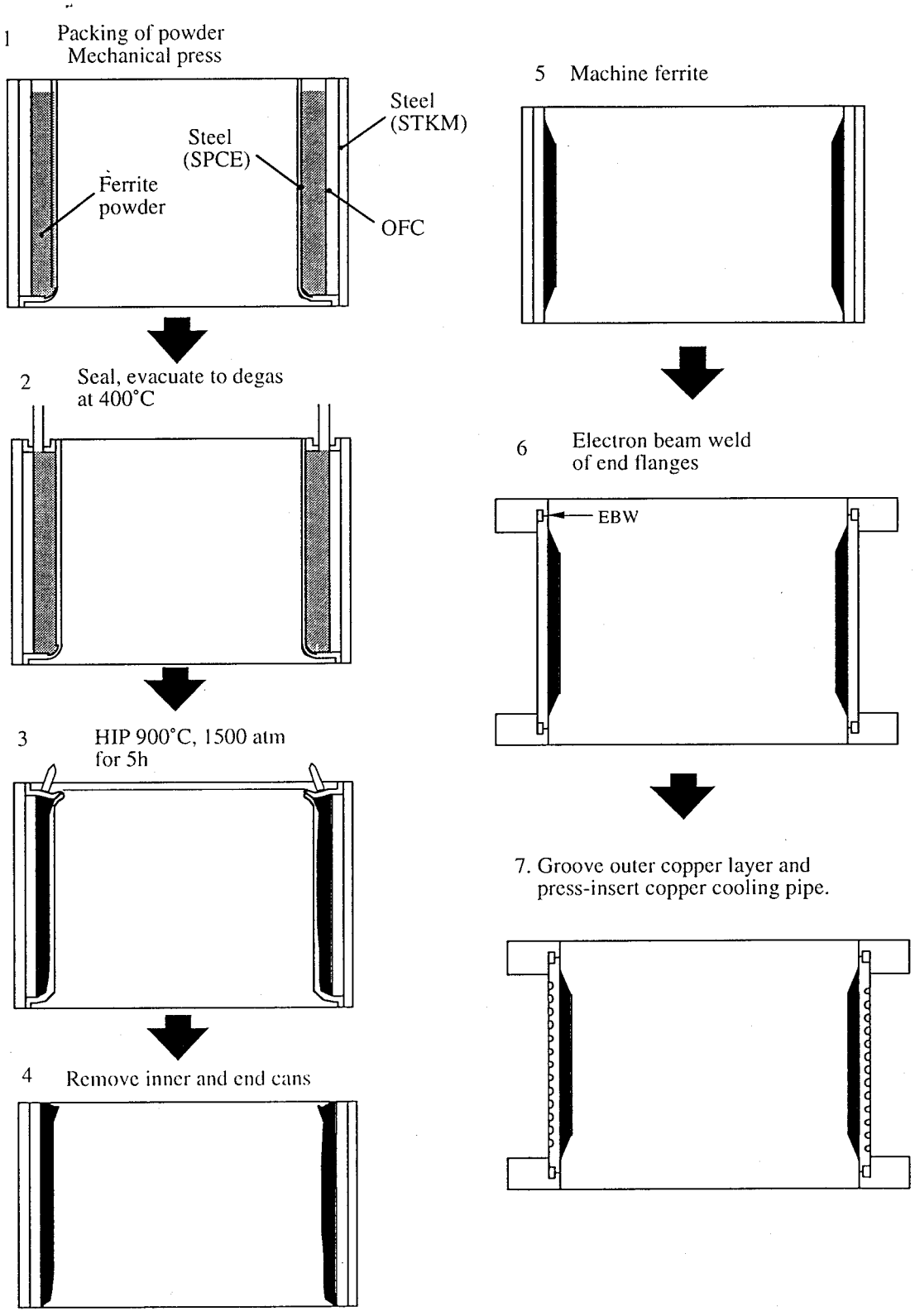

Fig. 7.2.2: Process of making a full-size ferrite absorber with HIP (Hot Isostatic Press).

7.3 Determining the HIP conditions

The conditions that had to be determined were:

(1) Pressure (initial pressure, ramp-up/ramp-down rate, maximum pressure)

(2) Temperature (ramp-up/ramp-down rate, holding temperatures, maximum temperature, holding time)

Since there had been no experience for us or company workers to HIP ferrite powder before determining most of the conditions were made on a trial-and-error basis.

The history of the HIP tests is shown with the HIP patterns chronologically in Appendix A. The points that determined some of the conditions are as follows:

(2) To avoid voids and delaminations, it was necessary to raise the pressure from 1000 to 1500 atm.
(3) The temperature and holding time was decided to complete the sintering and consolidate the ferrite with the lowest temperature for the copper not to get too soft and melt.
(4) The temperature and holding time during the cool-down was determined so as to release the stress that accumulates in the ferrite because of the difference between the thermal contraction rate of ferrite, copper and soft steel.

The problems that we faced in the course of the development are summarized in the next section (Section 7.4), which determined most of the HIP conditions.

The final HIP pattern we reached and have been using is shown in Fig. 7.3.

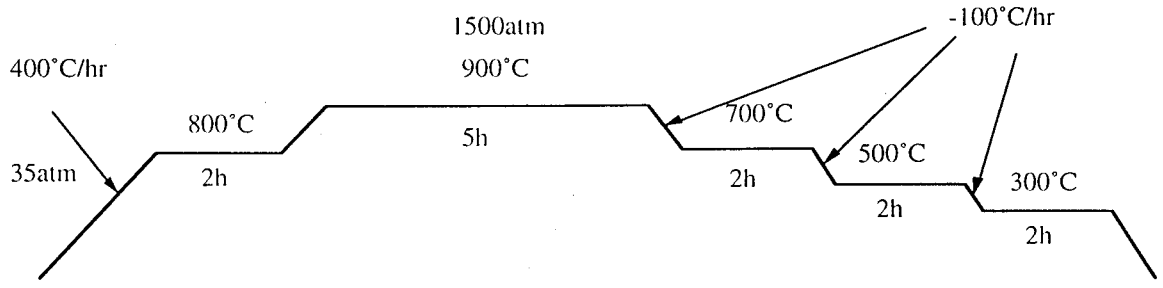

Fig. 7.3: Finally established HIP pattern used for the absorbers of KEKB SCC. Chronological changes of the HIP pattern are described in Appendix A.

7.4 Problems encountered

Though the idea of using pre-sintered ferrite powder and HIP seemed to be ideal, there was no exerience to use ferrite powder in the HIP company we used. The "trial-and-error" period started from the common sense of the staff who had some experience with powder HIPping and the information collected from engineers and researchers at TDK[1].

The problems we faced are:

- Leaks during HIP
- Cracks in the ferrite when a stainless steel ring was HIPped together
- Voids that appear after ferrite machining
- Delamination

These problems and the solutions we found are described in more detail in the subsections below.

7.4.1 Leaks during HIP

If there is a leak in the wall of the inner capsule during HIP, the ferrite fails to be sintered. At an early stage of the development, the inner capsule was made of a soft steel pipe and TIG-welded with a lid at the bottom. In this configuration, leaks happened frequently. Figure 7.4-1 shows a typical appearance when there was a leak during the HIP process. Compressed Ar gas that entered the capsule pushes the 2 mm-thick inner wall when the outside pressure is decreased. Relatively weak parts of the inner wall bulged as shown in the figure.

Since it was found that the welding at the bottom of the capsule is prone to leaking, possibly because the ferrite powder pushed the welding area and deformed it during packing, this welding seam was replaced with a spun inner capsule. With this new type of inner capsule, there have been few leaks. Figure 7.4-2 shows the rate of leaks during HIP. There have been no leaks in the last three HIP processes making a total of 22 absorbers.

[1] Because the pre-sintered powder was provided by TDK, Inc.

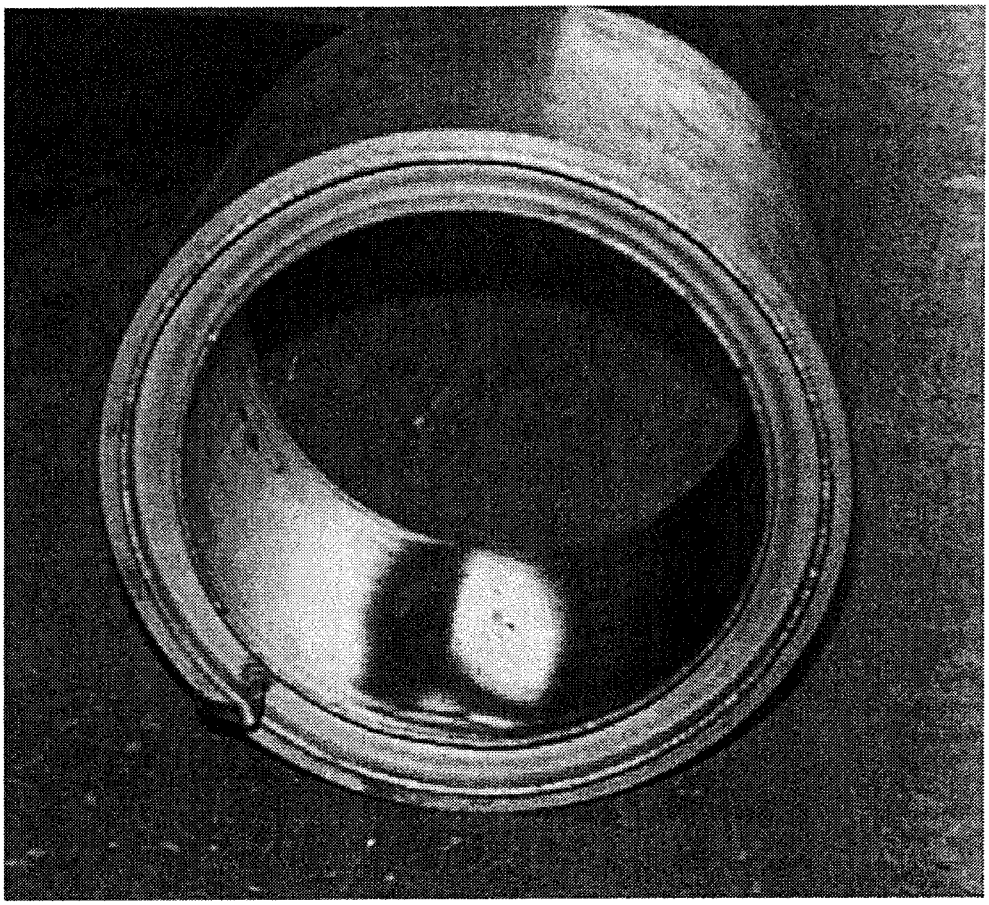

Fig. 7.4-1: Typical appearance when there was a leak during HIP.

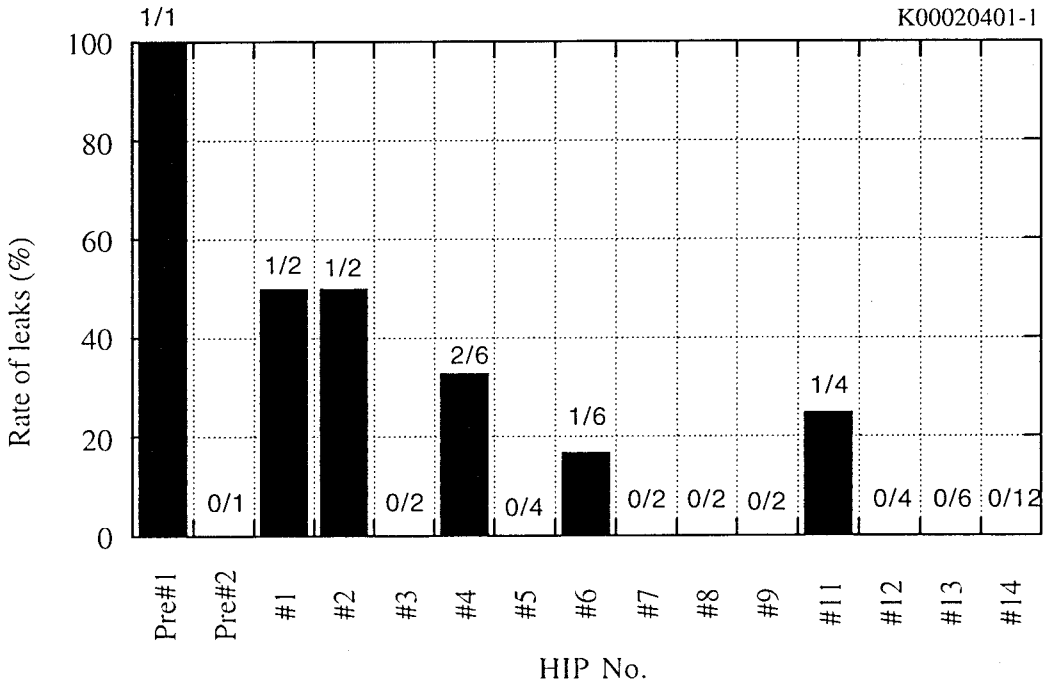

Fig. 7.4-2: Rate of leaks during HIP. The number inside of the chart shows the number of leaked absorber divided by the number of the total absorbers.

7.4.2 Ferrite cracks when a stainless steel ring was HIPped together

At the first HIP test, we tried to HIP a stainless steel SUS304 ring to facilitate the following electron beam welding because the welding of SS to SS is much easier due to low thermal conductivity of SS and stronger joints compared to SS/Cu welding. Figures 7.4-3 and 7.4-4 show some examples of the cracks. It was found these cracks had been caused by the accumulated stress in the ferrite during the cool-down from a HIP temperature of 900 °C. Stainless steel gets hard at higher temperature compared to copper and does not yield in the course of the cool-down, which causes the accumulation of stress in the ferrite since the contraction rate of ferrite is less than the surrounding SUS304.

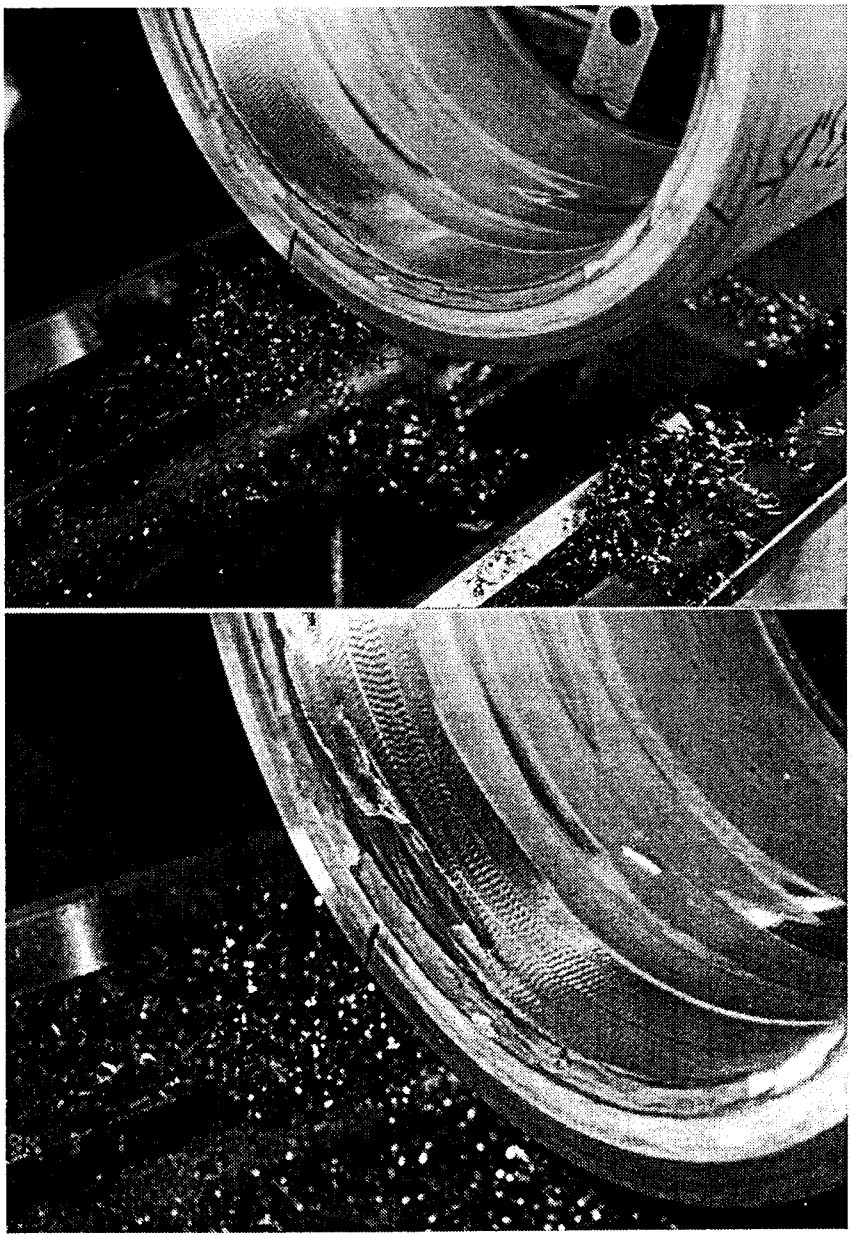

Fig. 7.4-3: Ferrite cracked when the inner capsule was being removed. The two stainless steel (SUS) rings that were added on the ends of the copper pipe to facilitate welding the end flanges. SUS/SUS welding is much easier and stronger than SUS/copper welding. Due to less ductility of SUS, more thermal stress was accumulated in ferrite and was released upon removing the capsule.

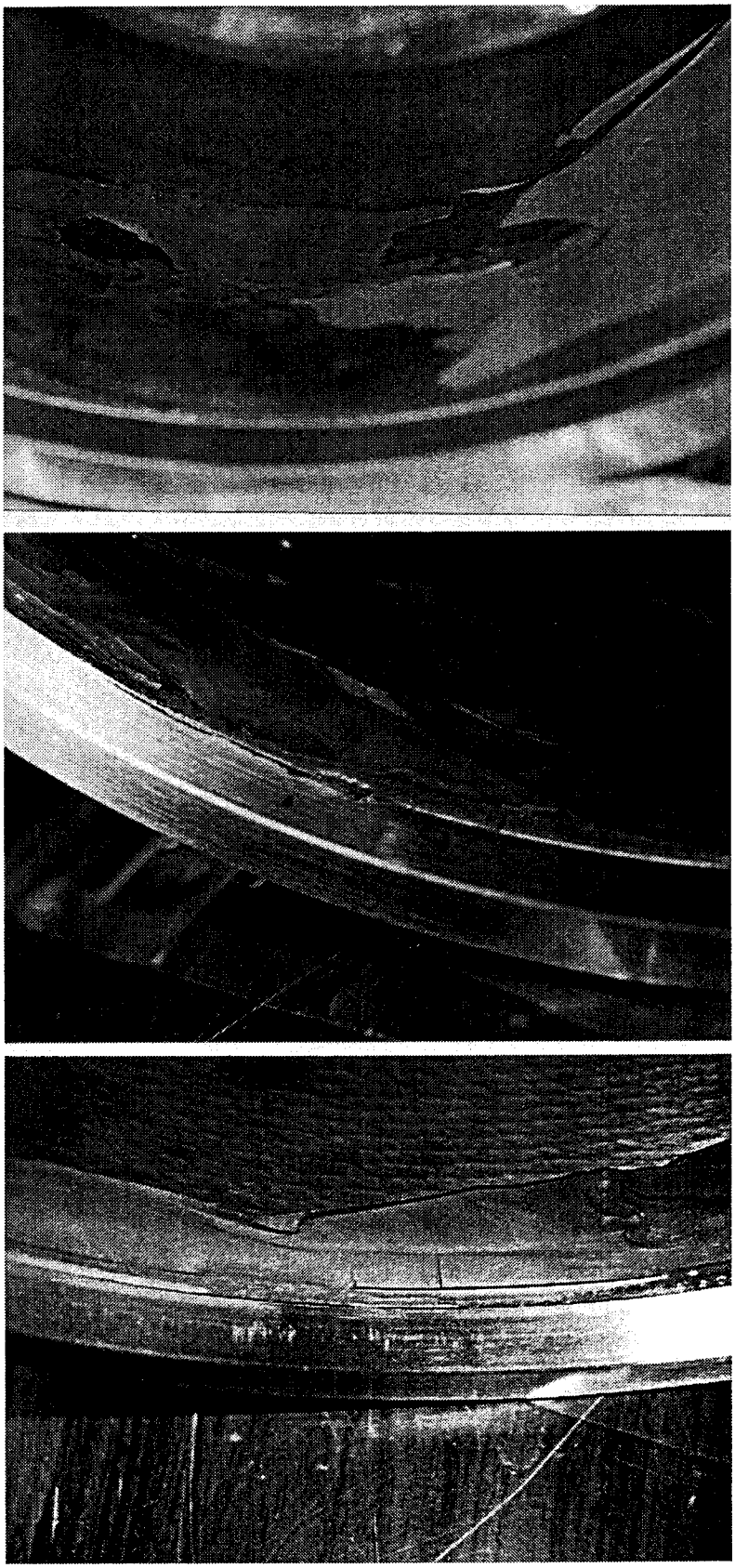

Fig. 7.4-4: Cracks that occurred during ferrite machining. This was caused by the accumulated stress in the ferrite during cool-down. Since stainless steel does not yield as much as copper, more stress accumulates in the ferrite. It turned out that it is impossible to use stainless steel as an outer layer for ferrite.

7.4.3 Voids that appear after ferrite machining,

Large visible voids of a few mm to cm long appeared after the first and second HIP as shown in Fig. 7.4-5. Firstly, we thought that this was because the packing of the ferrite powder had been inappropriate due to inexperience. It may have been the cause of large voids, but it was when the HIP pressure was increased from 1000 atm to 1500 atm that no voids were observed. Therefore, we concluded that the major reason was the insufficient pressure in HIPping.

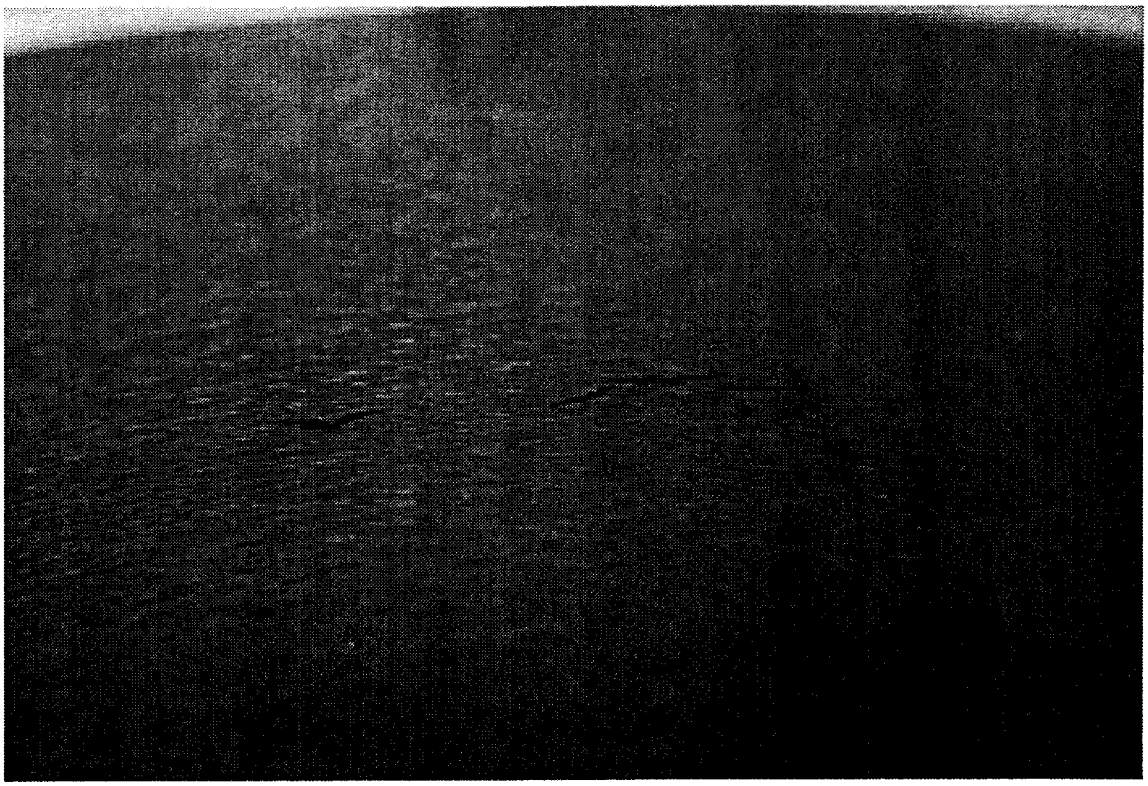

Fig. 7.4-5: Voids at the surface of the absorber #1S. (image full width = approx. 100 mm)

7.4.4 Delamination

Eliminating the stainless steel solved the first problem. Raising the HIP pressure from 1000 to 1500 atm, together with lengthening the degassing time solved the second problem. The third problem, delamination, become less since eliminating the stainless steel and raising the HIP pressure, which suggested that it is due to residual stress during cool-down. By modifying the pattern of the cooling so that the residual stress becomes as small as possible as shown in Fig. 7.3, the delamination problem was also eliminated.

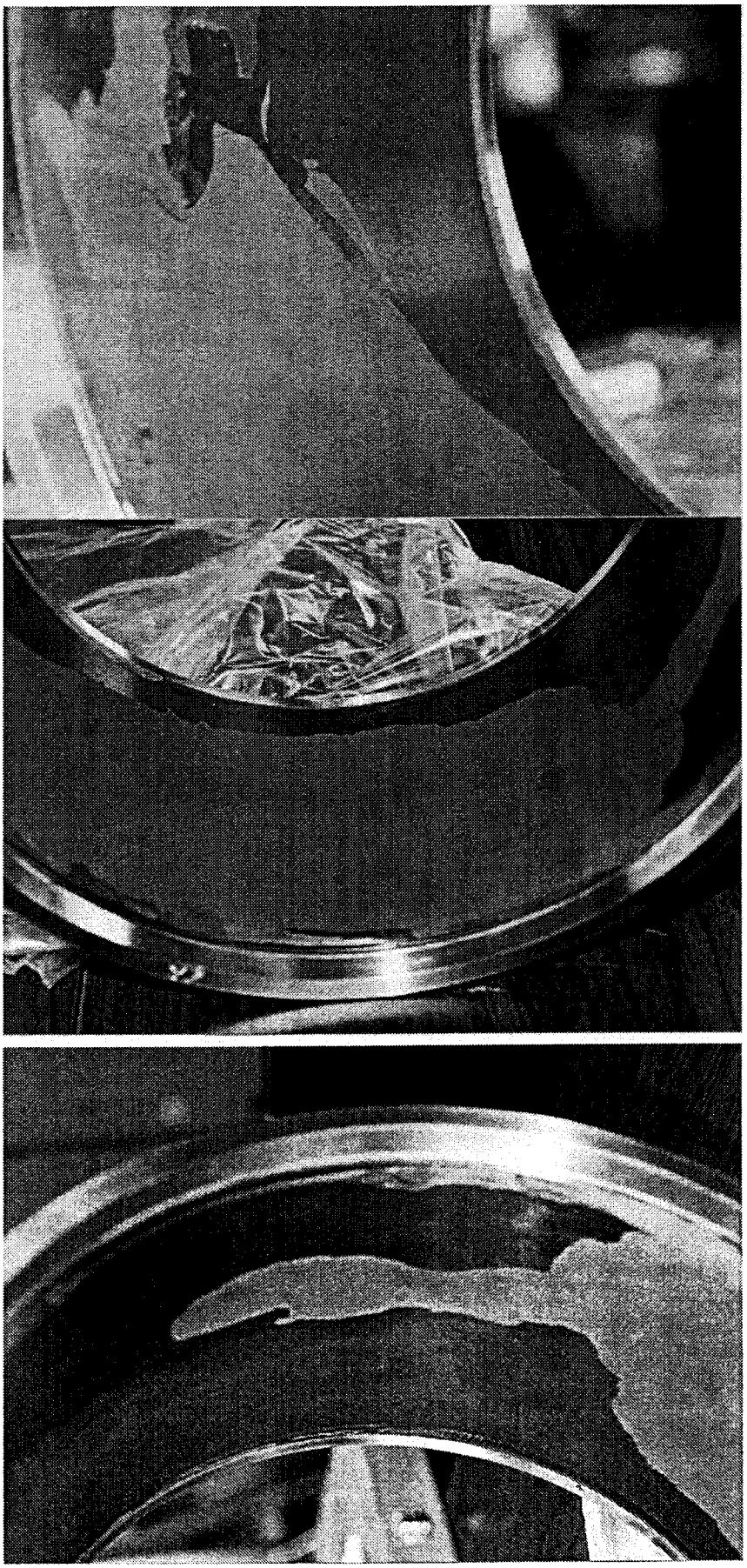

Fig. 7.4-6: Delaminations that occurred during ferrite machining. Absorber #2L2.

7.4.5 Cracks during baking

It was after the beam test at TRISTAN AR (Accumulation Ring) that this crack was found. Because the cracks were so narrow (10 μm>) we could not see them with the naked eye. When we happened to check the ferrite surface with a so-called probe microscope we found micro cracks. After this, we investigated the cause of the cracks and found that the baking prior to the installation caused the cracks. In the course of the investigation, a method called acoustic tomography was found to be the best way for inspecting cracks. We discuss the acoustic tomography, the investigation of cracks and its remedy in the following sections.

- **Acoustic tomography** [7]

Sound waves propagate through solids, liquids and gases. To inspect welds or defects, ultrasonic waves of a few MHz are normally used today since the space resolution is about a half of a wavelength. We have been using the pulse echo method; i.e. ultrasonic pulses are sent through a material in a medium that analyzes their echoes. When the wave pulses hit a material, some of the wave bounces back and some of them penetrate into the material. The reflection coefficient of ultrasound waves, when they go through medium 1 and hit a material 2, is described as follows.

$$\textbf{Reflection Coefficient} = \frac{P_r}{P_f} = \frac{Z_2 - Z_1}{Z_2 + Z_1} \qquad (7.4.5\text{-}1)$$

where P_r and P_r are the sound pressures of forward and reflected waves, and Z_1 and Z_2 are the acoustic impedances or a product of density and sound speed in the corresponding medium or material.

Acoustic tomography is the technology that visualizes the variation of the pressure of the sound waves that are reflected from the points of interest.

The detailed measurement procedure is described in Appendix C.

- **Principle of crack detection**

Since cracks usually include air or water in the gap and the reflection coefficient of sound waves at the cracks is so high (approx. 95%) almost all waves reflect at cracks. The reflected waves do not return to the receiver as shown in Fig. 7.4.5-1.

As a result, the sound pressure of the waves that return to the receiver gets lower than that returning from the places where there is no crack. In the image, the lower sound pressure becomes darker. In other words, if the gap or crack is located in parallel with the ferrite surface or at an angle such that the reflecting waves go back to the receiver, the obtained image gets brighter. In our experience, delaminations are such types of defects and create brighter images.

Figure 7.4.5-2 shows how the profile of the strength of each echo is displayed as an unfolded image. Horizontal and vertical directions show azimuthal and axial directions, respectively. These images are constructed by putting 9 images at every 40 degrees for SBP and 6 images at every 60 degrees for LBP. One can sometimes see the borderlines between neighbor images due to bad matching of the borders.

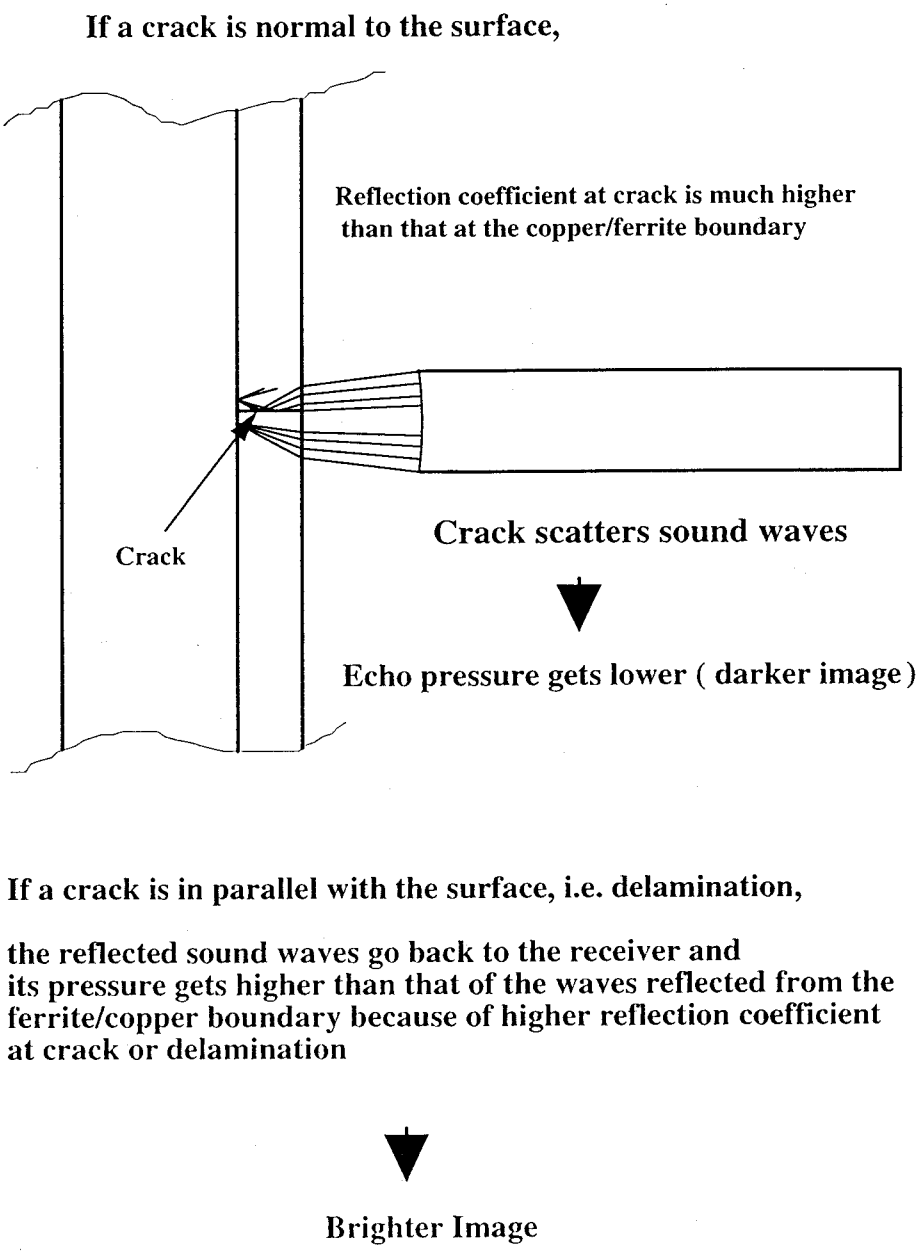

Fig. 7.4.5-1: Principle of crack detection.

Figure 7.4.5-3 shows the cracks found in the absorber tested in TRISTAN AR. Since the widths of the cracks were mostly less than 10 μm, i.e. narrower than the horizontal resolution of the machine, they were not detected by the surface echo, but as you can see in the bottom figure, they were detected by the boundary echo, i.e. reflecting a signal from the

ferrite/copper boundary, very clearly. It was confirmed with another method called color check, i.e. detecting colored fluid that was filled in the gaps, that most of these cracks open at the surface of ferrite, showing a pattern very similar to the bottom image of Fig. 7.4.5-3.

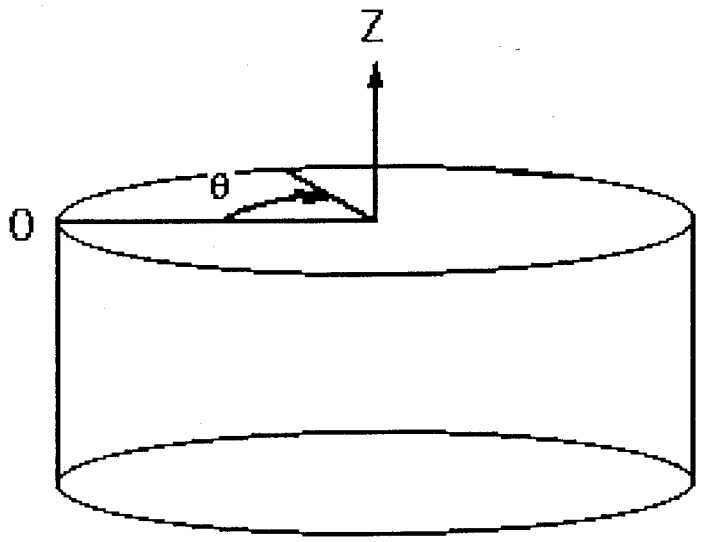

Fig. 7.4.5-2: The scanning direction of acoustic tomography. In the following images, horizontal direction is azimuthal , θ, and vertical direction is axial.

It was surprising to know how clearly the cracks could be detected, especially with the echoes from the ferrite/copper boundary (bottom image of Fig. 7.4.5-3). The excellent feature of this method is that the anomalies inside of the ferrite can be detected. Another example is shown in Fig. 7.4.5-28. The cracks shown here were made by press-inserting a cooling pipe in a groove machined on copper. Since the thickness of the copper was thinner than the designed value by 2.3 mm, pressure to insert the pipe was probably exerted more strongly on the ferrite and created cracks. These cracks were seen even with the naked eye. The top image of Fig. 7.4.5-4 is similar to the observation with the naked eye, indicating that the resolution of the surface echo is close to that of the human eye. As one can see in the bottom figure, the echoes from the ferrite/copper boundary clearly show how these open cracks are extended inside of the ferrite.

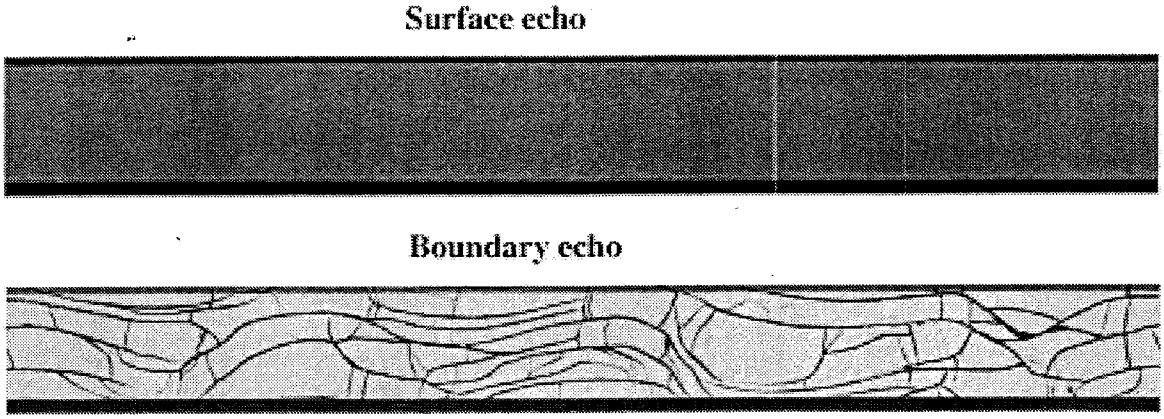

Fig. 7.4.5-3: Unfolded images of ferrite echoes from ferrite surface and ferrite/copper boundary. Horizontal and vertical directions correspond to azimuthal and axial direction, respectively. Dark bands at the top and bottom of each figure correspond to tapers. This absorber (#6S3) was used for beam tests in TRISTAN AR. Cracks are clearly seen in the boundary echo as black lines. Since the widths of cracks were less than 10 μm they could not be seen with surface echo (upper image). The vertical lines are not defects but the borderlines of images (the whole image consists of nine 40-degree wide images).

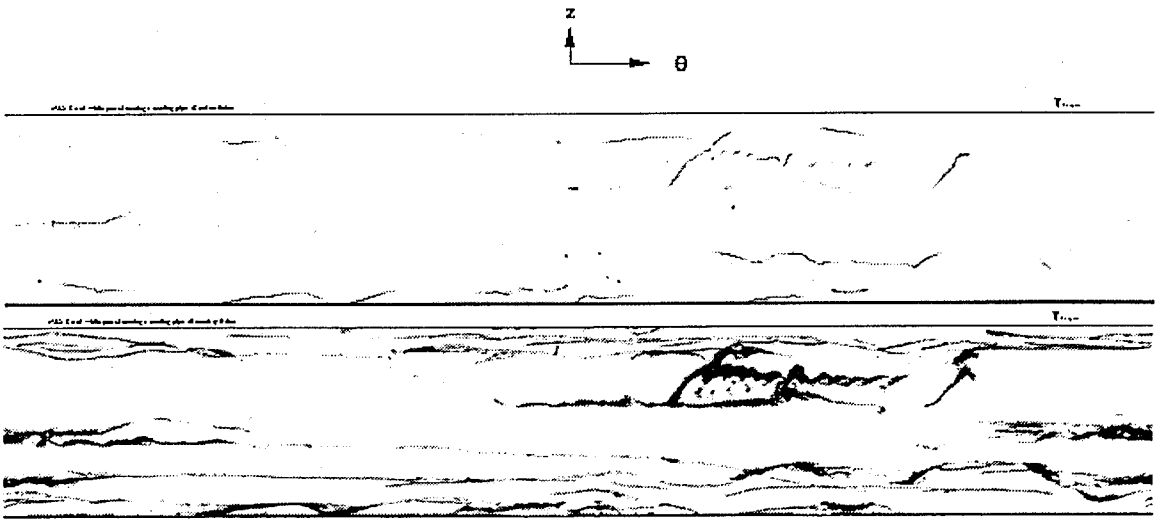

Fig. 7.4.5-4: Cracks caused by inserting a cooling pipe in the spirally machined groove on the outer surface of copper. Surface echo (top) and copper/ferrite boundary echo (bottom). These cracks were visible even with bare eyes. Since the resolution of surface echo is similar to human eyes, the top image was same as seen by human eyes. With boundary echo more information on the cracks, including the ones inside the ferrite, can be obtained as seen in the bottom image.

- **Investigating the cracks**

To begin investigating the cause of the cracks, firstly, we tested previously manufactured absorbers with acoustic tomography. In the results, we found that there were no cracks in the as-manufactured absorbers that have not undergone baking or high power tests. Cracks were found, however, among the absorbers that had undergone baking and high power tests.

Subsequently, using acoustic tomography, tests were carried out to answer the following questions.

1. Which is the cause of the cracks, baking or high power tests?
2. If baking is the cause, at what temperature does the absorber crack?
3. If high power tests are the cause, at what power does the absorber crack?

Firstly we obtained the above-mentioned echo images before baking, and then they were compared with those after baking.

Figure 7.4.5-5 shows the echo images from the ferrite/copper boundary before and after baking at 150 °C for about one month of an absorber #7LA with a 300 mm diameter. As you can see from the dark lines in the bottom figure, it cracked at baking. Another absorber #7LB with the same diameter baked at 110 °C also cracked as shown in Fig. 7.4.5-6, although the number of cracks were much less than the one shown in Fig. 7.4.5-3.

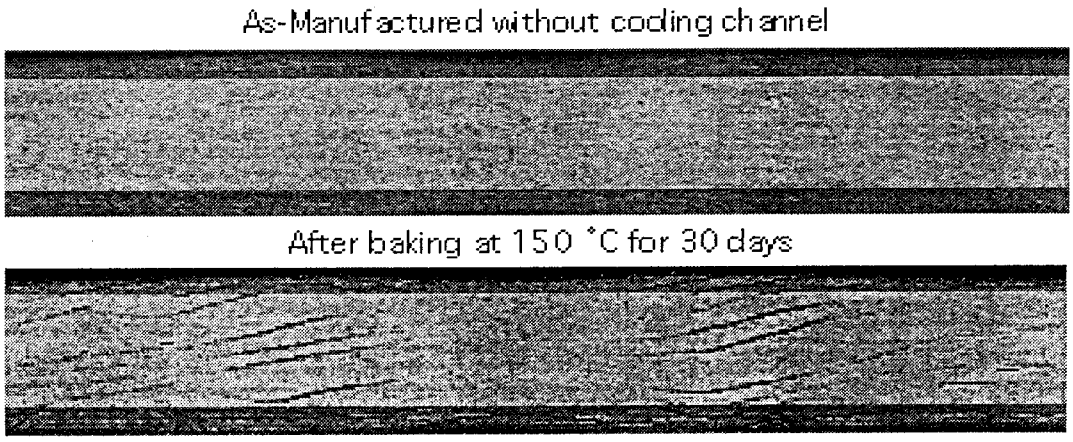

Fig. 7.4.5-5: Images of echoes from the ferrite/copper boundary. Absorber #7LA before (top) and after (bottom) baking at 150 °C for one month. This absorber did not have a groove for a cooling pipe.

In the case of the absorber tested in TRISTAN AR, since we did not know about the cracks, we baked it a number of times without much caution, which seemed to have increased the number of cracks.

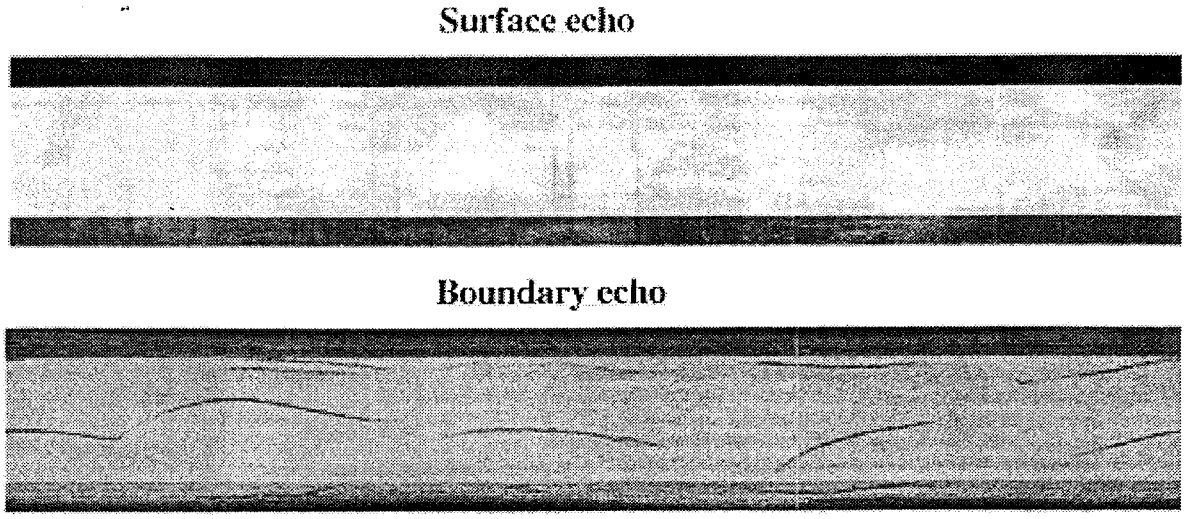

Fig. 7.4.5-6: An absorber (#7LB) with a 300 mm diameter after baking at 110 °C. Cracks are seen in the bottom image.

Therefore, although the possibility that some cracks occurred during the beam tests is not excluded completely, it is very low and so it is natural to conclude that the baking prior to the installation caused the cracks.

Actually, a long time before, we had heard some sounds that makes one think of cracks while baking the absorbers, but due to our poor inspection with only naked eyes, we could not find any cracks. In addition, in our experience, there seemed to be no damage even when baked up to 250 °C.

Secondly, to know at what temperature the absorber starts cracking, we tested from 60 °C. As shown in Fig. 7.4.5-7, the absorber #6L3, 300 mm diameter, was tested before and after baking at 60 °C then 70 °C with a ramping rate of 30 °C/h and holding time of one hour. As shown in the figure, cracks started at 60 °C $< T \leq$ 70 °C.

Thirdly, to check the high power test, we tested SBP at 5 kW and LBP at 7 kW, which are twice the power that we expected at KEKB. Tests were performed with a 508 MHz coaxial line. The absorber was water cooled at 5 L/min during the test. Results showed no cracks at these powers, indicating that cracks are not likely to happen during beam test at these powers.

Fourthly, we checked if the cracked absorber extends its cracks during high power tests. Results showed a negative. The cracks did not increase with high power tests as shown in Fig. 7.4.5-7.

Considering that the copper layer that surrounds the ferrite layer is cooled with water, i.e. copper does not expand much, there will not be much pulling force in the ferrite that leads to cracks.

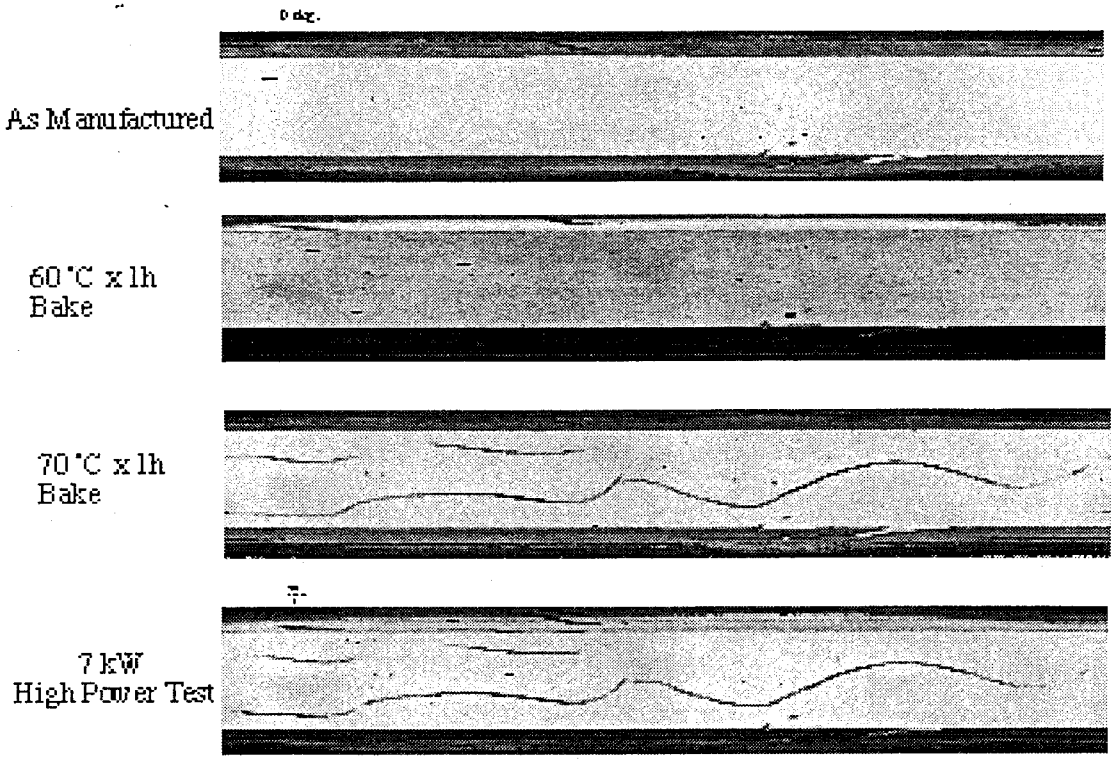

Fig. 7.4.5-7: Images of echoes from the ferrite/copper boundary. Absorber #6L3 (300 mm in diameter). Chronologically written from top to bottom. It was found that the cracks start at a temperature 60 °C < T ≤ 70 °C. Also, cracks did not extend with the 7 kW 508 MHz coaxial high power test (bottom image).

- **Remedy for cracks**

Taking into account that the thermal expansion coefficients of copper and ferrite are 18×10^{-6} and 8.5×10^{-6}, respectively, we assumed that the expanding force of copper surpasses the breaking strength of ferrite and thought of how to reduce the expansion of copper relative to the ferrite.

At first, baking ferrite from the inside using an infrared light or microwave while cooling the outside with water was considered. However, since instrumentation for this is costly and it is difficult to bake with this method after installing absorbers in the beam line, we decided to try the following first.

In the process of manufacturing, the copper layer is covered with another layer of 12 mm-thick soft steel [4]. Though we normally remove this layer after HIP, considering that the expansion coefficient of this soft steel is 11×10^{-6} and it is firmly bonded to copper by HIP, leaving this layer might help reduce the expansion of the copper. Thus, using an absorber with the soft steel layer left, we baked and checked if cracks occurred.

No cracks occurred after baking at 150 °C. Then, we reduced the thickness of soft steel to 3

mm so the configuration of the cooling pipe can be similar to the previous one with a larger diameter water cooling pipe (1/2 inches). Consequently, as shown in Fig. 7.4.5-8, no cracks appeared and it was confirmed that leaving the soft steel layer is effective to prevent cracks.

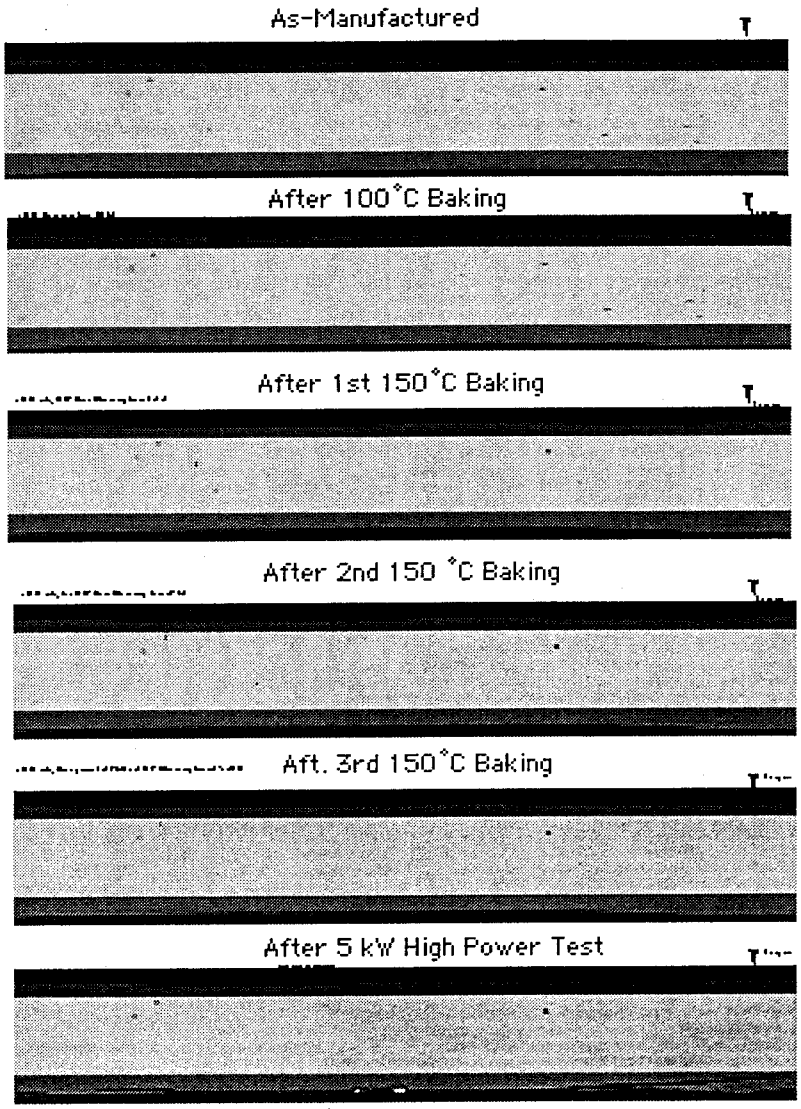

Fig. 7.4.5-8: Images of echoes from ferrite/copper boundary of absorber #11S2 with a 3-mm thick soft steel layer on the copper layer. With the soft steel layer left, cracks did not occur during baking at 150 °C. This is before making a groove for a cooling pipe.

Unfortunately, however, after making a spiral groove for a cooling pipe, as shown in Fig. 7.4.5-9, the absorber cracked, Fig. 7.4.5-10. This was probably due to the fact that the soft steel layer was removed at the groove. Also, cracks were found to occur sometimes during press-inserting the 1/2" cooling pipe because more force is needed to press 1/2" pipes as compared to 3/8" pipes. For this reason, although some absorbers adopted this method, we decided not to use this method for the next ones.

Since reducing the outgassing rate is very important for SCC's, having cracks does not seem to be a problem with the fact that there is no degradation of the absorbing characteristics, the performance of the superconducting cavities in the beam tests, we decided to bake the absorbers at 150 °C.

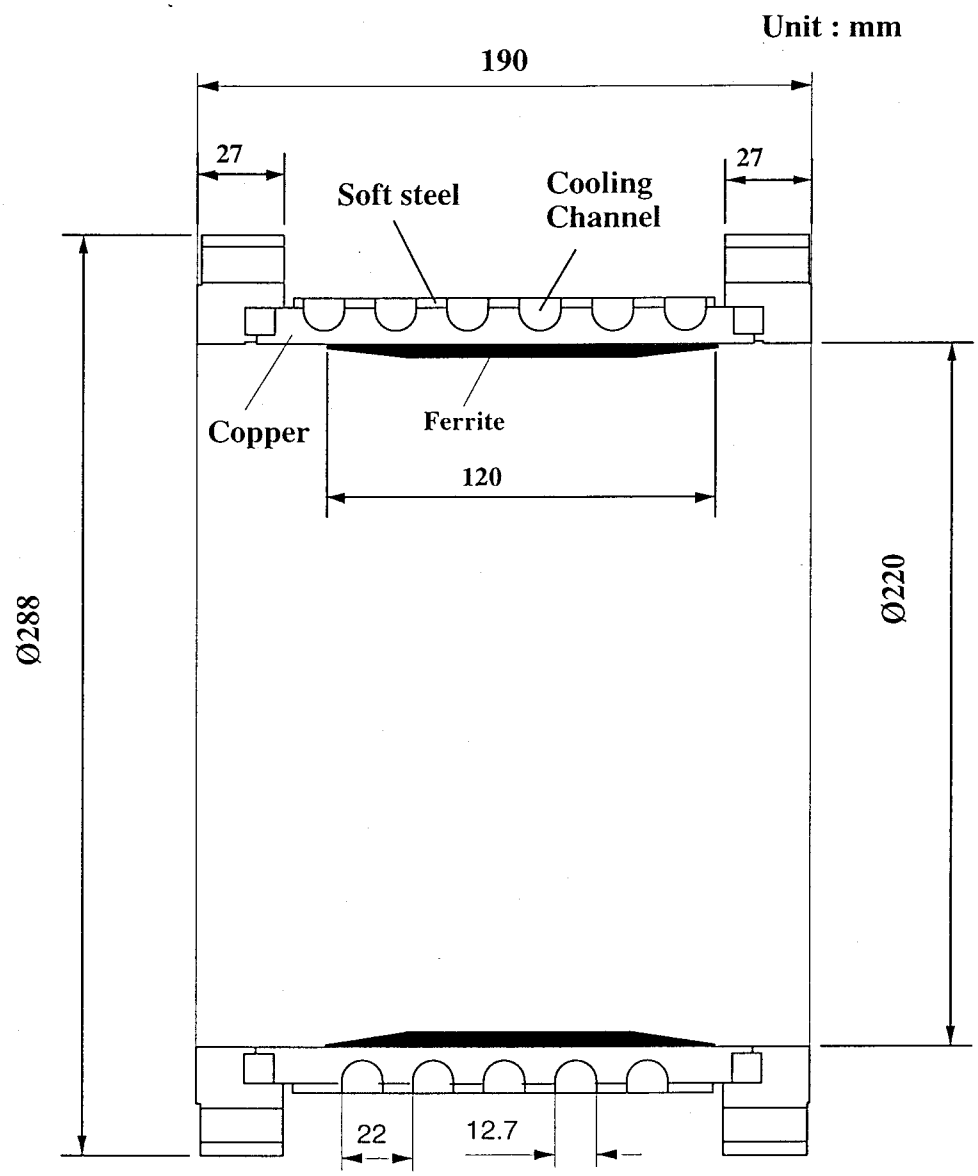

Fig. 7.4.5-9: Design with 3-mm thick soft steel on copper layer.

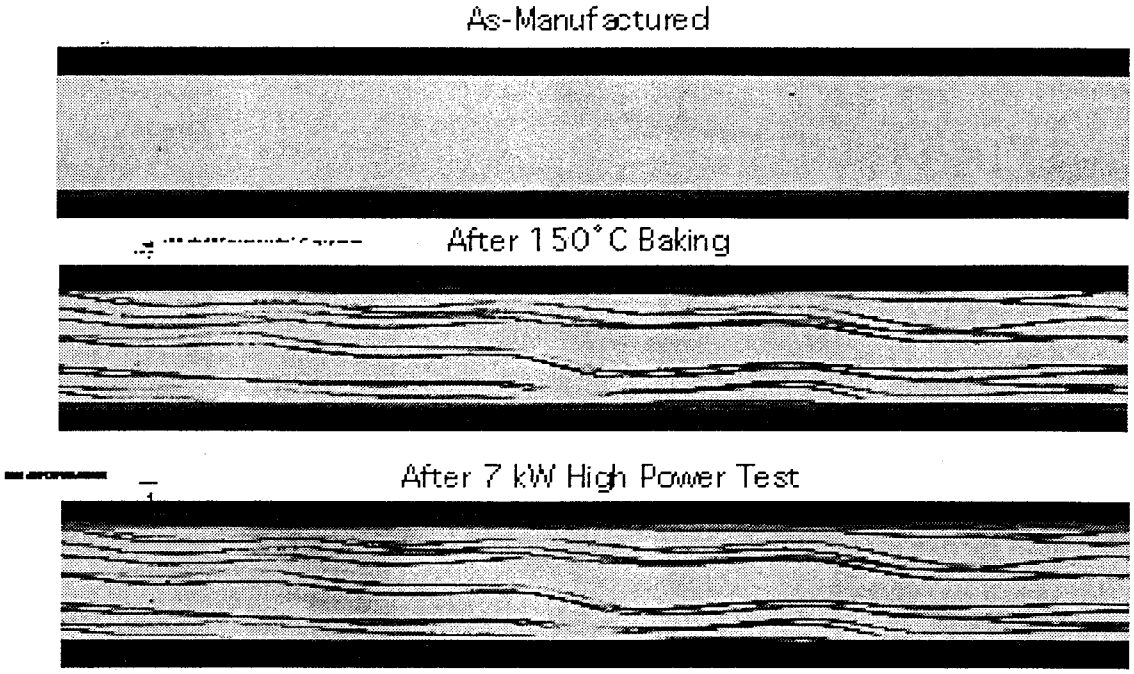

Fig. 7.4.5-10: Images of echoes from the ferrite/copper boundary of an absorber #12L2 with a 3-mm thick soft steel layer left on the copper layer to prevent cracks. After making a spiral groove for the cooling water pipe, the effect of the soft steel layer disappeared due to the groove and cracks occurred as shown in the middle figure. Cracks did not expand during the 7 kW high power test as shown in the bottom figure.

At present, to reduce the outgassing rate of the absorbers and to prevent cracks, the following procedure is adopted.

(1) Degas ferrite powder as much as possible.

(2) Prevent the degassed powder from being exposed to air again during the HIP procedure.

(3) After capsuling and before HIP, degas the powder at a higher temperature (400 °C) in the can.

(4) After HIPping, remove the inner can and machine the absorber, bake and degas the HIPped ferrite with a soft steel layer at 150 °C for 2 weeks or longer. (Though longer baking is better, construction schedule sometimes limits the baking time).

(5) After degassing, keep the ferrite from being exposed to air whenever possible. Make a cover and seal it with nitrogen gas during the following machining processes.

(6) Remove the soft steel layer and keep the baking temperature of the absorber lower than 60 °C after assembling with tapers, etc.

This procedure was adopted with the absorbers to be assembled with the four additional SCC's for D10 at Nikko.

7.5 Summary

We discussed the technique to make full-size absorbers. This is an application of HIP (Hot Isostatic Press), which is a relatively new technology. For the first time, the technique to make full-size HOM absorbers with this technique was established. Since it was the first trial, the work proceeded, in a sense, on a "trial and error" basis. Improving the tools and fixtures and establishing a controlled procedure lead to the success.

There have been problems. They were: leaks during HIP due to improper capsuling, cracks because of accumulated stress in the ferrite, voids and delaminations due to insufficient pressure/degassing, cracks during baking.

All the problems, except cracks during baking, were solved either by improving the tools or by optimizing the HIP conditions (pressure, temperature, etc.).

Cracks caused by baking were investigated intensively using acoustic tomography, which enables one to detect not only the defects at the ferrite/copper boundary, but also those inside of the ferrite. The investigation revealed:

(1) Cracks start at a temperature of $60\ ^\circ\mathrm{C} < T \leq 70\ ^\circ\mathrm{C}$.

(2) Cracks tend to run in the transverse direction.

(3) Cracks are caused by the pulling force of the copper layer due to the difference of thermal expansion coefficients.

(4) By leaving the soft steel layer that surrounds the copper layer, this crack can be prevented up to 150 °C.

With the above results, we decided to bake the absorbers with the soft steel layer remaining. If the outgassing rate was sufficiently low, we tried not to bake at temperatures higher than 60 °C.

In addition, in our experience, we have not had any practical problems in using cracked absorbers. Therefore, we will probably try to bake at higher temperature if necessary.

Chapter 8

Tests on full-size absorbers

8.1 Introduction

Using the HIP technique described in Chapter 7, we made full-size absorbers and checked the HOM damping capability, outgassing rate, loss factor and high power handling capability. The following sections show the results.

8.2 HOM Measurement

HOM's were measured using an aluminum model. This model was specially prepared for this measurement by machining the inside of a bulk aluminum precisely as designed in Chapter 6 and depicted in Fig. 6.2-6. Figure 8.2-1 shows the aluminum model and HOM absorbers.

A network analyzer (HP8720C) was used to measure the resonant frequencies and loaded Q

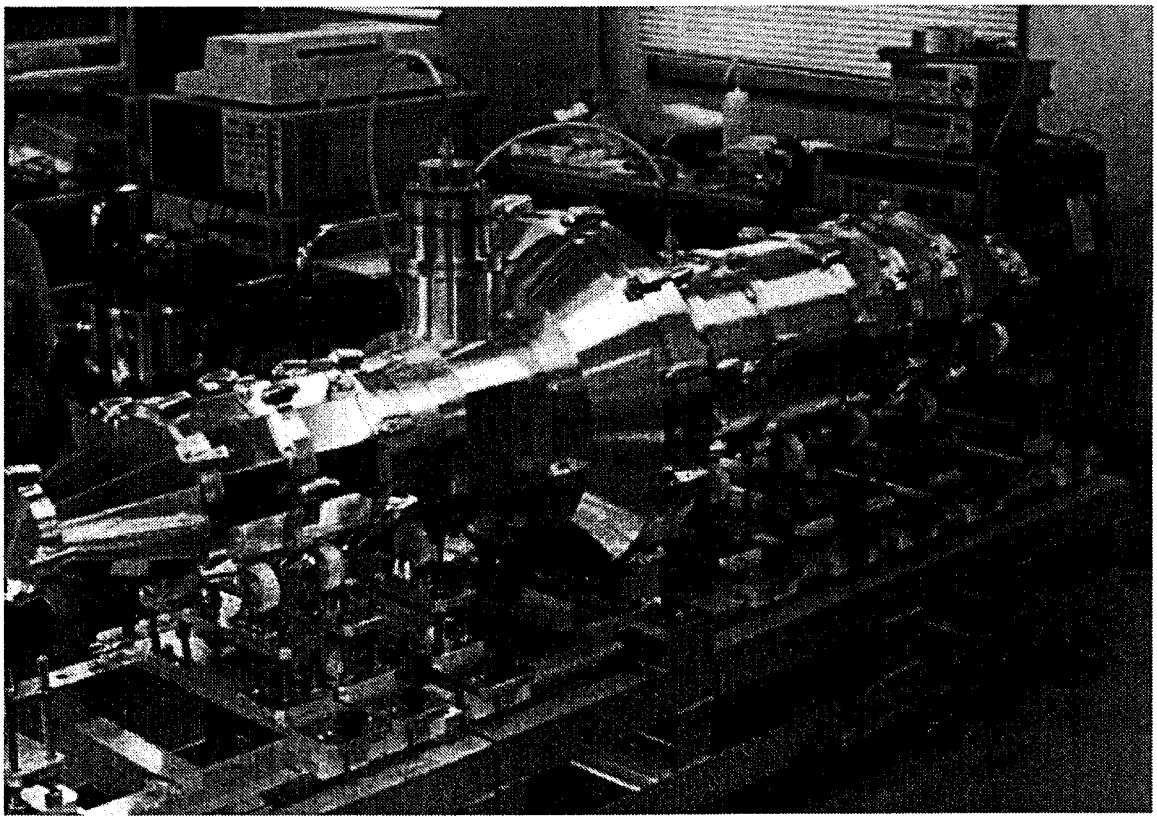

Fig. 8.2-1: Aluminum model with HOM absorbers. The shape of the cavity was precisely machined from bulk aluminum.

of each mode. This test is often called a low power test since it uses a power of the order of mW, which is much lower compared to the expected power of the order of kW. Tests using high power were conducted separately as will be shown in the later section.

An RF signal was fed through a port and the strengths of the fields formed in the cavity were measured by either an antenna or a loop, depending on the nature of the modes, e.g. a loop antenna in the cell to pick up the TM_{010} mode that has more magnetic fields in the cell.

Figure 8.2-2 shows the ratio of the signal strengths of output to input, so-called S_{21} . The top figure was obtained through blank aluminum pipes instead of HOM absorbers. The bottom figure was with the HOM absorbers. As one can see, the peaks or resonant modes became dull in the case with HOM absorbers, i.e. Q value was lowered, in other words, resonant modes are damped.

Figure 8.2-3 shows the measured Q_L and the Q_{HOM} calculated using CLANS for monopole modes [19] and CLANS2 [93] for multi-pole modes. As one can see in the figure, frequencies of most of the modes were identified, although the calculated Q values are about one order of magnitude higher than measured Q_L . This can be explained as follows. The external Q of antenna probe, $Q_{antenna}$, was much lower than the Q values and the measured Q_L was more influenced by the antenna since the measured Q_L, Q_{HOM} and $Q_{antenna}$ have the following relationship.

$$\frac{1}{Q_L} = \frac{1}{Q_{HOM}} + \frac{1}{Q_{antenna}} \qquad (8.2\text{-}1)$$

This has been confirmed by changing the length of antenna probe, but we did not try to measure the correct Q values because our main purpose was to identify the modes and check the codes. We used the calculated Q's for impedance calculations.

As seen in Fig. 8.2-3, the modes that have high Q values were identified to be mostly multi-pole modes. According to the results of the calculations made with CLANS2, these modes have very low R/Q's, resulting in low impedances. Consequently, they are much lower than the threshold of transverse mode instabilities.

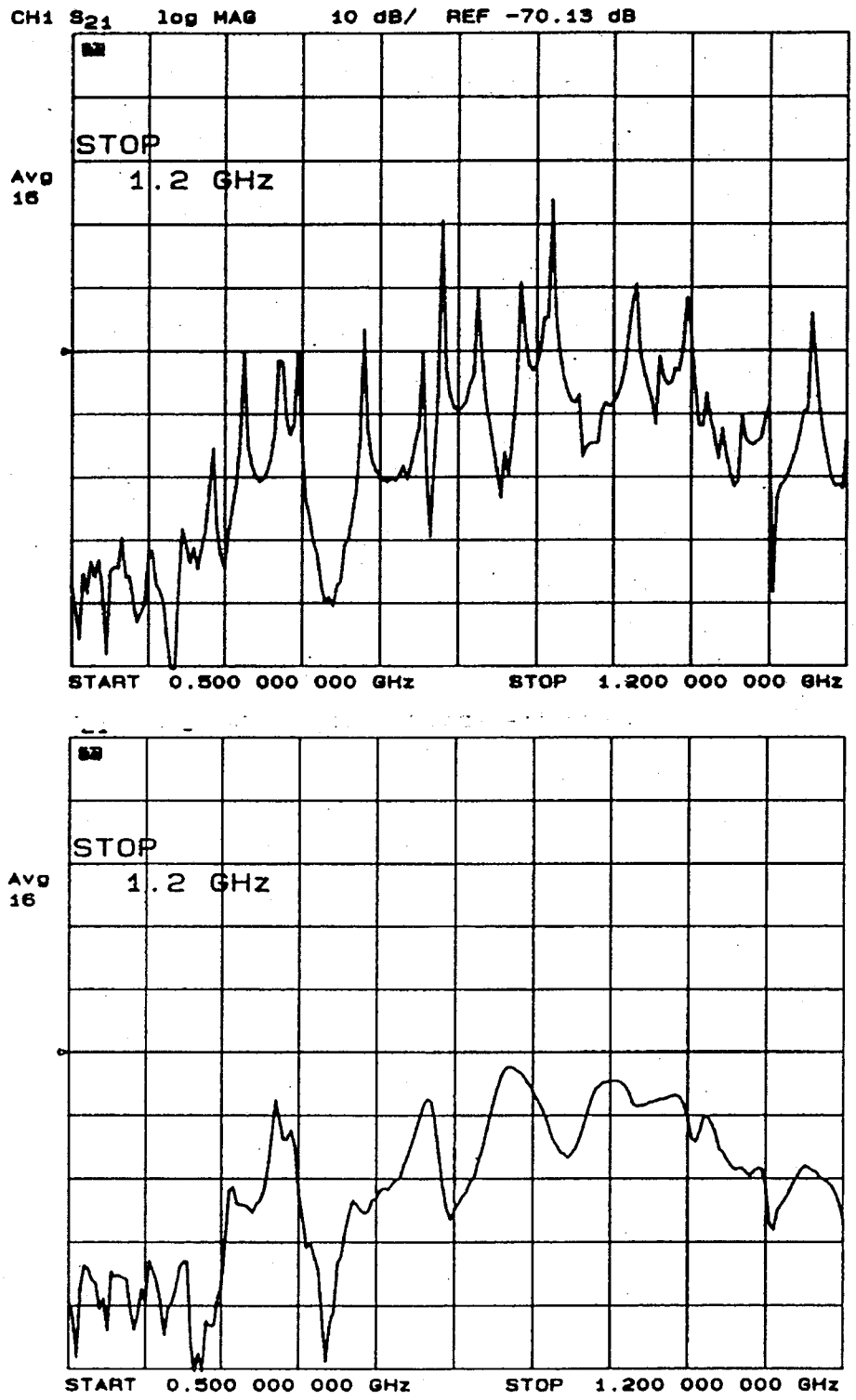

Fig. 8.2-2: S_{21} without ferrite absorber (top) and with ferrite absorber (bottom). Many modes are damped as shown by the dull peaks of the resonant modes in the bottom figure.

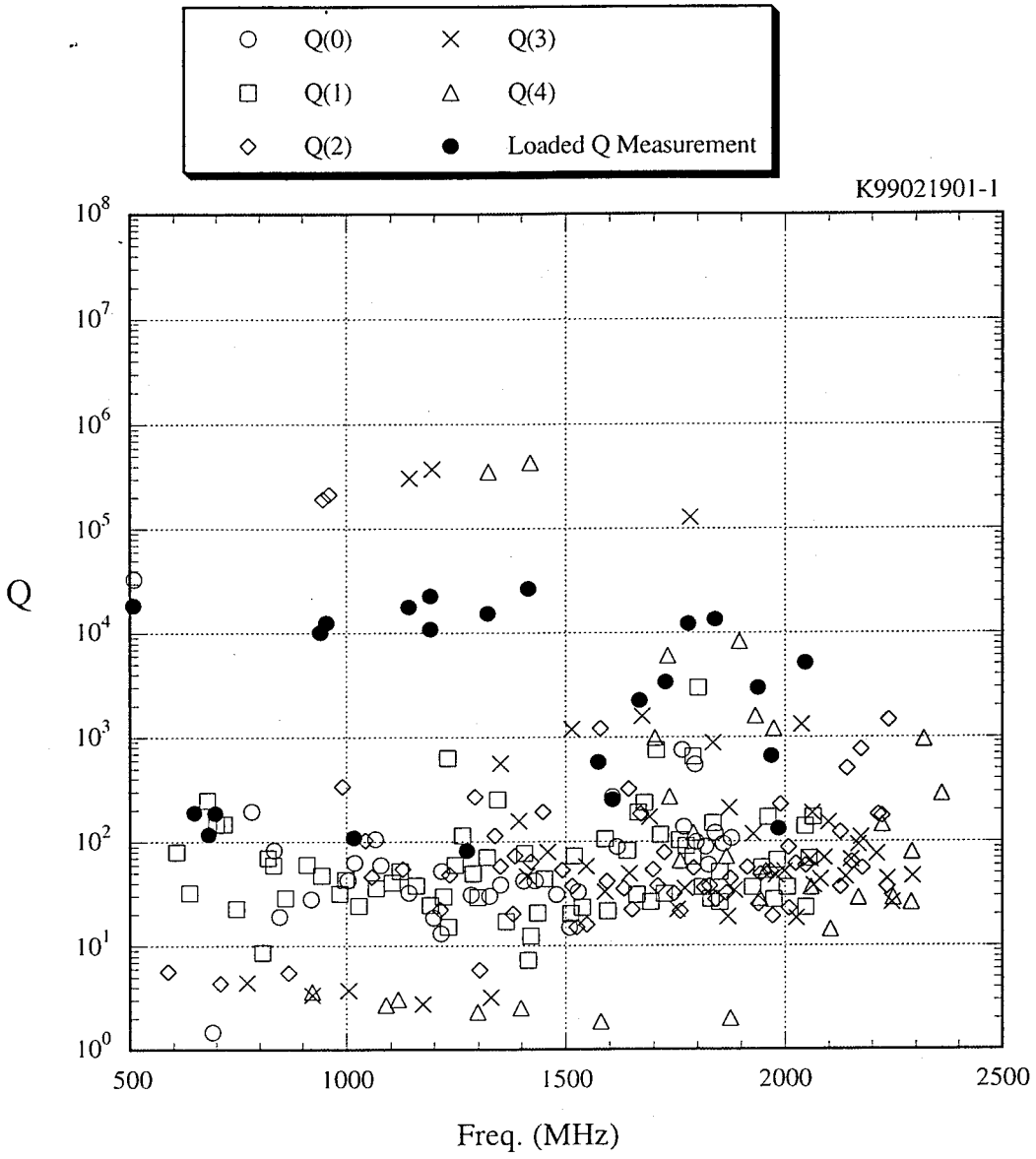

Fig. 8.2-3: Measured loaded Q depicted as solid circles and Q's calculated with CLANS.
Q(0): monopole, Q(1): dipole, Q(2): quadrupole, Q(3): sextupole and Q(4): octapole modes.

In Fig. 8.2-4, impedance of mono-pole modes that were calculated with CLANS is shown. In the figure, the thresholds of the impedance are depicted in 8 cavities with a solid line, which was calculated from Eq. (2.2.2-4). As one can see, all the modes are far below the threshold impedance, thereby no instability due to HOM will occur.

Also, the TM_{011} mode is the most dangerous mode below 1.5 GHz, the cut-off frequency of the beam duct (150 mm in diameter).

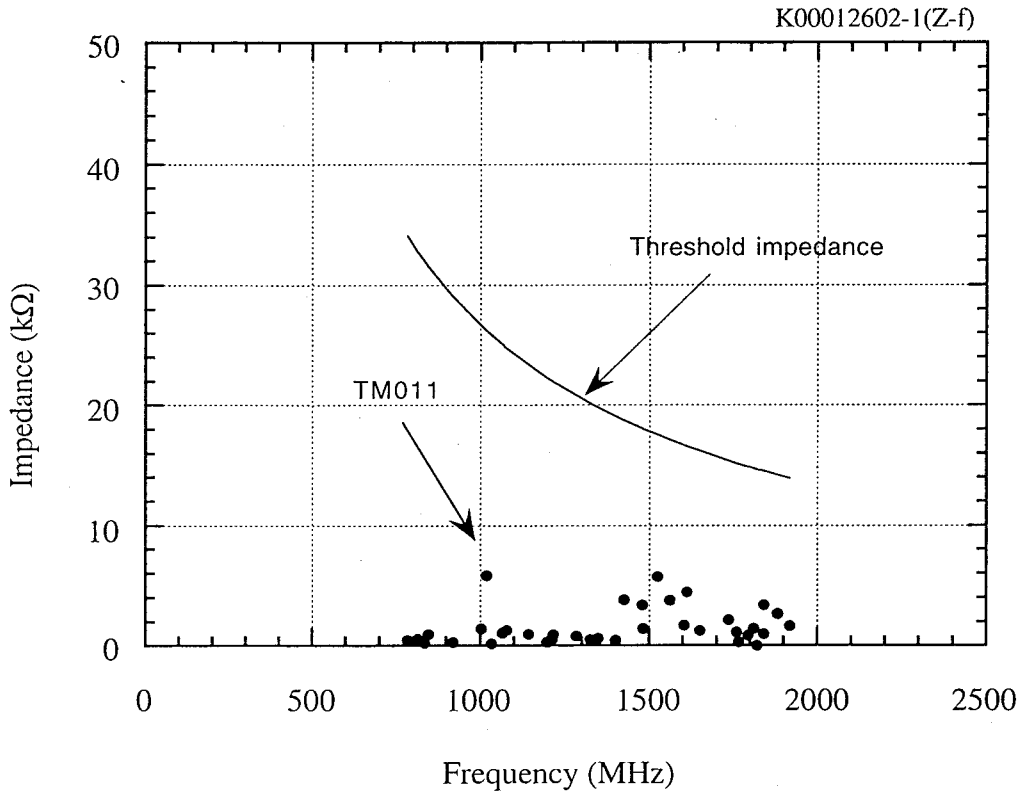

Fig. 8.2-4: HOM impedance of mono-pole modes as a function of frequency. A solid line is the threshold obtained from Eq. (2.2.2-4) in the case of 8 cavities.

8.3 Outgas measurement

Outgas is one of the most important factors in KEKB since UHV (1×10^{-9} Torr ≥) is required to get enough luminosity for sufficient beam lifetime. Moreover, it is even more important for superconducting cavities because excessive amount of condensed gases can trigger discharge in the cavity, thereby causing trips in our past experiences [4].

To estimate the outgas from the absorbers that was made with the HIP technique, we measured the outgassing rate of the full-size absorbers. Figure 8.3-1 shows the measurement setup, where the outgassing rate of the absorber was calculated by multiplying the pressure difference between P1 and P2, and the orifice conductance. To get high accuracy, a small orifice of 3.3 L/s was made. Another port for evacuation was made to shorten the time for pumping down the absorber up to a pressure low enough to use the ionization gauges designated as P1 and P2 in the figure. In addition, to know the gas species, a RGA (Residual Gas Analyzer) was equipped as shown in the figure.

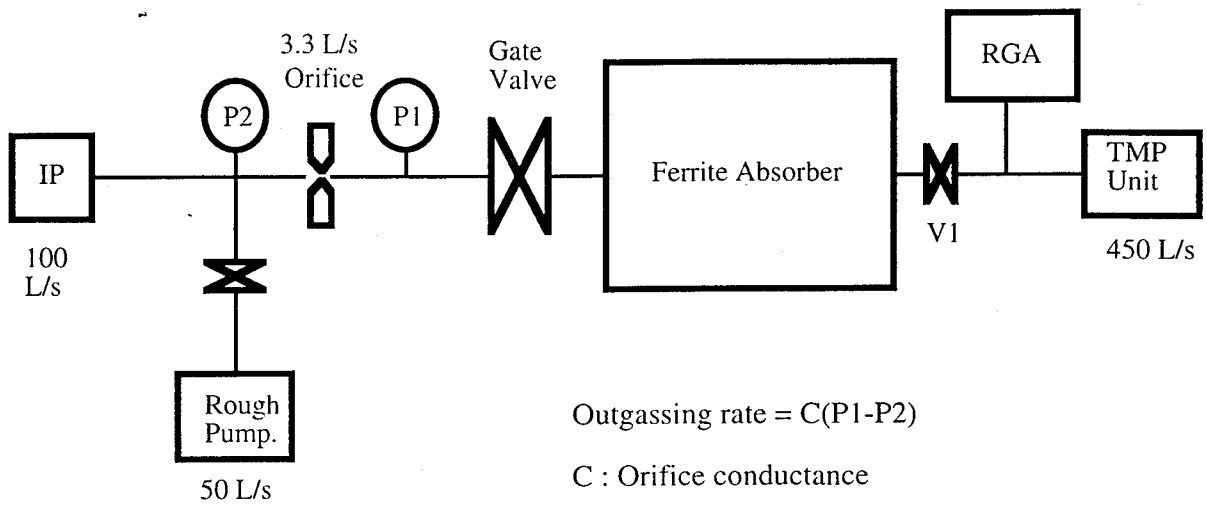

Fig. 8.3-1: Schematic representation of outgas measurement setup.

Figure 8.3-2 shows the outgassing rate of an LBP (Large Beam Pipe, the ferrite outer diameter is 300 mm and length 150 mm) as a function of time after the start of evacuation. The area occupied by ferrite is approximately 1380 cm^2.

In Fig. 8.3-2, solid circles show the first data. It was found that the outgas rate is about one order of magnitude higher than that of the IB-004 tiles even after 170°C x 13 days of baking. After an investigating the reason, we found that the pre-sintered ferrite powder absorbs enormous amounts of water from the air since the total area of fine particles of about 1 μm in diameter is large. Moreover, once the packed powder contains enormous amounts of water, it is difficult to degas it by hot degassing at about 300 °C after sealing the capsule.

As a measures to improve this situation, we tried to bake the powder in N_2 gas before packing into the capsule, then kept the time for the powder exposed to the air as short as possible. As a result, the outgas rate decreased about one order of magnitude before baking, as shown with solid squares in the figure. Since then (6^{th} HIP), this degassing of the powder became one of the routine processes.

Another study was to check if the outgassing rate changes when exposed to N_2 gas or air after baking. Because absorbers have to be vented to be assembled with cavities, it is exposed to either N_2 gas or air for a few hours. The absorber used for this experiment was the one shown with the solid circle in Fig. 8.3-2. The open circles show the result of the one exposed to N_2 for 3 hours. As shown in the figure, it takes a lot shorter time to reach the ultimate outgas rate, i.e. the baking effect remains for a long time. The one exposed to air showed similar results, although it increased about an order of magnitude if it was exposed to air for 38 days (depicted as crosses). However, the effect of baking still remains since the outgassing rate is about an order of magnitude lower than the initial value (solid circles).

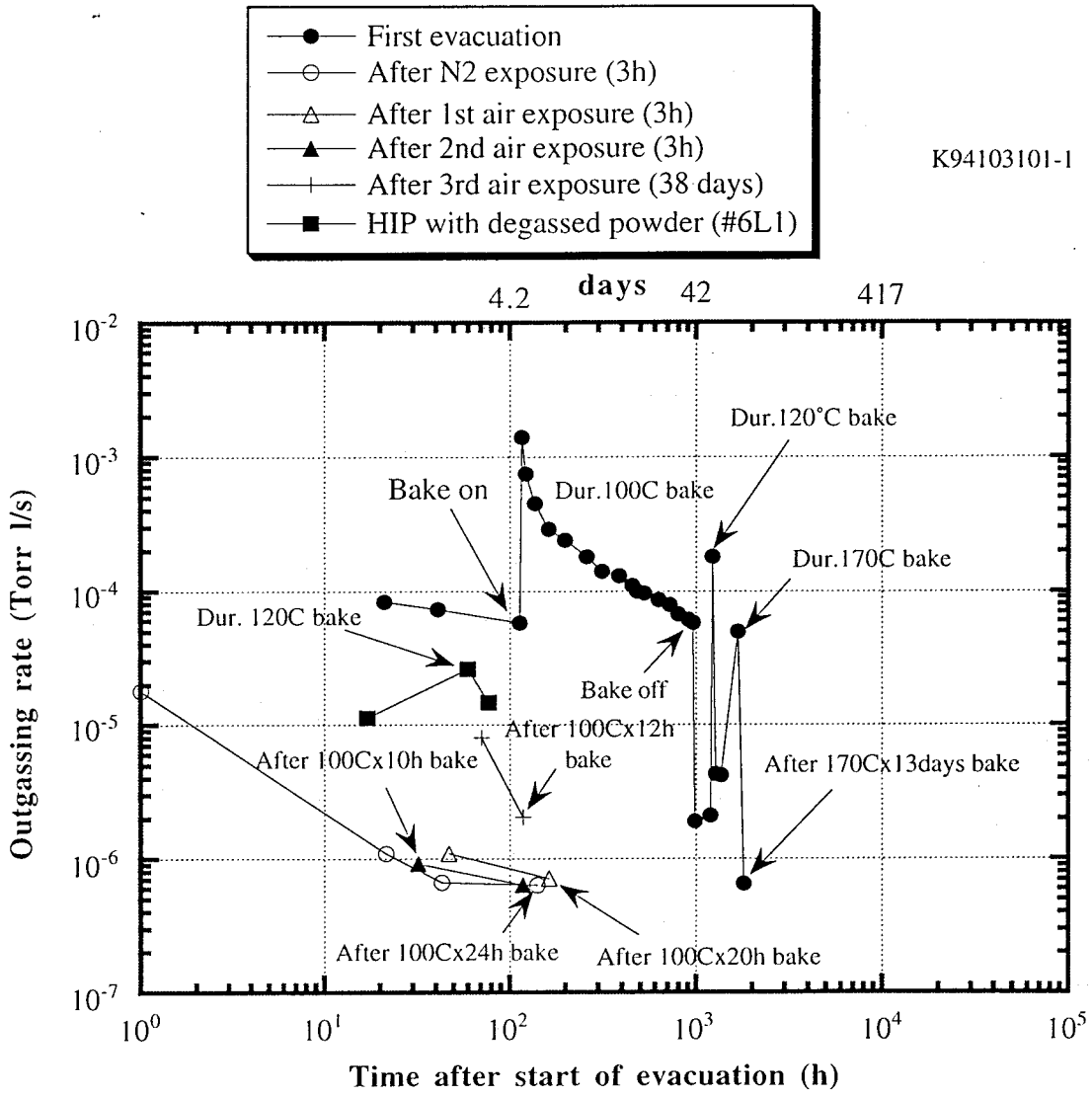

Fig. 8.3-2 : Outgassing rate of full-size absorbers as a function of pumping time. Change of outgassing rate due to exposures to nitrogen gas or air was also studied. In addition, the effect of using degassed powder was checked.

Figure 8.3-3 shows the partial pressures of some gas components that come out during baking. As one can see, the dominant gas is water. Therefore, the main purpose of baking is to remove this water. Other gases are CO, CO_2 and H_2. It should be noted that the decreasing rate of H_2 is much slower than other gases.

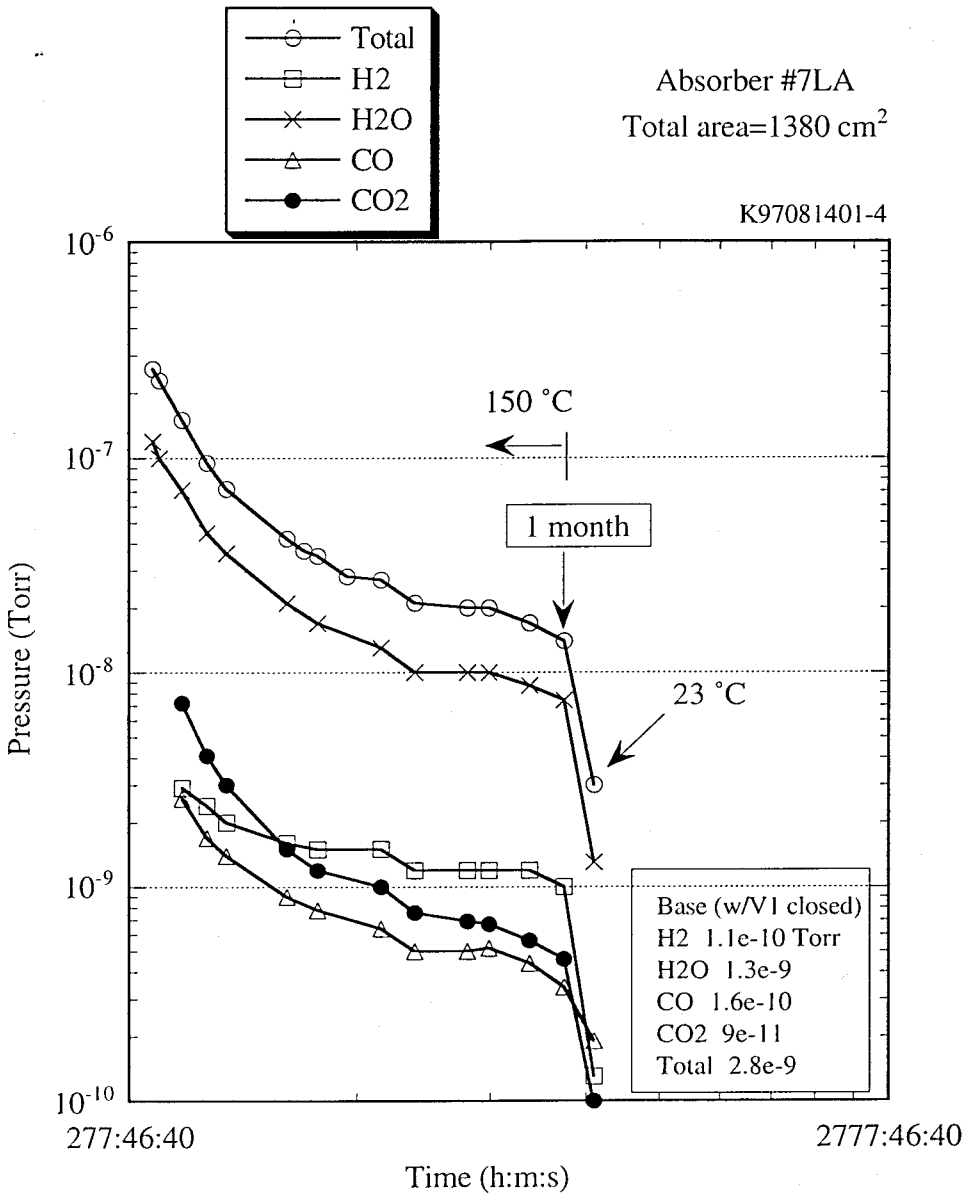

Fig. 8.3-3: Evolution of partial pressures of typical gases during baking.

Figure 8.3-4 shows the improvement of the outgassing rate after longer baking. As we learned, at the TRISTAN AR beam tests, the condensed gases on the surface of the cavity or coupler can cause trips and the amount of gases that enter the cavity should be as small as possible. We decided to bake each absorber for about one month at 150 °C. All the absorbers installed in the Nikko D11 tunnel at KEKB HER were baked in this manner. Solid circles in Fig. 8.3-4 depict the outgassing rate after 150 °C x 1-month baking.

From here, we will discuss the outgassing rate using this improved version.

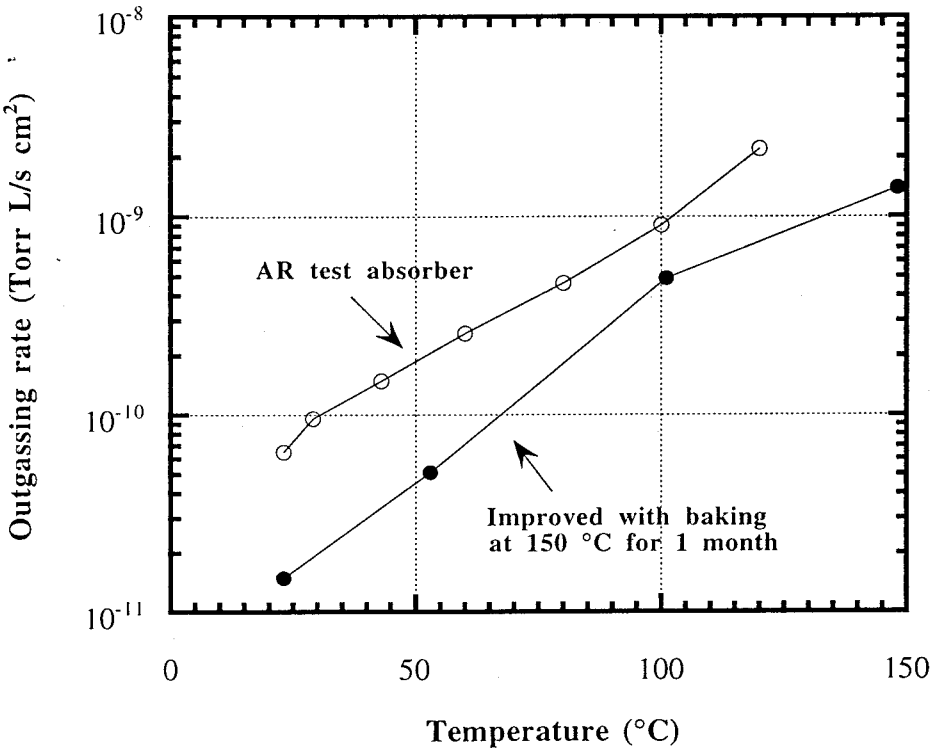

Fig. 8.3-4: Reduction of outgassing rate by baking at 150 °C for one month.

Figure 8.3-5 is the prediction of the average surface temperature as a function of total power dissipated in the ferrite, where the ratio of absorbed power at LBP and SBP is assumed to be 10:7, which was measured at previous beam tests.

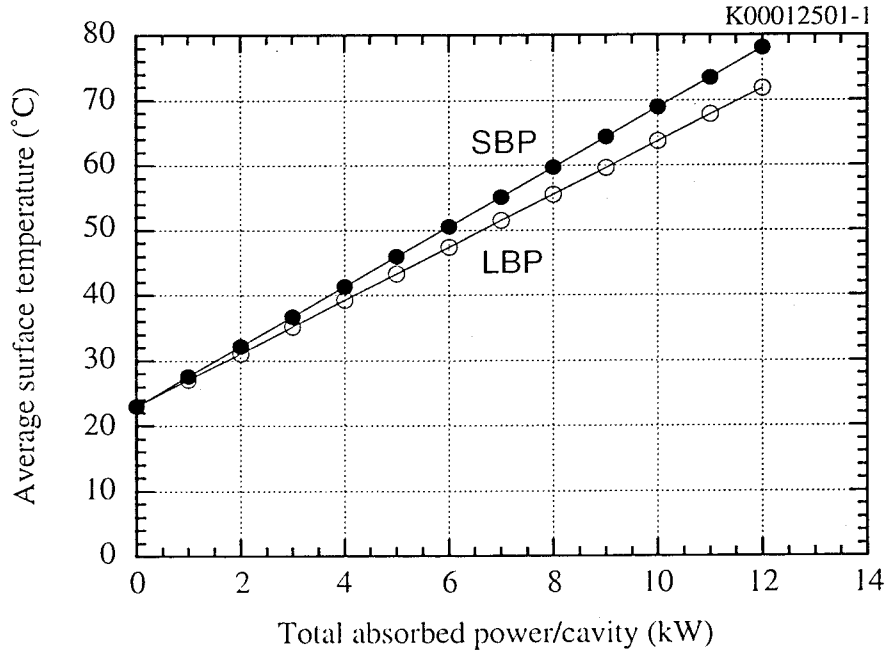

Fig. 8.3-5: Prediction of average surface temperature on SBP and LBP as a function of total absorbed power.

Here, for simplicity, it was assumed that the power is distributed uniformly on the ferrite surface, i.e. power density is obtained by dividing the total power by the total area of the

absorber. For example, at 6 kW, the average surface temperature is 51 °C and 48 °C for SBP and LBP, respectively, assuming that the inlet temperature of the cooling water is 23 °C.

Figure 8.3-6 is a prediction of the outgassing rate as a function of total absorbed power. One can see that the outgassing rate at 6 kW is about 9 x 10^{-8} Torr·L/s. Figure 8.3-7 is a prediction of the total amount of outgases from the absorbers after 3 months of continuous operation at a given absorbed power.

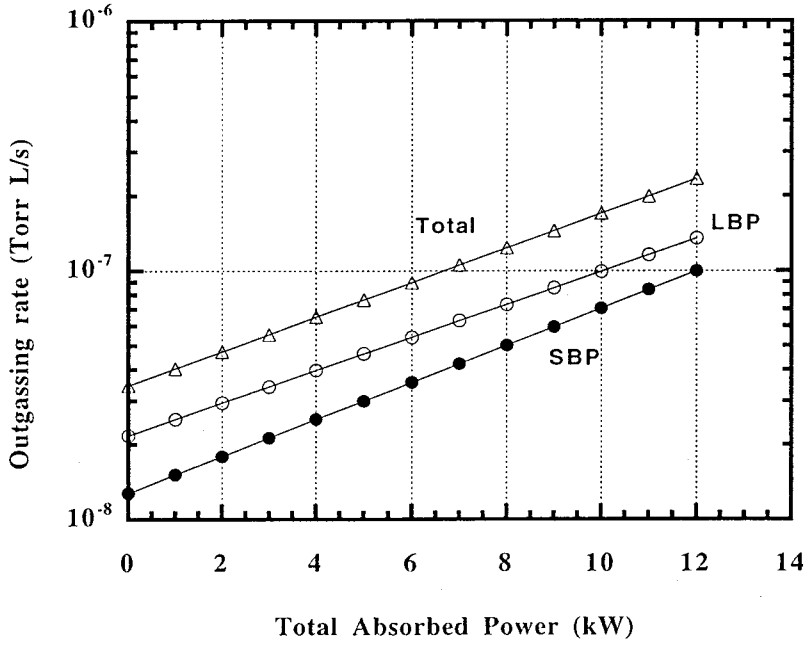

Fig. 8.3-6: Prediction of outgassing rate as a function of total absorbed power.

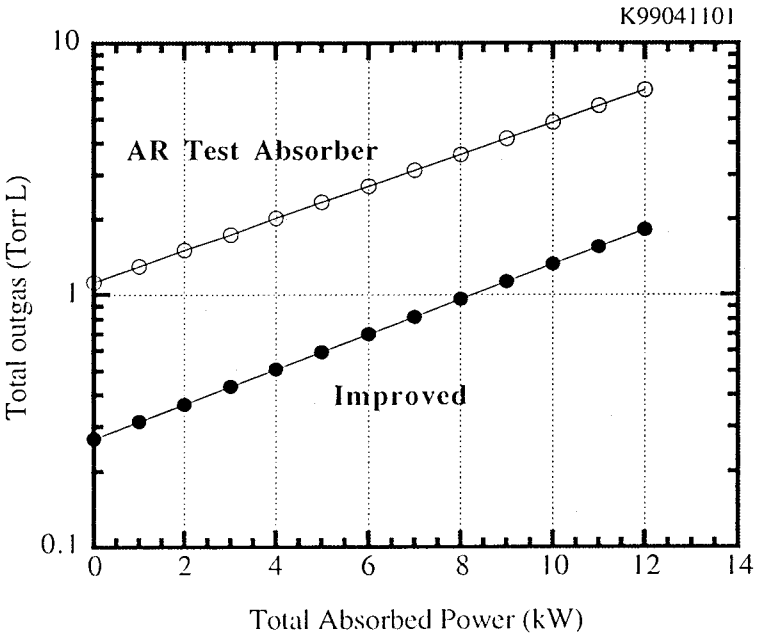

Fig. 8.3-7: Prediction of total amount of outgas from absorbers after 3 months of operation. "Improved" means thoses baked at 150 °C for one month.

It will amount to 0.7 Torr·L if the absorbed power is kept 6 kW in total, assuming that the source of the outgas is chiefly the HOM absorbers and that the other parts are negligibly small. With this value, no trips will probably occur according to our experience.

Since we still do not know the threshold of the total outgas in terms of trips yet, we have been measuring during each warm-up the total amount of outgas that was condensed on the cavity surface.

8.4 Loss factor of the absorber

Loss factor is the energy lost when a unit charge goes through a structure. To know this is important to estimate the power generated in the structure of interest and the power absorbed in the absorbers. Unfortunately, there have been no computer codes to calculate the loss factor of the structure that includes lossy materials. However, since superposition of the loss factors of the structure without lossy material and that of the lossy material alone are the same as the one for a structure with a lossy material, the total loss factor was calculated as the sum of the two.

We used a computer code ABCI to calculate the loss factor of the structure (cavity, dummy pipe and tapers) [14]. As for the absorbers, an analytic code developed by Akasaka for cylindrical absorbing materials attached inside of the metal was used [68].

To check if the analytical calculation gives a correct loss factor, the loss factor of an absorber was measured experimentally by a wire method, so-called synthetic pulse method [52]. Three mm-diam. inner conductor was set on the central axis and the loss factor was calculated using a network analyzer by comparing the inversely Fourier transformed S_{21} data of the pipes with and without an absorber.

Figure 8.4-1 shows the measured loss factor of SBP as a function of bunch length together with the results from the analytic calculation. The measured data for the bunch length shorter than 11 mm is not accurate due to a strong reflection for the frequencies corresponding to this data.

To check the effect of the diameter of the center conductor, we changed the diameter of the center conductor to 30 mm. As shown in the figure, with smaller diameter center conductor, the measured loss factor gets closer to the analytic calculation.

In the real situation, where there is no center conductor, the bunch size is much smaller than this and the loss factor will probably get close to the value obtained analytically.

Considering these facts, we concluded that the analytical calculation can give an accurate loss

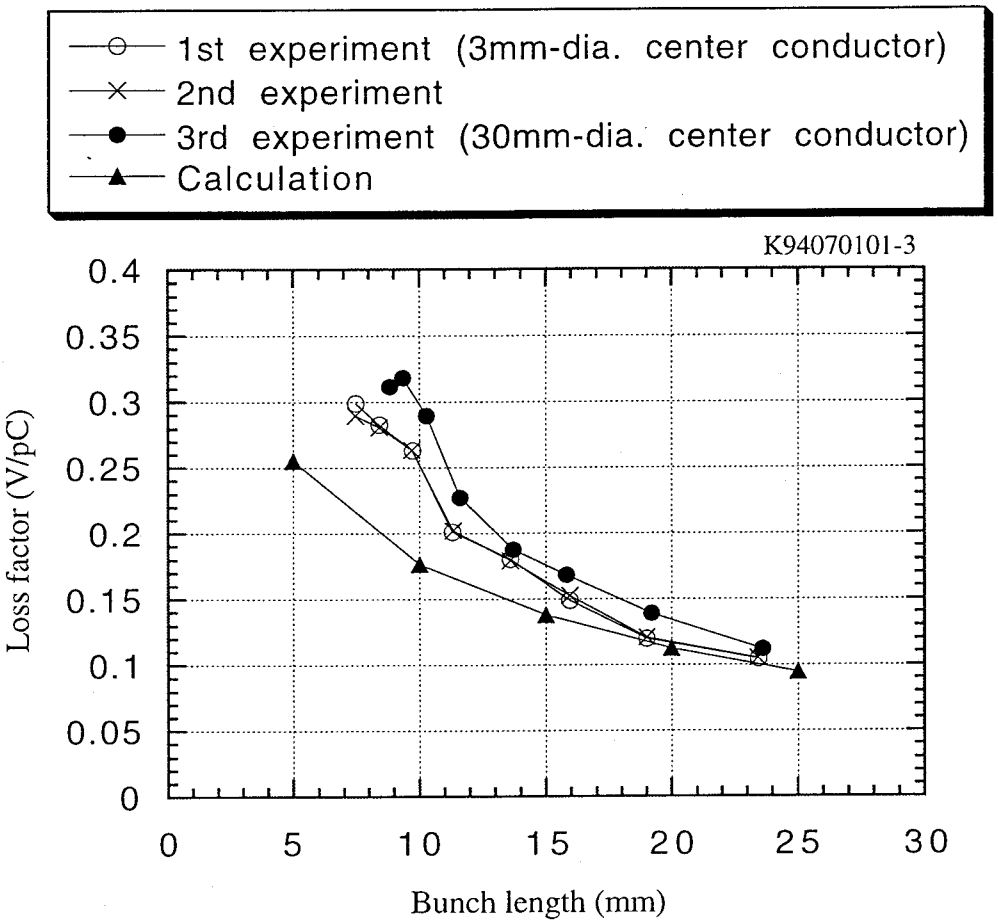

Fig. 8.4-1: Loss factor of SBP (ferrite o.d. = 220 mm, length = 120 mm, thickness = 4 mm).

factor and we have been using the analytic calculation for the estimations since then. Loss factors of SBP and LBP are 0.3 V/pC each and 0.6 V/pC in total at 4 mm.

8.5 High power tests

We tested the full-size absorbers with 508 MHz coaxial line because we had the available Klystrons that were used for TRISTAN, which can provide up to a few 100 kW. End cones to connect an absorber with the existing coaxial line flanges were made. Also, tapered inner conductors for both SBP and LBP were made so that the impedance matched along the line. The schematic drawing of the matched coaxial line is shown in Fig. 8.5-1. Figure 8.5-2 shows the block diagram of the measurement.

The absorber was cooled with water at 5 L/min. The absorbed power was measured by the temperature increase of the cooling water as well as the RF power measurements. Forward and reflected RF power at the entrance and exit of the absorber were measured by power

meters through pick-ups of about 30 dB, then the absorbed power was calculated as a subtraction of the power that exited through the absorber from that that entered.

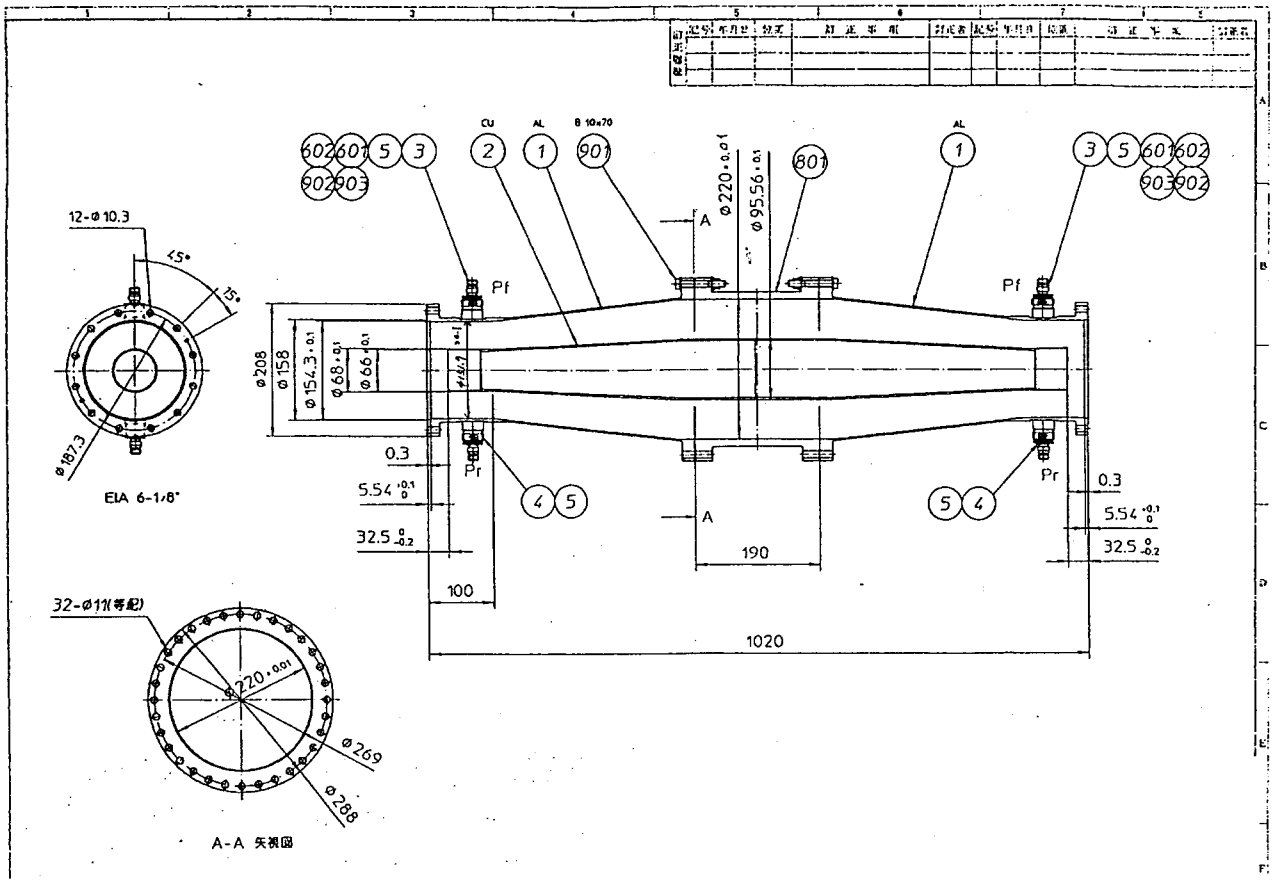

Fig. 8.5-1: A drawing of the high power test set up for 508 MHz coaxial line. (SBP) Unit: mm.

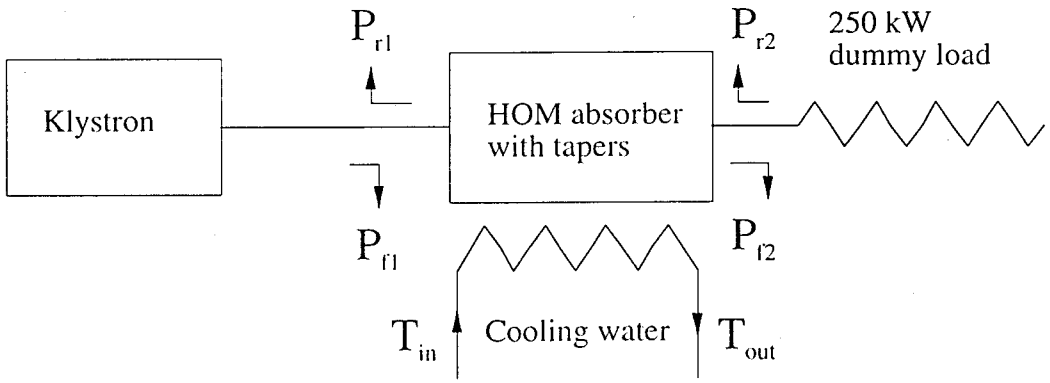

Fig. 8.5-2: A block diagram of the high power test.

Figure 8.5-3 shows the test set up. Figure 8.5-4 shows the absorption, reflection and transmission rates as a function of the power absorbed in the ferrite. The measured absorber was SBP (220 mm o.d. x 120 mm x 4 mm thick). The temperature near the front edge was

also plotted in Fig. 8.5-4. The decrease of absorption with increasing input power is probably due to the increase of the ferrite temperature as was shown in Section 4.6.

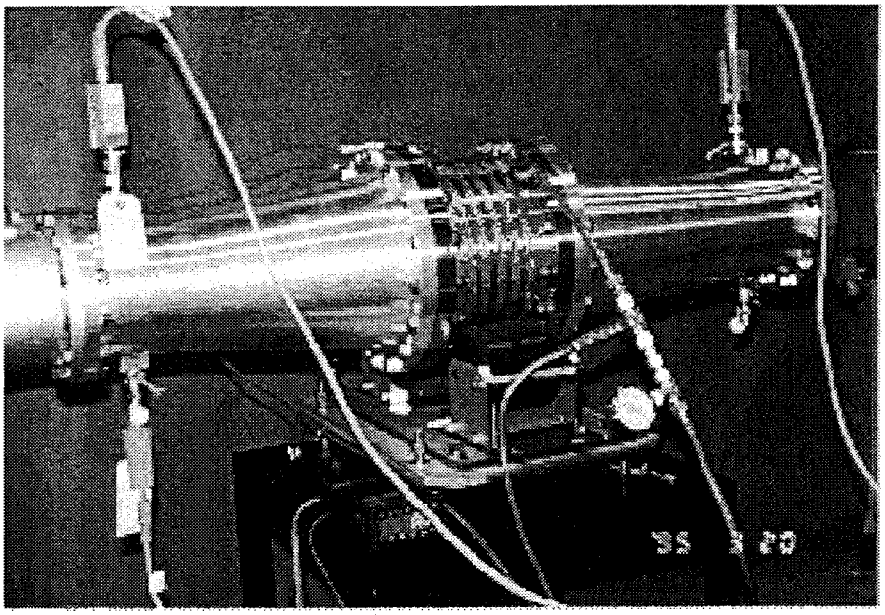

Fig. 8.5-3: The high power test set up using 508 MHz coaxial line.

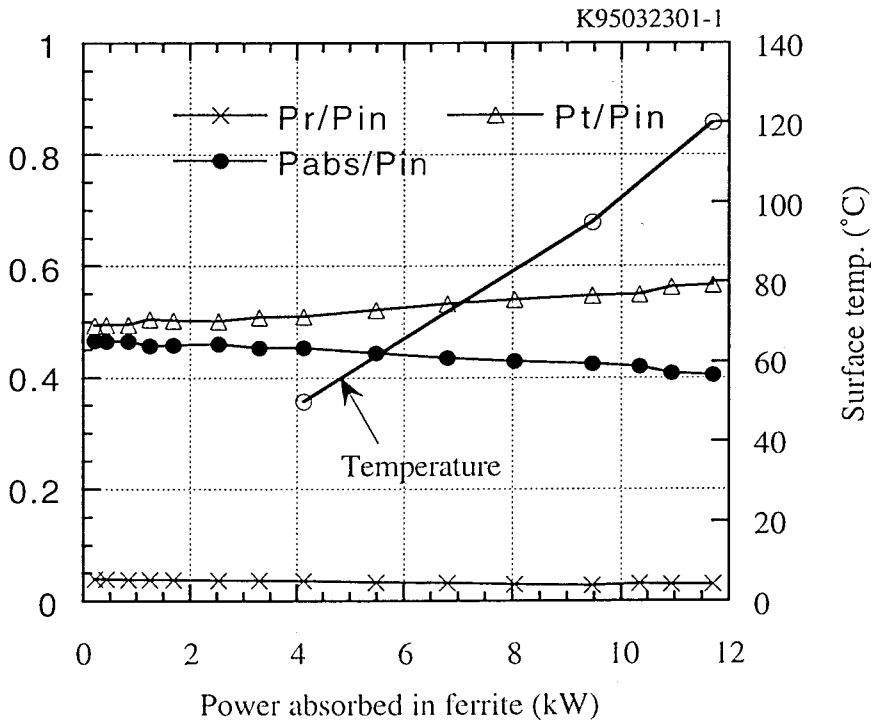

Fig. 8.5-4: Reflection, transmission and absorption rates as a function of absorbed power in the ferrite together with the temperature near the front edge.

Figure 8.5-5 shows how the surface temperature was measured with thermo-labels. Figure 8.5-6 shows the longitudinal profile of the ferrite surface temperature. With the effect of

tapers, the surface profile is nearly flat. Up to a power of 11.7 kW (average power density = 14.6 W/cm^2) was tested, which is about 4 times that expected at KEKB HER. LBP was also tested up to 14.8kW (average power density = 10.8 W/cm^2) [8].

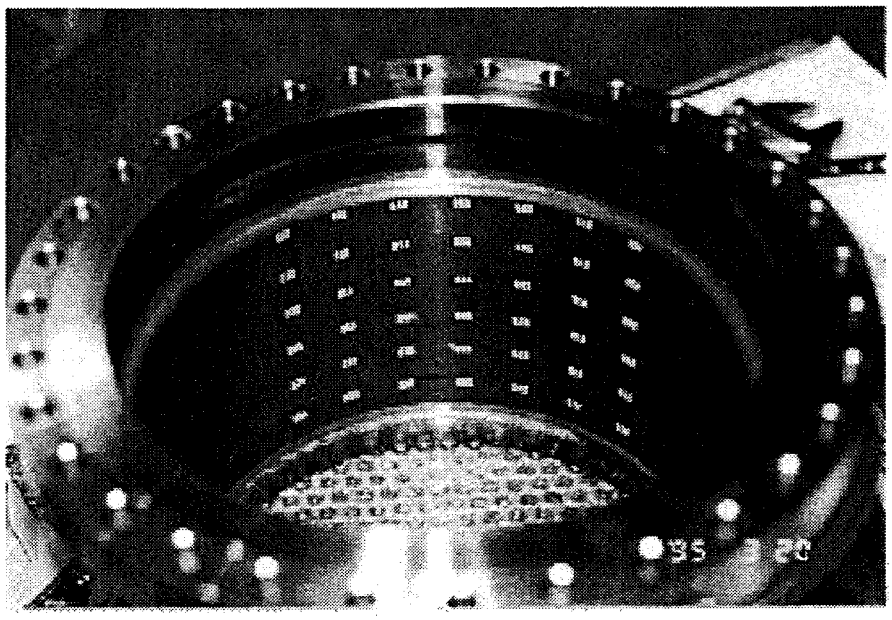

Fig. 8.5-5: Thermo-labels glued on the ferrite surface.

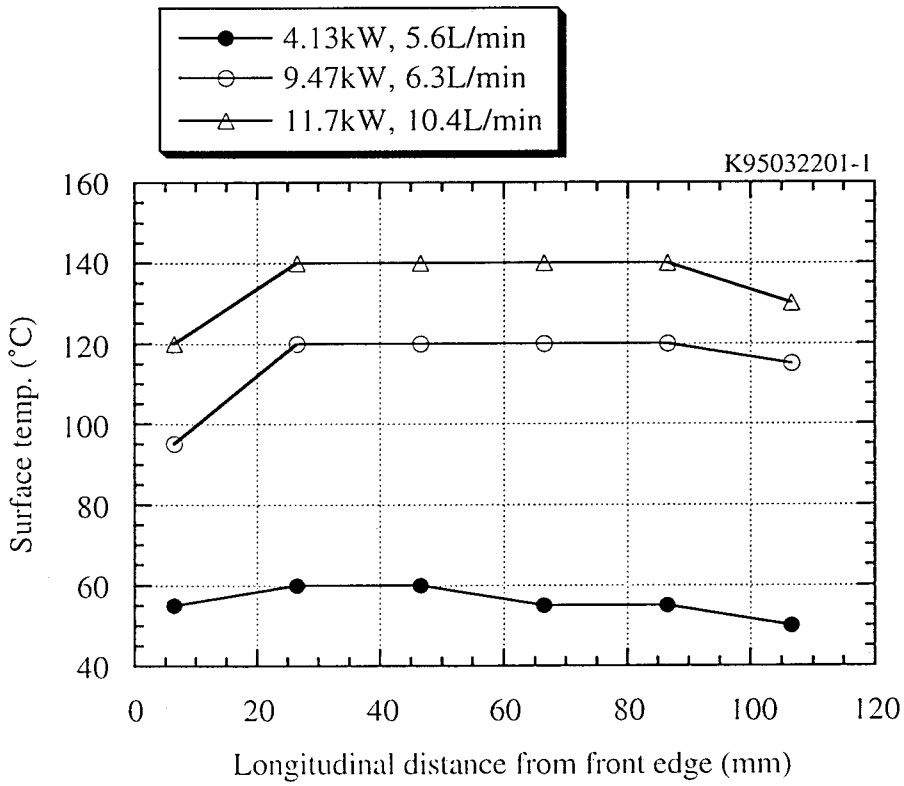

Fig. 8.5-6: Longitudinal temperature profile on the ferrite surface.

8.6 Summary

We discussed the tests using full-size absorbers. Results are summarized as follows.

1) HOM damping was checked with an aluminum model. Loaded Q was measured and compared with the results obtained with CLANS and CLANS2. The modes with low Q's agreed well, but those with high Q's showed much lower value, probably an influence from the external Q of the coupler. Qualitatively, many modes were identified.

2) HOM impedances were calculated and showed lower than the threshold of longitudinal instabilities.

3) We measured the outgassing rate from the absorber. We found that the outgassing rate from a full-size absorber was about one order of magnitude higher than the standard ferrite tile. This was because of insufficient degassing of water that was adsorbed on the powder surface before packing for HIPping. To improve this situation, we tried to degas the powder before packing in an N_2 atmosphere, and then the outgassing rate became comparable with that of standard tiles.

4) We tested the effect of venting N_2 gas and air on the outgassing rate after baking. We found that the reduced outgassing rate lasts for a long time and there was no practical degradation of vacuum after being vented for assembly with other parts of SCC.

5) We showed that we could reduce the outgassing rate of the absorber to a sufficiently low level by baking at 150 °C for about one month (or its equivalent).

6) The loss factor of a full-size absorber was measured with the synthetic pulse method and was compared with an analytical calculation. They agreed well at longer bunch lengths. Although the measured loss factor was higher at shorter bunch lengths, since the measurement accuracy gets lower as the bunch length gets shorter, we concluded that analytical results are more accurate, taking into account the effect of center wire as well.

7) High power tests were performed with 508 MHz coaxial line. The ferrite surface temperature was monitored with thermo-labels. SBP and LBP were tested up to a power of 11.7 kW (average power density = 14.6 W/cm^2) and 14.8 kW (average power density = 10.8 W/cm^2), respectively, which is about 4 times that expected at KEKB HER. We normally test SBP and LBP up to 5 kW and 7 kW on a regular basis. There have been no problems with these powers.

Chapter 9

Beam Tests in Accelerators

9.1 Introduction

Since there had been no experience with this type of absorber in accelerators, as a final stage of the tests to check its performance, we installed a full-size absorber in TRISTAN MR (Main Ring) and beam tested in 1995 [13]. The main objective of this test was to know if there was any problem we had not considered.

The final tests were conducted with a SCC module in TRISTAN AR (Accumulation Ring) in 1996. Needless to say, the main objective of this test was to check the feasibility of the whole module equipped with a high power coupler and HOM absorbers. In these tests, a full-size SBP and a full-size LBP were installed with the SCC.

In the following sections, these beam tests are described.

9.2 Test at TRISTAN Main Ring [13]

9.2.1 Instrumentation

Figure 9.2.1-1 depicts the dimensions of the assembled chamber for the beam test of an LBP (300 mm o.d. , 150 mm long, and 4 mm thick). The diameter of the end gate valves was 100 mm. RGA (Residual Gas Analyzer) was set at one of the ports near the ion pump.

Figures 9.2.1-2 and 9.2.1-3 are of the chamber installed at the Nikko colliding point and that after the beam test at an assembly area, respectively. As shown in the picture, RF pick-up ports were made on the adjacent pipe and end cones to check HOM's.

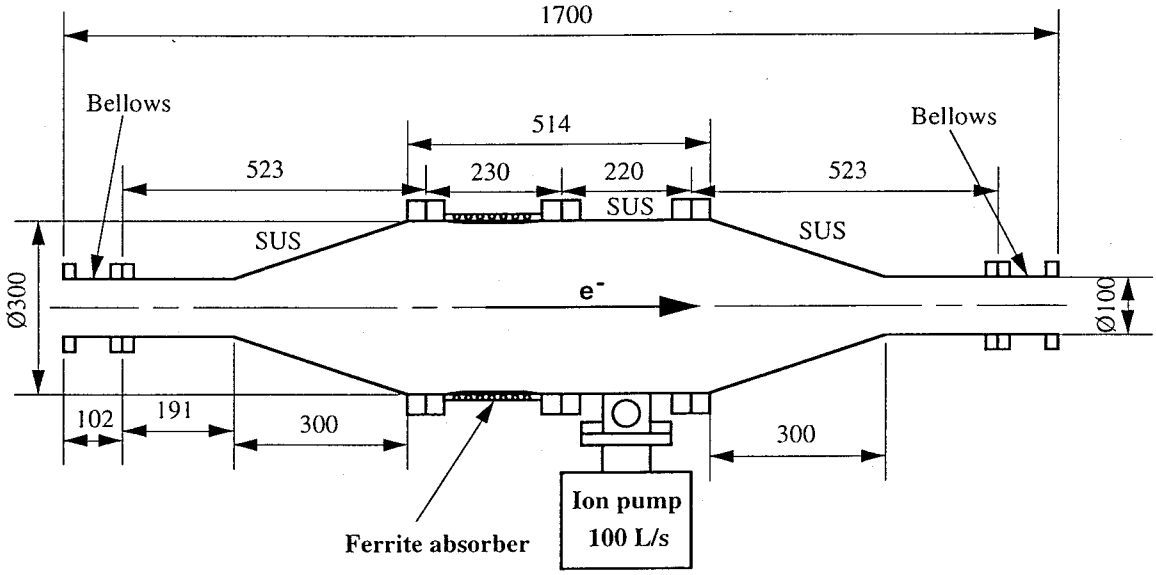

Fig. 9.2.1-1: Set up of the chamber to test the ferrite absorber at TRISTAN MR. Size of the absorber is the same as LBP of KEKB-SCC.

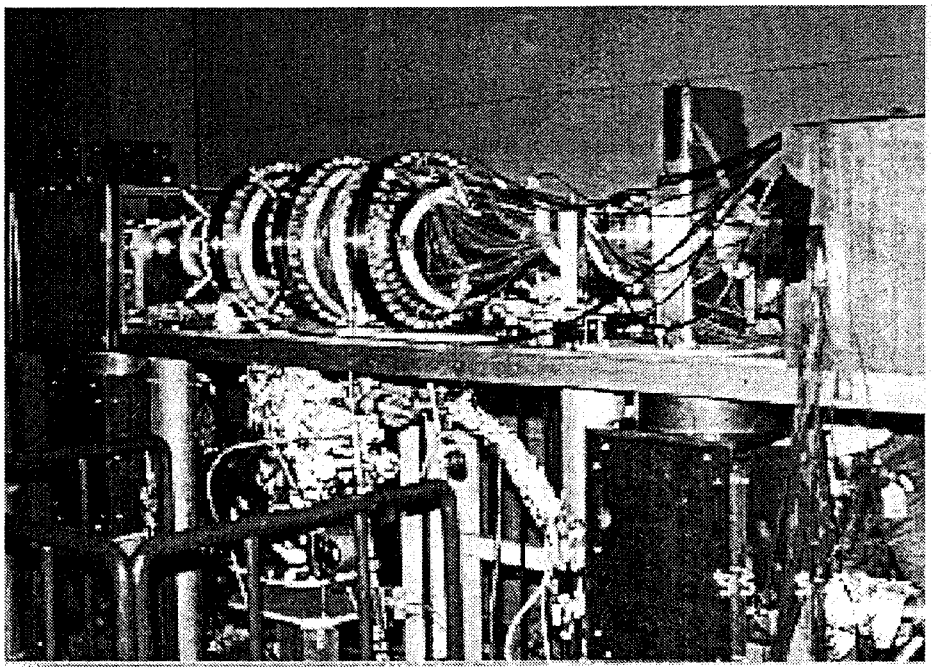

S99040808

Fig. 9.2.1-2: The experimental set up after installed in the Nikko tunnel.

S99040809

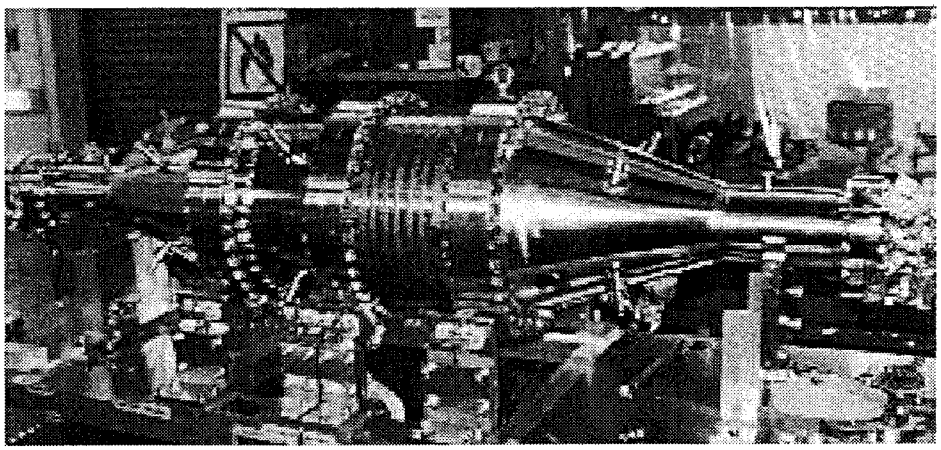

Fig. 9.2.1-3: The absorber and chambers after the tests and while being transported to an assembly area.

9.2.2 Absorbed power

Absorbed power was measured by using the temperature increase of cooling water and its flow rate. The maximum absorbed power in the ferrite was 273 W.

9.2.3 Loss factor

The loss factor was calculated with the formula below [13].

$$k\,[\mathrm{V/pC}] = \frac{P_{loss}[\mathrm{W}] \cdot N_b \cdot f_r[\mathrm{kHz}]}{\{I_b[\mathrm{mA}]\}^2} \times 10^{-3} = \frac{P_{loss}[\mathrm{W}] \cdot N_b}{\{I_b[\mathrm{mA}]\}^2} \times 9.933 \times 10^{-2} \qquad (9.2.3\text{-}1)$$

where,

k : Loss factor

I_b : Beam current

N_b : Number of bunches

f_r : Revolution frequency (99.33 kHz).

Figure 9.2.3-1 shows the loss factor as a function of bunch length. Here the bunch length was measured with a streak camera for reasons to be discussed below. In Fig. 9.2.3-1, the solid lines are the predictions. The lines designated as "structure" are the results from the calculation with ABCI, and "ferrite" calculated analytically. In the figure, the contribution of the power whose frequency is lower than 2.3 GHz, which is the cut-off frequency of TM01

mode of the beam pipe with 100 mm in diameter.

From the results, the power absorbed was much more than the power predicted for f<cut-off, and close to the value with all the frequencies.

As one can see, the measured loss factor increased with shorter bunches and it was about 40 % higher than the predicted value at a bunch length of 4 mm. On the other hand, it was lower for longer bunch lengths.

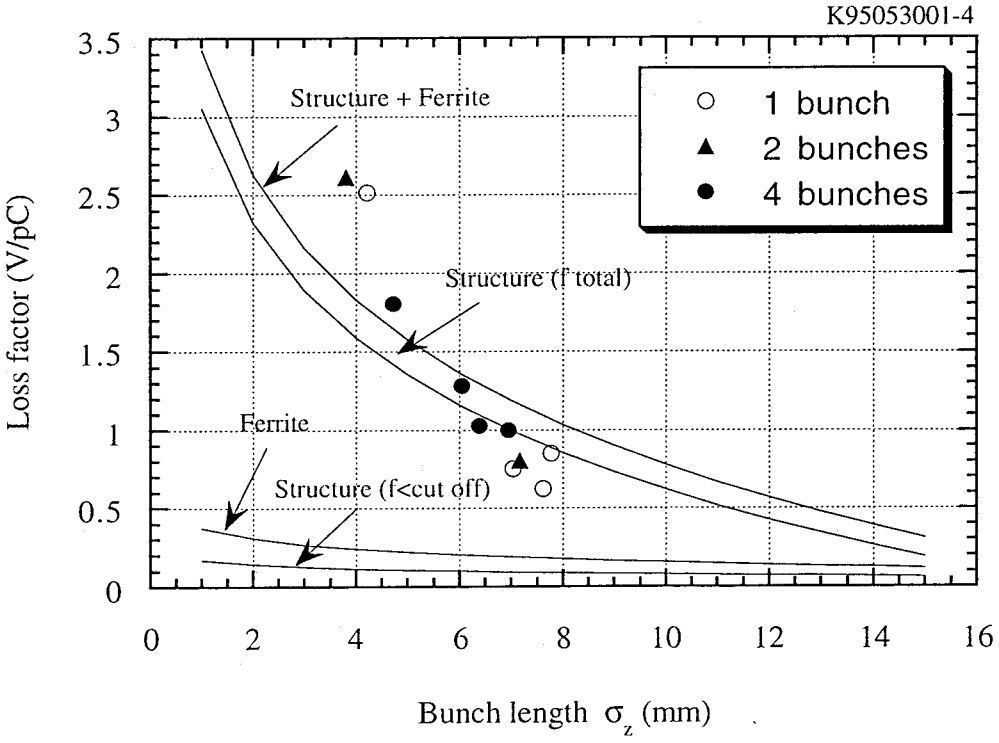

Fig. 9.2.3-1: The loss factor as a function of bunch length. Solid lines show results from the calculations with ABCI and analytical calculations for ferrite.

To check the accuracy of the bunch length measurement, the longitudinal profiles of the bunches were examined since the bunch length was calculated from full-width at half maximum (FWHM), i.e. bunch length = FWHM/2.35, whereas the ABCI calculation assumed a Gaussian shape.

Figure 9.2.3-2 shows the longitudinal bunch profiles together with the gaussian profiles that have the same bunch lengths. As one can see, there is a tendency that, as a bunch gets shorter the tail gets shorter, and sometimes the width of the bunch becomes narrower than the Gaussian profile near the top. This suggests that there are higher frequency components for shorter bunches and lower frequency components for the longer bunches compared to the Gaussian bunches, which might have caused the difference between the measurements and

predictions.

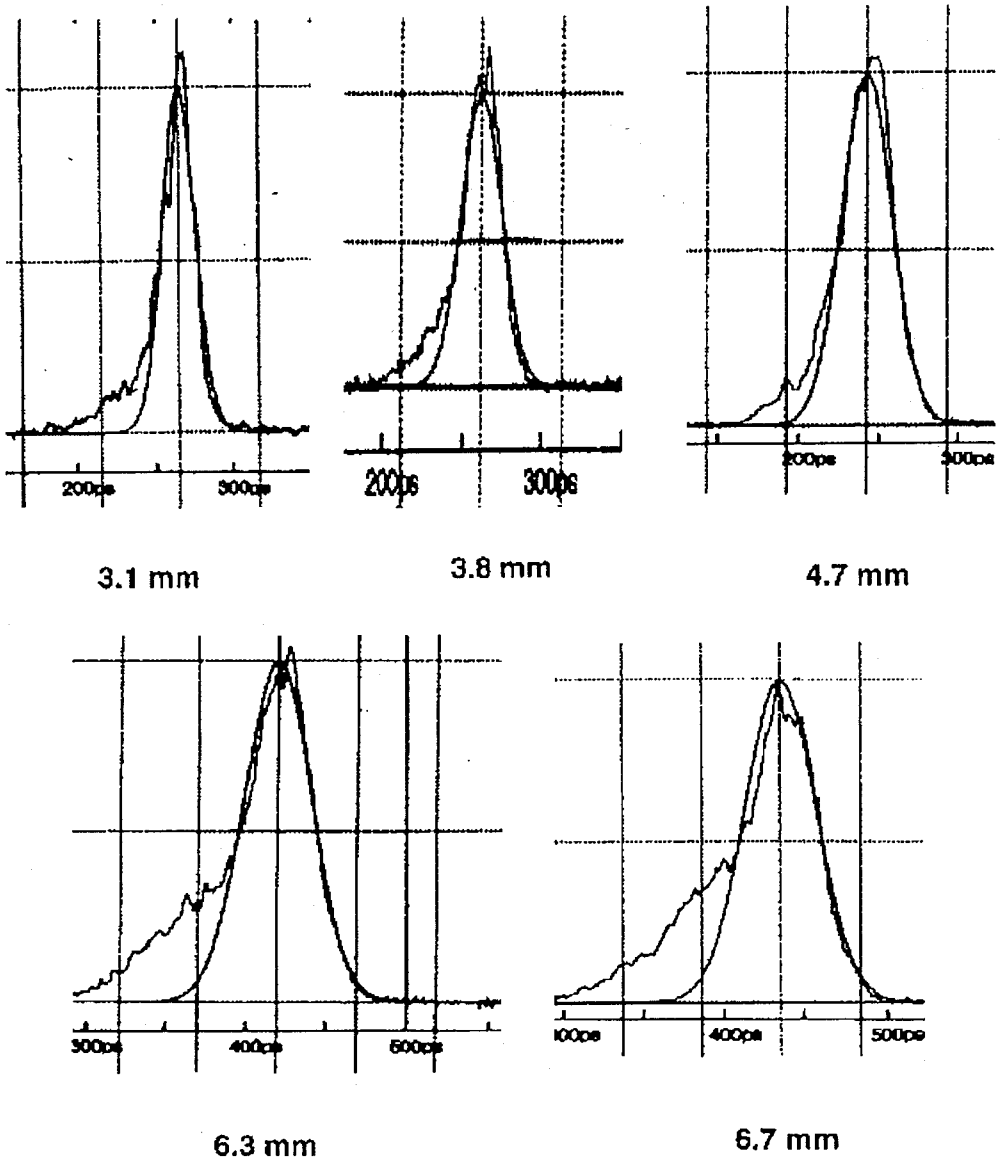

Fig. 9.2.3-2: Real longitudinal bunch shapes compared with Gaussian bunches. Real shapes were recorded with a streak camera.

Another unknown factor about the loss at the absorber is how much of the power generated in the chamber was absorbed at the absorber as well as how much of the power that entered the chamber got absorbed at the absorber.

If the effect of a bunch shape is negligible, the insight that can be drawn from the result is that, at a bunch length shorter than approximately 5 mm, the power entering the chamber increases rapidly. This, however, will probably depend largely on the shape of other components outside of the chamber, such as bellows. Since we did not know the details outside of the chamber, further consideration with regard to this assumption was not possible.

9.2.4 Mode measurements

The signals picked up through the antenna at tapers and extension beam pipe were analyzed with a spectrum analyzer. We searched excited modes up to 6.5 GHz. The maximum signal was obtained at 2.405 GHz and it was identified as a monopole mode using URMEL, but there was a discrepancy on the Q value between the calculation with SEAFISH (87 at 2.412 GHz) and measurement (~1000 at 2.405 GHz).

Horizontal displacement of the beam orbit up to 10 mm did not show visible change in the RF signals.

9.2.5 Outgas

Before installation in the tunnel, the outgas rate per unit area of this absorber was measured to be 1 x 10^{-10} Torr L/s cm^2 at room temperature after baking at 120 °C for 5 days. When installing in the tunnel, it was vented with filtered N_2 gas. It took about 11 hours to reach 3 x 10^{-8} Torr, which was much faster than the initial pumping, confirming the fact that the time to pump down after being exposed to air gets much shorter, once it has been baked as discussed in Section 8.3.

1) Vacuum

Before the first beam test, it was baked at 100 °C for 6 hours, and the pressure went down to 5.7 x 10^{-9} Torr at ~28 °C. Figure 9.2.5-1 shows the pressure as a function of the absorbed power at the ferrite. The legend is written from top to bottom chronologically. There was a whole day (24 hrs) without a beam between the 1st and 2nd tests in the legend. "Off center" means horizontal shift of the beam orbit from the beam axis in the absorber. The positive sign is the outward shift and negative the inward.

As shown in the figure, at the 2nd test, the pressure was lower at the same power, which indicates that the pressure tends to decrease due to the degassing effect of the beam.

As one can see, when the beam was shifted horizontally to +/- 10 mm off center, the pressure increased significantly, compared to the centered beam. Analyzing the data on the temperature distribution showed that this pressure increase was probably due to the photo desorption and associated temperature rise at the tapers with the X-ray irradiation. Moreover, it was observed that the temperature at the tapers increased with the current and became higher than that of the absorber, which must have contributed to the pressure rise. Based on this experiment, we installed cooling pipes on tapers from then on.

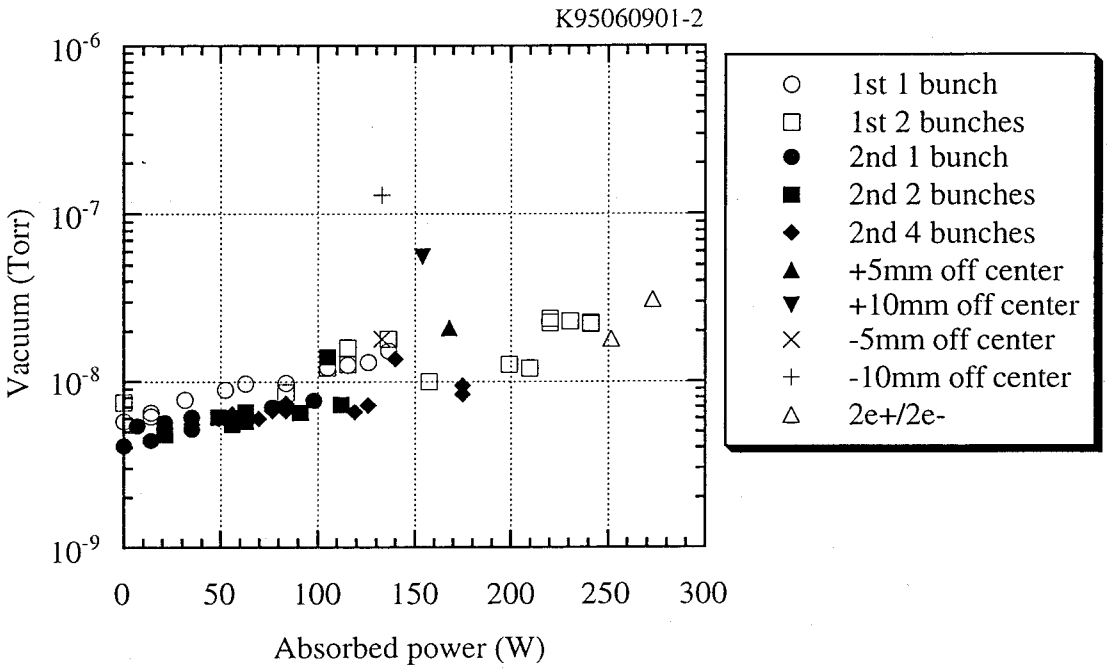

Fig. 9.2.5-1: Vacuum as a function of absorbed power in the absorber with various beam conditions.

2) Components of outgas

The major gas components before running the beam was H_2O (28%), H_2 (27%) and CO (23%). With the first beam running, when the pressure increased, the increased gases were H_2 and CO. For example, when the pressure increased to 3.2 x 10^{-8} Torr at 3.8 mA, the gas consisted of H_2 (40%), H_2O (17%) and CO (17%), indicating the outgas was from the SUS chamber, not from the absorber.

When the orbit was shifted horizontally outward by 10 mm, desorption of H_2 and CO were enhanced, i.e. H_2 (51%), CO (27%) and H_2O (6%). As discussed above, this seems to be the gas components when the taper, made of stainless steel (SUS304), was irradiated by X-ray.

Since the maximum absorbed power in the ferrite was only 273 W, the average ferrite surface temperature was probably lower than 35 °C. Therefore the outgas from the absorber did not seem to have contributed to the pressure rise much.

On reflection, the major gases during baking at 120 °C in the previous bench test were H_2, H_2O, CO and CO_2.

9.3 Tests at TRISTAN AR (Accumulation Ring)

In 1996, there were three periods when we could test a fully equipped SCC module with full-size HOM absorbers on up-stream (LBP) and down-stream (SBP) of the electron beams. In the following subsections, instrumentation and results will be described, putting emphasis on the HOM absorbers.

9.3.1 Instrumentation [6]

Figure 9.3.1-1 shows a schematic view of the cavity module installed in TRISTAN AR. The only difference from KEKB-HER design is that it has shorter end tapers and smaller diameter gate valves, i.e. at AR the diameter was 100 mm, whereas at KEKB it was enlarged to 150 mm. This modification was made to reduce the loss factor of the structure, thereby reducing the power load to the absorbers, which will be discussed in Section 9.3.3. [4]

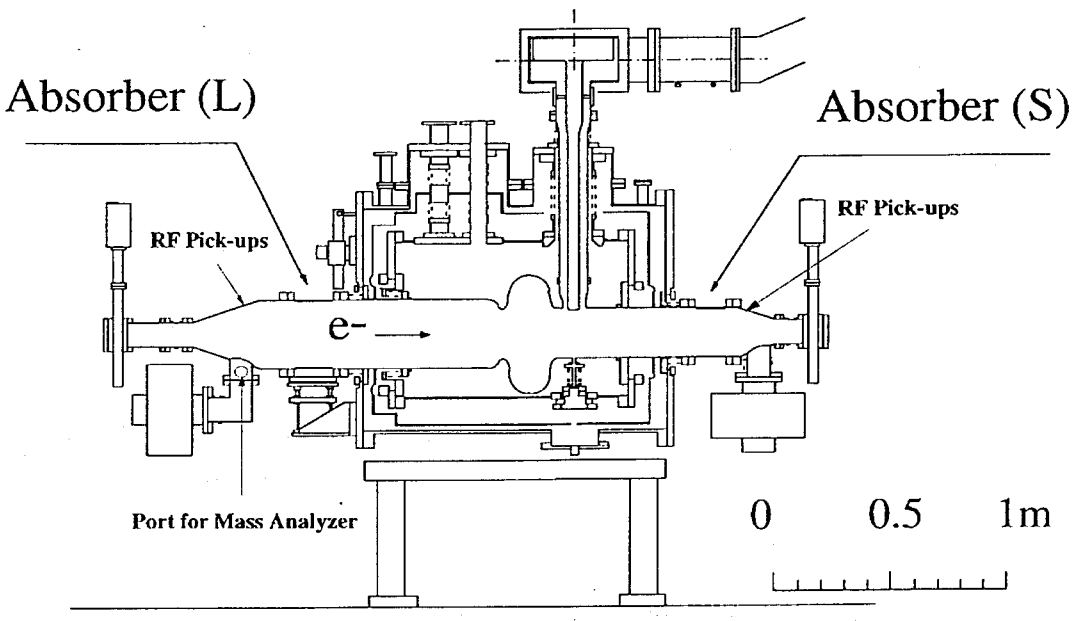

Fig. 9.3.1-1: Schematic of the cavity module installed in TRISTAN AR (Accumulation Ring).

This module consists of a SCC, a cryostat, an input coupler, two HOM absorbers, two tapers with ducts and ports for gauges, two 270 L/s ion pumps and two gate valves.

3) Assembly of Absorbers

Absorbers were degreased and rinsed with ethanol using a closed system with ultrasonic agitation. Then they were assembled with tapers, bellows and gate valves. Before assembling with the SCC, the two absorbers were pre-assembled and baked at about 120 °C for a few days. Finally, after being vented with filtered pure nitrogen gas, they were attached to the SCC in a clean hut of class ~1000.

4) Installation of sensors

Two cold cathode gauges were set on both the up-stream and down-stream tapers. To analyze the gas species, an RGA was set on the duct attached to the up-stream taper. Two rows of 8 circumferencially distributed thermo-couples were taped on the outer surface of the absorbers. Moreover, two sets of Pt thermometers were inserted in the inlet and outlet water of the copper cooling pipes as well as a digital flow rate meter for precise calorimetric measurements of absorbed power. Also, three RF pick-up antennas were set at 0, 45 and 90 degrees from the top of each taper.

5) Software

The software consisted of a GP-IB based data acquisition system operated with a software named LabView. A total of about 130 data was taken and stored in a MO (Magneto-Optical device) every 30 sec. These data were retrieved with another application software named Kaleida Graph for further analyses.

9.3.2 Absorbed power

The maximum power absorbed went up to 4.2 kW in total. Figure 9.3.2-1 shows the typical absorbed power as a function of beam current at accelerating fields (Eacc) = 4.1 and 6.2

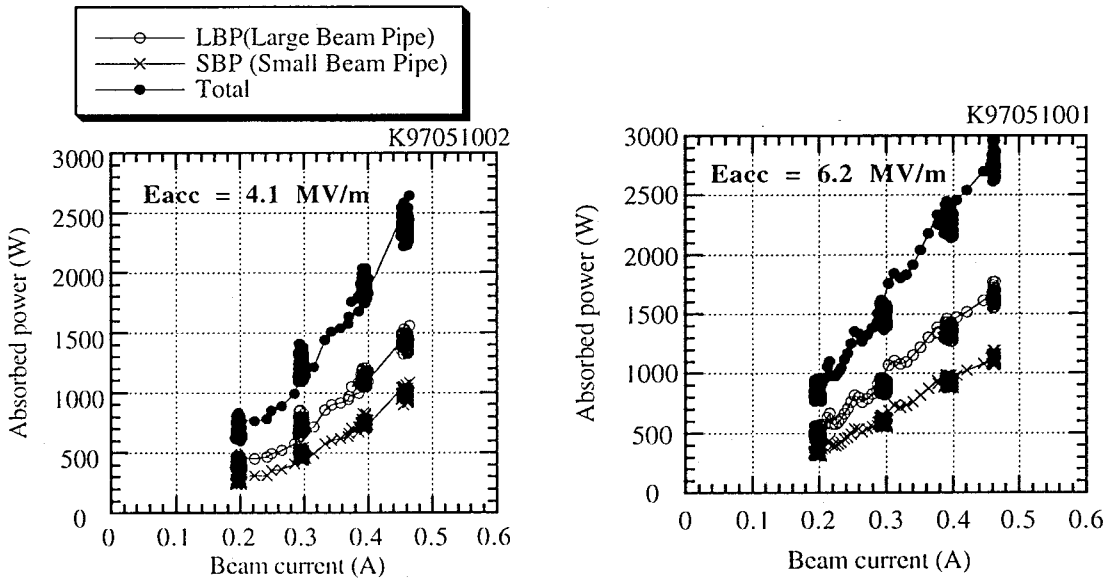

Fig. 9.3.2-1: Absorbed power as a function of beam current at different cavity accelerating fields.

MV/m. The cavity voltage can be obtained by multiplying the gap length of 0.243 m with Eacc. As one can see, the absorbed power did not increase quadratically because the bunch length got elongated with higher currents, resulting in the decrease of the loss factor as shown in the next Section. The uncertainty of the absorbed power was mainly due to the fluctuation

of the inlet water temperature caused by the temperature-regulation system of the cooling unit.

No symptoms of degradation on the absorbers and cavity were observed up to a current of 0.57 A, which was limited by other components of the ring.

9.3.3 Loss factor

The loss factor was measured calorimetrically by calculating the heat transferred to the cooling water. Figure 9.3.3-1 shows the results as a function of the bunch length measured with the Streak camera, together with the prediction calculated with ABCI for the structure without ferrite and analytically for ferrite as described in Section 9.2.3. As shown in Fig. 9.3.3-1, the loss factor was lower than predicted at the bunch length longer than ~4 cm, about the same around 2 cm, and then seems to get higher than predicted when the bunch length gets shorter, except for a group of data around 2.5 cm that is 10-30% lower than predicted for some reason.

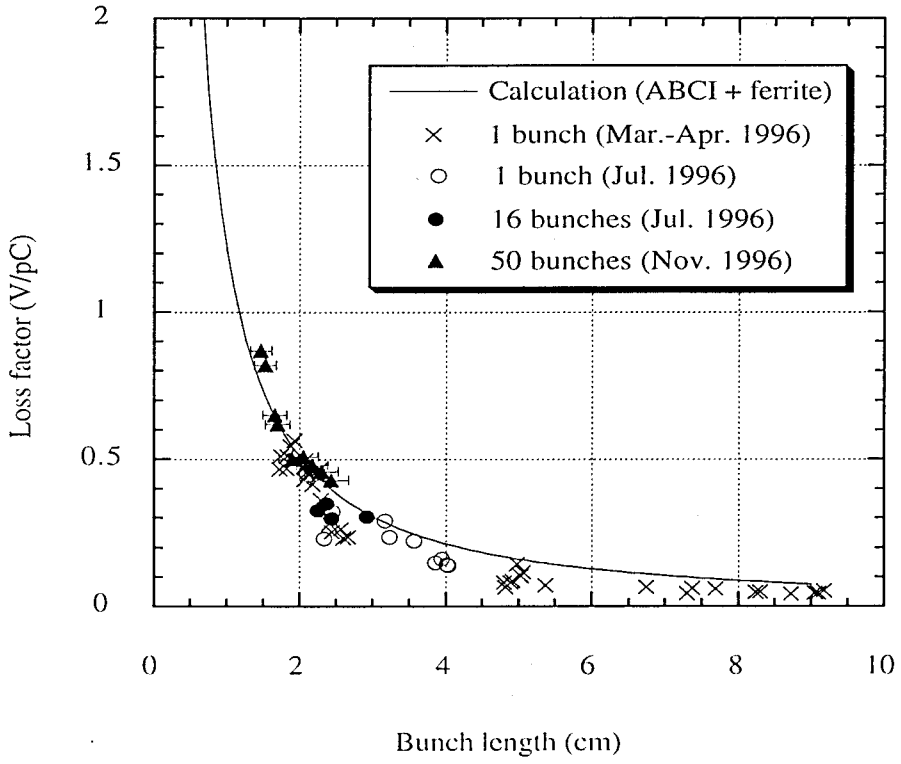

Fig. 9.3.3-1: Loss factor as a function of bunch length. Solid line is the sum of calculation

- Bunch length

Unfortunately, we could not get a bunch length shorter than 1.5 cm that is far from the KEKB design value, 0.4 cm. Figure 9.3.3-2 shows the bunch length measured with a streak camera as a function of total beam current at different cavity voltages. As one can see, bunch lengths became longer with the beam current. Also, increasing cavity voltage did not help to shorten it at shorter bunch lengths. To obtain the bunch lengths as short as possible with absorbed power large enough to measure the loss factor precisely, we used 50 bunches with bunch-by-bunch feedback on.

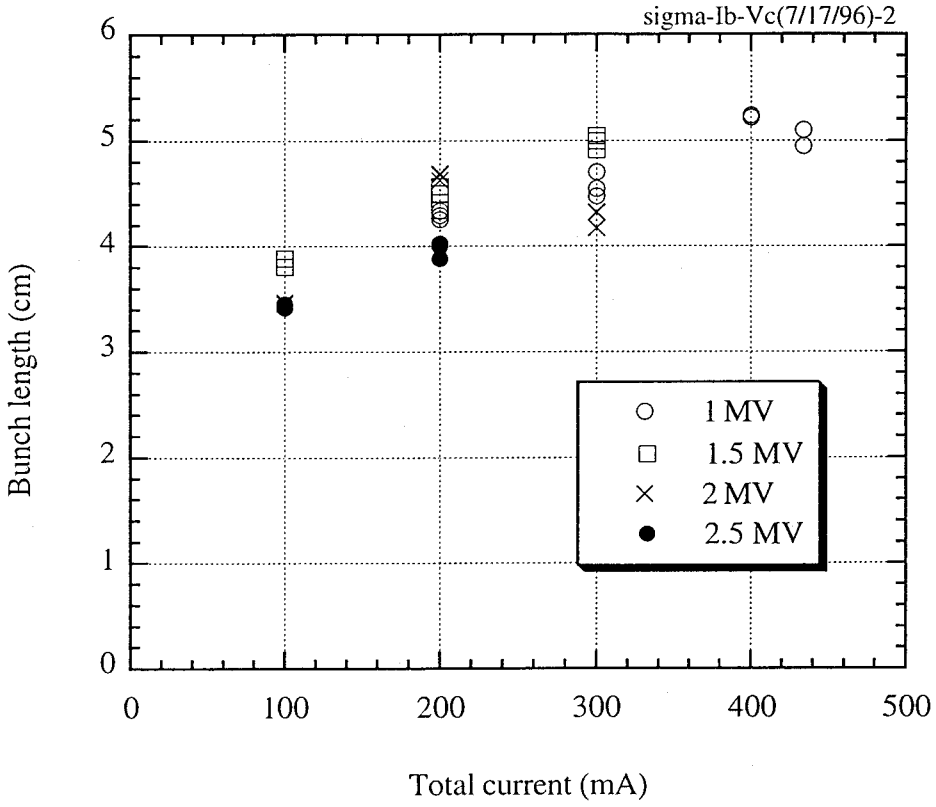

Fig. 9.3.3-2: The bunch length measured with Streak camera as a function of total current and cavity voltage.

Nevertheless, it was confirmed that the loss generated with the broadband impedance of the structure can be absorbed by the damper and the loss measured agrees well with the calculation of bunches shorter than 4 cm.

6) Calculation of loss factor for KEKB module

Based on the results obtained at the AR tests, we could predict the approximate power to be handled at KEKB. If we use the AR-type structure, the loss factor is about 2.9 V/pC and the total power to be handled is about 7 kW plus some narrow band HOM power of 1 - 2 kW, which leads to 8 - 9 kW in total. From the viewpoint of outgassing from the absorbers, we decided to modify the structure to lower the loss factor, i.e. we made the end tapers longer

and the diameter of the end flanges larger from 100 mm to 150 mm.

Figure 9.3.3-3 shows the loss factor calculated for both AR-type and KEKB-type that includes these modifications. As one can see, the loss factor at a bunch length of 4 mm became 1.84 V/pC, which is a 37 % reduction at $\sigma_z = 4$ mm as compared to AR-type.

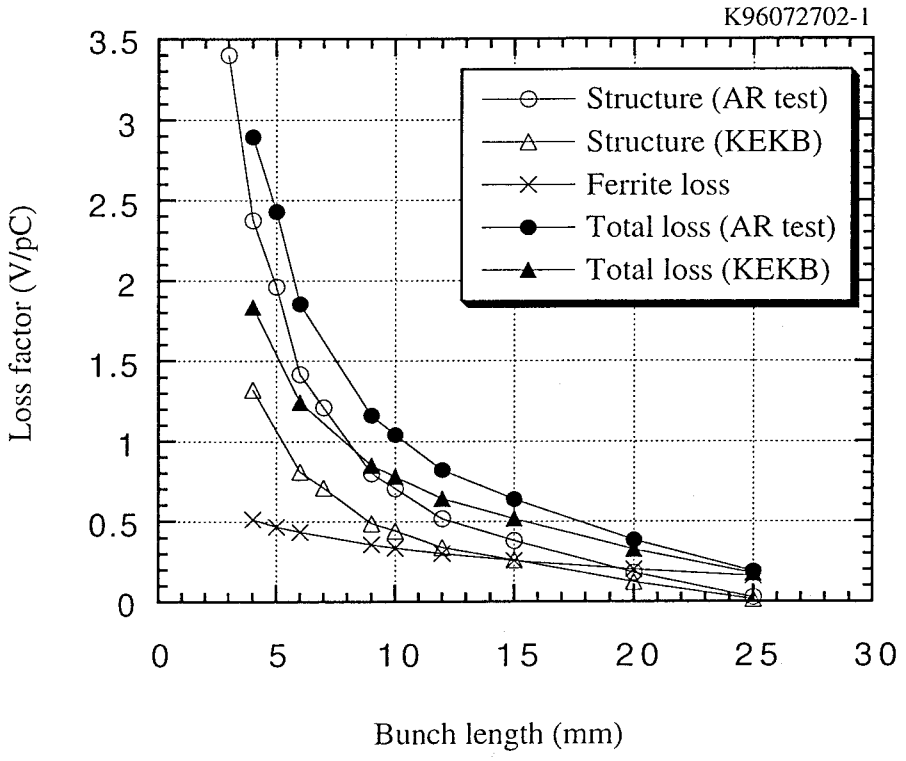

Fig. 9.3.3-3 : The loss factor for the KEKB module. For comparison, the data on the AR test is also shown. Modifications to lower the loss factor was made for the KEKB module.

9.3.4 Mode measurements

The HOM modes were searched with a spectrum analyzer. With our tuner, up to 400 kHz of fundamental mode were searched and no significant increase of HOM was found, confirming the capability of damping.

9.3.5 Outgas

We had three periods of time for tests. In the first two periods, however, we experienced frequent trips. On the contrary, in the third period, the number of trips decreased drastically. The decrease of the trips was attributed to excessive gases that entered from the adjacent

beam ducts being exposed to air during the preceding shutdown period. Thanks to the addition of NEG pumps and ion pumps at the ducts, the pressure became more than one order of magnitude lower in the third period. This made us worried about outgases from the absorbers, although they did not affect the cavity in these tests. Thus, we decided to check the outgas from the absorber and reduce it if necessary.

7) Gas species detected with the RGA

An RGA (Residual Gas Analyzer) was set on a duct at the up-stream taper. The most gas detected was hydrogen during the beam tests, probably because the cavity was at 4.2 K, at which other gases condense on the low temperature surface.

The summary of the observations is as follows.

1. The back ground level of RGA increases with cavity fields higher than ~6 MV/m.
2. The amount of hydrogen increases with beam currents.
3. It also increases during aging of the input coupler.
4. At E_{acc}= 8.3 MV/m, I_b= 400 mA with SCC on, the amount of hydrogen is much higher (~x3<), compared to the operation (450-500 mA) with SCC off.
5. Apart from hydrogen, the observed mass numbers during warm-up are 18, 16, 12, 28, Much less than hydrogen.

9.4 Summary

Two tests were conducted with beams. One is the absorber-alone test. The other is with a SCC. The results of these tests are summarized as follows.

1) Test at TRISTAN MR

- An LBP was tested with two tapers on both sides.
- Maximum Absorbed power was 273 W, measured from the temperature rise of cooling water and flow rate.
- The loss factor was calculated from the absorbed power and compared with the prediction made by ABCI for the structure and by analytic calculation for the ferrite. The results showed that the measured loss factors are slightly lower at bunch length longer than ~6 mm, but tend to go higher with shorter bunches. The drastic increase of the loss factor around 4 mm may be attributed to the distortion of bunch shapes and the power entering from outside of the chamber.
- We found a sharp signal (Q ~1000) at 2.405 GHz, but we could not identify this mode.
- This was the first test to confirm that the baking effect lasts longer even after venting with gases. Increase of pressure during beam test was not the gases from the absorber but the gas from the taper made of SUS304 irradiated with X-ray.

2) Tests at TRISTAN AR

- This was the first test with SCC and main objective was to check if this damping scheme would work and could store high intensity beams stably.
- There were three periods of tests. Due to the gases that entered from the outside ducts, the SCC caused frequent trips in the first two tests. In a sense, these tests were important to make us notice that lowering the pressures outside the cavity is very important.
- Thanks to the strengthening the pumping power of the neighbor ducts, in the third test, we could store 0.57 A without problems and proved the feasibility of the damped cavity scheme.
- The maximum absorbed power went up to 4.2 kW without any problem.
- The loss factor was measured in a similar manner as the MR test. The data was more accurate because of a higher power than the MR test. The results showed good agreement with the predictions at bunch lengths of 1.5 - 2 cm. At longer bunches, it was lower than predicted.

Chapter 10

Installation and Operation at KEKB HER

10.1 Introduction

The installation and operation at KEKB HER, our final goal of the development, started in the summer of 1998. Four SCC modules with two HOM absorbers each were installed in the Nikko D11 tunnel in August. Then, after connecting the cavities with beam pipes, LHe transfer lines, waveguides, and various cables, we started commissioning the system in December 1998. In the following sections, details of installation and operation are described with some operating experiences.

10.2 Installation

Prior to the assembly with the cavity modules, the HOM absorbers were high-power tested up to 5 kW and 7 kW for SBP and LBP, respectively, with a 508 MHz coaxial line as described in Section 8.5. After being degreased with ~ 4 ppm ozonized ultra-pure water and rinsed with filtered ultra-pure water, they were pre-assembled with tapers, bellows and gate valves as shown in Fig. 10.2-1. Then, these pre-assembled units were baked at ~150 °C at tapers for about one day. Then the HOM absorbers were baked at 55 °C[1] for about one month or longer to reduce the outgassing rate.

In parallel with the pre-assembly described above, 4 SCC's were tested vertically to check the performance, i.e. obtaining Q-E_{acc} curves. Then, they were chipped off and stored till they were assembled with the other parts.

The assembly of the whole module went as follows.

1) In a class 100 clean room, the cavity was vented with a filtered pure nitrogen gas.

2) Two extension beam pipes were connected with the cavity, which would serve as a heat transition between the cavity and the HOM absorbers.

3) The cavity with extension pipes were transferred to another assembly area and inserted in the cryostat.

---

[1] This temperature was set to avoid cracks in the ferrite.

4) An input coupler was mounted and the cavity was evacuated to check for leak tightness.

5) The cavity was vented again with filtered pure nitrogen to assemble with other parts of the cryostat.

6) Finally, the pre-assembled units of a HOM absorber, a taper, a bellows and a gate valve, were connected with the extension pipes of the cavity.

7) Evacuated and leak tested as well as checked the positions of the major points, such as the center of gate valves.

The assembled module was transferred to a test area for testing to confirm the performance.

After the performance tests, the whole modules were stored at a storage area till the four modules became ready to be installed. Then, the four modules were transferred to the tunnel and installed at the planned position and aligned with the beam line.

After the installation of SCC modules and connecting ducts[2], LHe transfer lines, the waveguides and cooling system for the HOM absorbers were installed. Besides, since there was some degradation of cavity performance at the horizontal tests[3] prior to the installation into the tunnel, we baked the absorbers at 150 °C for about one month after the installation in the tunnel[4]. Since the expected outgassing rate of the absorbers is less than 1.5×10^{-11} Torr·L/s·cm^2 at room temperature as shown in Section 8.3, the total outgassing rate of the absorbers per SCC module is 5.2×10^{-8} Torr·L/s, considering the area of SBP (800 cm^2) and LBP (1380 cm^2). As will be shown in Section 10.3.4, the outgassing rates of each module are different, according to the amount of gases that were desorbed during the warm-up of the cavity (Table 10.3.4-1). It suggests that there are large differences in outgassing rates of the absorbers, which is under investigation now.

As to the installation of the HOM absorbers, each cavity module has its own cooling unit for HOM absorbers with a capacity of 11.6 kW at 20°C. The normal operating condition is 5 L/min at 23°C. The separate cooling system eases the control of cooling and minimizes the down time of KEKB caused by any failure related to the cooling system. Also, the cooling unit is the same type as the one used for coaxial tests of absorbers so that one unit of the running system can be replaced in a short period of time in case of failure.

---

[2] Each duct has 5 NEG pumps and one 400 L/s ion pump to reduce the pressure at the ducts so that little gases enter the SCC modules during operation.

[3] Tests after assembly with cryostat are called horizontal tests since the cavity is in a horizontal position.

[4] While ramping the temperature, we observed some vacuum bursts, which suggested that some cracks had run in the ferrite.

10.3 Operation

10.3.1 Performance of the cavities

Figure 10.3.1-1 shows the unloaded quality factor, Q_0, of the four cavities as a function of accelerating field (E_{acc}). In the figures, open circles are the results of the cavity themselves measured in a vertical cryostat. Open squares are the results of bench tests after being fully equipped with a horizontal cryostat and other parts before installation in the tunnel. Solid triangles and solid circles are the results measured in the tunnel on Nov. 27, 1998, before the first operation and on Jan. 13, 1999, and second operation.

Although the designed voltage for operation was 1.5 MV or 6 MV/m per cavity, we set our target at 10 MV/m and $Q_0 \geq 1 \times 10^9$ to have enough margin for a stable operation and in the case of an operation with fewer modules. Cavity RA could not reach this target due to a defect on the equator. After the defect was ground off, the cavity showed nearly 10 MV/m. Cavity RB surpassed our record on vertical tests (15 MV/m) [88], reaching 19 MV/m. Using the numbers given in Table 1, one could obtain a surface peak field of 35 MV/m and magnetic field of 750 Gauss. To our knowledge, this is the highest value ever reached with 500 MHz range cavities at 4.2 K. Cavity RC degraded during the first vertical test due possibly to some damage created by discharge.

As to the results after full assembly and installation, the remarkable point is that very little degradation from the cavity-alone tests (vertical tests) occurred compared to the results of TRISTAN cavities [89]. Note that the highest fields are not marked in Fig. 10.3.1-1 since it is difficult to measure Q_0 at very high fields in horizontal tests due to a limitation of available power, and partly because it is not necessary to obtain it with some risk of degradation. Cavity RA got even better in Q_0 for some reason. As for cavity RB, we did not try to go much higher because the field is more than enough for operation and available power.

Since beam commissioning started in Dec. 1998, the system has been supplying 6 MV and working very smoothly without any trouble. The maximum current has been 0.51 A and the power delivered to the beam per cavity is 370-380 kW/cavity up to the end of Apr, 1999.

So far, there has been no symptom of degradation due to the HOM absorbers.

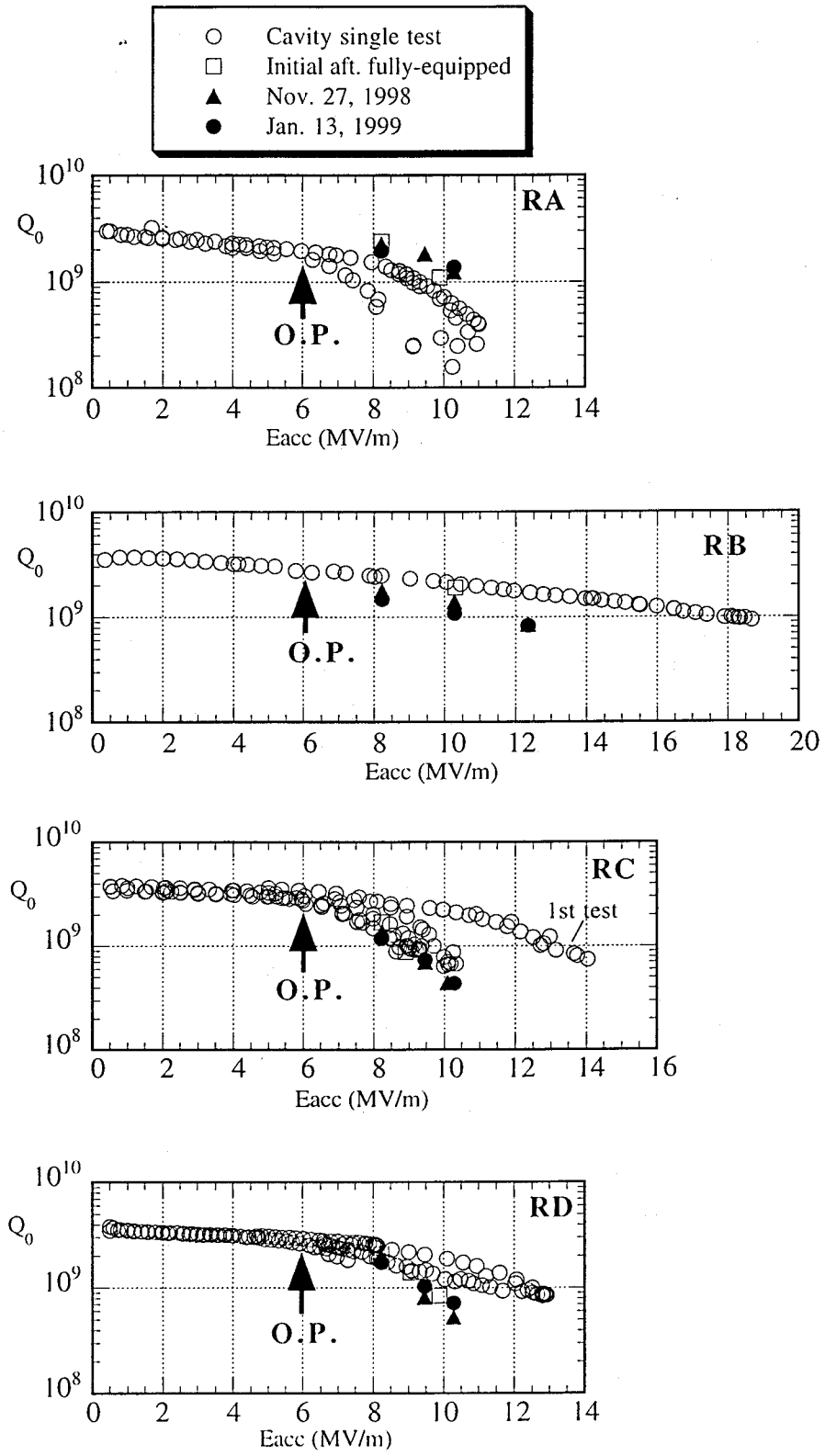

Fig. 10.3.1-1: Unloaded Q vs. accelerating field of all the cavities. "O.P." stands for operation point.

10.3.2 Absorbed power and loss factor

Figure 10.3.2-1 shows the power calculated from the difference of the inlet and outlet water temperature and the flow rate as a function of beam current. This data was taken when the beam was coasting in order to minimize the inaccuracy due to delay of thermal response compared to the change of current. The fluctuation of the signal is caused by the fluctuation of the inlet temperature to regulate the temperature. The accuracy of measurements gets less at lower power due to small temperature differences between the inlet and outlet water. If one takes the lower envelope of each curve, we can obtain the correct values since the power should not be negative at a zero current. All the data is shifted so that the power becomes zero with no current.

This data was taken with 8 trains of 40 bunches. The bunch separation was 5 RF buckets. If the loss factor is constant, i.e. bunch length does not change, and the number of bunches is unchanged during the coasting, power should increase quadratically with current as shown in the formula below. One can see this dependence in Fig. 10.3.2-1.

The maximum power absorbed was 10.6 kW in total and the measured power for each cavity the same, which indicates no difference on HOM damping characteristics among all the cavity modules [91].

Figure 10.3.2-2 shows the loss factor calculated with Eq. (9.2.3-1) except for the revolution frequency of KEKB, 99.46 kHz. The error bar of the measured value corresponds to the distribution of all the four modules. As shown in Fig. 10.3.2-2, the measured data was slightly lower than the calculation at a bunch length of 6 mm. Whether it will stay lower than the calculation or will go higher than that is not clear yet, although the results of the beam test carried out at TRISTAN MR showed that it tends to become higher than the calculation with shorter bunches as shown in Section 9.1.3.

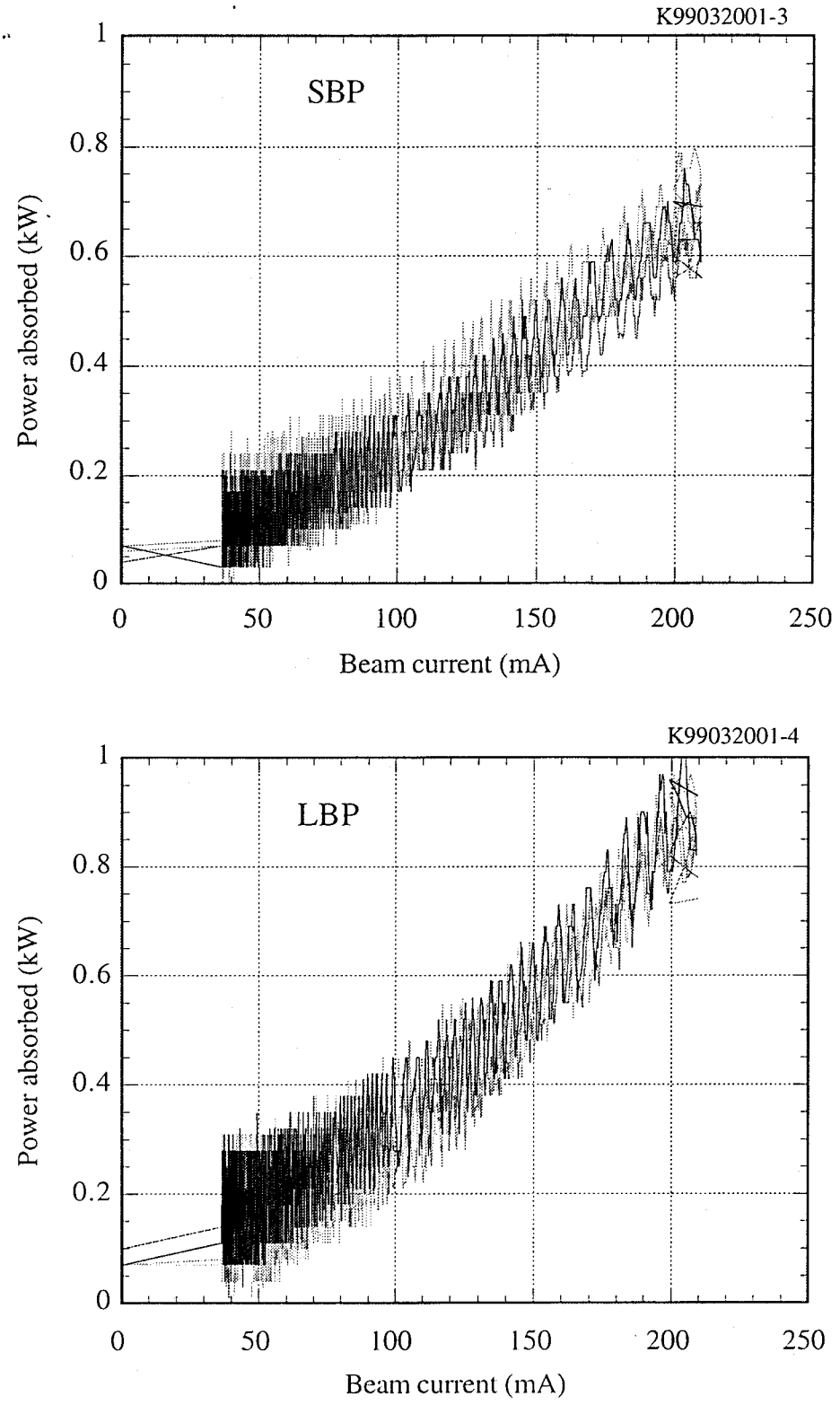

Fig. 10.3.2-1: Power absorbed at the absorbers S and L versus beam current. Data of 4 modules are put in the same figure. Lower envelopes of the curves give correct values. Fluctuation is due to the temperature of the inlet water being regulated.

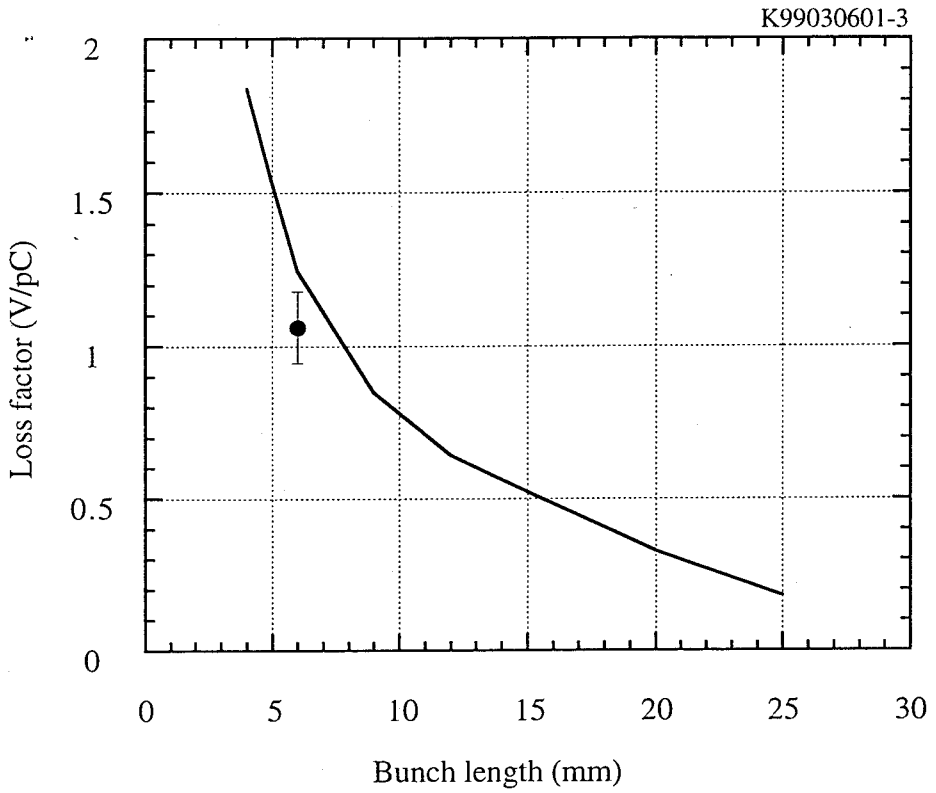

Fig. 10.3.2-2: Loss factor versus bunch length. The solid line is the sum of ABCI calculation for the cavity structure with cones without absorber and analytic calculation for the absorber. Error bar denotes the difference between modules.

10.3.3 Mode damping

In order to monitor the HOM's, we made two pick-up ports on each of the end cones of the cavity module. One is located on the top of the cone and the other at 90 degrees or on the same level of the beam axis. The picked-up signals are monitored through SMA cables that go to the D11 control room.

10.3.4 Outgas

To date (January 2000), the trips related to outgas have been rarely observed. The data on vacuum and outgas are summarized below.

- **Vacuum**

Figure 10.3.4-1 shows the time evolution of pressure in the cavities and at the adjacent beam ducts. Considering the importance of making the amount of gas flowing into the cavity as small as possible for stable operation, we installed five 400 liter/s NEG pumps and one 300 liter/s ion pump on the duct between each module. The effective pumping speed at the neighboring ducts is ~77 L/s·m [90]. As one can see in Fig. 10.3.4-1, the base pressure of the

ducts is normally 0.6 to 0.7 nTorr at present. It is certain that this good vacuum is contributing to the stable operation.

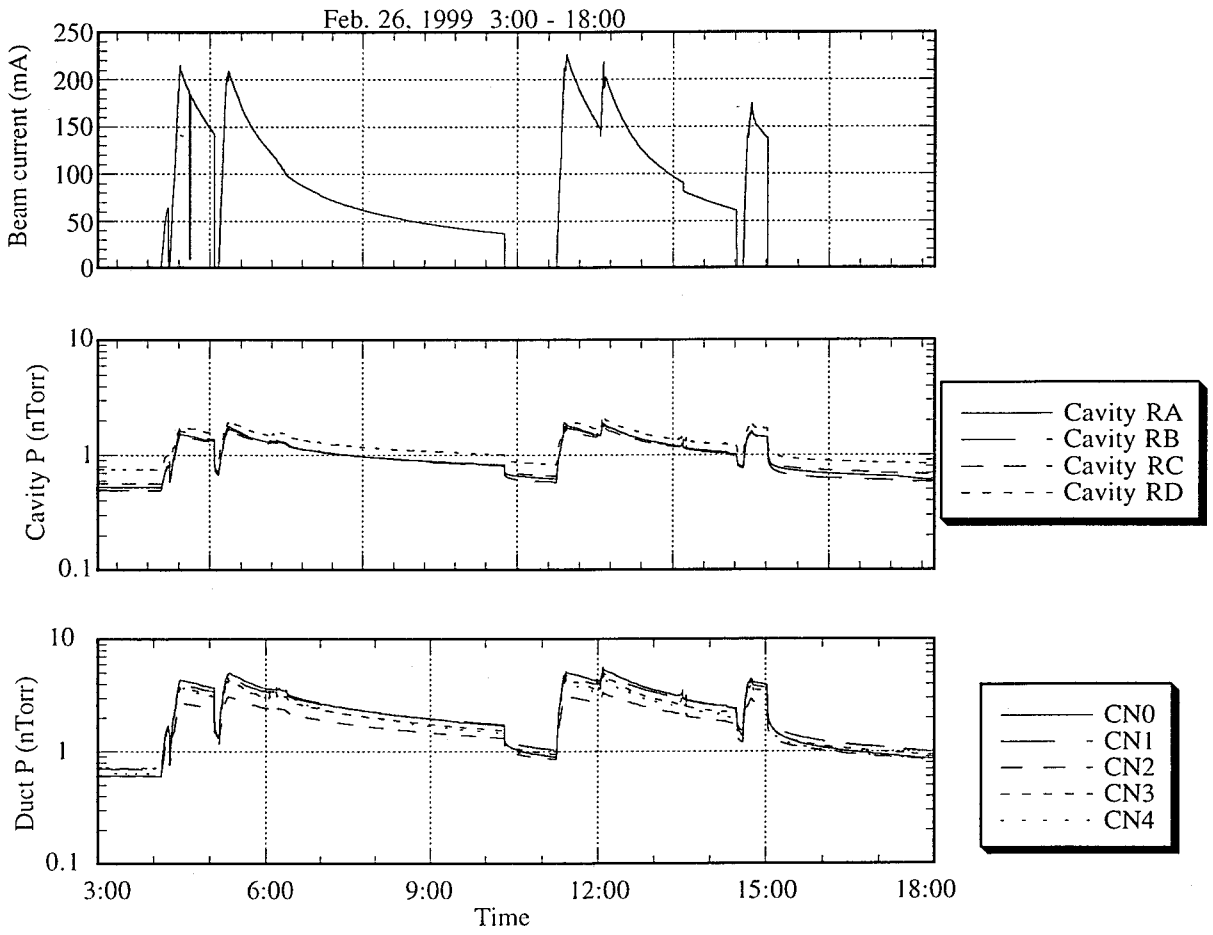

Fig. 10.3.4-1 : Typical trend of pressure during beam operation

Figure 10.3.4-2 shows the pressure increase with current. The pressure goes up linearly with currents. The cavity RD is showing relatively higher pressure as seen in Fig. 10.3.4-2 for some reason, although the slope is the same as the others are. The extrapolated pressure at 1.1 A is 5.7-6.8 nTorr. Compared with the last test in TRISTAN AR where the pressure went up to ~10 nTorr with 400 mA, this looks promising. However, taking into account that if the beam loss is much higher with a shorter bunch length and the pressure increases non-linearly, we should keep watching it very carefully. It will be important to find appropriate indicators on the condition of trips in terms of pressure or amounts of gas condensed on the cold surface, although it is of course desirable to have few trips in the future as it is now.

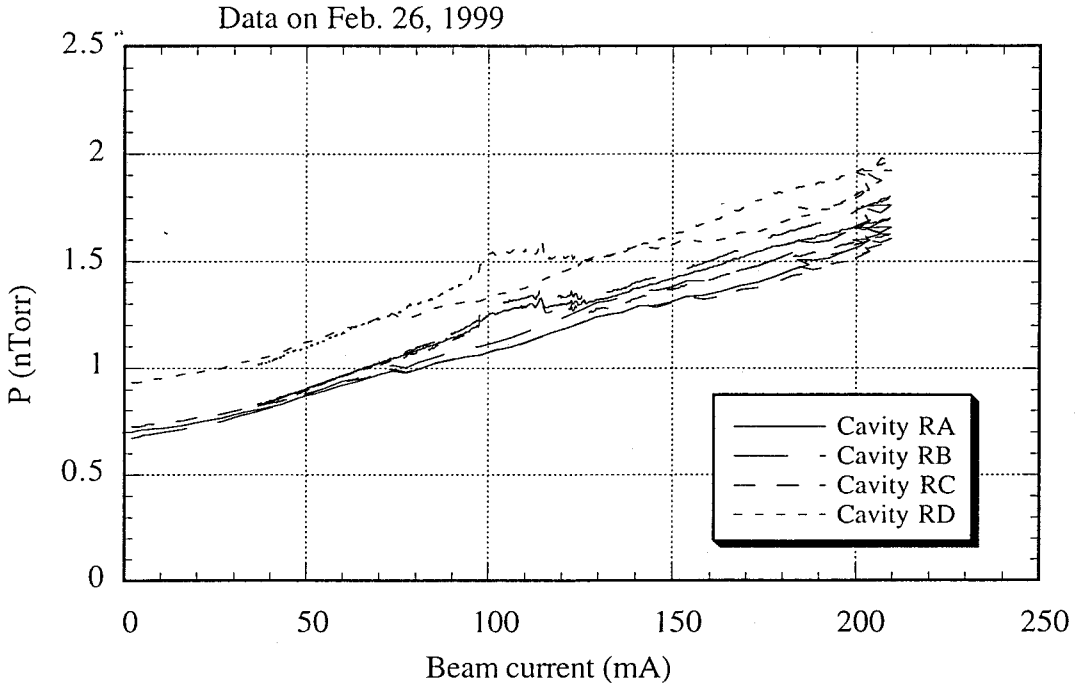

Fig. 10.3.4-2 : Pressure at SCC versus beam current.

- **Outgas**

Outgas has been one of the major concerns since trips are often triggered by condensed gases as we have experienced in the past. As of Dec. 1999, there have been no symptoms of degradation due to outgas or condensed gases on the cavities and coupler surfaces.

As absorbed power goes up with current in the future, the gas load from HOM absorbers will increase because the surface temperature of the absorbers will increase. It will be important to monitor the vacuum constantly and check the amount of condensed gases when the cavity is warmed up.

For this purpose, we installed a data collection system that can store digital data at the fastest rate of 2 sec. We normally store the beam current, vacuum of cavity and coupler, input and reflected power, cavity temperature, and liquid helium level every 10 sec. An advanced feature of this system is the capability of monitoring data on the internet, thereby one can monitor the real time data from anywhere in the world when connected to the internet with a browser such as Netscape Communicator or Internet Explrorer. Some of our present web pages are shown in Appendix D. It has been very useful and time saving since we have been able to watch the system from home.

The data taken with these collection systems can be viewed with software[5], which is unfortunately not real time. Also, we can get text data that is analyzed with different software such as Excel and Kaleida Graph.

Figure 10.3.4-3 shows the desorption of gases from cavity surfaces during warm-up. The gases that were desorbed at corresponding temperatures are shown as well.

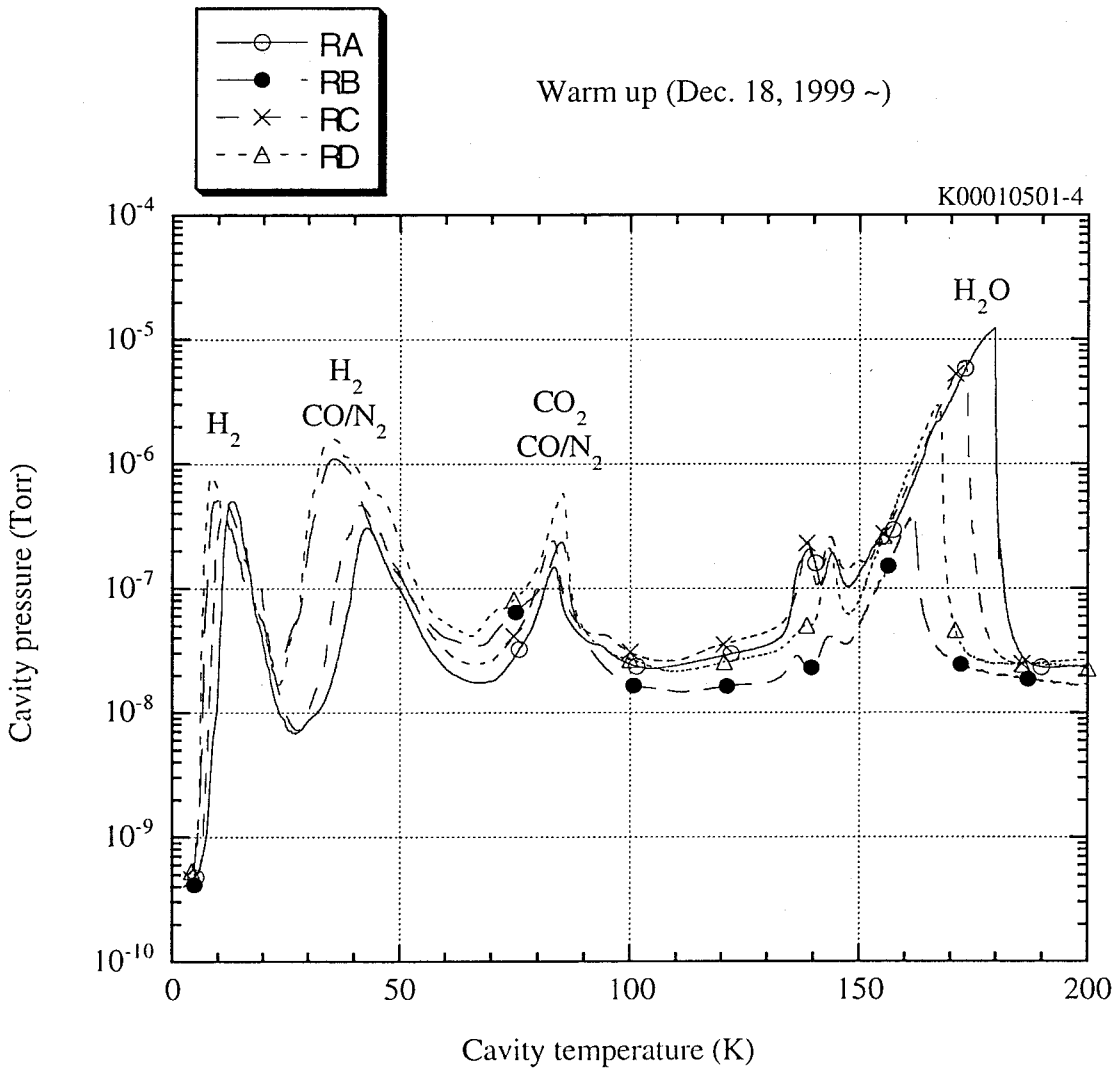

Fig. 10.3.4-3: Pressure as a function of cavity temperature upon warm-up of the cavities.

Cavity RA and RC had large amounts of water condensed on the surface. Total effective pumping speed of one module is 291 L/s (153 L/s at SBP and 138 L/s at LBP).[6] By

[5] Currently this software is run on Windows95.

[6] Nominal pumping speed of each pump is 306 L/s. Conductances of the pumping ducts are included.

multiplying the pressure integral over a time period with this effective pumping speed, the total amount of gas condensed on the cavity surface can be roughly estimated. Table 10.3.4-1 summarizes the result. As one can see, the total amount of desorbed gas differs from one cavity to another significantly. As shown in Fig. 10.3.4-3, the major contribution to this difference is water. As discussed in Section 8.3, since the major component of outgas from absorbers, if it is not baked well, is water, it is likely that the absorbers of RA and RC have not been baked well. The baking history of these absorbers is under investigation.

An interesting fact is that, at the peak around 35 K, RA has the lowest amount of gas (H_2 , CO/N_2) that desorbed. It may suggest that water does not contribute to trips from the following experiences.

1) We have not had trips frequently with this amount of water at KEKB HER.

2) In TRISTAN, a warm-up to ~80 K could reduce trips, which implies that the gases that desorb up to ~80 K are responsible for the trips.

If this is true, RD and RB would start having trips after they adsorbed excessive amount of gases since they condensed more gases than others at the above temperature range. Anyway, as we have more statistics, we will know more about it.

Table 10.3.4-1: Total amount of desorbed gases during warm up on Dec. 18, 1999.

Cavity name	Pressure integral [Torr·sec]	Total desorbed gas[*1] [Torr·L]
RA	0.10298	30.0
RB	0.0095815	2.79
RC	0.066766	19.4
RD	0.033672	9.80

[*1]Effective pumping speed of 291 L/s was multiplied with pressure integral.

Table 10.3.4-2 summarizes the cavity pressures after the beam run (before warm-up) on Dec. 18, 1999 together with the data of the AR cavity on Mar. 30, 1996 when it was warmed up to about 85 K after frequent trips.

As one can see, the pressure of AR cavity after frequent trips is more than a factor of 2.5 higher than KEKB cavities. Moreover, since the pressure after re-cooldown from 85 K

allowed the AR cavity to desorb the gases, H_2 (or CO/N_2) is likely to be responsible for the trips. Pressure with no beam might be a good indicator for the trips in the future.

Table 10.3.4-2: Comparison of cavity pressures after the beam run and cool-down.

Name of cavity	Pressure right before cool-down ($x10^{-10}$ Torr)*1	Pressure after re-cooldown to 4.2 K ($x10^{-10}$ Torr)
RA	4.7	2.7
RB	3.7	1.6
RC	4.6	2.5
RD	5.1	2.7
AR-cavity (1st test)	13	2.7

*1No beam, before warm-up of KEKB cavities (on Dec. 18, 1999), and of AR cavity (Mar. 30, 1996) after frequent trips. KEKB cavities have not had frequent trips.

10.4 Summary

Since the start of commissioning in December 1998, four SCC modules have been operating very smoothly with significantly few trips. The system has been supplying 6 MVs in total. The maximum current has been 0.51 A and the maximum power delivered to beam has been 370-380 kW/cavity up to the end of Apr, 1999. So far, there has been no symptom of degradation due to the HOM absorbers.

The maximum power absorbed was 10.6 kW in total and the measured power for each cavity is the same, which indicates no difference in HOM damping characteristics among all the cavity modules [91].

Loss factor at σ_z = 6 mm is slightly lower than predicted, although we have not analyzed much of the data yet.

Thanks to the low pressure of the neighbor ducts, the cavity pressure has been low, probably contributing to the stable operation. The pressure without beam after a few months of operation is a factor of 2.5< lower than the AR- test when we had frequent trips.

The gas desorption curves during warm-up indicate that there are differences in the amount of condensed gases. The major difference is the amount of water, which indicates that there were absorbers that were not baked out well. However, considering the continuing stable operation, the amount of water may not contribute to trips. Other components such as H_2 might be more serious.

Chapter 11

Summary

We discussed the development of HOM absorbers for KEKB SCC's (Superconducting Cavities). The absorber requires sufficient HOM damping, UHV (Ultra High Vacuum, ~1×10^{-9} Torr ≥) compatibility, high power handling capability (5 W/cm^2<), free of particulate that degrades SCC, some electric conductivity to prevent increases in charges and sparks.

The originality and creativity of the work lies in the fact that, to overcome the weakness or the low bending strength of ferrite that leads to unsuccessful bonding of tiles, a new technique of making an absorbing layer (on the order of several mm) of ferrite on a large diameter copper pipe (up to 300 mm now) was established and proved to be applicable to making HOM absorbers.

This new technique involves HIP (Hot Isostatic Press) technology, which is a relatively new technology and still finding new applications. Although this absorber was developed for SCC's, it can be used for other parts of accelerators that demands similar requirements, e.g. two absorbers have been manufactured and used for the HOM's in the area that has large tapers for the future crab cavities at the Tsukuba area of KEKB HER.

Since there was a limitation on the time for R&D, there are areas that remain to be pursued, for example, attempting to make an absorber that has higher thermal conductivity by mixing with another powder that has higher thermal conductivity, which will be useful for handling higher power.

Although more detailed summaries are written in the end of major chapters, the important points are summarized below.

- An original way of manufacturing HOM absorbers made of ferrite, which involves HIP (Hot Isostatic Press) technique, has been developed. This method proved to be one of the most suitable ways to make an absorbing layer with a fragile material such as ferrite.

- The absorbers made this way were tested with low power using a network analyzer and proved to show a good mode damping capability.

- High power tests using a 508 MHz coaxial line showed its power handling capability of more than 14 W/cm^2 which is 5 times that required for KEKB-HER.

- A Beam test at TRISTAN MR showed its feasibility to be used in accelerators with the fact that no spark, damage or degradation was observed up to a single bunch current of 4.4 mA, which is 20 times that of KEKB-HER.

- Beam tests at TRISTAN AR showed that these absorbers could be used with superconducting cavities at high currents (tested up to 0.57 A). Namely, it showed the expected damping capability, no degradation of cavities due to the absorbers being observed, and there was no damage or degradation with the beam operation.

- The eight absorbers installed in Nikko D11 tunnel of KEKB HER with four SCC modules have been working well without any problems as well as the stable performance of the cavities.

- The power absorbed through the 8 absorbers installed in KEKB HER agrees well with the prediction made with computer codes at a bunch length of about 6 mm.

- The operating pressure has been kept low enough not to start RF trips

12 Acknowledgments

There are many people involved in the development of HOM absorbers.

First of all, I am grateful to the workers of Kinzoku-Giken, Inc., N.Gamo, T.Hamasaki, S.Iida, T.Nakae, H.Nakagawa, Y.Natsume, S.Tachibana and others for their help and advice in establishing the manufacturing technique, especially the part that uses HIP, as well as K.Ishino and H.Takashina of TDK, Inc. for kindly providing the pre-sintered powder for testing and his co-workers' advice in HIP techniques, and S.Kokura who helped me with the tests of brazing and hot pressing ferrite when he used to work for Hitachi-Kyowa Engineering, Inc.

Secondly, I would like to thank E.Noguchi of Suzuno-Giken, Inc. for corresponding swiftly to my needs and demands in making many apparatuses and fixtures for experiments. I had been very demanding throughout the period of development and construction.

I have been indebted to Y.Kijima and Y.Ishi of Mitsubishi Electric Company, K.Sennyu of Mitsubishi Heavy Industries, Co. Ltd., T.Tanaka of Furukawa Electric, Co. Ltd. , and K.Numajiri of Suzuno-Giken, Inc. for helping me in the tests carried out at KEK.

I would like to thank M.Kudo and N.Taniyama of Micro Denshi, Inc. for providing 2.45 GHz power sources and helping me test the absorbers.

As for the inspection and diagnostics of the absorbers, I have been indebted to Y.Arima, T.Morita and Y.Nagano of Hitachi-Kenki FineTech, Inc. for teaching me how to use the acoustic tomography machine and kindly letting me use it for most of the absorbers.

I am grateful to W.Hartung and D.Moffat for some calculations and ultrasonic tests for the bonding as well as fruitful discussions.

I would like to thank K.Asano of Akita-Kosen, E.Ezura, T.Furuya, K.Hosoyama, S.Kurokawa, M.Izawa, S.Mitsunobu and T.Takahashi for advice, help and encouragement as well as K.Akai, H.Nakanishi, S.Yoshimoto and other RF group members and SCC cryogenic group members for various assistance.

On a more personal level, I would like to thank my mother and father for their continuous love and encouragement.

Finally, I would like to thank my wife and lifetime partner, Allyson, for her enormous effort to support my work and my life. Without her support and pressure, I would never have been able to finish this work.

13 Bibliography

[1] W. Hartung; "The interaction between a beam and a layer of microwave-absorbing material", PhD thesis, May 1996.

[2] M. Kobayashi and T. Masukawa; "CP VIOLATION IN THE RENORMALIZABLE THEORY OF WEAK INTERACTION" , Prog.Theor.Phys.49:652-657,(1973).

[3] S. Kurokawa; "KEKB and JLC, Electron-Positron Collider Projects in Japan", 7th Pacific Physics Conference (7APPC), Beijing, China, August 19-23, 1997. KEK Preprint 97-213.

[4] T. Furuya et al.; "A Prototype Module of a Superconducting Damped Cavity for KEKB", 5th European Particle Accelerator Conference (EPAC96), Sitges (Barcelona), Spain, June 10-14, 1996. KEK Preprint 96-58.

[5] S. Mitsunobu et al.; "Superconducting Cavities", XVII International Conference on High Energy Accelerators, Dubna, Russia, Sept. 7-12 (1998). KEK Preprint 98-153.

[6] T. Tajima et al.; 1997 Particle Accelerator Conference and International Conference on High Energy Accelerators, May 12-16, 1997, Vancouver, BC, Canada. KEK Preprint 97-87.

[7] T. Tajima et al.; Proceedings of the 7th Workshop on RF Superconductivity,

[8] T. Tajima et al.; 1995 Particle Accelerator Conference and International Conference on High Energy Accelerators, May 1-5, 1995, Dallas, Texas, U.S.A., KEK Preprint 95-77

[9] K.Asano, et al.; "Ozonized Ultrapure water Treatment of Nb Surfaces for Superconducting RF Cavities", 9th Meeting on Ultra High Vacuum Techniques for Accelerators and Storage Rings, KEK, Japan, March 3-4 (1994). KEK Preprint 93-216.

[10] J.L.Laclare; "Coasting beam longitudinal coherent instabilities", General Accelerator Physics Course, Jyvaskyla, Finland, Sept. 7-18 (1992). CERN-94-01, P. 349.

[11] K.Saito ; in an article in High Energy News (in Japanese)

[12] T.Tajima et al.; 5th European Particle Accelerator Conference (EPAC96), Sitges (Barcelona), Spain, June 10-14, 1996. KEK Preprint 96-75

[13] T.Tajima et al.; KEK Report 96-7, June 1996.

[14] Y.H.Chin et al.; "User's guide for ABCI version 8.8", LBL-35258, UC-414 (1994).

[15] CAS - CERN Accelerator School: 5th General accelerator physics course, http://preprints.cern.ch/cernrep/1994/94-01/94-01_v1.html

[16] CAS - CERN Accelerator School and Rutherford Appleton Laboratory :Course on rf engineering for particle accelerator

[17] K.Akai ; KEK Accelerator Seminar, OHO94 (1994)

[18] M.Izawa; KEK Accelerator Seminar, OHO93 (1994)

[19] D.G.Myakishev and V.P.Yakovlev; 1991 Particle Accelerator Conference, San Francisco, p. 3002.

[20] Hewlett Packard, Product Note 8510-3.

[21] T.Tajima et al.; "Bonding of a Microwave-absorbing Ferrite, TDK IB-004, with Copper for the HOM Damper of the KEK B-Factory SC Cavities", 6th Workshop on RF Superconductivity CEBAF, Virginia, U.S.A., Oct. 4-8, 1993. KEK Preprint 93-152.

[22] This measurement was done by MAC SCIENCE, Inc.

[23] R.E.Newnham et al.; Proceedings of the Workshop on Microwave-Absorbing Materials for Accelerators, Feb. 22-24, 1993, CEBAF, Virginia, U.S.A.

[24] W.H.Sutton; Microwave Processing of Ceramic Materials. Ceram. Bull. 68, p. 376 (1989).

[25] S. Chikazumi ; "Physics of Magnetism", Wiley, New York, (1964).

[26] W.Hartung, et al. ; Proceedings of the Workshop on Microwave-Absorbing Materials for Accelerators, p. 162, Feb. 22-24, 1993, CEBAF, Virginia, U.S.A.

[27] S.Noguchi et al. ; Proc. 5th Symp. on Acc. Sci. Technol., Sept. 26-28, p. 122 (1984).

[28] T.Furuya et al. ; Proc. 13th Int. Conf. High Energy Acc., Aug. 7-11, Novosibirsk, U.S.S.R., (1986).

[29] H.Padamsee ; Proceedings of the Workshop on Microwave-Absorbing Materials for Accelerators, p. 14, Feb. 22-24, 1993, CEBAF, Virginia, U.S.A.

[30] MAFIA is a product of CST, Inc. Information is available at info@cst.de , web at www.cst.de

[31] SEAFISH is a program written by M. DeJong.

[32] J. C. Slater ; "Microwave Electronics", p. 85, D. Van Nostrand Company, Inc. (1950).

[33] O. M. Akselsen ; "Review, Advances in brazing of ceramics", J. Mater. Sci. 27, 1989 (1992).

[34] J. G. Li ; "Wetting and interfacial bonding of metals with ionocovalent oxides", J. Am. Ceram. Soc. 75, p. 3118 (1992).

[35] J. G. Li, L. Coudurier and N. Eustathopoulos ; "Work of adhesion and contact angle isotherm of binary alloys on ionocovalent oxides", J. Mater. Sci. 24, 1109 (1989).

[36] G.P.Rodrigue ; Proceedings of the Workshop on Microwave-Absorbing Materials for Accelerators, p. 85, Feb. 22-24, 1993, CEBAF, Virginia, U.S.A.

[37] R.F.Davis ; Proceedings of the Workshop on Microwave-Absorbing Materials for Accelerators, p. 143, Feb. 22-24, 1993, CEBAF, Virginia, U.S.A.

[38] T.Kageyama ; Text of KEK Accelerator Seminar OHO'94.

[39] T.Koseki et al. ; 5th European Particle Accelerator Conference (EPAC96), Sitges (Barcelona), Spain, June 10-14, 1996.

[40] M.Izawa et al. ; 5th European Particle Accelerator Conference (EPAC96), Sitges (Barcelona), Spain, June 10-14, 1996.

[41] Y.Takeuchi et al. ; Proc. 1995 Particle Accelerator Conference and International Conference on High-Energy Accelerators, p. 1797, Dallas, Texas, U.S.A., May 1-5, 1995. KEK Preprint 95-69.

[42] Y.Takeuchi et al. ; 5th European Particle Accelerator Conference (EPAC96), Sitges (Barcelona), Spain, June 10-14, 1996. KEK Preprint 96-59.

[43] F.Hinode and S.Sakanaka; Proc. 1995 Particle Accelerator Conference and International Conference on High-Energy Accelerators, p. 1756, Dallas, Texas, U.S.A., May 1-5, 1995. KEK Preprint 95-45.

[44] T.Koseki et al. ; 4th European Particle Accelerator Conference (EPAC94), London, U.K., June 27-July 1, 1994. KEK Preprint 94-60.

[45] F. Caspers; "Measurements of complex permeability and permittivity of ferrites for the LHC injection kicker", LHC Project Note 203 (1999).

[46] F. Caspers; "Experience with UH-compatible microwave absorbing materials at CERN", Proceedings of the Workshop on Microwave-Absorbing Materials for Accelerators, p. 311, CEBAF, Virginia, U.S.A., Feb. 22-24, 1993.

[47] D. Moffat et al.; Proceedings of the Workshop on Microwave-Absorbing Materials for Accelerators, p. 321, CEBAF, Virginia, U.S.A., Feb. 22-24, 1993.

[48] W. Hartung; Ph. D thesis at Cornell Univ., May 1996.

[49] I.E.Campisi et al.; Proceedings of the Workshop on Microwave-Absorbing Materials for Accelerators, p. 269, CEBAF, Virginia, U.S.A., Feb. 22-24, 1993.

[50] T.Tajima et al.; "R&D on HOM Absorbers for Superconducting B-Factory at KEK", Proceedings of the Workshop on Microwave-Absorbing Materials for Accelerators, p. 331, CEBAF, Virginia, U.S.A., Feb. 22-24, 1993. KEK Preprint 93-6.

[51] T.Tajima et al.; "Development of HOM Absorber for KEK B-Factory SC Cavities", 6th Workshop on RF Superconductivity CEBAF, Virginia, U.S.A., Oct. 4-8, 1993. KEK Preprint 93-153.

[52] M.Izawa et al.; Rev. Sci. Instrum. 63 , 363 (1992).

[53] KEKB B-Factory Design Report, KEK Report 95-7 (1995).

[54] K.Akai ; 8th Workshop on RF Superconductivity, Padova, Italy, October 6-10, 1997. KEK Preprint 97-244.

[55] K.Akai et al.; Proc. EPAC98, p. 1749, Stockholm, June 22-26, 1998. KEK Preprint 98-82.

[56] N.L.Loh and Y.L.Wu ; Materials & Manufacturing Processes, 8 , p. 159 (1993).

[57] This apparatus is located at Hitachi-kenki, Inc. and has been kindly offered to use.

[58] T.Iseda, Y.Kutukake and N.Nomaki ; Joining of ceramics, glass + metal. German Weld. Soc., DVS-Berichte, 66 41 (1980).

[59] M.Naka and M.Maeda ; "Application of ultrasound on joining of ceramics to metals", Engineering Fracture Mechanics 40 951 (1991).

[60] From catalogue of TDK, Co. Ltd.

[61] K. Oide, et al. ; "Commisioning of the KEKB B-Factory", The 18th Particle Accelerator Conference (PAC99), New York City, U.S.A., Mar. 29 - Apr. 2, 1999. KEK Preprint 99-8.

[62] This test was carried out at Hitachi-Kyowa Engineering, Inc.

[63] K.Kuniya et al. ; "Thermal Conductivity, Electrical Conductivity and Specific Heat of Copper-Carbon Fiber Composite", J. Japan Inst. Metals, 49 906 (1985).

[64] A.W.Chao ; "Physics of Collective Beam Instabilities in High Energy Accelerators", John Wiley & Sons, Inc. (1993).

[65] H. Wiedemann ; "Particle Accelerator Physics – second edition", Springer-Verlag (1999).

[66] F.J.Sacherer; Proc. 9th Int. Conf. High Energy Acc., 347 (1974).

[67] R.J.Ditchburn et al.; "NDT of Welds: state of the art", NDT & E International, 29 111 (1996).

[68] N.Akasaka ; private communication.

[69] T.Tajima et al. ; "The Superconducting Cavity System for KEKB", The 18th Particle Accelerator Conference, New York City, U.S.A., Mar. 29 - Apr. 2, 1999. KEK Preprint 99-49.

[70] F.Takasaki; "STATUS OF KEKB ACCELERATOR AND DETECTOR, BELLE", 19th International Symposium on Lepton and Photon Interactions at High-Energies (LP 99), Stanford, California, 9-14 Aug 1999.

[71] W.Hartung et al.; "Measurement of the Interaction Between a Beam and a Beam Line Higher-Order Mode Absorber in a Storage Ring", 1995 Particle Accelerator Conference and International Conference on High Energy Accelerators, May 1-5, 1995, Dallas, Texas, U.S.A., CLNS 95/1339

[72]

[73] National Center for Excellence in Metalworking Technology, "Development of a HIP Modeling System for Large Complex Parts", http://www.ncemt.ctc.com/thrustAreas/powder/devhip/

[74] E.Chojnacki et al.; "Beamline RF Load Development at Cornell", 1999 Particle Accelerator Conference, New York, NY, U.S.A. (1999).

[75] W.Hartung et al.; "Measurement of the Interaction Between a Beam and a Beam Line Higher-Order Mode Absorber in a Storage Ring", 1995 Particle Accelerator Conference and International Conference on High Energy Accelerators, May 1-5, 1995, Dallas, Texas, U.S.A.

[76] J. Knobloch; "Advanced Thermometry Studies of Superconducting RF Cavities", Ph. D thesis, Cornell Univ. CLNS THESIS 97-3.

[77] http://www-jhf.kek.jp/JHFwelcome.html

[78] http://www.ornl.gov/sns/Cong.Brief.htm

[79] http://www.cern.ch/LHC/

[80] http://www-acc.kek.jp/WWW-ACC-exp/KEKB/KEKB-home.html

[81] http://tesla.desy.de/

[82] http://www.lns.cornell.edu/public/CESR/

[83] M.S. Zisman; "B Factory RF System Design Issues", Proc. B-Factorie The State of the Art in Accelerators, Detectors and Physics, pp. 144-149, SLAC-400, Nov., 1992.

[84] S. Belomestnykh et al.; "Commissioning of the Superconducting RF Cavities for the CESR Luminosity Upgrade", The 18th Particle Accelerator Conference (PAC99), New York City, U.S.A., Mar. 29 - Apr. 2, 1999.

[86] S. Belomestnykh et al.; "The interaction between a Beam and a Superconducting Cavity Module: Measurements in CESR and CESR-Phase III Goals", International Workshop on Collective Effects and Impedance for B-Factories, KEK, Tsukuba, Japan, June 12-17, 1995. SRF 950905-12.

[87] This measurement was performed at a laboratory of ULVAC corporation.

[88] T.Tajima et al.; 5th Workshop on RF Superconductivity, DESY, Hamburg, Germany, August 19-24,1991. KEK Preprint 91-193.

[89] S.Noguchi et al.; "Recent status of the TRISTAN superconducting rf system", EPAC '94 London, UK ; 27 Jun - 1 Jul 1994. KEK Preprint 94-43.

[90] Y.Suetsugu; private communication.

[91] T. Furuya et al.; "Recent status of the superconducting cavities for KEKB", 9th Workshop on RF Superconductivity, Santa Fe, NM, U.S.A., Nov. 1-5, 1999. KEK Preprint 99-158.

[92] H. Lengeler; "Superconductivity in Particle Accelerators", CERN Accelerator School, CERN 89-04, 10 March 1989.

[93] D.G.Myakishev and V.P.Yakovlev; "CLANS2-A Code for Calculation of Multipole Modes in Axisymmetric Cavities with Absorbing Ferrites", Proc. PAC99, p. 2775, New York (1999).

[94] I.S.K.Gardner et al.; "Status of the European Spallation Source Design Study", Proc. PAC97, p. 988, Vancouver, BC, Canada, May 12-16, 1997.

[95] Y. Yamazaki; "Cavity Systems which Suppress Coupled-Bunch Instabilities", A lecture presented at the 1994 US-CERN-Japan Joint Accelerator School Topical Course, "Frontiers of Accelerator Technology", Maui, Hawaii, Nov. 3-9, 1994. KEK Preprint 95-6.

[96] T. Weiland; "Single Mode Cavities - A Possibility for Fighting Collective Beam Instabilities", DESY 83-073, Sept. 1983.

[97] K. Akai et al.; "Operational Experience with the TRISTAN Superconducting RF system", 1991 Particle Accelerator Conference, San Francisco, U. S. A., KEK Preprint 91-35.

[98] E. Kako et al.; "Long Term Performance of the TRISTAN Superconducting RF Cavities", 1991 Particle Accelerator Conference, San Francisco, U. S. A., KEK Preprint 91-38.

[99] Y. Kojima; "Beam Test of A Three-cell Structure in the TRISTAN Accumulation Ring", 2nd Workshop on RF Superconductivity, CERN, July 184.

[100] T. Furuya et al.; "500 MHz Three-cell Superconducting Cavity", Proc. 5th Symposium on Accelerator Science & Technology, KEK, Sept. , 1984, p. 122.

14 Appendices

Appendix A: History of HIP Tests

Table A-1: History of the absorbers manufactured with HIP. S, L and XL designate 220 mm, 300 mm and 109 mm in outer diameter of the absorber, respectively. XS has been used for reduced size tests at 2.45 GHz. "S" and "L" are designated as "SBP" and "LBP" in the thesis.

Serial No.	Date of HIP	HIP Pattern	Problems	Remarks
Tile HIP	Jul. 5, 1992	Fig. A-1	-	
Pre-#1	Sept. 6, 1993	Fig. A-2	Leak	For 2.45 GHz test o.d. 109 mm
Pre-#2	Sept. 24, 1993	Fig. A-3	-	
#1 (S1, L1)	Dec. 8, 1993	Fig. A-4	L1 Leak S: 25 big voids	1st full size HIP
#2 (L2)	Feb. 17, 1994	Fig. A-4	L1 Leak L2: Large delamination	
#3 (L2)	May 6, 1994	Fig. A-4	-	L1: Sliced as ring
#4 (S2, L2, XS2)	June 3, 1994	Fig. A-4	XS1, L1 Leak S1: 20 small voids S2: 10 small voids L2: 102 small voids XS2: 1 small void	S#2: used for outgas test, baked up to 250 °C.
#5 (S'4)	June 30, 1994	Fig. A-5	-	No voids

S' : Diameter is the same as S, but its length is short (60 mm).

Table A-1 (Cont'd)

Serial No.	Date of HIP	HIP Pattern	Problems	Remarks
#6 (S3, L3)	Dec. 21, 1994	Fig. A-6	S1 Leak (#2) S#1:Large crack L#1, #3: 1 delamination each	S#3, L#1: used at beam tests at TRISTAN AR
#7[1] (L2)	May 10, 1995	Fig. A-7	Insufficient mode damping	
#8 (S2)	June 3, 1995	Fig. A-7	-	
#9 (S2, L2)	Oct. 8, 1996	Fig. A-7	-	
#10 (S2, L2)	May 7, 1997	Fig. A-7	All leaked.	Inappropriate ferrite powder with PVA
#11 (S2, L2)	June 19, 1997	Fig. A-7	L1 leak (#2)	
#12 (S2, L2)	Aug. 7, 1997	Fig. A-7	-	
#13[2] (Crab 3 x 2)	Dec. 22, 1998 Dec. 25, 1998	Fig. A-7	-	Installed at the area for future crab cavities.
#14 (S6, L6)	July 19, 1999 July 26, 1999	Fig. A-7	-	To be used for D10 SCC modules

[1]Copper powder, 10 vol %, was mixed to improve thermal conductivity.

[2]Outer diameter of ferrite is 240 mm and length is 170 mm.

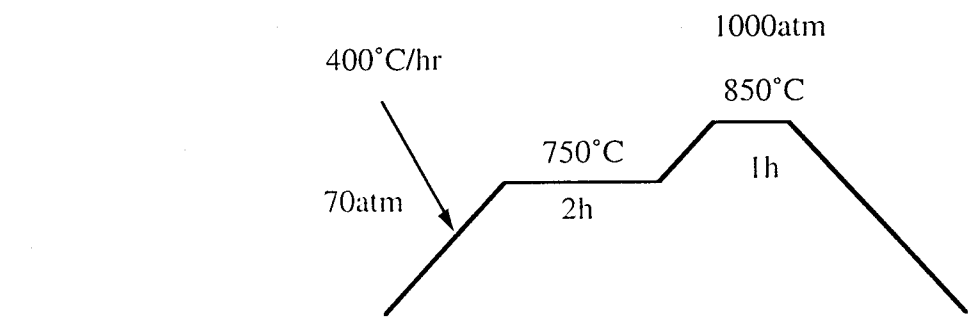

Fig. A-1

Pre-#1 1993.9.6 2.45GHz (i.d.100 mm)

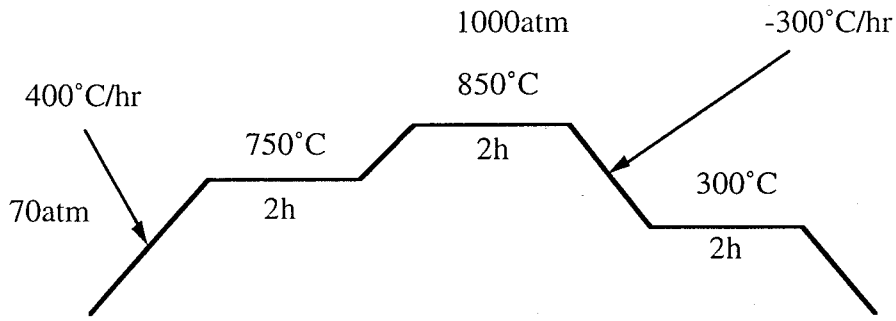

Fig. A-2

Pre-#2 2.45GHz 1993.9.24

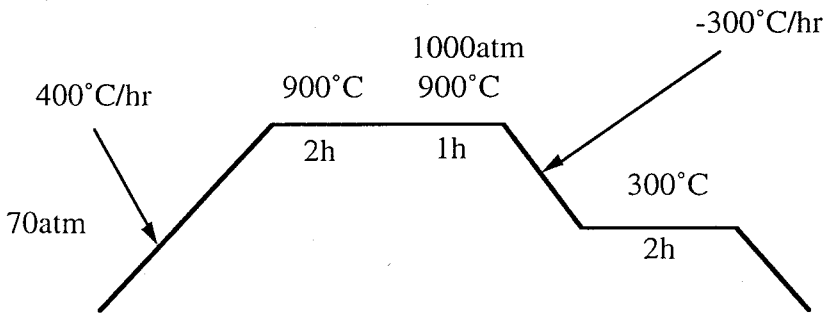

Fig. A-3

1st HIP (S,L 1 each) 1993.12.8

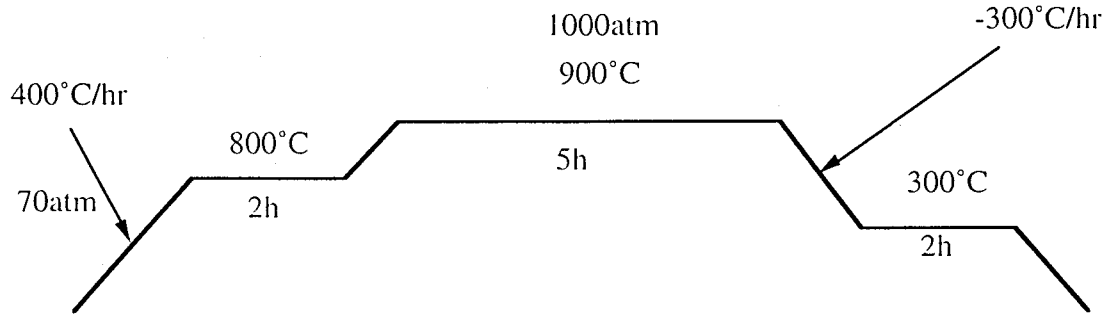

Fig. A-4

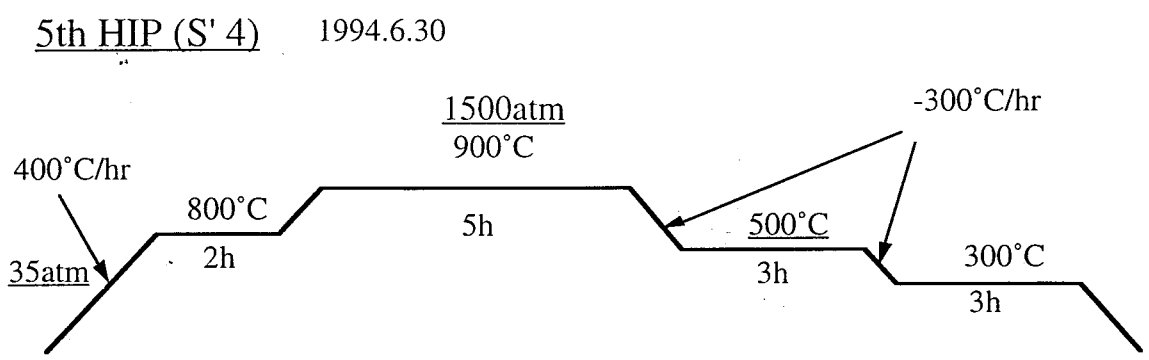

Fig. A-5

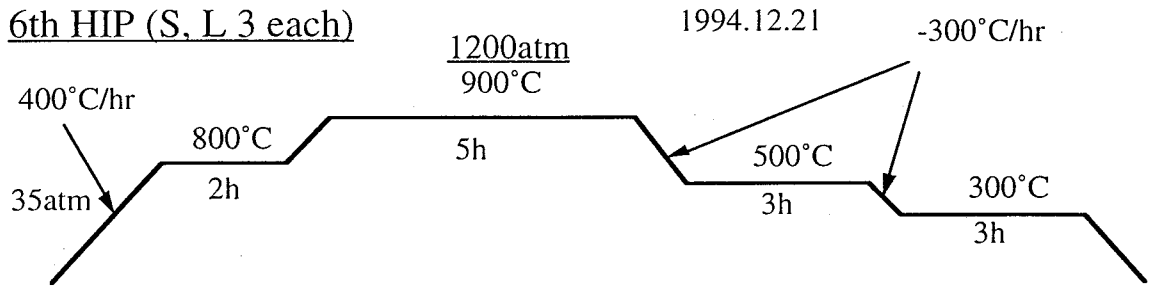

Fig. A-6

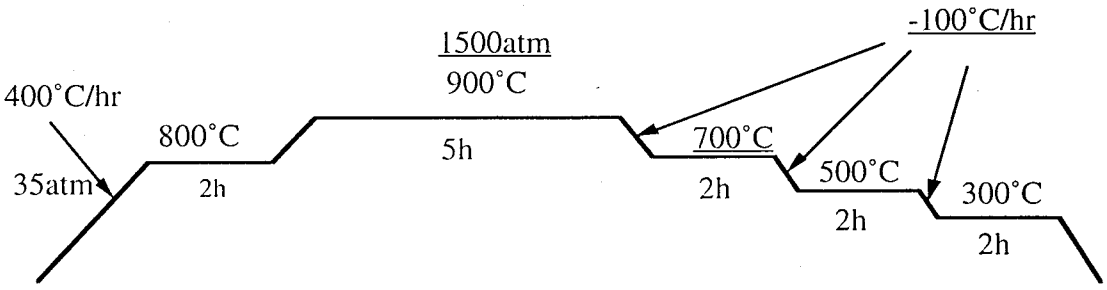

Fig. A-7

Appendix B:
Photographs of the process to make full-size absorbers

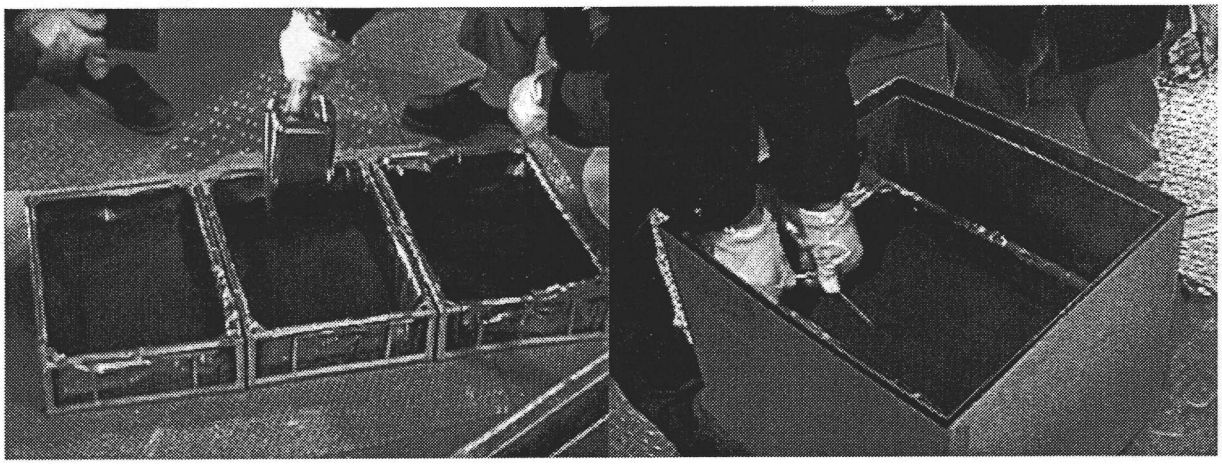

Fig. B-1(a): Ferrite powder to be degassed (left). (b): Thermo-couple is being set in the powder (right).

Fig. B-1 (c): Being inserted into a furnace. (d): Putting on a lid for more thermal insulation.

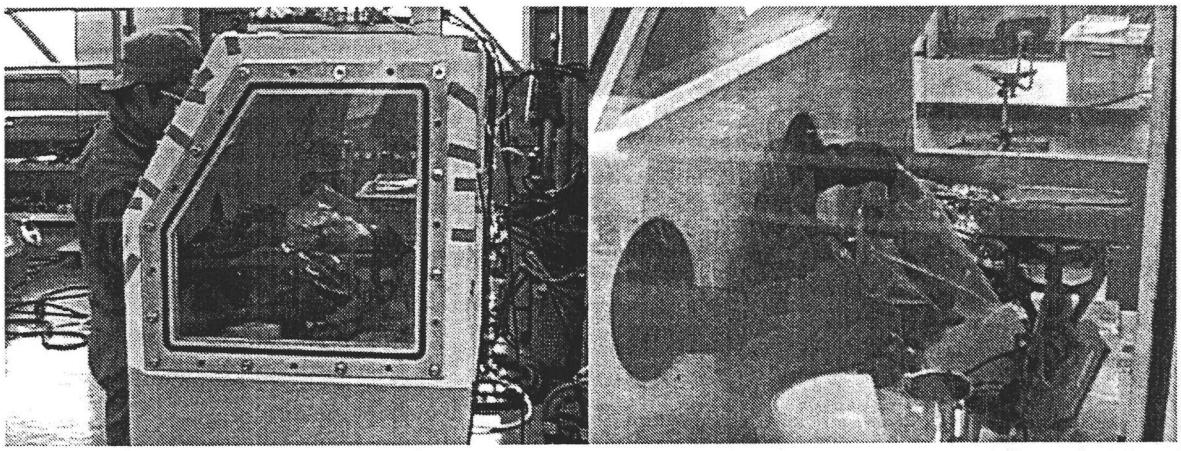

Fig. B-2: Ferrite powder is divided into small amount and put into plastic bags in a nitrogen-filled glove box so that the powder is not exposed to air.

Fig. B-3: The bags filled with ferrite powder and nitrogen are put into a stainless steel container (shown above) and filled with nitrogen for transport. Every effort to keep the powder from touching the air is conducted so that the powder does not adsorb water from the air again. If it does, the effect of degassing disappears.

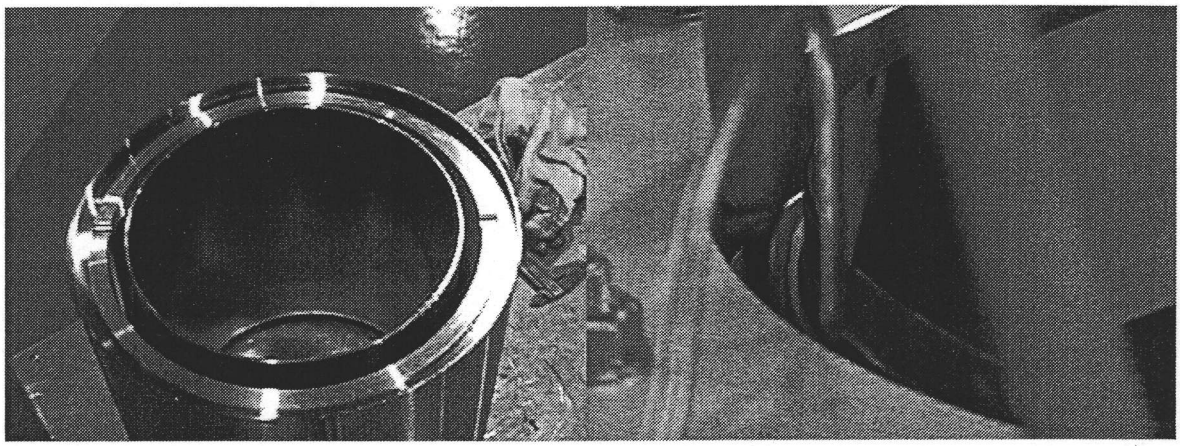

Fig. B-4: Assembly before feeding ferrite powder (left), and ferrite is being fed with a vibrator in the gap of inner can made of SPCE (2.3 mm-thick soft steel) and OFC/OFHC (12 mm-thick Oxygen Free Copper) (right).

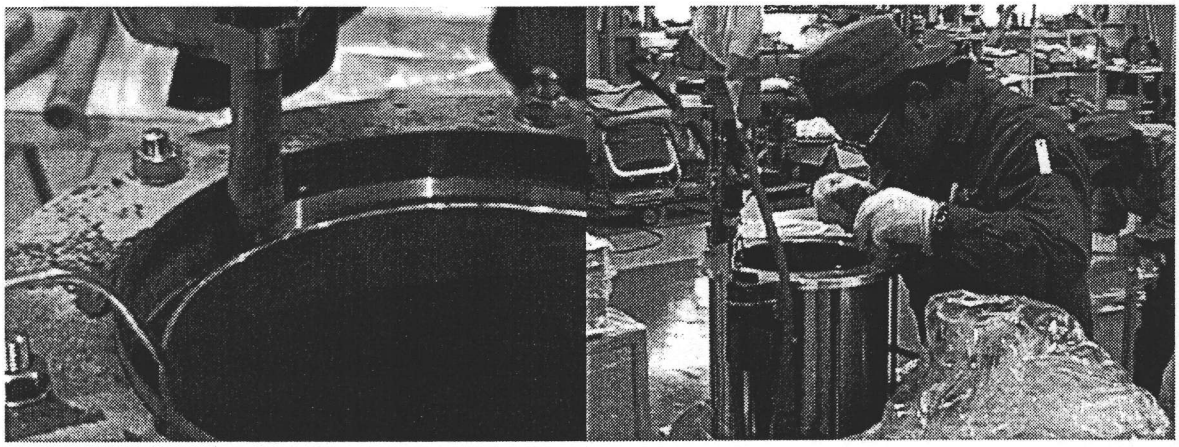

Fig. B-5: While powder is being fed, nitrogen gas is fed in the gap slowly through a small tube for powder to come into contact with the air as little as possible (left). After the vibration feed, the flatness of the surface level is checked and corrected by human eyes so the next pushing will not be uneven (right).

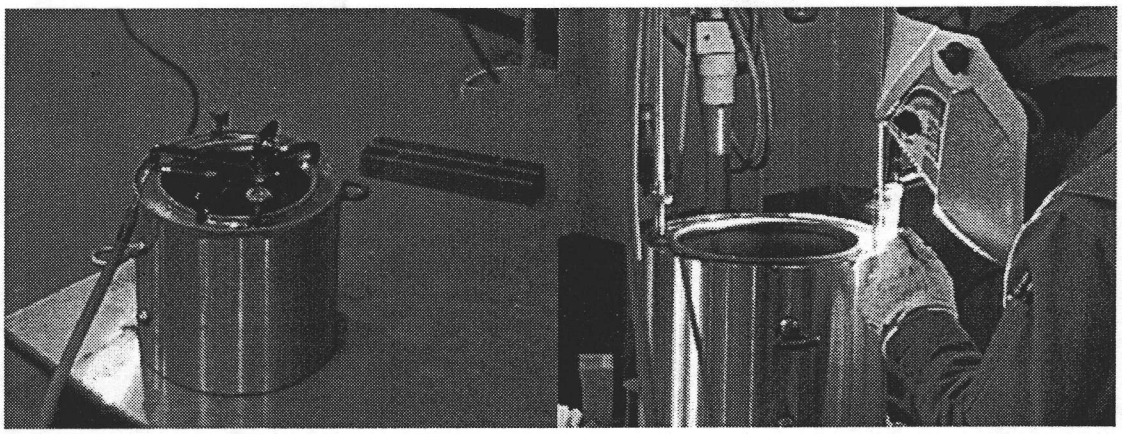

Fig. B-6: After the gap is filled with ferrite powder, a lid with two ports for evacuation is TIG welded.

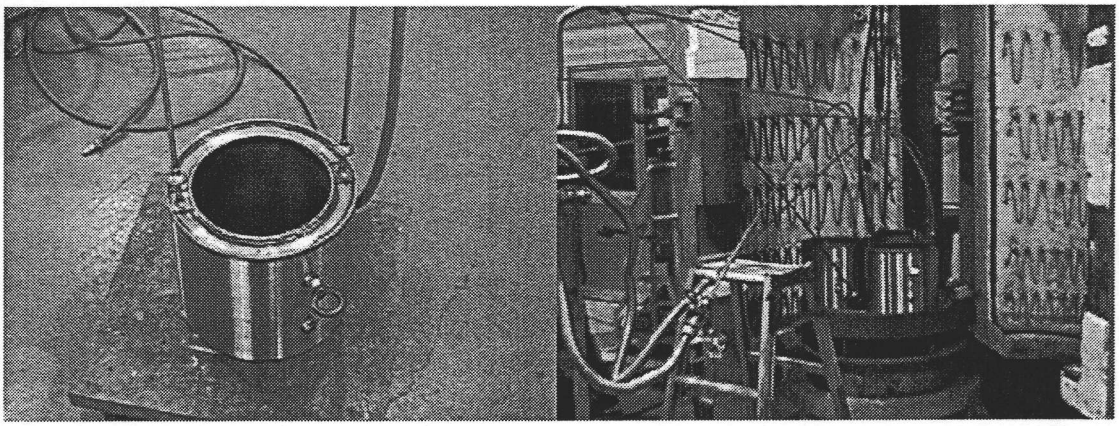

Fig. B-7: Two stainless steel pipes for evacuation are welded to the ports (left) and the absorbers are put in a furnace for degassing at a high temperature. The degassing temperature is raised to 400 °C and kept for about one day until the pressure at the gauge (the one closer to the absorber) gets less than 1 - 2 x 10^{-3} Torr at 400 °C.

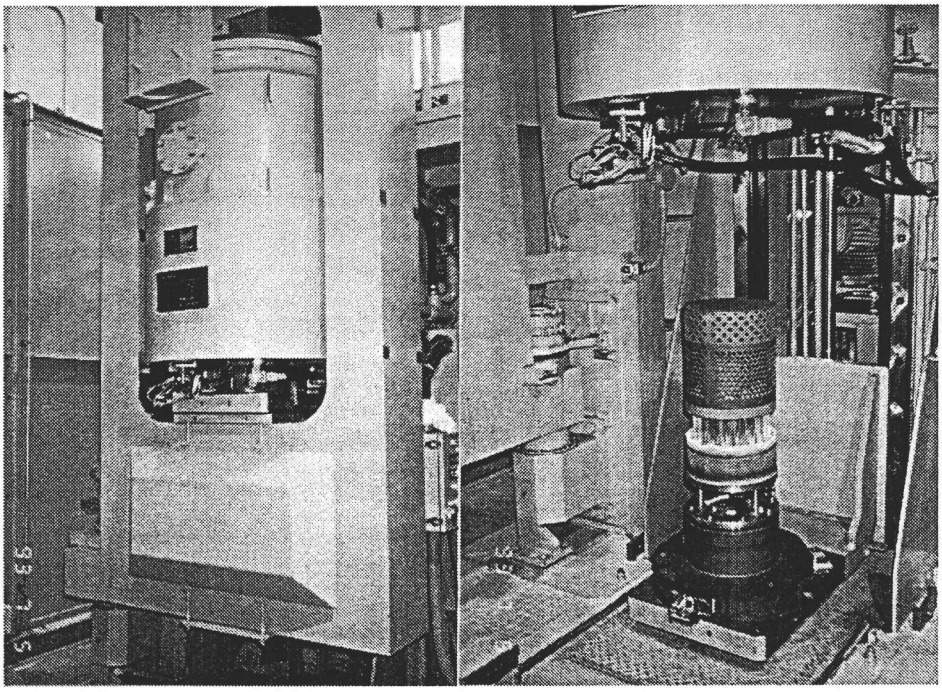

Fig. B-8: A Furnace of HIP. Ferrite powder is HIPped with Ar gas at 1500 atm and 900 °C for 5 hours. The established HIP pattern is described in the text.

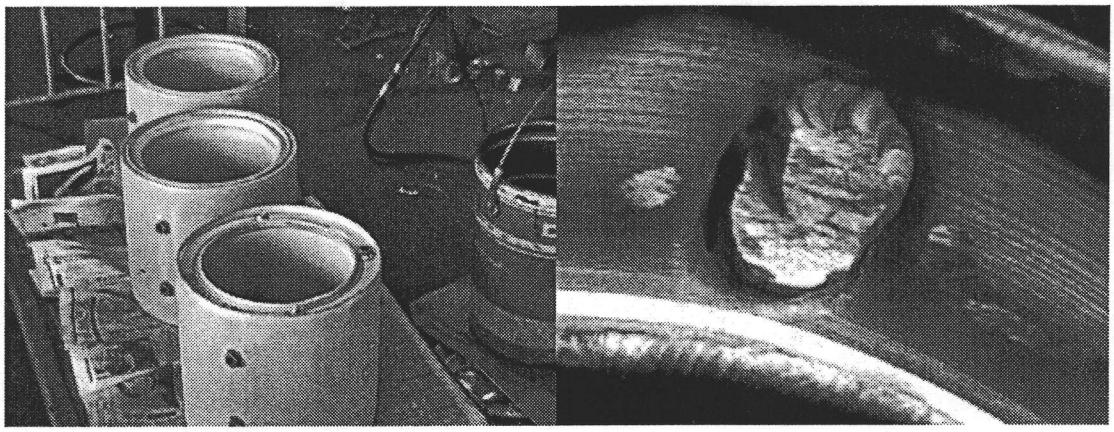

Fig. B-9: After HIPping, evacuation ports are cut (left). Inside of the evacuation ports are filled with copper (right) because copper gets very soft and moves easily at 900 °C.

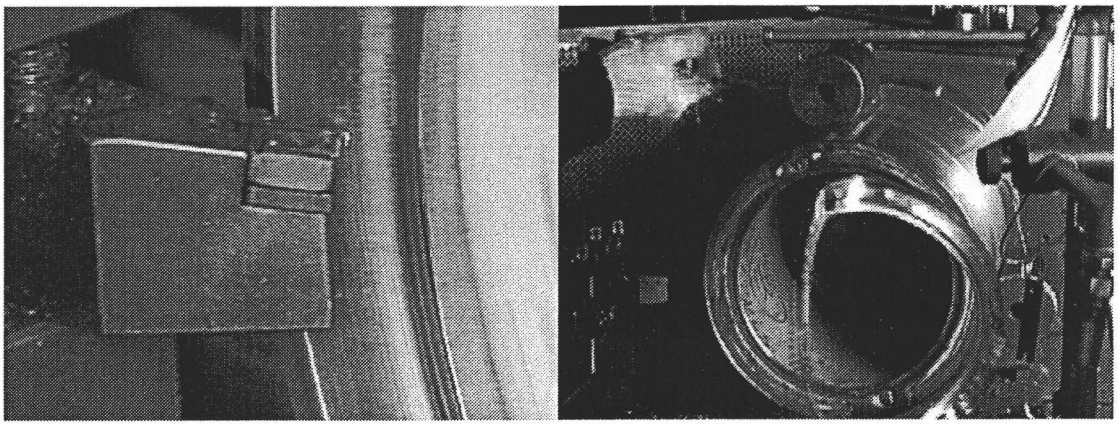

Fig. B-10: Lids and inner capsule are removed with a diamond tool.

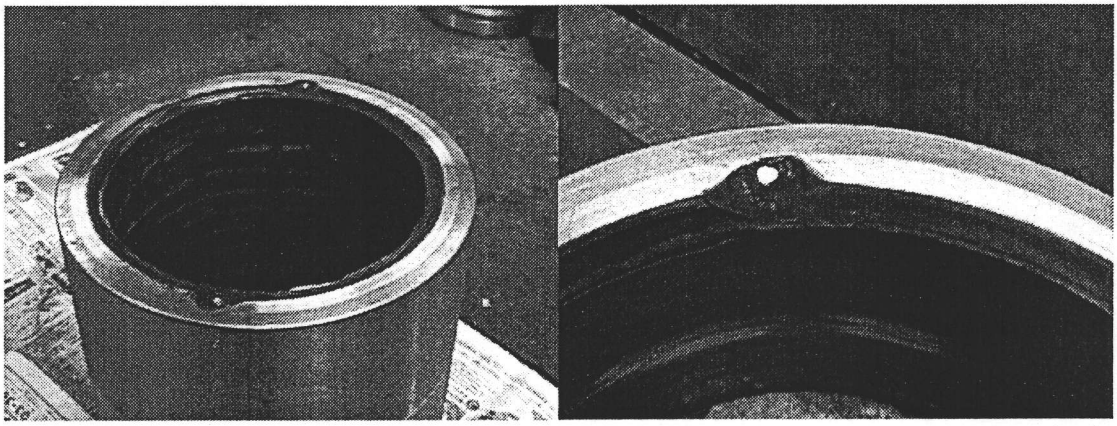

Fig. B-11: After the inner capsule is removed (left). The two dents for evacuation (12 mm wide and 3 mm deep) are filled with copper during HIPping (right)

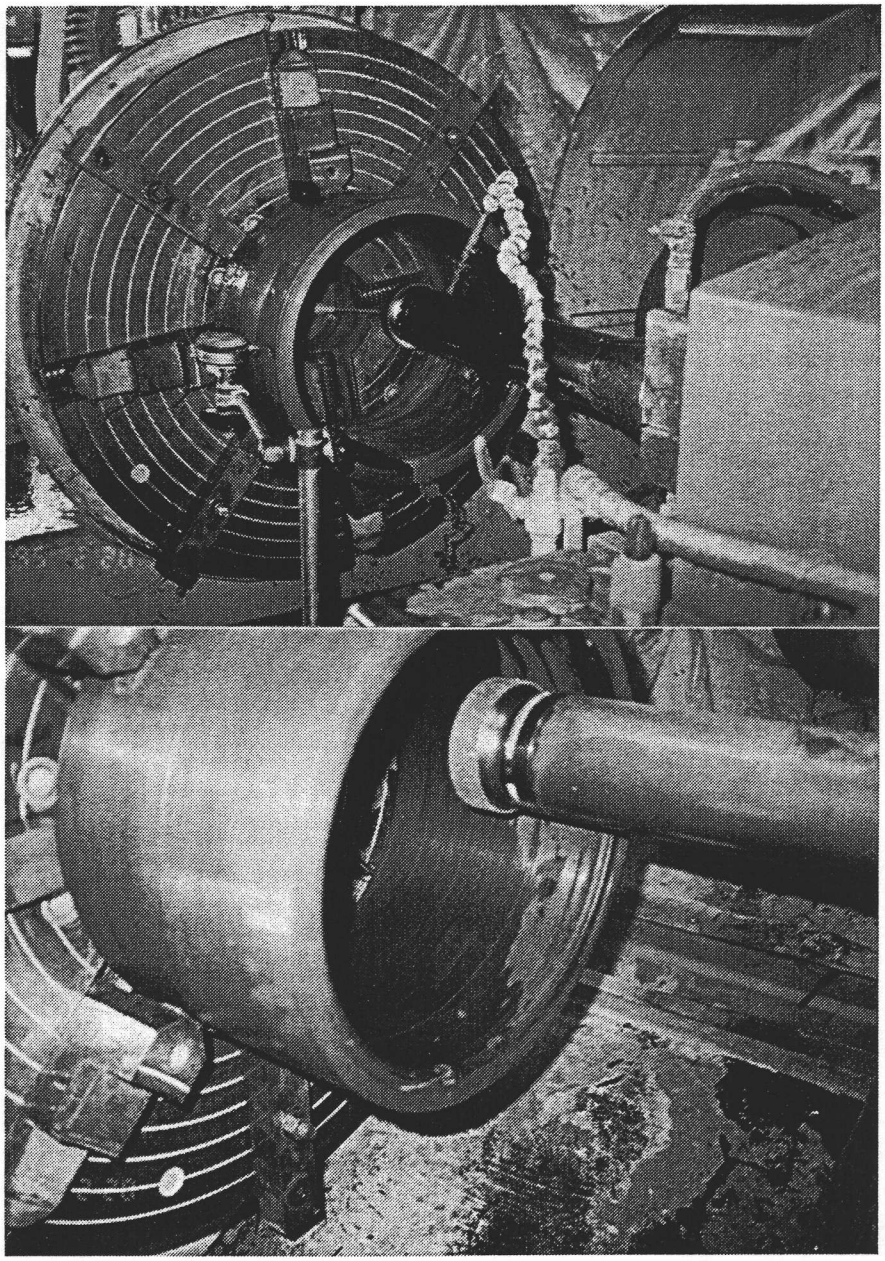

Fig. B-12: Ferrite is machined/shaped with a grinder whose surface is coated with diamond powder. To prevent heating up, it is cooled with water (top).

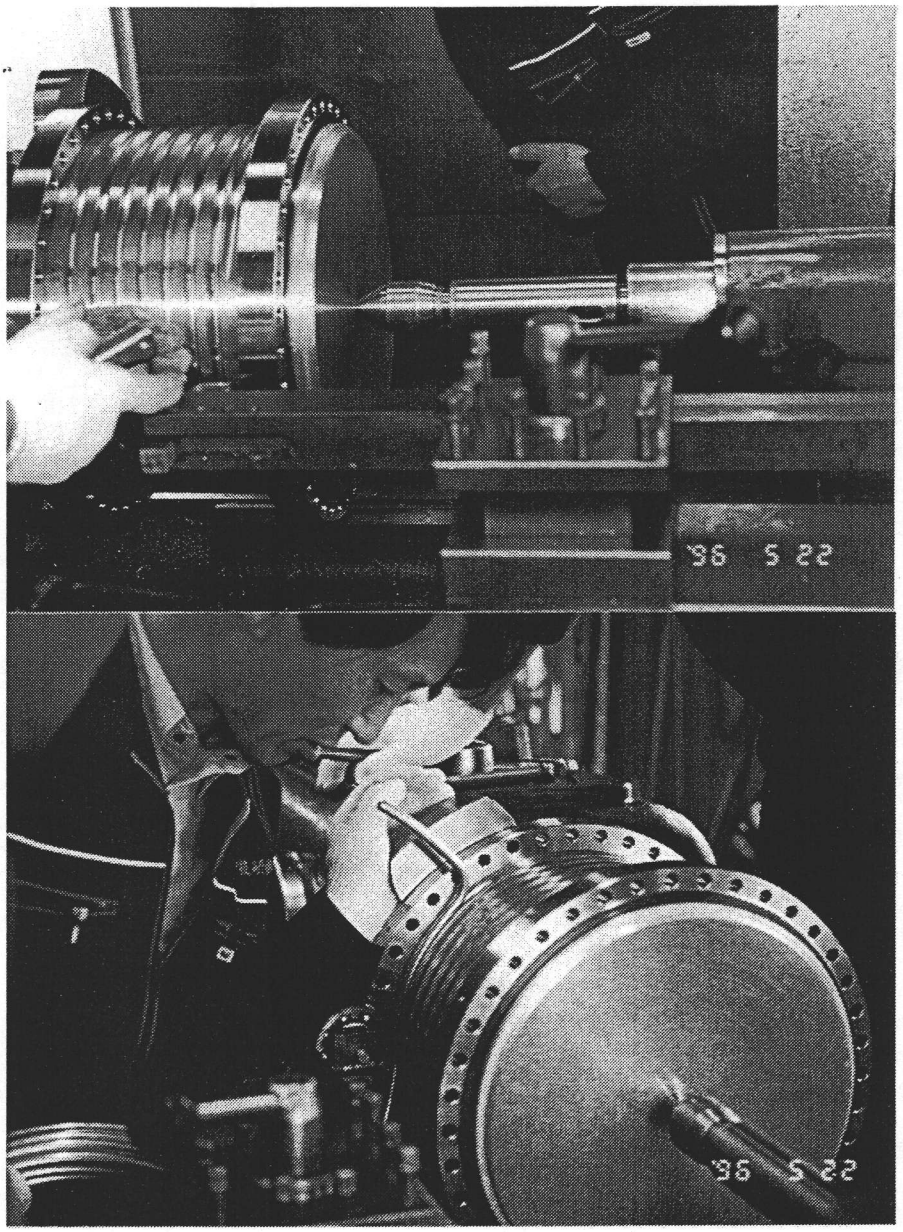

Fig. B-13: After two flanges are electron beam welded, a round groove is machined spirally on the outer surface of copper and a 3/8"-diam. and 0.8 mm-thick copper pipe is press-inserted in the groove for cooling.

Appendix C: Measurement procedure of acoustic tomography

We first set a HOM absorber on a rotatable table in water as a medium for sound waves to propagate. Then we set a transducer (transmitter/receiver) that is concave so the wave can converge on the surface of interest as shown in Fig. C-1. A picture of the whole set-up is shown in Fig. C-2.

The subsequent procedure is as follows.

(1) Set the distance between the ferrite surface and the sensor to about 1 inch (focal length).
(2) Looking at the sound pressure reflected from the surface on an oscilloscope, the position and angle of the transducer are adjusted in such a way that the monitoring pressure becomes the highest.
(3) Move the transducer to the center of the area to be scanned and input in the software the region and increment of the steps of data taking during scanning. In azimuthal direction, we normally scan 40 deg. and 60 deg. for SBP and LBP, respectively, at one time. In axial direction, we scan the whole length at one time. Data is taken every 0.08 degrees and 0.12 degrees in azimuthal direction and 0.24 mm and 0.30 mm in axial direction, for SBP and LBP, respectively.
(4) Start scanning the ferrite by moving the transducer in an axial direction and rotating the absorber in CW and CCW. When the series of scanning is finished, the absorber moves back to the starting position automatically.
(5) Store the data in computers manually, then rotate the absorber so the next scan can start.
(6) Repeat (4) and (5) till 360 degrees are covered.
(7) Monitoring the oscilloscope, moves the transducer toward the ferrite so that the sound waves focus on the boundary of copper and ferrite, i.e. the echo pressure gets highest on the monitor, as shown at the bottom of Fig. 5.4-23. We call this echo the "boundary echo".
(8) Repeat (4) to (6).
(9) The obtained images are stored as TIFF images and put together as an unfolded image of the whole surface as shown from Fig. 5.4-25.

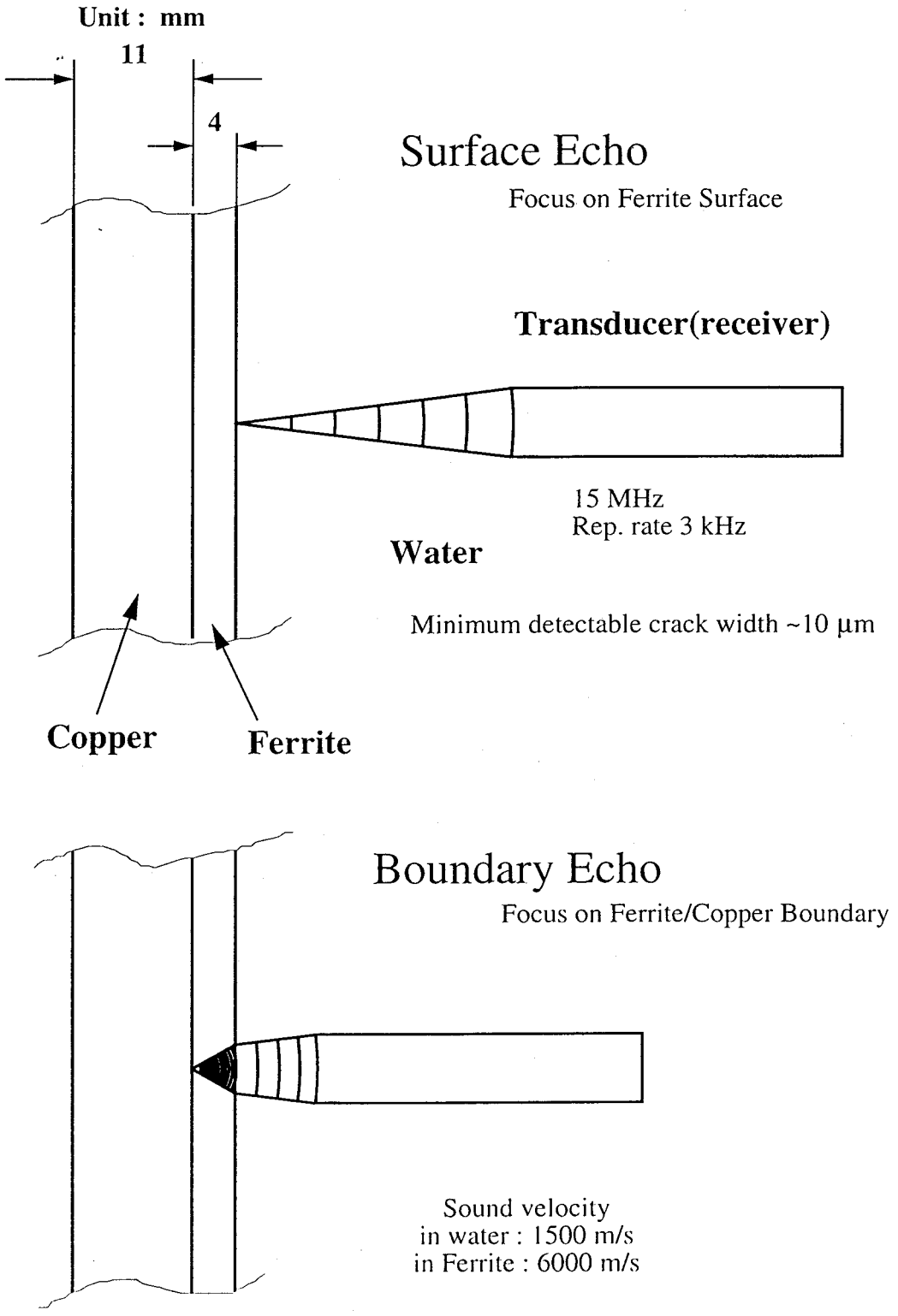

Fig. C-1: Schematic of acoustic tomography. Measurements of the echo from the ferrite surface and that from the boundary between the ferrite and copper.

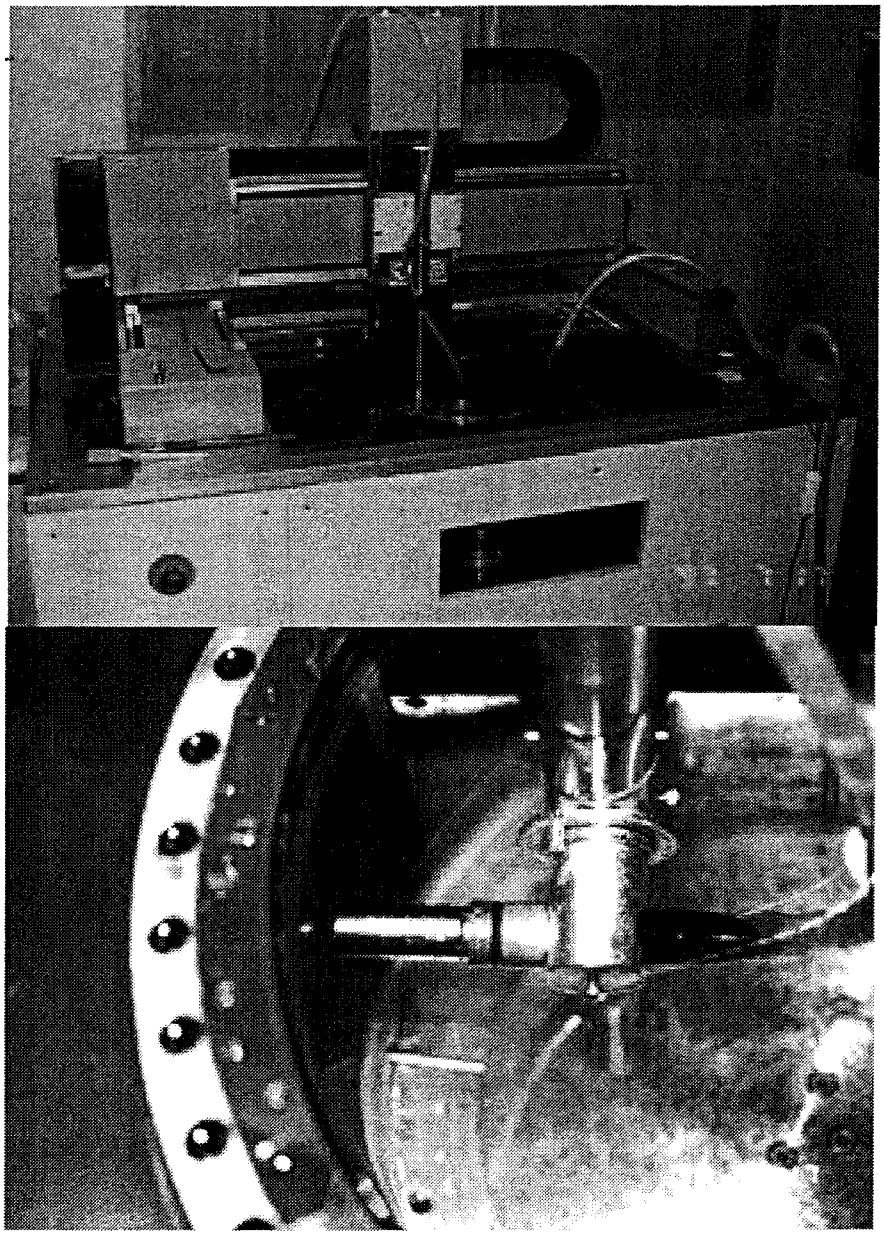

Fig. C-2: Apparatus for acoustic tomography. Water reservoir and moving arm at the end of which acoustic sensor is attached (top). An absorber is immersed in water and measured (bottom) [57].

Appendix D:

Some web pages for monitoring SCC's

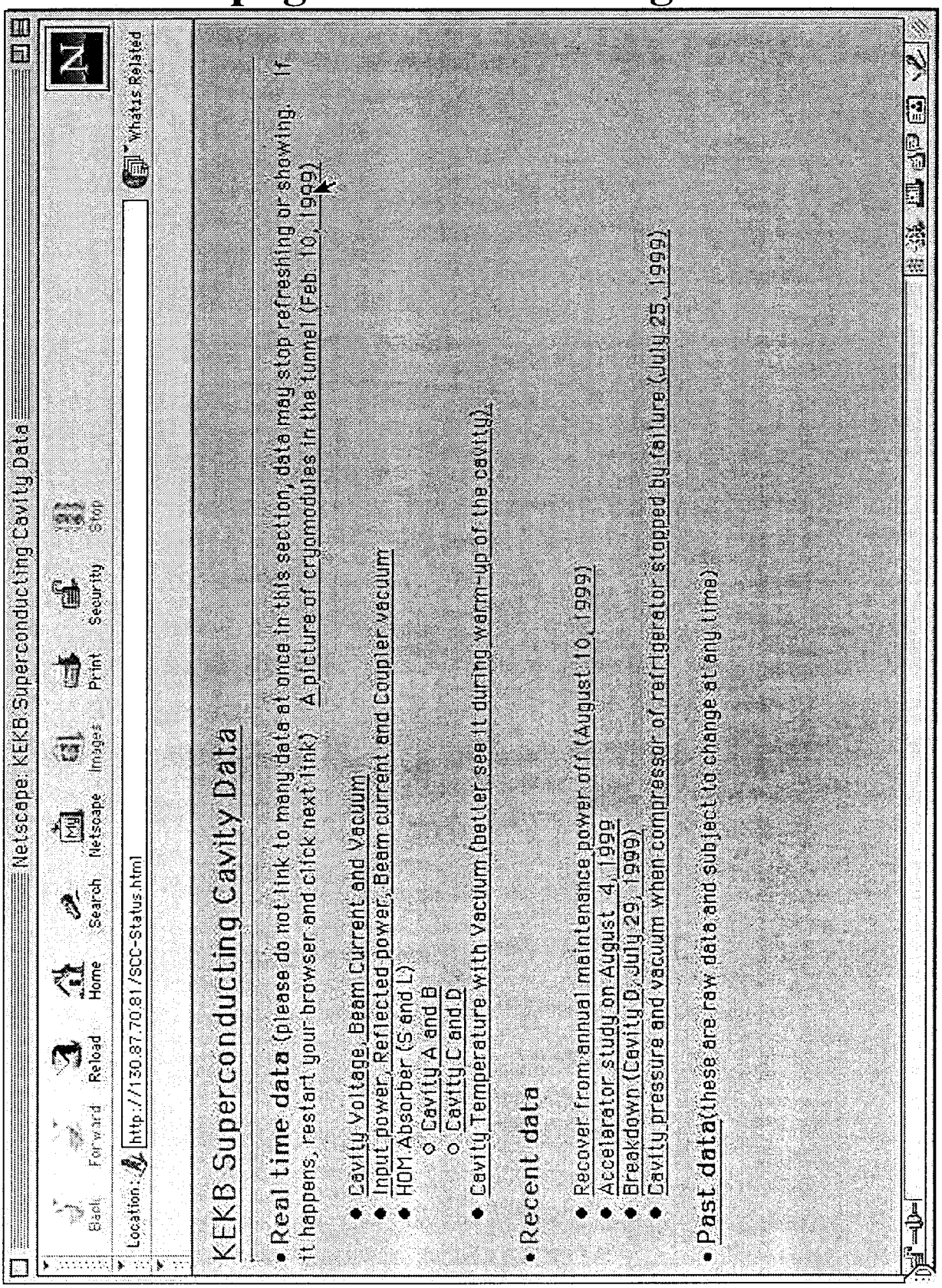

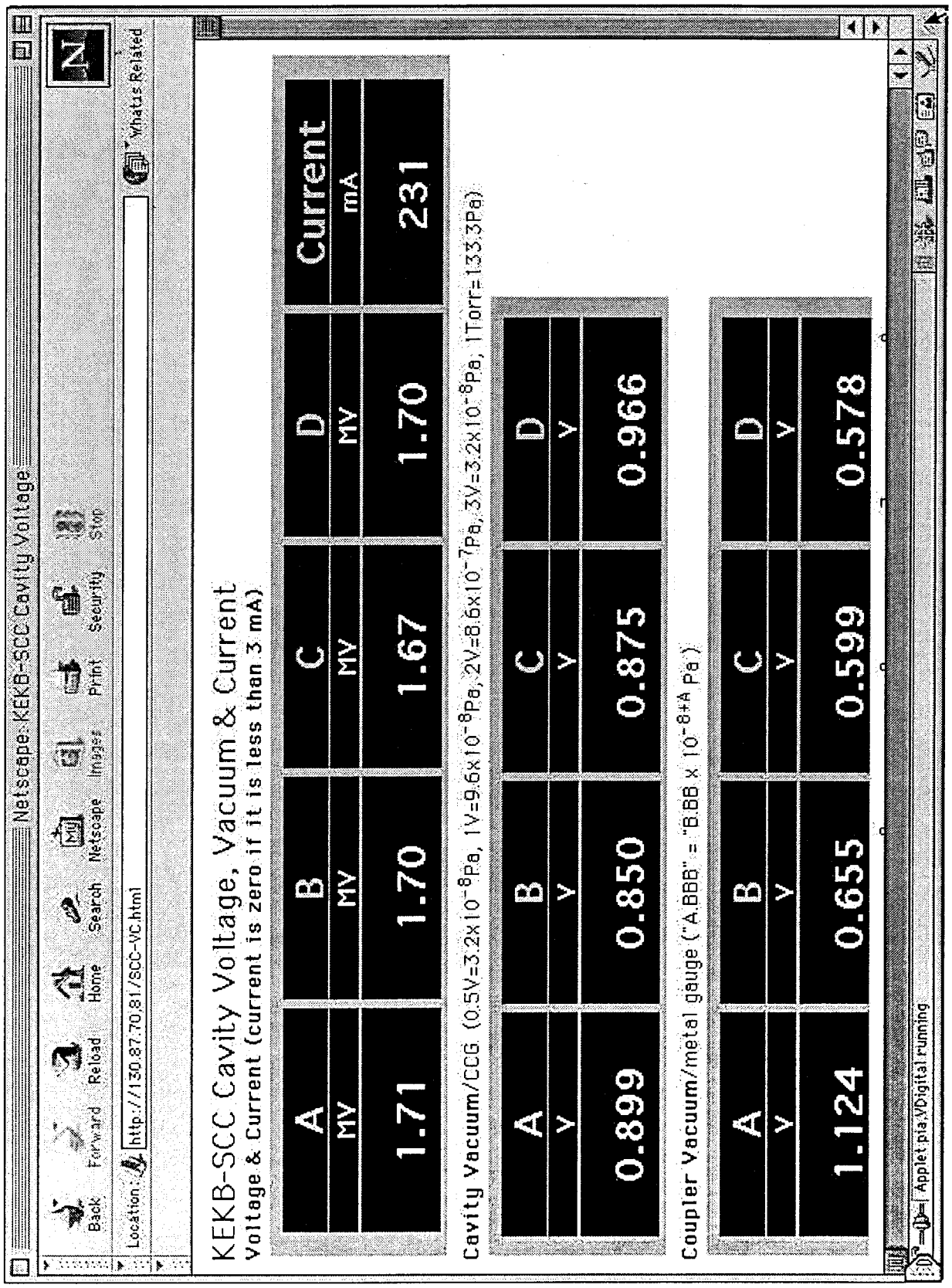
Netscape: KEKB-SCC Cavity Voltage
Back
Forward
Reload
Home
Search
Netscape
Images
Print
Security
Stop
Location: http://130.87.70.81/SCC-VC.html
What's Related
KEKB-SCC Cavity Voltage, Vacuum & Current
Voltage & Current (current is zero if it is less than 3 mA)
A MV 1.71
B MV 1.70
C MV 1.67
D MV 1.70
Current mA 231
Cavity Vacuum/CCG (0.5V=3.2x10-8Pa, 1V=9.6x10-8Pa, 2V=8.6x10-7Pa, 3V=3.2x10-8Pa, 1Torr=133.3Pa)
A V 0.899
B V 0.850
C V 0.875
D V 0.966
Coupler Vacuum/metal gauge ("A.BBB" = "B.BB x 10-8+A Pa")
A V 1.124
B V 0.655
C V 0.599
D V 0.578
Applet pia.VDigital running

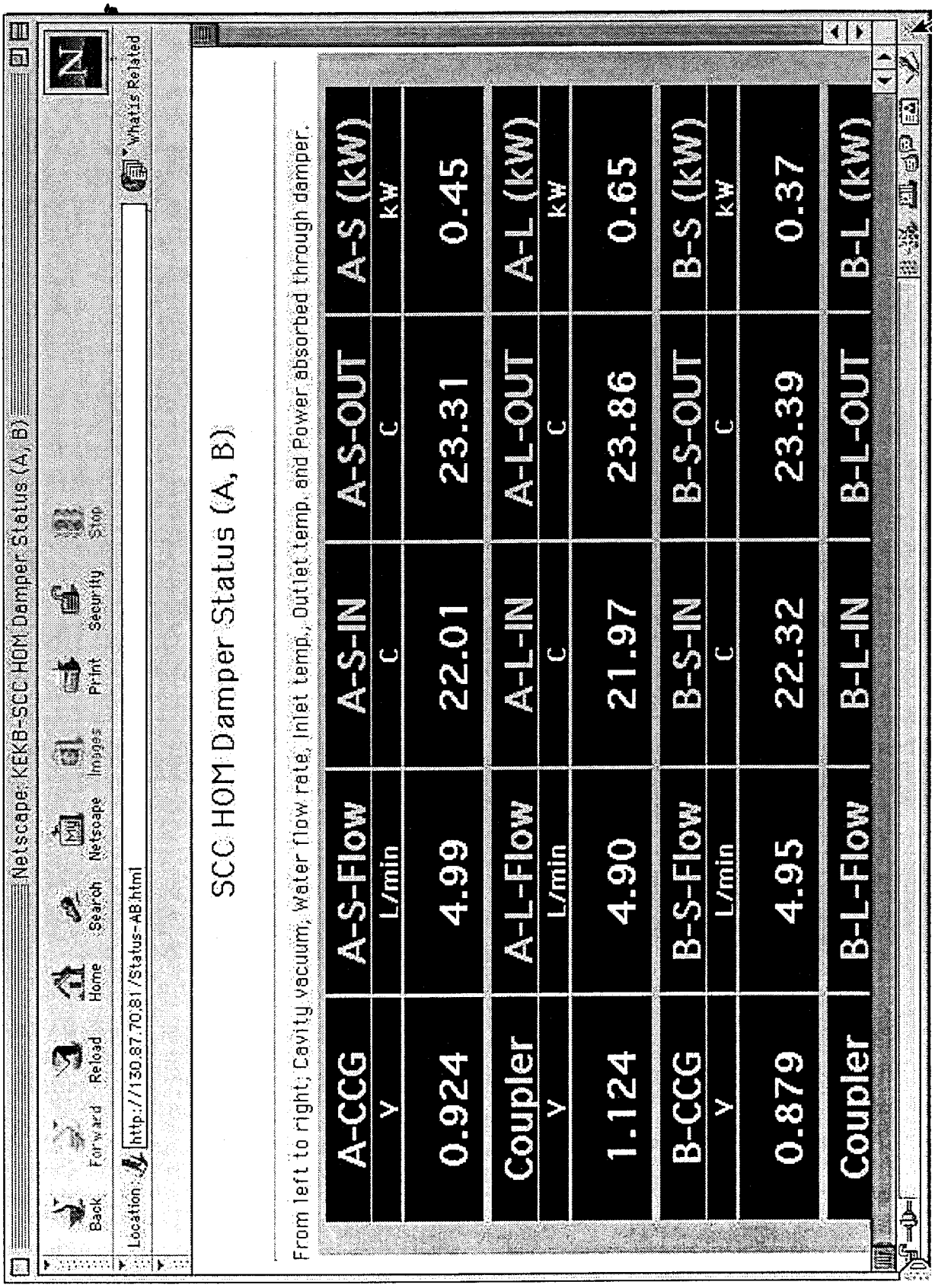
Netscape: KEKB-SCC HOM Damper Status (A, B)
Back
Forward
Reload
Home
Search
Netscape
Images
Print
Security
Stop
Location: http://130.87.70.81/Status-AB.html
What's Related
SCC HOM Damper Status (A, B)
From left to right; Cavity vacuum, Water flow rate, Inlet temp., Outlet temp, and Power absorbed through damper.
A-CCG
V
0.924
Coupler
V
1.124
B-CCG
V
0.879
Coupler
A-S-Flow
L/min
4.99
A-L-Flow
L/min
4.90
B-S-Flow
L/min
4.95
B-L-Flow
A-S-IN
C
22.01
A-L-IN
C
21.97
B-S-IN
C
22.32
B-L-IN
A-S-OUT
C
23.31
A-L-OUT
C
23.86
B-S-OUT
C
23.39
B-L-OUT
A-S (kW)
kW
0.45
A-L (kW)
kW
0.65
B-S (kW)
kW
0.37
B-L (kW)